

THE DEVELOPMENT OF $\text{CuIn}_{1-x}\text{Al}_x\text{Se}_2$ THIN FILMS FOR USE IN PHOTOVOLTAIC SOLAR CELLS

PARESH SURESH NASIKKAR

A thesis submitted in partial fulfilment of the requirements of the University of Northumbria at Newcastle upon Tyne for the degree of Doctor of Philosophy.

Research undertaken in the
Northumbria Photovoltaics Applications Centre (NPAC)
in the
School of Computing, Engineering and Information Sciences.

September 2008

ABSTRACT

The aim of the work presented in this thesis was to develop CuInSe_2 (CIS) and $\text{CuIn}_{1-x}\text{Al}_x\text{Se}_2$ (CIAS) thin films for application in photovoltaic (PV) solar cells. The purpose of the addition of aluminium (Al) in CIS thin films was to modify the energy band gap of the thin films to be nearer to the optimum for PV energy conversion and to replace the less abundant element, gallium (Ga) in $\text{CuIn}_{1-x}\text{Ga}_x\text{Se}_2$ (CIGS) solar cells. This also makes possible the production of tandem solar cells using CIAS to make the wide energy band gap top cell and the CIS to make the narrow energy band gap lower cell. The use of very thin CIS and CIAS absorber layers in solar cell structures was also investigated; the aim was to reduce the amount of indium (In) in cell production.

The CIS and CIAS absorber films were prepared by a sequential two step method in which Cu-In and Cu-In-Al precursor layers were magnetron sputter deposited onto Mo-coated soda lime glass (SLG) substrates; the CIS or CIAS was then formed by heating in a selenium (Se) containing environment. Thin film solar cells were developed in the substrate configuration and had the structure Ni-Al/Indium tin oxide (ITO)/i-ZnO/CdS/CIAS/Mo/SLG. In order to achieve high efficiency solar cells it is an important to optimise the back contact molybdenum (Mo) layer, the absorber layer, the CdS buffer layer, the window layer and top contact layers. The work described in this thesis focused on the optimisation of the back contact and absorber layers.

The thin films were characterised mainly using X-ray diffraction (XRD), energy dispersive X-ray analysis (EDS), scanning electron microscopy (SEM), secondary ion mass spectroscopy (MiniSIMS), atomic force microscopy (AFM) and using spectroscopy measurements to investigate the effect of processing conditions on the composition, crystal structure, surface morphology and the optical properties of the films. The solar cells were characterised by current-voltage (I - V) and incident photon-to-photocurrent conversion efficiency (IPCE) measurements.

Both Mo single and bilayer structures were investigated. It was found that single layers had better properties than Mo bilayers. The optimisation of the Mo deposition sputtering process yielded Mo layers which had good adherence and were conformal to the glass substrates, had low resistivity ($29 \mu\Omega\cdot\text{cm}$), were pin hole free and had good crystallinity.

The influence of Cu-In precursor layers with thicknesses in the range 90-400 nm on the microstructure of the CIS thin films (thicknesses in the range 400-1600 nm) was investigated. Solar cells fabricated from the CIS films of thicknesses 500 nm and 900 nm yielded highest cell conversion efficiencies of 4.3% and 8.2%, respectively.

The selenisation of the magnetron sputter deposited Cu-In-Al precursor layers was carried out at a temperature of 550°C. Films were poor in surface quality and adhesion. Films prepared from the precursor layer with $n [(Al/(Al+In))] = 0.21$ had a non-uniform Al depth profile towards the bottom of the film. Although the film was found to be photoactive its effective energy band gap was 0.98 eV suggesting the properties of CIS. This confirmed incomplete mixing of Al in the thin films which was considered to be segregated at the bottom of the film.

The thinner layers of Cu-In-Al precursors with thicknesses in the range 0.55-1.00 μm and $n [(Al/Al+In)]$ in the range 0.28-0.54 were magnetron sputter deposited. The precursor layers showed the prominent binary $AlCu_4$ compound with a uniform distribution of Al in the layer. Thin films converted from these precursor layers of thicknesses in the range 1.3-2.0 μm were fairly uniform in surface structure. Films with $x \approx 0.2$ were found to have an energy bandgap of 1.10 eV and were also photoactive. Solar cells fabricated from this absorber film yielded a highest cell efficiency of 4.9%.

Environmental impact assessments have been made on materials and the processes used in the fabrication of CIS and CIAS and solar cells. It was found that there is no critical environmental impact of materials and associated processes involved in the fabrication of CIS and CIAS thin film solar cells.

List of contents

	Page
Abstract	i
List of contents	iii
List of figures	viii
List of tables	xvi
List of symbols	xviii
List of abbreviations	xx
Acknowledgements	xxv
Author's declaration	xxvi
Chapter 1 INTRODUCTION	1
Chapter 2 BACKGROUND THEORY	10
2.1 Solar Spectrum	11
2.2 Optical Absorption in a Semiconductor	13
2.3 Indirect and Direct Bandgap Semiconductors	17
2.4 P-n Junction (Thermal Equilibrium Condition)	19
2.5 The Diode Equation	23
2.6 Heterojunctions	28
2.7 Current Transport Mechanisms in Heterojunction Semiconductor	31
2.8 Solar Cells Theory	35
2.9 Optimum Energy Bandgap for Single Junction Solar Cells	44
2.10 Polycrystalline Thin Films for use in Solar Cells	46
2.11 Thin Film CuInSe ₂ based Solar Cell Structures	48
2.12 Losses in Real CuInSe ₂ Photovoltaic Solar Cells	50
Bibliography–Chapter 2	53
Chapter 3 LITERATURE REVIEW	54
3.1 Properties of CuInSe ₂ -based Absorber Material	55

3.2 Historical Development of CuInSe ₂ -based Thin Film	
Solar Cells	58
3.2.1 Single crystal CuInSe ₂ material	58
3.2.2 Polycrystalline CuInSe ₂ thin films	59
3.2.3 Cu(In,Ga)Se ₂ thin films	64
3.3 Major Research Groups and Companies Working on	
CuInSe ₂ -based Thin Films	68
3.3.1 Co-evaporation from elemental sources	68
3.3.2 Selenisation of sputter deposited metallic precursor	
layers	70
3.3.3 Electrodeposition	72
3.3.4 Spray pyrolysis technique	73
3.4 CuAlSe ₂ and Cu (In, Al)Se ₂ Absorber Layers	74
3.5 Deposition of the Back Contact Molybdenum Layer	80
3.6 Buffer Layers	83
3.7 Window Layers and Front Contacts	84
Chapter 4	85
EXPERIMENTAL PROCEDURE	
4.1 Device Processing of CuInSe ₂ -based Thin Film Solar	
Cells	86
4.1.1 Substrate cleaning	86
4.1.2 The sputtering process	88
4.1.2.1 Effects of process parameters on the sputtering	
process	90
4.1.2.2 Essential process steps before actual sputter	
deposition	90
4.1.2.3 DC and RF magnetron sputtering depositions	91
4.1.2.4 Magnetron sputtering deposition systems	92
4.1.2.4.1 Nordiko 2000 RF magnetron sputtering	
system	92
4.1.2.4.2 Kurt J Lesker magnetron sputtering system	95
4.1.3 Selenisation process	97
4.1.4 The etching process using KCN solution	100
4.1.5 CdS buffer layer deposition	100

4.1.6 Window layer depositions	102
4.2 Material Characterisation Methods	103
4.2.1 X-ray diffraction technique	103
4.2.2 Scanning electron microscopy and energy dispersive X-ray spectroscopy	110
4.2.3 Optical spectral measurements (transmittance and reflectance)	114
4.2.4 Secondary ion mass spectroscopy	116
4.2.5 Atomic force microscopy	118
4.2.6 Four-point probe method	119
4.3 Solar Cell Characterisation Methods	123
4.3.1 Current-density versus voltage measurements	123
4.3.2 Incident photon-to-photocurrent conversion efficiency measurements	125
4.3.3 Photoactivity testing of the absorber layer	127
Bibliography–Chapter 4	129
Chapter 5 RESULTS AND DISCUSSIONS	130
5.1 Molybdenum as a Back Contact Layer	131
5.1.1 Effect of argon sputtering gas pressure and flow on structural and electrical properties of the Mo films	131
5.1.2 Effect of argon sputtering gas flow on structural and electrical properties of the Mo films	138
5.1.3 Mo bilayer deposition	143
5.1.4 Discussion	146
5.2 CuInSe ₂ Absorber Layers	153
5.2.1 The Cu-In precursor layers	153
5.2.2 Selenisation of sputter deposited Cu-In precursor layers	160
5.2.3 Conversion of thinner layers of Cu-In precursors into CuInSe ₂ absorber films	167

5.2.4 Discussion	180
5.3 CuInSe ₂ Thin Film Solar Cells	186
5.3.1 Fabrication of CuInSe ₂ thin film solar cells	186
5.3.2 <i>J-V</i> characteristics of solar cells made from thinner absorber films B and D	188
5.3.3 Incident photon to photocurrent conversion efficiency measurement	191
5.3.4 Discussion	191
5.4 Thicker CuIn _{1-x} Al _x Se ₂ Absorber Thin Films	201
5.4.1 The Cu-In-Al precursor layers	201
5.4.1.1 Deposition of binary Al-In compounds	201
5.4.1.2 First set of Cu-In-Al precursor layers	204
5.4.2 Selenisation of sputter deposited Cu-In-Al precursor layers	208
5.4.3 Fabrication of solar cells based on sample KJL-C (N66D) absorber layers	218
5.4.4 IPCE output of Cu(In,Al)Se ₂ solar cells	220
5.4.5 Discussion	220
5.5 Thinner CuIn _{1-x} Al _x Se ₂ Absorber Films and Solar Cells	226
5.5.1 The thinner layers of Cu-In-Al precursors	226
5.5.2 Annealing of the Cu-In-Al precursor layers for different temperatures and pressures	230
5.5.2.1 Annealing of the Cu-In-Al precursor layers for different temperatures	230
5.5.2.2 Annealing of the Cu-In-Al precursor layer at different Ar pressures	234
5.5.3 Selenisation of the thinner layers of Cu-In-Al precursors	236
5.5.4 The solar cell fabrication using thinner CIAS absorber films	246
5.5.5 Discussion	249

Chapter 6 ENVIRONMENTAL IMPACTS OF MATERIALS AND PROCESSES RELATED TO CuInSe₂ AND

	Cu(In,Al)Se₂ THIN FILM SOLAR CELLS	259
	6.1 Introduction	260
	6.2 The Soda Lime Glass Cleaning Process	267
	6.3 The Back Contact Molybdenum Deposition on SLG	268
	6.4 The Cu-In and Cu-In-Al Precursor Layer Depositions and CuInSe ₂ /Cu(In,Al)Se ₂ Absorber Formations on Mo- coated Glass Substrates	270
	6.5 KCN Etching Process	276
	6.6 CdS Deposition by CBD method	277
	6.7 ZnO, TCO and Front Metallic Ni-Al Layers Depositions	280
	6.8 Discussion	281
Chapter 7	CONCLUSIONS AND FUTURE WORK	284
	7.1 Conclusions	285
	7.2 Future Work	291
	List of References	293
	APPENDICES	316
	Appendix I	317
	Appendix II	325
	Appendix III List of Publications and Presentations During PhD	326

List of figures

	Page
Chapter 2	
Figure 2.1	The graph shows solar spectrum irradiance curves for space (AM0) and terrestrial (AM1.5) conditions 12
Figure 2.2	Optical absorption in a semiconductor..... 14
Figure 2.3	(a) Optical absorption in a semiconductor under illumination and (b) exponential decay of incident photon flux..... 15
Figure 2.4	Energy band structures of indirect (Si) and direct bandgap (GaAs) semiconductors..... 18
Figure 2.5	(a) <i>P</i> -type and <i>n</i> -type semiconductor material before junction formation, (b) flow of electrons and holes after <i>p-n</i> junction formation in thermal equilibrium..... 20
Figure 2.6	A forward bias applied to the <i>pn</i> junction semiconductor... 24
Figure 2.7	(a) Energy-band diagram of semiconductors <i>p</i> -type CuInSe ₂ and <i>n</i> -type CdS before junction formation; (b) Energy-band alignment between CuInSe ₂ and CdS semiconductors forming <i>p-n</i> junction heterojunction..... 29
Figure 2.8	Tunnelling-recombination mechanism in heterojunction.... 32
Figure 2.9	Conduction mechanisms in heterojunction semiconductors. 34
Figure 2.10	(a) A <i>p-n</i> junction under illumination, (b) an equivalent circuit of an ideal solar cell..... 36
Figure 2.11	Schematic diagram of <i>J-V</i> characteristic of a solar cell in dark and under illumination..... 38
Figure 2.12	Simple equivalent circuit for a solar cell including series and shunt resistances..... 41
Figure 2.13	Effect of (a) increasing series resistance and (b) decreasing shunt (parallel) resistance on the solar cell output (current-voltage) curve..... 42
Figure 2.14	Thin film solar cell structures..... 49

Figure 2.15	Reflection and absorption of incident photons in CIS-based thin film solar cell.....	51
--------------------	--	----

Chapter 3

Figure 3.1	Alloying with Ga or Al changes energy band gap and lattice constants a and c	57
Figure 3.2	Cross-sectional view of the CdS/CuInSe ₂ solar cell developed by ARCO Solar	61
Figure 3.3	Energy band gap variations in absorber films with content x [$x = X/(In+X)$; where X can be Ga or Al].....	75

Chapter 4

Figure 4.1	The flow chart of fabrication of CuInSe ₂ and Cu(In,Al)Se ₂ thin film solar cells with available equipment used and processes mentioned in a square bracket.....	87
Figure 4.2	The principle of the sputtering process.....	89
Figure 4.3	Schematic diagram of Nordiko 2000 RF magnetron sputtering system.....	93
Figure 4.4	Photograph of the Nordiko 2000 RF magnetron sputtering system.....	94
Figure 4.5	The arrangement of SLG substrates on the platen.....	94
Figure 4.6	Photograph of the Kurt J Lesker magnetron sputtering system.....	96
Figure 4.7	Schematic diagram of tube furnace and magnified view of a graphite box with the sample.....	98
Figure 4.8	Photograph of the tube furnace with the graphite box inside the tube and temperature profile of the central zone of the tube furnace	99
Figure 4.9	Schematic diagram of CBD setup.....	101
Figure 4.10	Working principle of X-ray diffractometer.....	105
Figure 4.11	Simplified diagram of the XRD instrument in the θ - 2θ configurations.....	106

Figure 4.12	Photograph of the Siemens D5000 X-ray diffractometer.....	106
Figure 4.13	Diffraction peak width at FWHM.....	109
Figure 4.14	Effect of lattice strain on peak position.....	109
Figure 4.15	Photograph of the FEI Quanta 200 (EDS) and Oxford Instrument (SEM) systems.....	111
Figure 4.16	Electron beam interactions with thin film in EDS analysis.	113
Figure 4.17	Photograph of the Shimadzu Solidspec3700 spectrophotometer in the laboratory.....	115
Figure 4.18	Basic working principle of SIMS instrument.....	117
Figure 4.19	Photograph of a bench-top MiniSIMS instrument.....	117
Figure 4.20	Schematic diagram of AFM instrument.....	120
Figure 4.21	Schematic diagram of four point probe method for resistivity measurement.....	121
Figure 4.22	Series (R_S) and shunt (R_{Sh}) resistance calculations by using $J-V$ characteristic of solar cell.....	124
Figure 4.23	Experimental setup for IPCE measurement.....	128
Figure 4.24	Schematic diagram of photoactivity testing set up for the absorber layers.....	128
Figure 4.25	The waveform shows photoactive or non-working types of the absorber layers.....	128

Chapter 5

Figure 5.1	The plot of Mo film growth rate and resistivity with pressure variations inside the main chamber.....	134
Figure 5.2	XRD patterns of the Mo layers (a) in the range 10-90 degrees and (b) the main Mo (110) reflection for various Ar pressures.....	135
Figure 5.3	The plots of (a) FWHM variation of the Mo main (110) peak and (b) percentage strain on as-deposited Mo films as a function of Ar pressure inside the main chamber.....	137
Figure 5.4	SEM surface images of Mo thin films for various Ar	

	pressures; (a) 2.6 mTorr, (b) 5.3 mTorr, (c) 7.8 mTorr and (d) 10 mTorr	139
Figure 5.5	SEM cross-sectional image of the Mo thin film on the SLG substrate.....	139
Figure 5.6	Variations in the Mo film (a) growth rate and (b) resistivity with Ar gas flow in the main chamber	141
Figure 5.7	The graphs of the Mo films (a) FWHM width of the prominent (110) peak and (b) percentage strain versus Ar gas flow.....	142
Figure 5.8	The SEM surface morphology image of one of the Mo layers (Sample-N137Q) sputter deposited at higher pressure (100 mTorr) shows many pinholes.....	144
Figure 5.9	Flow chart diagram of CuInSe ₂ thin film solar cell processing.....	154
Figure 5.10	EDS at.% ratio variation with Cu/In power ratio.....	157
Figure 5.11	The XRD pattern of the sputter deposited Cu-In precursor layers (Sample-N94) on the Mo-coated glass substrate.....	158
Figure 5.12	(a) The EDS spectrum and (b) the SEM surface image of the sputter deposited Cu-In precursor layers (Sample-N94) on the Mo-coated glass substrate	159
Figure 5.13	Temperature profile for single-step and two-step selenisation process in a graphite box.....	161
Figure 5.14	XRD spectra of films selenised at different temperatures; 250°C (Sample-N161J1), 350°C (Sample-N161J2) and 500°C (Sample-N161J3).....	162
Figure 5.15	SEM images of surface of the films selenised at different temperatures; (a) 250°C (Sample-N161J1), (b) 350°C (Sample-N161J2) and (c) 500°C (Sample-N161J3).....	165
Figure 5.16	XRD of CIS thin films on glass substrate produced by using the Se cap layer.....	166
Figure 5.17	SEM images of the surface (left) and cross-sectional view (right) of the CIS thin film on Mo-coated glass substrate	

	selenised at 500°C	166
Figure 5.18	XRD graph of the different thickness Cu-In precursor layers of the samples B (130 nm), D (240 nm) and F (400 nm).....	169
Figure 5.19	SEM (left) and AFM (right) surface images of the Cu-In precursor layers of different thicknesses of samples (a) B (130 nm), (b) D (240 nm) and (c) F (400 nm).....	171
Figure 5.20	MiniSIMS depth profile of the Cu-In precursor layer of sample D (240 nm).....	172
Figure 5.21	XRD pattern of the CIS films of the samples B (500 nm), D (900 nm) and F (1600 nm).....	173
Figure 5.22	Preferential orientation variation with CIS absorber film thickness.....	173
Figure 5.23	SEM (left) and AFM (right) surface images of the CIS thin films of samples: (a) B (500 nm), (b) D (900 nm) and (c) F (1600 nm).....	174
Figure 5.24	Grain size variations with the CIS absorber film thicknesses.....	176
Figure 5.25	MiniSIMS depth profile of CIS thin film of sample F (1600 nm).....	177
Figure 5.26	Energy band gaps of the CIS films on the glass substrates of thicknesses; a = 500 nm (sample B), b = 900 nm (sample D) and c = 600 nm (sample F).....	179
Figure 5.27	Photograph shows the final stages of CIS fabrication process.....	187
Figure 5.28	Distributions of output parameters (V_{OC} , J_{SC} , FF and η) in the CIS thin film solar cells of the samples B and D with cell location	189
Figure 5.29	J - V characteristics for solar cells included absorber layers B (500 nm) and D (900 nm) of different thickness.....	190
Figure 5.30	IPCE spectra for solar cells of the absorbers B (500 nm) and F (1600 nm).....	192
Figure 5.31	Photograph shows shadowing loss due to the measuring	

	probe in contact with solar cell in the I - V measurement.....	196
Figure 5.32	Comparison between J - V characteristics of the solar cell fabricated in this work (cell D) and NREL's highest efficient CIS and CIGS solar cells with 1 μ m-thick CIGS absorber layer.....	198
Figure 5.33	XRD spectra of sputter deposited Al-In layers of different compositions.....	203
Figure 5.34	SEM images of surface morphology of sputter deposited Al-In layers (a) AlIn-1, (b) AlIn-2, (c) AlIn-3 and (d) AlIn-4.....	205
Figure 5.35	(a) The EDS spectrum and (b) the SEM picture of the cross-sectional view of the sample AlIn-3 on the SLG substrate.....	206
Figure 5.36	XRD patterns of the Cu-In-Al precursors of the samples (a) KJL-A, (b) KJL-B, (c) KJL-C, (d) KJL-D, (e) KJL-E and (f) KJL-F.....	209
Figure 5.37	XRD graph of the films selenised from the Cu-In-Al precursor layers (a) KJL-A, (b) KJL-B, (c) KJL-C, (d) KJL-D, (e) KJL-E and (f) KJL-F.....	210
Figure 5.38	XRD of the main reflection (112) of CIS (no Al) and Al content absorber films.....	212
Figure 5.39	SEM surface (left) and cross-sectional (right) images of films selenised on Mo-coated SLG substrates; (a) KJL-A, (b) KJL-B and (c) KJL-C.....	214
Figure 5.40	SEM surface (left) and cross-sectional (right) images of films selenised on Mo-coated SLG substrates; (d) KJL-D, (e) KJL-E and (f) KJL-F.....	215
Figure 5.41	MiniSIMS depth profile of the absorber film prepared from the Cu-In-Al precursor layer of the sample KJL-C (N66D).	217
Figure 5.42	Flow chart diagram of CIAS thin film solar cell processing.	219
Figure 5.43	IPCE spectrum of the solar cells including the absorber film prepared from the Cu-In-Al precursor layer of the sample KJL-C (Sample-N66D).....	221

Figure 5.44	XRD patterns of the Cu-In-Al precursor layers on the Mo-coated SLG substrate; (a) KJL-G and (b) KJL-I.....	228
Figure 5.45	SEM image of surface morphology of the Cu-In-Al precursor layer with $n = 0.28$ (Sample: KJL-G).....	228
Figure 5.46	MiniSIMS depth profiling scan of the Cu-In-Al precursor layer of the sample K181K (equivalent to sample KJL-G) with $n \approx 0.28$	229
Figure 5.47	XRD pattern of the Cu-In-Al precursor layers (Sample KJL-I) selenised at different temperatures in a Se environment: (a) 250°C, (b) 400°C and (c) 550°C.....	232
Figure 5.48	SEM surface morphology of the selenised films prepared from the Cu-In-Al precursor layers (Sample KJL-I) at different temperatures; (a) 250°C, (b) 400°C, (c) 500°C and (d) 550°C.....	233
Figure 5.49	SEM surface morphology of the films selenised from the Cu-In-Al precursor layers (Sample KJL-I) for Ar pressures; (a) 1 mbar, (b) 5 mbar and (c) 10 mbar.....	235
Figure 5.50	XRD patterns of the (112) reflections for CIS ($x = 0$) and CIAS films with increasing Al content (n) in the precursors	237
Figure 5.51	Variations in (a) intensity and (b) FWHM of the prominent CIS or CIAS (112) diffraction peak with n content in the Cu-In-Al precursor layers.....	239
Figure 5.52	Variation in lattice spacing $d(112)$ of the selenised film with Al content in the precursor layer	240
Figure 5.53	Lattice constants a and c of the films selenised from the precursor layers with variation in ' $n = (Al/Al+In)$ ' content..	240
Figure 5.54	The SEM surface morphology (left) and the cross-sectional images (right) of the CIAS films; (a) KJL-G, (b) KJL-H and (c) KJL-I.....	242
Figure 5.55	MiniSIMS spectra of the CIAS film on the glass substrate selenised from the Cu-In-Al precursor layer of the sample K181K (from the same batch of KJL-G ($n \approx 0.28$)).....	243

Figure 5.56	The plot of $(\alpha h \nu)^2$ versus $(h \nu)$ for the sample K181K CIAS film ($n \approx 0.28$ in the precursor layer) on the SLG substrate .	245
Figure 5.57	V_{OC} , J_{SC} , FF and η distributions in CIAS thin film solar cells fabricated using absorber films of sample N172H4 (similar to sample KJL-G).....	247
Figure 5.58	J - V characteristic for the CIAS thin film solar cell C5G fabricated using absorber films of sample N172H4 (similar to sample KJL-G).....	248
 Chapter 6		
Figure 6.1	The constituent layers in CuInSe_2 based solar cells manufactured by major companies.....	261
 Appendices		
Appendix I		
Figure A	Pressure inside the Nordiko 2000 Rf magnetron sputtering system chamber with different Ar gas flow and throttle valve settings.....	317
Figure B	Normalized transmittance (top) and reflectance (bottom) versus wavelength pattern of CIS thin films of samples (a) B (500 nm); (b) D (900 nm) and (c) F (1600 nm).....	318
Figure C	The graph of transmittance versus wavelength of optimised CdS, i-ZnO and ITO layers.....	319
Figure D	The graph of $(\alpha h \nu)^2$ versus $h \nu$ of good quality optimised i-ZnO and ITO layers.....	320
Figure E	The graph of transmittance (%) versus wavelength of CIAS thin film on the glass substrate prepared from the precursor layer with $n = 0.28$ (Sample KJL-G).....	321
Figure F	Phase diagram of Cu-In alloy.....	322
Figure G	Phase diagram of Al-In alloy.....	323
Figure H	Phase diagram of Cu-Al alloy.....	324

List of tables

	page
Chapter 3	
Table 3.1	Summary of CuInSe ₂ -based absorber layer deposition techniques and solar cell parameters reported by leading researchers around the World..... 79
Chapter 5	
Table 5.1	Summary of sputter deposition settings established during Mo film depositions..... 132
Table 5.2	Table of the average values of Mo film growth rate, sheet resistance, resistivity according to Ar flow and pressure settings..... 134
Table 5.3	XRD data of the Mo films for different Ar pressure and flow settings..... 136
Table 5.4	Thickness and resistivity values obtained in Mo bilayer depositions for different parameters..... 145
Table 5.5	The research work reported by research groups (working on CuInSe ₂ -based thin film solar cells) around the World on the Mo layers deposited using a sputtering technique..... 152
Table 5.6	EDS results of the precursor layers in at.% of Cu and In with variation in power applied to Cu target for fixed In target power of 80 W..... 156
Table 5.7	Summary of data obtained using XRD and EDS techniques on the selenised CuInSe ₂ films at different temperatures.... 163
Table 5.8	EDS and XRD data analyses of the Cu-In precursor layers and CuInSe ₂ thin films with different thicknesses..... 168
Table 5.9	Comparison of the solar cell parameters reported by NREL and the University of Uppsala groups with those described in this thesis..... 197
Table 5.10	The Al-In samples with compositions in at.% measured by

	EDS.....	202
Table 5.11	EDS compositional analyses and thicknesses of the Cu-In-Al precursor layers with metal target power settings.....	207
Table 5.12	XRD phases detected for the precursor layers and thin films of samples KJL-A to KJL-F.....	211
Table 5.13	The Cu-In-Al precursor layers of varying Al content.....	227
Table 5.14	XRD analyses of CuInSe ₂ and Cu(In,Al)Se ₂ thin films.....	238
 Chapter 6		
Table 6.1	Environmental impact assessment of material used in CuInSe ₂ and Cu(In,Al)Se ₂ based thin film solar cells.....	262

List of symbols

Symbol	Description	Unit
a, c	Lattice constants	Å
N	Ideality factor	-
α	Absorption coefficient	cm ⁻¹
C_{hkl}	Texture coefficient	-
D	Diffusion coefficient	cm ² /s
D_n	Diffusion coefficient of electrons	cm ² /s
E_g	Energy bandgap	eV
E_C	Bottom of conduction band	eV
E_V	Top of valence band	eV
E_F	Fermi energy level	eV
E_i	Intrinsic Fermi level	eV
E	Electric field	V/cm
h	Planck constant	J-s
$h\nu$	photon energy	eV
h, k, l	Miller indices	-
I	Current	mA
I_{SC}	Short circuit current	mA
I_S	Reverse saturation current of the diode	mA
J	Current Density	mA/cm ²
J_{SC}	Short circuit current density	mA/cm ²
J_0	Saturation current density.	mA/cm ²
k	Boltzmann constant	J/K
kT	Thermal energy	eV
L_p	Diffusion length of holes	nm or μm
L_n	Diffusion length of electrons	nm or μm
n	Density of free electrons	cm ⁻³
n_i	Intrinsic density	cm ⁻³
n_{no}	Equilibrium electron densities in the n	cm ⁻³
n_{po}	Equilibrium electron densities in the p -sides	cm ⁻³
n_n	Electron densities at non-equilibrium at the boundaries of the depletion region in the n - region	cm ⁻³
n_p	Electron densities at non-equilibrium at the boundaries of the depletion region in the p - region	cm ⁻³
p	Density of free holes	cm ⁻³

p_{no}	Equilibrium hole density on the n -type side of the semiconductor	cm^{-3}
p_{po}	Equilibrium hole density on the p -type side of the semiconductor	cm^{-3}
q	Electronic charge	C
R_S	Series resistance	$\Omega \cdot \text{cm}^{-2}$
R_{Sh}	Shunt or parallel resistance	$\Omega \cdot \text{cm}^{-2}$
t	Thickness	nm or μm
μ_n	Electron mobility	$\text{cm}^2/\text{V}\cdot\text{s}$
μ_p	Hole mobility	$\text{cm}^2/\text{V}\cdot\text{s}$
V_0	Potential difference between p -type side and n -type side of a semiconductor	V
V_{OC}	Open circuit voltage	V
x_p	Minority carrier densities at the boundary of the depletion region (p -type side)	cm^{-3}
x_n	Minority carrier densities at the boundary of the depletion region (n -type side)	cm^{-3}
τ	Lifetime or decay time	s
ϕ_0	Photon flux	photons/ cm^2/s
ρ	Resistivity	$\Omega \cdot \text{cm}$
λ	Wavelength	nm or μm or \AA
η	The solar cell conversion efficiency	%
ν	Frequency of light	Hz
θ	Angle	$^\circ$
σ	Degree of preferred orientation	-
χ	Electron affinity	eV

List of abbreviations

A

AFM	Atomic force microscopy
Ag	Silver
AgCl	Silver chloride
Al	Aluminium
Al ₂ O ₃	Aluminium oxide
ALD	Atomic layer deposition
AM	Air mass
Ar	Argon
ARC	Antireflection coating
a-Si:H	Amorphous silicon
at.%	Atomic percentage

B

BSF	Back surface field
-----	--------------------

C

CuInSe ₂	Copper indium diselenide
CuInS ₂	Copper indium disulphide
CuIn _{1-x} Ga _x Se ₂	Copper indium gallium diselenide
CuGaSe ₂	Copper gallium diselenide
CuCl ₂	Copper dichloride
CuAlSe ₂	Copper aluminium diselenide
Cu ₂ Se	Copper selenide
Cu(In,Ga)(S,Se) ₂	Copper indium gallium disulphur diselenide
Cu(In,Al)Se ₂	Copper indium aluminium diselenide
Cu	Copper
CS(NH ₂) ₂	Thiourea
Cr	Chromium
COSHH	Control of Substance Hazardous to Health
CIS	Copper indium diselenide
CIGS	Copper indium gallium diselenide
CIAS	Copper indium aluminium diselenide
CuIn _{1-x} Al _x Se ₂	Copper indium aluminium diselenide
CF	Correction factor
CdTe	Cadmium telluride

CdS	Cadmium sulphide
CdCl ₂	Cadmium chloride
Cd	Cadmium
CBD	Chemical bath deposition
CAS	Copper aluminium diselenide
D	
DC	Direct current
DI	De-ionised
E	
EC	European Commission
ED	Electrodeposition
EDS	Energy dispersive X-ray spectroscopy
EU	European Union
F	
fcc	Face centred cubic
FF	Fill factor
Fig.	Figure
FWHM	Full width at half maximum
G	
Ga	Gallium
GaAs	Gallium arsenide
GaCl ₃	Gallium trichloride
Ga _x Al _{1-x} As	Gallium aluminium arsenide
GB	Graphite box
H	
H ₂	Hydrogen
H ₂ Se	Hydrogen selenide
H ₂ SeO ₃	Hydrogen selenide trioxide
HSE	Health and Safety Executive
I	
i:ZnO	Intrinsic zinc oxide
ICDD	International Centre for Diffraction Data
ID	Identification
IDLH	Immediately Dangerous to Life and Health
IEC	Institute of Energy Conversion
In	Indium

In(O,H)S	
In ₂ S ₃	Indium trisulphide
In ₂ Se ₃	Indium triselenide
InCl ₃	Indium trichloride
InP	Indium phosphide
IPA	Iso-propyl alcohol
IPCE	Incident photon-to-photocurrent conversion efficiency
IFE	Institute of Physical Electronic
ISET	International Solar Electric Technology
ITO	Indium tin oxide
J	
JCPDS	Joint Committee on Powder Diffraction Standards
K	
KCN	Potassium cyanide
KJL	Kurt J Lesker
M	
mfp	Mean free path
Mn	Manganese
Mo	Molybdenum
MSDS	Material safety data sheet
N	
N ₂	Nitrogen
Na	Sodium
NaOH	Sodium hydroxide
NaSe	Sodium selenide
Nb	Niobium
NH ₃	Ammonia
NH ₄ Cl	Ammonium chloride
Ni	Nickel
NREL	National Renewable Energy Laboratory
O	
O ₂	Oxygen
OEL	Occupation exposure limit
OSHA	Occupational Safety and Health Administration
P	
PDF	Powder diffraction file

PEL	Permissible exposure limit
Pt	Platinum
PV	Photovoltaic
PVD	Physical vapour deposition
Q	
QE	Quantum efficiency
R	
R%	Percentage reflectance
RE	Reference electrode -
RF	Radio frequency
rpm	Rotation per minute
RTP	Rapid thermal process
S	
S	Sulphur
sccm	Standard cubic centimetres per minute
Se	Selenium
SE	Secondary electrode
SEL	Stack elemental layer
SEM	Scanning electron microscope
Si	Silicon
SIMS	Secondary ion mass spectroscope
SiO _x	Silicon oxide
SLG	Soda-lime glass
SPSM	Screen printing and sintering method
STC	Standard test condition
T	
T%	Percentage transmittance
Ta	Tantalum
TCO	Transparent conductive oxide
Ti	Titanium
TLV	Threshold limit value
TWA	Time weighted average
U	
USA	United States of America
UK	United Kingdom
UV-VIS-NIR	Ultraviolet-visible-near infrared

V	
V	Vanadium
W	
W	Tungsten
WE	Working electrode
X	
Xe	Xenon
XPS	X-ray photoelectron spectroscopy
XRD	X-ray diffraction
Z	
(Zn,In)Se	Zinc indium selenide
Zn	Zinc
ZnO:Al	Aluminium doped zinc oxide
ZnMgO	Zinc magnesium oxide
ZnO	Zinc oxide
ZnS	Zinc sulphide
ZnSe	Zinc selenide

Acknowledgements

I would like to thank my supervisors, Dr. Ian Forbes, Dr. Robert Miles and Mrs Kathleen Hynes (formerly at Northumbria University), for giving me an opportunity to continue research studies in thin film solar cells area. I am also thankful for their suggestions and help during the course of PhD. They provided valuable support during writing up of my thesis.

I would also like to thank Dr. Guillaume Zoppi for his help for research work and discussions during my PhD studies. I am also very grateful to Prof. Nicola Pearsall (Director of NPAC) for her help and support during conferences and other administrative work. I would like to thank research technician-Mr James Scott who always helped me for an additional technical jobs related to Nordiko sputtering system and furnaces. I would like to thank Mr. Bob Best for his help during microscopy work.

I am very much thankful to research colleagues (at Supergen consortium member Universities), Dr. Phillip Dale (formerly at Bath University), Mr. John Major (Durham University) for their help with IPCE and AFM measurements, respectively.

I would like to thank Mr. David Ridley for his help during my thesis writing. There are other many present and past research colleagues linked with NPAC to whom I would like to say many thanks for their assistances. They are listed as follows (not in a particular order); Mr. Ogah Ogah, Mrs. Kabita, Dr. Jayaraman Ramachandran, Dr. Thomas Bauer, Dr. David Johnston and Dr. Hari Mohan Upadhyaya. There are also friends in research room with whom I found friendly and enjoyable moments. I also wish to say thanks to research staffs Prof. Fary Ghassemlooy and Dr. Krishna Busawon for creating research and friendly environment.

I am thankful to School of Computing, Engineering and Information Sciences for research studentship for three years and administrative support during my PhD studies.

Finally I would like to thank my parents for their encouragement and support during the PhD studies in the UK. My father always inspired me in continuing research studies in the area of photovoltaic solar cells.

Author's declaration


I declare that this work has not been submitted for any other award and that it is all my own work.

MiniSIMS measurements on the samples were performed by Dr. Guillaume Zoppi at NPAC, Northumbria University.

IPCE measurements were performed by Dr. Phillip Dale (formerly at Bath University).

AFM measurements on CuInSe₂ thin films were performed by Mr. John Major at Durham University.

Name: Paresh Suresh Nasikkar

Signature: 

Date: 04.02.2009

CHAPTER 1

INTRODUCTION

The direct conversion of sunlight into electricity is known as the “photovoltaic (PV) effect”. This effect was first reported by Becquerel, in 1839, when he observed that a voltage was produced across two electrodes immersed in an electrolyte when the electrodes were illuminated [1]. In 1877, Adams and Day observed the PV effect in an all-solid-state device made of selenium (Se) [2]. Although it was realised in the late 1900s and throughout the early part of the 20th century that there was potential to generate power using solar radiation, the dream was not a practical proposition until 1954, when Chapin *et al.* produced a crystalline silicon (c-Si) solar cell with an efficiency of 6%, at Bell labs USA [3]. It was found that such cells could be used to power remote communications systems as a replacement to the lead acid batteries used at that time as these were very unreliable. The Si solar cells were made by growing boules of Si using the Czochralski method, sawing wafers from the boule, and then diffusing phosphorus impurities into the (*p*-doped) wafers to form a *p-n* junction. To the present day c-Si devices are produced using these processes. By 1958 it was realised that solar cells were also the best option for providing power for space satellites (and space vehicles) in the rapidly expanding space industry. By the early 1970s almost all space satellites were powered using c-Si solar cells with efficiencies of approximately 12% [4]. They were also deployed for a wide range of other applications, including supplying power for consumer products and for generating power in remote locations e.g. street lighting and water pumping.

In 1956, Loferski showed that the optimum energy band gap (E_g) used to make a solar cell was 1.5 eV and that semiconductors other than Si ($E_g = 1.12$ eV), such as indium phosphide (InP) ($E_g = 1.4$ eV), gallium arsenide (GaAs) ($E_g = 1.42$ eV) and cadmium telluride (CdTe) ($E_g = 1.5$ eV) could also be used to better match

the solar spectrum [5]. InP, GaAs and CdTe all have direct energy band gaps and high optical absorption coefficients (α) for photons with energies $> E_g$ such that only a few microns of material are needed to absorb most of the incident light. On the other hand Si has an indirect energy band gap and consequently low optical absorption coefficient. This means that 200 microns of Si are needed to absorb the same proportion of light. Further as the photons generate carriers far from the pn junction, the carriers need to diffuse long distances to be collected. This can only be achieved by purifying the Si to a very high level and by growing very good crystals of Si, free from crystal defects, as these can act as “recombination centres” for the photogenerated charge carriers. These processes add to the production costs for Si homojunction devices. It was realised that “thin film solar cells” made using direct energy band gap materials had the potential to be made much more cheaply than Si devices.

In 1954, Reynolds *et al.* reported a PV solar cell device which was a heterojunction between cuprous sulphide and cadmium sulphide ($p\text{-Cu}_2\text{S}/n\text{-CdS}$) [6]. A year later, Carlson and his research team at the Clevite Research Centre, Ohio, demonstrated a similar device fabricated using thin films of these materials [7]. In 1964, interest in $p\text{-Cu}_2\text{S}/n\text{-CdS}$ cells was stimulated when a satellite powered by Si solar cells failed and it was realised the failure was due to radiation damage in outer space. It was found that $p\text{-Cu}_2\text{S}/n\text{-CdS}$ thin film solar cells were strongly resistant to radiation in the space environment [8]. However for this application the thin films cells did not replace Si devices as more detailed studies showed that they were inherently unstable and improved Si solar cell design minimised this problem [9]. It was however later found that cells based on the use of single crystal GaAs and InP could be produced that were not only more efficient but had better radiation resistant

than Si [10]. Almost all solar cells deployed for space applications now use cells based on the use of III-V compounds and alloys epitaxially grown using metal-organic chemical vapour deposition (MOCVD) on germanium (Ge) substrates [11]. These have been produced with efficiencies $> 40\%$ when used with concentrated sunlight [12].

The performance of c-Si solar cells has continued to improve, so that it is now possible to produce devices with efficiencies up to 24.7% in the laboratory [13] and modules, made by connecting cells together as a unit, with efficiencies up to 22.7% [14]. These higher efficiencies are mainly due to improved “passivation” of the surfaces of the devices, the development of “light trapping schemes” and improved contacting technologies [11].

An alternative technology has been developed based on the use of “multicrystalline silicon (m-Si)”. This material is produced by pouring molten (+ boron dopant) Si into a container and allowing it to cool. Wafers are cut from the *p*-type boule and then processed to make solar cells by diffusing in phosphorous impurity atoms. The highest efficiency of a m-Si solar cell is 20.3%, approximately 4-5% lower than that of the highest efficiency c-Si solar cell. The best module efficiencies are now 15.3% [15]. The main advantages of using m-Si are that the production cost is lowered to 80% of that of c-Si solar cells and the cells are less sensitive to the quality of Si feedstock used [16].

In the today’s global market 94% of the total solar cell production is by the manufacture and sale of single crystal and multicrystalline Si solar cells [17]. In 2006-7, the company “Q-cells”, in Germany, was the largest producer of single and multicrystalline Si solar cells with an annual production 370 MW [18]. Currently the cost of a c-Si wafer based PV module is \$ 4/ W_p (W_p = watt peak). With future

developments the cost is estimated to reduce to \$ 1-1.50/W_p within the next 10 years. This is higher than the target cost of \$ 0.33/W needed to make PV generated electricity cost competitive with other forms of power generation [17].

To generate power on a large scale and to be cost competitive with alternative forms of power generation, two main strategies have been adopted. One approach is the development of high efficiency solar cells. This strategy is based on the use of the high efficiency III-V compounds and alloys grown on Ge. These devices, initially developed for space applications, can in principle be used for terrestrial power generation in “concentrator systems” where a large area mirror or lens is used to focus light onto a small PV cell. The disadvantages of this approach are the need to track the Sun to maximise the output and that these systems can only be used in parts of the world where there is unimpeded sunlight. The other approach is the development of low cost thin film solar cells. These minimise material usage and hence material costs and relax the need for high purity and crystallinity because a long minority carrier diffusion length is no longer required; this reduces manufacturing costs. The production process can also be fully automated reducing production costs further. Despite the early failure of the Cu₂S/CdS technology, three distinct types of thin film cell have since been developed and commercialised: amorphous Si (a-Si:H), CdTe and Cu(In,Ga)Se₂ (CIGS) solar cells.

Despite substantial success with a-Si:H technology during the latter part of the 20th century, the efficiencies of single junction a-Si:H based solar cells remains low (< 4%) due to degradation under illumination due to the ‘Staebler-Wronski’ effect [19]. Although double and triple junction cells and “micromorph cells” have been developed with improved stability, industrially produced cells and modules have efficiencies < 6% [16]. Manufacturers are trying to improve module efficiencies

to > 7% as they claim that this would make these devices acceptable to PV system designers.

Cadmium telluride was recognised in the 1950s as a potential solar cell material due to its near optimum direct energy band gap and it has continued to be developed ever since [5]. In the last decade progress with this material has been extremely impressive with solar cells produced in the laboratory with efficiencies up to 16.5% [20] and modules with efficiencies > 10% [21]. The two major companies manufacturing CdTe based cells and modules are ANTEC GmbH in Germany and First Solar in USA. These companies now claim that their costs of production are such that the cost of electricity generated is close to that of using fossil fuels (\$ 1.25/W) [22]. The major problem with this technology are concerns with respect to using Cd, a highly toxic metal and the consequent need for controlled disposal of modules after use.

Solar cells based on the use of the chalcopyrite compounds such as CuInSe_2 (CIS) and CIGS are relatively recent developments. Interest was stimulated by the production of a 10% efficient CIS cell by Mickelson and Chen in 1982 [23]. Since that time there has been much activity worldwide to develop these solar cells based on the use of CIS and CIGS [22]. CIS has a direct energy band gap of 1.04 eV with a high absorption coefficient ($\alpha \approx 10^5 \text{ cm}^{-1}$) for photons with energies greater than the energy band gap [24, 25]. The reason for incorporating Ga in CIS is that it increases the energy band gap towards the optimum value of 1.5 eV. It is found that cell performance increases with Ga content up 1.3 eV, partly due to the increase in energy band gap and partly due to the Ga inducing improvements in material quality. However it is found that increasing the energy band gap to values greater than 1.3 eV [$(\text{Ga}/(\text{Ga}+\text{In})) = 0.4$ to 0.5], results in a rapid decrease in cell performance due to

reduction in open circuit voltage and fill factor [26]. At the present time CIGS solar cells have been produced with efficiencies up to 19.9% in the laboratory [27]. A wide range of deposition methods exist for CIS-based absorber layers, the most widely used methods being co-evaporation from elemental sources and the chalcogenisation of pre-deposited metallic precursor layers [28]. The former method has resulted in the highest efficiency devices using the “three stage co-evaporation deposition process” developed at NREL; while the latter method is considered to be better for large scale production [27]. Several companies across the world are now involved with the large scale production of CIS based thin film solar cells. These include Global Solar, Nanosolar, Daystar and Miasolé in the USA, Würth Solar and Avancis in Germany and Showa Shell in Japan [22]. Despite the success of this technology there is a concern with the lack of abundance of Ga and In when the technology moves to very large scale production over the next decade.

The purpose of the work presented in this thesis aims to minimise these problems. Three different approaches have been used:

1. The development of CIS solar cells with thin absorber layers of these materials. This eliminates Ga and uses less In.
2. The replacement of Ga by Al to produce $\text{CuIn}_{1-x}\text{Al}_x\text{Se}_2$ (CIAS) rather than CIGS as Al is more abundant than Ga.
3. Enhancing device efficiency by the development of chalcopyrite tandem solar cells using CIAS upper cells with CIS lower cells (CIGS cannot be used to make upper cells because its energy band gap is too narrow).

In CIGS, the replacement of Ga with Al to form CIAS has the added advantage that less Al is needed, compared to Ga, to produce the same energy band gap because CuAlSe_2 has a much wider energy band gap than CIGS [29-31]. This is

also thought to lead to less stress in the chalcopyrite lattice structure permitting the production of CIAS with $E_g > 1.3$ eV without a degradation of efficiency [31]. The wider E_g will also result in an increase in open circuit voltage and fill factor and hence improvement in the solar conversion efficiency [32]. Another useful factor is that incorporating Al in CIS could make it possible to develop an upper cell in a multijunction device. In this way replacing Ga with abundant and cheap Al will lead towards the development of higher efficiency devices.

CIAS has been synthesised in the USA using the co-evaporation method and the layers used to produce solar cells with efficiencies up to 16.9% [32]. Work on producing CIAS using co-evaporation and the 2-stage selenisation of stacked precursor layers however remains limited [30, 33].

The main aim of the research work here is to produce thin films of CIS and CIAS, by the sputter deposition of the metallic precursor layers followed by an anneal using elemental Se with the aim of optimising the steps to produce good quality CIS and CIAS thin films, and consequently efficient solar cells.

This thesis gives background theory (chapter 2) relevant to understanding how *pn* junction PV solar cells work, the key parameters used to describe cell performance and how these are influenced by the chemical and physical properties of the semiconductors used to make the device. This is followed by in-depth literature reviews (chapter 3) of CIS, CIGS and CIAS technologies. This is followed in turn by the experimental procedure (chapter 4) section that gives details on how the layers are synthesised, and on the material and device characterisation methods used.

Chapter 5 gives the results obtained in this work. These include work on the development of the depositions processes used to deposit the back contact Mo layer, the deposition processes for producing the metallic precursor layers, the selenisation

processes used to form the CIS and CIAS and the optimisation and characterisation of the solar cells produced using these layers.

An environmental impact assessment was also carried out to identify the risk factors that may cause damage to the environment and human health. This work is given in chapter 6.

Chapter 7 reviews and critically appraises all the information produced in this work and discusses the possibilities for future work.

CHAPTER 2

BACKGROUND THEORY

2.1 Solar Spectrum

The surface temperature of the Sun can be approximated by a black body radiating at 5800K. This results in it radiating 4×10^{26} W mainly as electromagnetic radiation from the ultraviolet to infrared region (0.2 to 3 μm). This results in the intensity of solar radiation in free space at the mean distance of the earth from the sun being 1367 W/m^2 [34, 35]. The solar spectrum incident for a given application is referred to as its “air mass (AM) spectrum”. The “air mass” is defined by: $\text{AM} \equiv 1/\cos z \equiv \sec z$, where z is the angle measured from the zenith. AM0 corresponds to the solar spectrum in space while AM1 is the solar spectrum at the Earth’s surface when the Sun is directly overhead; the incident power is then 925 W/m^2 [35]. The AM1.5 spectrum is that incident at angle, $\sec^{-1} 1.5$, to the zenith at the Earth’s surface when it has passed through the Earth’s atmosphere. It is the solar spectrum appropriate for assessing the performance of solar cells, used for terrestrial applications. The incident power is set to be 1 kW/m^2 for PV panel testing under the AM1.5 Global, direct and diffuse spectrum. The difference between AM0 and AM1.5 is depicted in figure 2.1. This is due to atmospheric attenuation of sunlight and is mainly attributed to infrared absorption due to water content in atmosphere, and the scattering of sunlight by airborne dust and aerosols, and ultraviolet light absorption due to ozone layer [35].

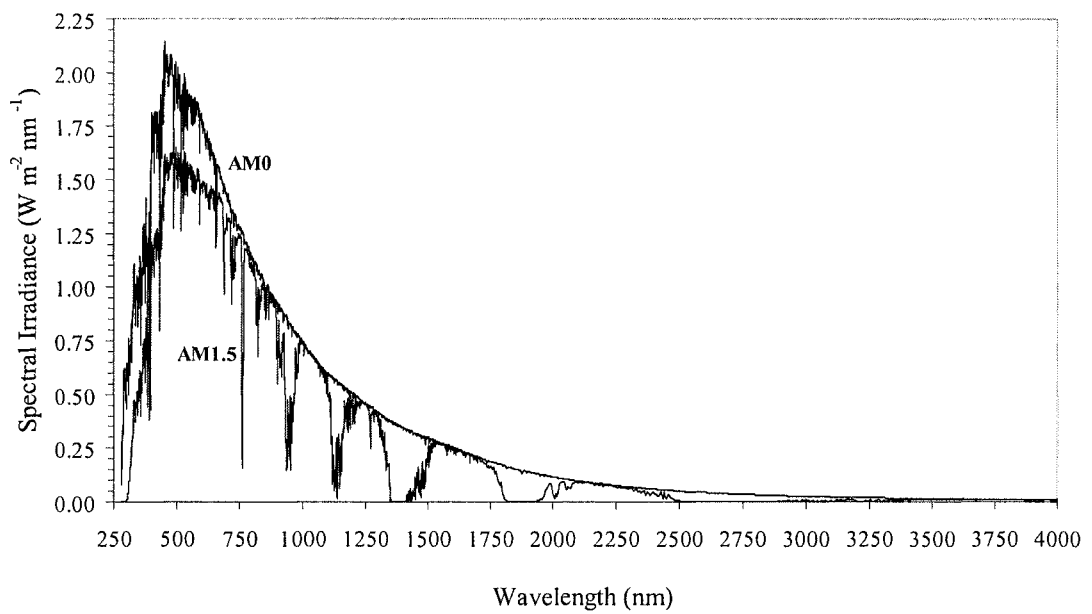


Figure 2.1 The graph shows solar spectrum irradiance curves for space (AM0) and terrestrial (AM1.5) conditions (Reproduced from [36]).

2.2 Optical Absorption in a Semiconductor

When light shines on a semiconductor the incident light interacts with the semiconductor. The three main types of process that take place in semiconductor are depicted in figure 2.2:

- a) If the photon energy ($E_{ph} = h\nu$) is equal to the energy band gap (E_g) of the semiconductor i.e. $E_{ph} = E_g$, electron-hole pairs are created.
- b) If the $E_{ph} > E_g$, electron hole pairs are generated and the excess energy ($h\nu - E_g$) is dissipated as a heat.
- c) If $E_{ph} < E_g$ then the light is transmitted or photon get absorbed in the forbidden band gap in the energy states which are present due to defects or chemical impurities. This is extrinsic transition denoted by E_t .

Absorption coefficient (α)

Figure 2.3 (a) shows light of photon energy $h\nu > E_g$ and photon flux ϕ_0 (in photons/cm²/s) incident on a semiconductor. The intensity of the photon flux reduces with the distance travelled through the semiconductor. For example if photon flux $\phi(x)$ travelled a small distance Δx , the number of photons absorbed within Δx distance is given in equation 2.1. On the right hand side of equation the proportionality constant α is known as the absorption coefficient.

$$\phi(x + \Delta x) - \phi(x) = \frac{d\phi(x)}{dx} \Delta x = -\alpha \phi(x) \Delta x \quad (2.1)$$

or it can be written as

$$\frac{d\phi(x)}{dx} = -\alpha \phi(x) \quad (2.2)$$

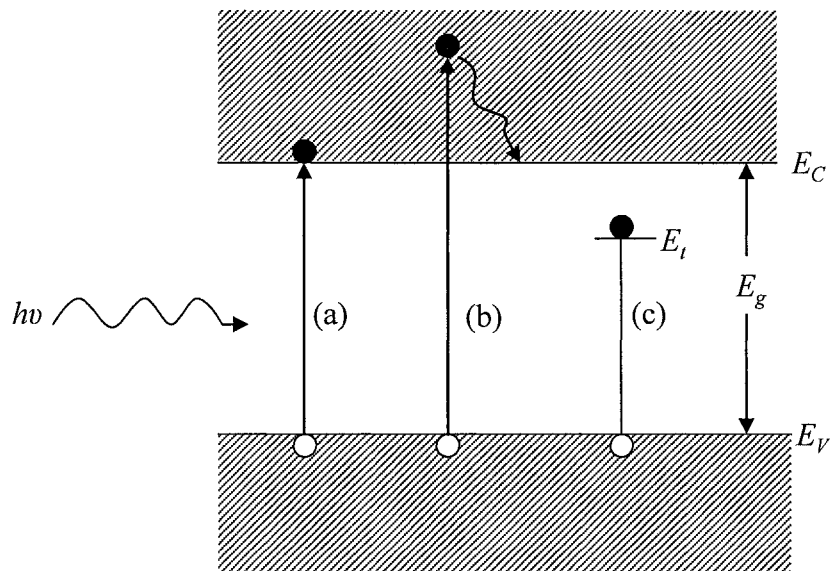


Figure 2.2 Optical absorption in a semiconductor.

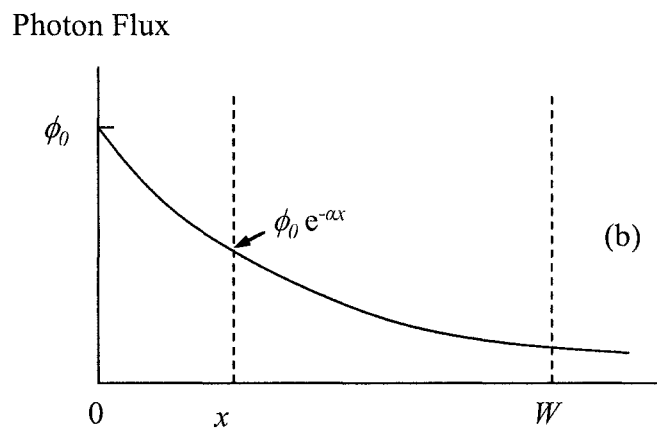
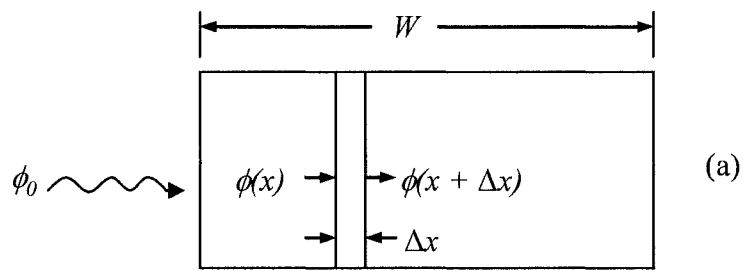


Figure 2.3 (a) Optical absorption in a semiconductor under illumination and (b) exponential decay of incident photon flux (derived from [35]).

The right hand side of the expression is negative due to the decrease in the intensity of the photon flux.

By considering boundary conditions, $\phi(x) = \phi_0$ at $x = 0$ (Fig. 2.3 (b)), the equation 2.2 can be written,

$$\phi(x) = \phi_0 e^{-\alpha x} \quad (2.3)$$

For $x = W$, the other end of the semiconductor, equation 2.3 becomes,

$$\phi(W) = \phi_0 e^{-\alpha W} \quad (2.4)$$

From above expression, it is clear that if $W \gg 1/\alpha$, most of the light will be absorbed. If $W = 1/\alpha$, which is called an “optical absorption length”, then equation 2.4 becomes,

$$\phi = \phi_0/e.$$

2.3 Indirect and Direct Bandgap Semiconductors

An indirect semiconductor is one in which a transition from the valence band to the conduction band requires a change in crystal momentum (\bar{p}) for the electron. Silicon (Si) is an indirect type of semiconductor with an energy band gap of 1.12 eV, at 300K. In a direct semiconductor there is no such change required in crystal momentum. Gallium Arsenide (GaAs) is a direct type of semiconductor with an energy band gap of 1.42 eV. Figure 2.4 shows the difference in the energy band diagrams for Si and GaAs. According to figure 2.4, in Si, for an electron to make a transition from the valence band to the conduction band, it requires energy equal to or greater than E_g and in addition to that, it also needs some change in the crystal momentum ($\bar{p} = \bar{p}_c$). This must be supplied by interaction with a quantised lattice vibration- “a phonon”. There is no such requirement for GaAs because an electron can make transition without a change in crystal momentum ($\bar{p} = 0$).

For photovoltaic applications, the semiconductors with direct types of energy band gap are advantageous for making solar cells because thinner layers can be used to absorb the same amount of light due to its high value for optical absorption coefficient for photons with energies greater than the energy band gap and hence minimising material and deposition costs.

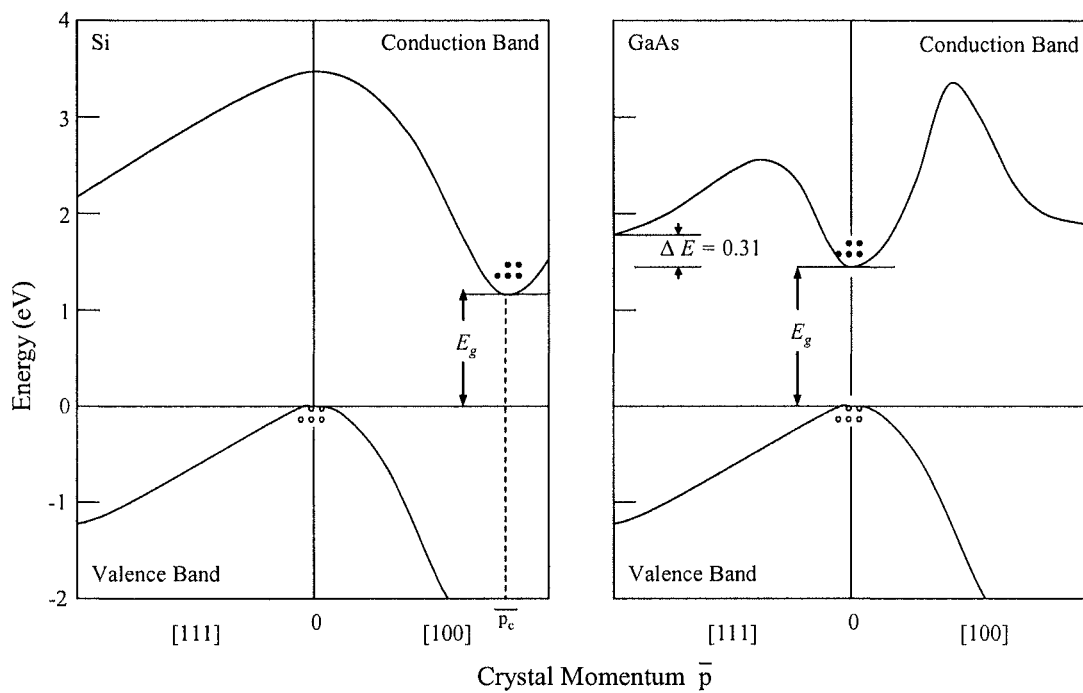


Figure 2.4 Energy band structures of indirect (Si) and direct bandgap (GaAs) semiconductors [The filled circles (•) indicates electrons and hollow circle (◦) holes.] (Reproduced from [35]).

2.4 P-n Junction (Thermal Equilibrium Condition)

When uniformly doped p -type and n -type semiconductor materials are joined together a p - n junction is formed as shown in figure 2.5.

For an ideal p - n diode the following assumptions are made [37]:

- i) Due to a carrier concentration gradient at the junction, holes from p -type side diffuse into the n -type side leaving the p -type side uniformly depleted of holes up to a distance x_{p0} from the junction. Similarly electrons diffuse from the n -side to the p -type side, leaving the n -type side uniformly depleted of electrons up to a distance x_{n0} from the junction.
- ii) The width ' w ' between x_{p0} and x_{n0} is known as the "depletion region" or the "transition region", hence $w = x_{n0} + x_{p0}$. For an ideal diode it is assumed that in this region no recombination or generation takes place.
- iii) The positive space charge formed near the n -type side and the negative space charge formed near the p -type side create an electric field (E) which produces drift currents of electrons and holes, so that net current flow across the junction is zero for zero bias applied. Because $E = -dV/dx$ and E is finite, a potential difference (V_0) between the neutral n -type side (V_n) and the neutral p -type side (V_p) is developed such that $V_0 = V_n - V_p$.

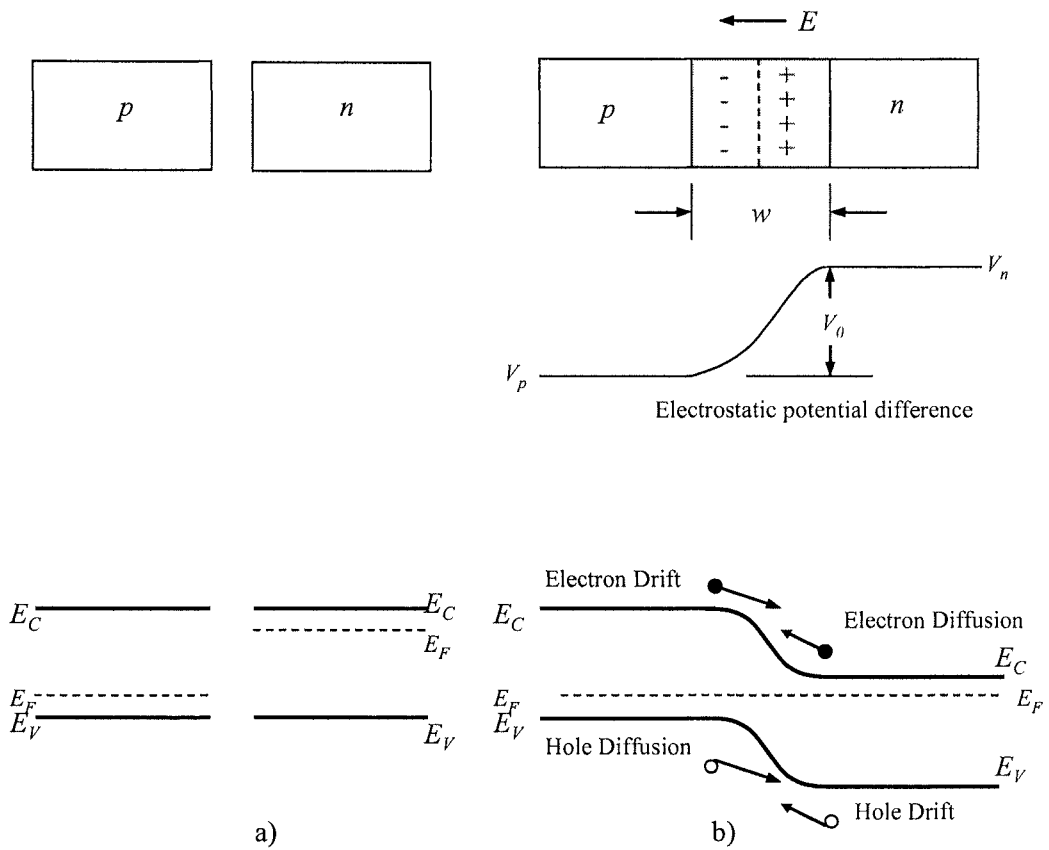


Figure 2.5 (a) *P*-type and *n*-type semiconductor material before junction formation, (b) flow of electrons (●) and holes (○) after *p-n* junction formation in thermal equilibrium [37].

If J_p (diffusion) \equiv the diffusion current due to diffusion of holes from p -type side to n -type side, then:

$$J_p(\text{diffusion}) = q D_p \frac{dp}{dx} \quad (2.5)$$

If J_p (drift) \equiv the drift current of holes from p -type side to n -type side, then:

$$J_p(\text{drift}) = q \mu_p p E \quad (2.6)$$

In thermal equilibrium:

$$J_p(\text{diffusion}) = J_p(\text{drift}) \quad (2.7)$$

From equations 2.5 and 2.6, equation 2.7 can be written as

$$q D_p \frac{dp}{dx} = q \mu_p p E \quad (2.8)$$

By substituting, $E = -\frac{dV}{dx}$ and using the ‘‘Einstein relation’’, $D_p = \frac{kT\mu_p}{q}$ in

equation (2.8), gives,

$$\begin{aligned} -\frac{q}{kT} \left(\frac{dV}{dx} \right) &= \frac{1}{p} \left(\frac{dp}{dx} \right) \\ -\frac{q}{kT} \left(\int_{V_p}^{V_n} dV \right) &= \int_{p_n}^{p_p} \frac{1}{p} dp \\ -\frac{q}{kT} (V_n - V_p) &= \ln p_p - \ln p_n = \ln \left(\frac{p_p}{p_n} \right) \\ V_0 &= \frac{kT}{q} \ln \left(\frac{p_p}{p_n} \right) \quad (2.9) \end{aligned}$$

In equation 2.9, $p_p = N_a$, density of acceptors on the p -type side, and according to the ‘‘law of mass action’’, $p_n = n_i^2 / N_d$ (where, N_d = donor concentration on the n -type side). Therefore equation 2.9 becomes,

$$V_0 = \frac{kT}{q} \ln \left(\frac{N_a N_d}{n_i^2} \right)$$

From equation 2.9 and according to the equilibrium condition, $p_p n_p = n_i^2 = p_n n_n$) it can be written as [37],

$$\frac{p_p}{p_n} = \frac{n_n}{n_p} = e^{qV_0/kT} \quad (2.10)$$

The equation 2.10 is useful in calculation of the I - V characteristics of a pn junction.

2.5 The Diode Equation

When a forward bias V is applied across the pn junction (Fig. 2.6), the electric field strength at the junction is reduced. This results in the diffusion of electrons from the n -type side into the p -type side, and diffusion of holes from the p -type side into the n -type side. The electron concentration at the edge of $-x_{p0}$ is increased by an amount, Δn_p and the hole concentration at x_{n0} by an amount Δp_n . There is said to be “steady state injection” of electrons from the n -type side to the p -type side and steady state injection of holes from the p -type side to the n -type side. As the electrons continue to diffuse beyond $-x_{p0}$ into the p -type side the injected carriers recombine with majority carrier holes. The distribution of excess electrons (δ_n) is then given by:-

$$\delta_n = \Delta n e^{-x_p/L_n}$$

where L_n is the electron diffusion length.

This creates current flow due to electrons (I_n) where:

$$I_n = qAD_n \frac{d(\delta_n)}{dx} \quad (2.11)$$

Similarly at x_{n0} the hole concentration (entering into n -type side) is increased by Δp_n . As the holes diffuse into the n -type side the injected carriers recombine with majority carriers electrons so that the net excess hole concentration (δ_p) can be written as,

$$\delta_p = \Delta p e^{-x_n/L_p}$$

where L_p is the hole diffusion length.

Likewise:

$$I_p = -qAD_p \frac{d(\delta_p)}{dx} \quad (2.12)$$

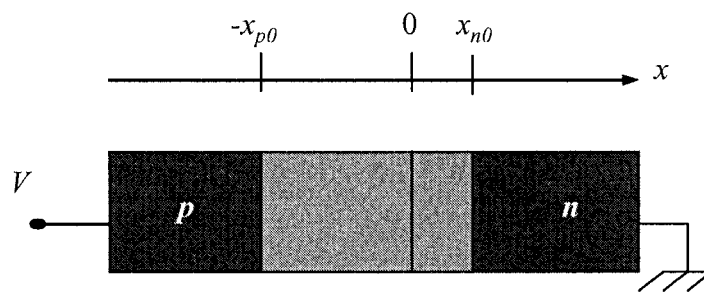


Figure 2.6 A forward bias applied to the pn junction semiconductor.

From equations 2.11 and 2.12 the total current flow in the semiconductor,

$$I = I_n + I_p \quad (2.13)$$

In thermal equilibrium, the ratio of holes concentration on each side is given by:

$$\frac{P_p}{P_n} = e^{qV_0/kT} \quad (2.14)$$

For a forward bias, V it becomes:

$$\frac{p(-x_{p0})}{p(x_{n0})} = e^{q(V_0-V)/kT} \quad (2.15)$$

Taking $p_p = p(-x_{p0})$, then from equations 2.14 and 2.15, it can be written as,

$$\frac{p(x_{n0})}{P_n} = e^{(qV/kT)}$$

$$\text{or } p(x_{n0}) = P_n e^{(qV/kT)}$$

$$\Delta p_n = p(x_{n0}) - p_n = p_n e^{(qV/kT)-1} \quad (2.16)$$

Similarly for Δn_p ,

$$\Delta n_p = p(-x_{p0}) - n_p = n_p e^{(qV/kT)-1} \quad (2.17)$$

From equation 2.12, the hole diffusion current (I_p) at any point x_n in the n -type side can be written as,

$$\begin{aligned} I_p(x_n) &= -qAD_p \frac{d(\delta_p)}{dx_n} \\ &= -qA \frac{D_p}{L_p} \Delta p_n e^{-x_n/L_p} = qA \frac{D_p}{L_p} \delta p(x_n) \quad (2.18) \end{aligned}$$

The total injection of holes (total hole current (I_p)) into the n -type side can be written by substituting $x_n = 0$ in the equation 2.18,

$$I_p(x_n = 0) = qA \frac{D_p}{L_p} \Delta p_n = qA \frac{D_p p_n}{L_p} (e^{qV/kT} - 1) \quad (2.19)$$

Similarly, at $-x_{p0}$, the injection of electrons into p -type material results into an electron current (I_n), can be given by,

$$I_p(x_p = 0) = -qA \frac{D_n}{L_n} \Delta n_p = qA \frac{D_n n_p}{L_n} (e^{qV/kT} - 1) \quad (2.20)$$

By adding equations 2.19 and 2.20 gives total current flow, I , can be written as,

$$I = I_n + I_p$$

$$I = qA \left[\frac{D_p p_n}{L_p} + \frac{D_n n_p}{L_n} \right] (e^{qV/kT} - 1)$$

$$I = I_0 (e^{qV/kT} - 1) \quad (2.21)$$

$$\text{where } I_0 = qA \left[\frac{D_p p_n}{L_p} + \frac{D_n n_p}{L_n} \right]$$

Equation 2.21 is known as the “*ideal diode equation*”.

Real diodes

1. For diodes made from semiconductors with $E_g > 1$ eV, recombination in the depletion region dominates at 300K. In the forward bias condition, the forward current I_F of free carriers in the depletion region is given by [35]

$$I_F = \frac{n_i q w A}{2 \tau_r} e^{qV/2kT}$$

where τ_r is the “recombination lifetime”.

In some temperature ranges there may be a mixture of current flow due to diffusion and the recombination mechanism. The forward current can be given by

$$I_F \propto e^{qV/NkT}$$

where N is known as the “ideality factor”. It has value between 1 and 2. When the diffusion current dominates $N = 1$ and when recombination in the depletion region dominates $N = 2$.

2. In the reverse bias condition, if $E_g > 1$ eV generation in the depletion region dominates and the current is given by:-

$$I_R = \frac{n_i q w}{\tau_g}$$

where τ_g is the “generation lifetime”.

3. The series resistance R_S of a solar cell is due to bulk resistance of the n and p -type materials and resistances of the metallic contacts to the n and p -type materials. When it cannot be ignored the I - V characteristic by equation 2.21

$$I = I_0 [e^{q(V - IR_S)/kT} - 1]$$

4. Leakage resistance R_L is due to shorting path or paths through the junction at the peripheral of the junction. If its value greater than 100Ω then its effect can be ignored for solar cell devices.

2.6 Heterojunctions

If a p - n junction is formed between two dissimilar semiconductors with different energy band gaps ($E_{g1} \neq E_{g2}$) and electron affinities ($\chi_1 \neq \chi_2$) then it is referred to as a “heterojunction”. When the semiconductors are in intimate contact charge is transferred until the Fermi level is equal across the two layers. This causes the appearance of a “spike” in the conduction band, ΔE_C and a “notch” in the valence band, ΔE_V (Fig. 2.7). The spike acts as barrier to the electron flow in the semiconductor. For this reason it is desirable to select a combination of materials of energy levels which produce a small spike (or no spike) so that maximum conduction can occur. Conduction in such a heterojunction can be limited by:-

1. The diffusion of electron and holes across the junction (Anderson diffusion model [38]).
2. Thermionic emission over the spike (thermionic emission model of Perlman and Feucht model [39]).
3. Tunnelling through the spike (tunnelling model of Rediker, Stopek and Ward [40]).
4. By tunnelling of carriers to interband states at the junction where they recombine (tunnelling-recombination model developed by Riben and Feucht [41]).

For CdS/CuInSe₂, p - n junction heterostructure the energy band diagram is given in figure 2.7.

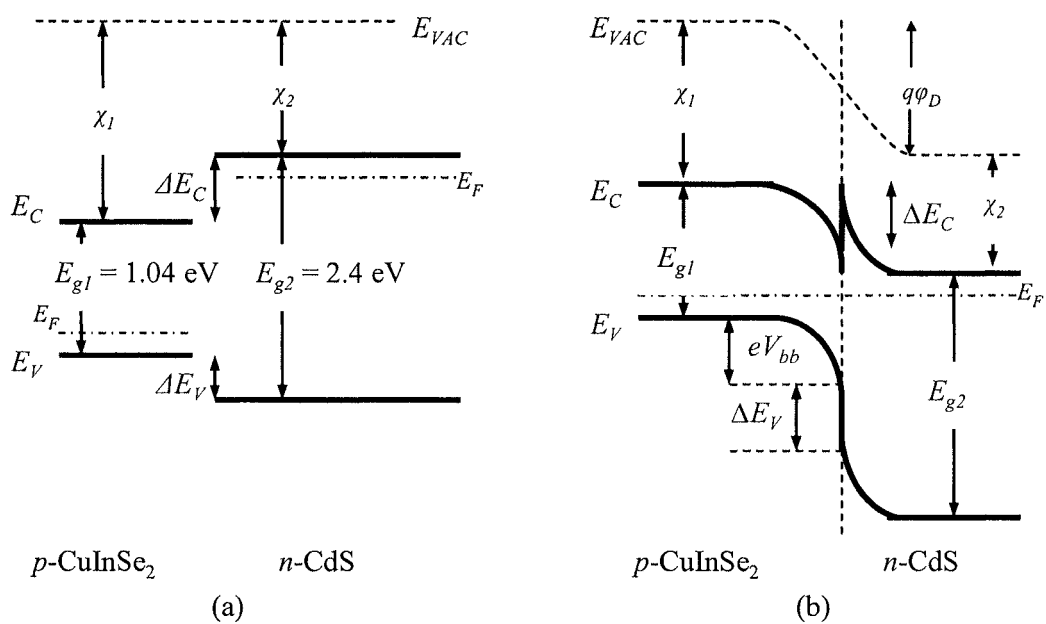


Figure 2.7 (a) Energy-band diagram of semiconductors p -type CuInSe₂ and n -type CdS before junction formation;
 (b) Energy-band alignment between CuInSe₂ and CdS semiconductors forming p - n junction heterojunction [42].

These conduction mechanism models have been synthesised into an equation given as:

$$J = J_{00} \exp\left(\frac{-\phi}{kT}\right) \exp\left(\frac{qV}{NkT}\right) = J_0 \exp\left(\frac{qV}{NkT}\right)$$

where, $J_0 = J_{00} \exp\left(\frac{-\phi}{kT}\right)$ and

ϕ is the “barrier height” or “activation energy” for the conduction process.

Wei and Zunger have published a review on the status of the energy-band offsets expected in a CuInSe₂/CdS heterostructure [43].

Photoexcitation occurs due to incident photons penetrating through the larger band gap of *n*-type material (CdS), which acts as a “window”, and then get absorbed in the *p*-type region. Minimum loss occurs for the light that penetrates through the window layer to the junction. However a lattice mismatch, approximately 1.1% [44], at the junction between the two semiconductors (CuInSe₂/CdS) gives rise to localised interface states that create recombination centres in the junction region. These defects tend to increase the reverse saturation current density J_0 , and to reduce the open circuit voltage V_{OC} , seriously degrading solar cell performance. It is an essential criterion in heterojunction semiconductor structure to prefer materials with close lattice matching to minimise the density of interface states.

2.7 Current Transport Mechanisms in Heterojunction

Semiconductor

The tunnelling-recombination mechanism was considered in more detailed by Donnelly and Milnes to explain the conduction process in a heterojunction (Fig. 2.8) [45]. They considered that the current flow was limited mainly due to recombination at the interfaces. According to their model the current flow (J) can be written as:

$$J = qSN_B \exp\left(\frac{-q\Delta E_0}{kT}\right) \exp\left(\frac{qV}{NkT}\right) \quad (2.22)$$

where N_B is the doping in the base, ΔE_0 is the thermal activation energy for the conduction process and S is the interface recombination velocity, given by:

$$S = V_{th} \sigma N_I$$

where V_{th} is thermal velocity of electron, σ is the capture cross-section of the interface states and N_I is the density of empty interface states N_I is given by:

$$N_I = \frac{\Delta a}{a^3}$$

where Δa is the difference between the lattice constants of the two materials in the heterojunction and a is the average lattice constant in the plane of the heterojunction.

The equation 2.22 can be written in the form

$$J = J_{00} \exp\left(\frac{-q\Delta E}{kT}\right) \exp\left(\frac{qV}{NkT}\right)$$
$$J = J_0 \exp\left(\frac{qV}{NkT}\right) \quad (2.23)$$

where $J_0 = J_{00} \exp\left(\frac{-q\Delta E}{kT}\right) = J_{00} \exp\left(\frac{-\phi}{kT}\right)$ [ϕ is 'barrier height'].

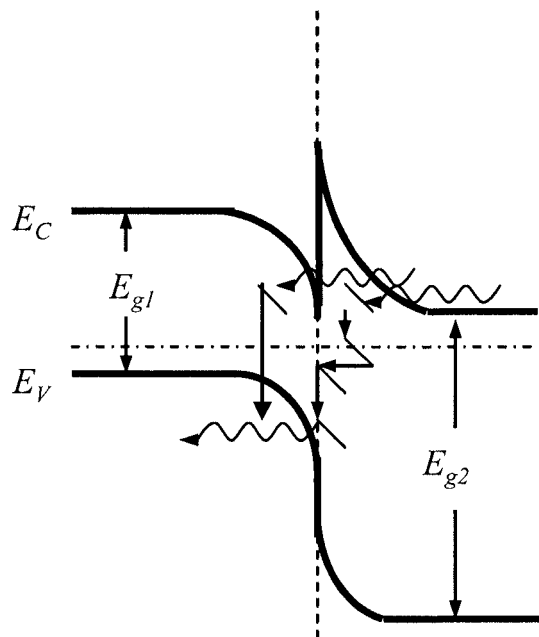


Figure 2.8 Tunnelling-recombination mechanism in heterojunction (Ribben and Feucht model).

A plot of $\ln J_0$ versus $1/T$ is useful to determine the type of conduction mechanism in heterojunction semiconductors e.g. whether the conduction mechanism is “thermally activated” or a “quantum mechanical tunnelling process”. If there is no variation in J_0 with temperature ($1/T$) then the conduction is due to a tunnelling process; otherwise it is due to a thermally activated conduction process (Fig. 2.9).

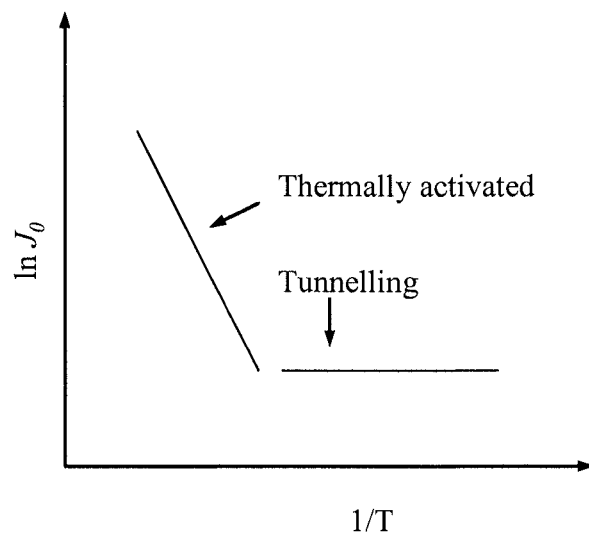


Figure 2.9 Conduction mechanisms in heterojunction semiconductors.

2.8 Solar Cells Theory

Most solar cells are p - n junction semiconductor devices and consist of a shallow p - n junction formed on the surface, a front grid contact, a back Ohmic contact and an antireflection coating (ARC) on the front surface.

When the sunlight is incident on the solar cell photons that have energies less than band gap makes no contribution to the cell output. Only photons with energy greater than E_g excite electrons from the valence band to the conduction band (Fig. 2.10 (a)). The excited electrons leave behind free states called holes. These electron-hole pairs are separated due to the internal electric field within the depletion region (of width w) of the p - n junction and driven through the external detection circuit. The flow of carriers into the external circuit constitutes an electric current. This phenomenon is known as the “photovoltaic effect”.

The current-voltage (I - V) characteristic of an ideal solar cell obeys the ideal diode equation in the dark. However under illumination the photocurrent (I_L), adds to the reverse current and therefore the I - V characteristic is given by [35]

$$I = I_0(e^{qV/kT} - 1) - I_L \quad (2.24)$$

The equivalent circuit of an ideal solar cell is shown in figure 2.10 (b).

For the condition $V = 0$, $I_L = I_{SC}$ where I_{SC} is the “short circuit current”.

For the condition $I = 0$, $V = V_{OC}$ where V_{OC} is the “open circuit voltage”.

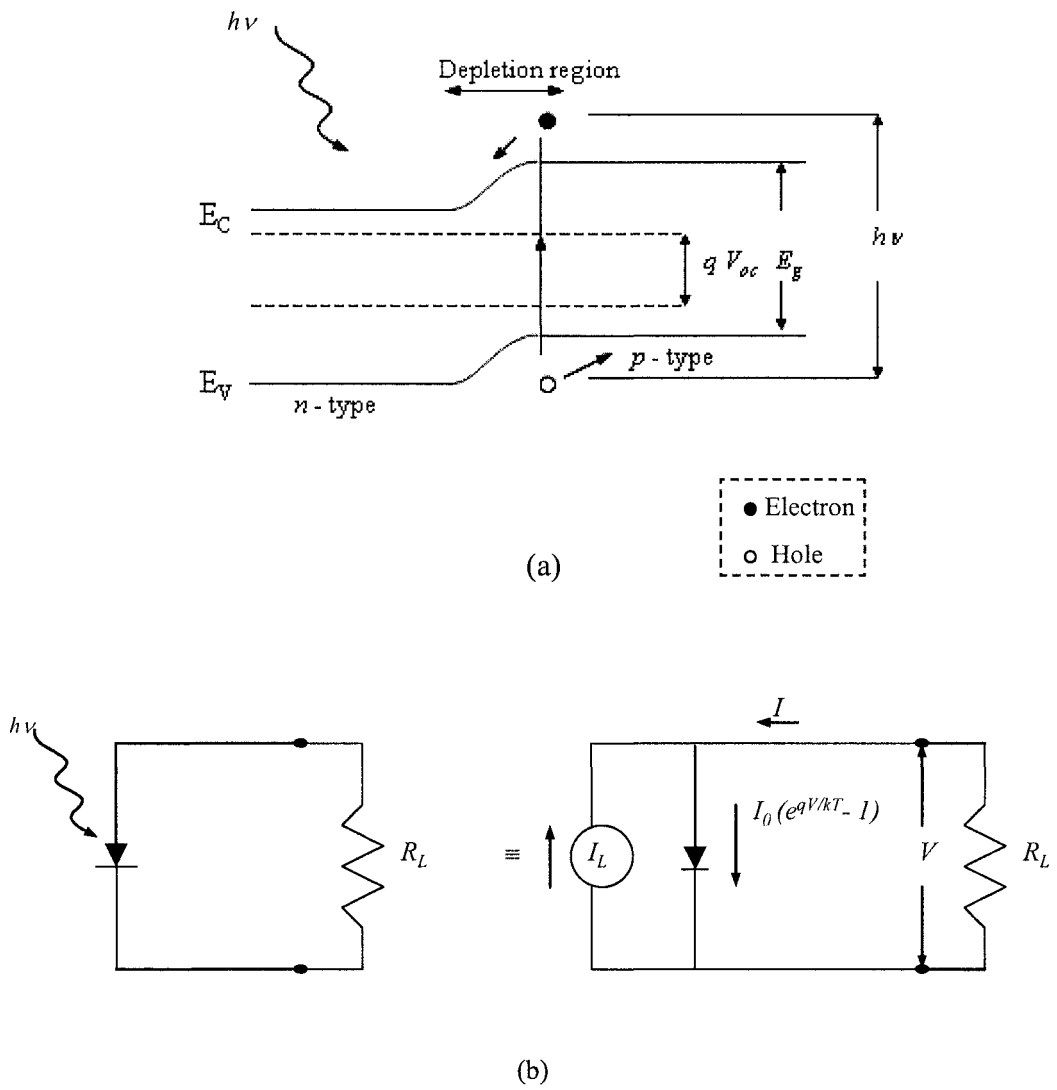


Figure 2.10 (a) A p - n junction under illumination, (b) an equivalent circuit of an ideal solar cell (Reproduced from [35]).

For an ideal diode I_0 is given by

$$I_0 = qN_c N_v \left[\frac{1}{N_A} \sqrt{\frac{D_n}{\tau_n}} + \frac{1}{N_D} \sqrt{\frac{D_p}{\tau_p}} \right] e^{-E_g/kT} \quad (2.25).$$

The current density J for a solar cell of an area A is given by, $J \equiv I/A$. The J - V characteristics of a solar cell in the dark and under standardised illumination are given in figure 2.11.

From the J - V curve under illumination it is possible to determine the most important parameters that describe solar cell performance. These are the short circuit current (I_{SC}), the open circuit voltage (V_{OC}), the fill factor (FF) and the solar conversion efficiency (η). FF tells how well the maximum-power rectangle fills the area covered by the J - V curve. The cell conversion efficiency is the ratio of maximum power generated to the power of incident radiation.

It is always required to get larger values of photo generated current density (J_L) and V_{OC} to yield best cell performance. If all photogenerated electron-hole pairs are collected as photocurrent then a maximum value of J_L can be achieved. Therefore light absorption and minority carrier collection are the deciding factor to reach a J_L value in the range 80-90% of the maximum value [9]. The maximum value of V_{OC} can be estimated by dividing E_g of the absorbing material by the electronic charge i.e. (E_g/e).

For short circuit current condition, equation (2.24) becomes

$$I_{SC} = -I_L \quad (2.26)$$

$$\text{and} \quad I_L = g_{opt} A e (L_n + L_p + w).$$

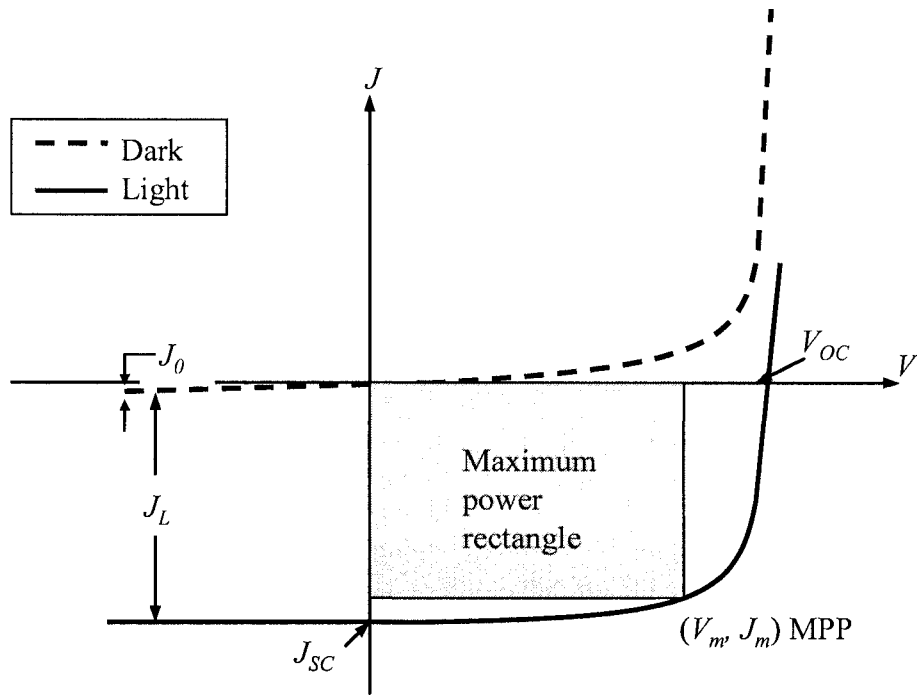


Figure 2.11 Schematic diagram of J - V characteristic of a solar cell in dark and under illumination.

where $g_{opt} \equiv$ optical generation rate i.e. the number of carriers generated/unit volume/sec, $A (L_n + L_p + w)$ is the generation volume and e is the charge on each electron.

For the open circuit voltage condition, $I = 0$, and :-

$$V_{OC} = \frac{kT}{q} \ln \left[\frac{I_L}{I_0} + 1 \right]$$

Generally $I_0 \approx 10^{-10}$ A and $I_L \approx 10^{-3}$ A and hence $I_L/I_0 \gg 1$. Hence :-

$$V_{OC} = \frac{kT}{q} \ln \left[\frac{I_L}{I_0} \right] \quad (2.27)$$

As I_L is proportional to power of incident radiation, V_{OC} varies logarithmically with incident power.

The solar cell output power (P) is given by,

$$P = IV = I_0 V (e^{qV/kT} - 1) - I_L V \quad (2.28)$$

To obtain maximum power, the required condition is $dP/dV = 0$ and $V = V_m$.

By solving equation 2.28 and rearranging,

$$V_m = \frac{kT}{q} \ln \left[\frac{1 + (I_L/I_0)}{1 + (qV_m/kT)} \right] \approx V_{OC} - \frac{kT}{q} \ln \left[1 + \frac{qV_m}{kT} \right] \quad (2.29)$$

$$I_m = I_L \left[\frac{qV_m}{kT} \right] e^{qV_m/kT} \approx I_L \left[1 - \frac{1}{qV_m/kT} \right] \quad (2.30)$$

V_m and I_m values are shown in figure 2.11 and are the voltage and current at the maximum output power point P_m ,

$$P_m = I_m V_m = I_L \left[V_{OC} - \frac{kT}{q} \ln \left[1 + \frac{qV_m}{kT} \right] - \frac{kT}{q} \right] \quad (2.31)$$

An important figure of merit in solar cell design is the FF which is ideally equal to 1. It is defined as,

$$FF \equiv \frac{J_m V_m}{J_{SC} V_{OC}} \quad (2.32)$$

The power conversion efficiency of a solar cell for an incident radiation (P_{in}) is given by:

$$\eta (\%) = \frac{I_m V_m}{P_{in}} = \frac{FF I_{SC} V_{OC}}{P_{in}} \times 100 \quad (2.33)$$

The solar cell efficiency, η , can be improved by maximising J_{SC} , V_{OC} , and the FF. All of these solar parameters are defined for particular illumination conditions e.g. AM1.5 Global Spectrum, the standard test condition (STC) (25°C) and incident power density of 1000 Wm⁻² for terrestrial applications.

➤ Non-ideal photovoltaic solar cell

A simplified equivalent circuit of a real solar cell is shown in figure 2.12. The solar cell performance is strongly affected by the contact resistances and by leakage current across the device. It can also be affected by several factors, including recombination of the generated carriers due to impurities and defects in the forbidden band of the semiconductors and also due to surface defects. The diode component in the circuit represents these recombination processes along with the effects of series (R_S) and parallel or shunt (R_{Sh}) resistances taken into consideration.

The R_S comes from the resistance of the cell material to electron and hole current flow, particularly through the contact resistance (at the metal-semiconductor interfaces). It can seriously degrade the solar cell performance because it reduces FF and J_{SC} . For an ideal solar cell R_S is zero (Fig. 2.13 (a)). The R_{Sh} arises mainly due to leakage current across the junction, via external defects. It must be as large as possible for better performance of the solar cells (Fig. 2.13 (b)).

The diode equation can be written with R_S and R_{Sh} included [46],

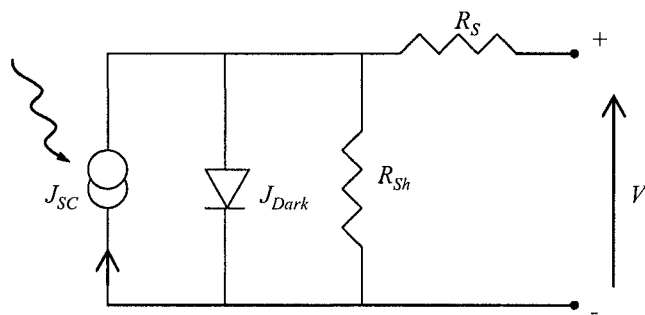
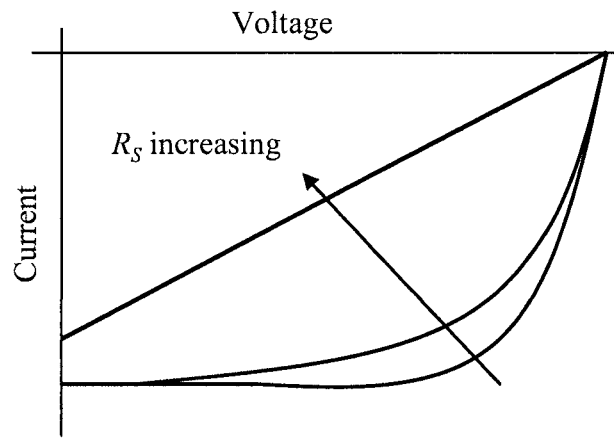
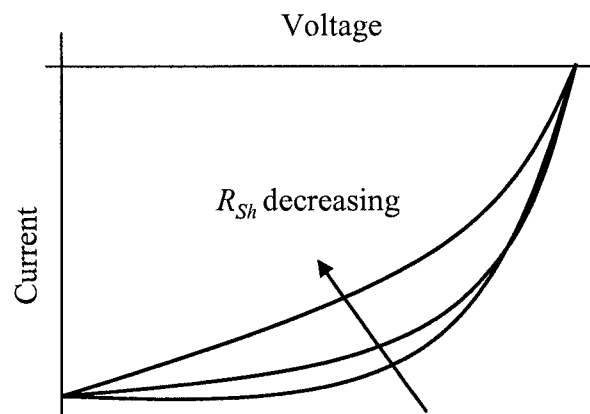


Figure 2.12 Simple equivalent circuit for a solar cell including series and shunt resistances.



(a)



(b)

Figure 2.13 Effect of (a) increasing series resistance and (b) decreasing shunt (parallel) resistance on the solar cell output (current-voltage) curve.

$$J = J_0 \left(\exp\left(\frac{q(V + JAR_S)}{NkT}\right) - 1 \right) + \frac{(V + JAR_S)}{R_{Sh}} - J_L \quad (2.34)$$

In the equation (2.34) R_S and R_{Sh} are in Ωm^{-2} and N is the diode ideality factor.

2.9 Optimum Energy Bandgap for Single-Junction Solar Cells

In order to improve the performance of single-junction solar cells, it is necessary to maximise both J_{SC} and V_{OC} (equation 2.33 and Fig. 2.11). The maximum value of J_{SC} is obtained if the incident light gets absorbed in a material of small energy band gap as then a large part of the solar spectrum is absorbed increasing the optical generation rate. However V_{OC} is low for small energy band gap material. V_{OC} can be obtained for wider energy band gap material but then J_{SC} is small because a smaller fraction of the incident solar spectrum is absorbed. There is therefore, an optimum bandgap for maximising the product $J_{SC} \times V_{OC}$, to ensure maximum efficiency of the solar cell. The optimum energy band gap for a single junction solar cell is found near to 1.5 eV [47].

The quantum efficiency (QE) is the ratio of the number of electron-hole pairs generated to the number of incident photons of a particular wavelength. For an ideal solar cell QE is equal to one; however for actual solar cells it is less than unity. The photocurrent J_{SC} is given by [46]:-

$$J_{SC} = q \int b_s(E) QE(E) dE$$

where $QE(E)$ = is the quantum efficiency

E = the photon energy

$b_s(E)$ = The incident spectral photon flux density i.e. the number of incident photons of energy between E and $E+dE$ on unit area in unit time.

QE depends upon the optical absorption coefficient of the absorber layer of the solar cell and the efficiency of charge separation and accordingly charge collection in the device. QE of the solar cell can be given as function of either

incident photon energy (E) or wavelength (λ). Both E and λ are defined by the relationship [46]

$$E(eV) = \frac{hc}{\lambda} = \frac{1240}{\lambda(nm)} \quad (2.35).$$

2.10 Polycrystalline Thin Films for use in Solar Cells

Thin films of II-VI and I-III-VI₂ based compound semiconductors deposited using low cost deposition methods on inexpensive substrates (e.g. soda-lime glass (SLG)) are found to be polycrystalline i.e. made up of small crystallites separated by grain boundaries. At grain boundaries recombination is enhanced and they are therefore responsible for significant loss in photovoltaic performance. In addition, due to charge trapping at grain boundaries, there is a possibility of the formation of a potential barrier which obstructs carrier transport [48].

Absorber layer requirements in polycrystalline thin film solar cells

- i) Semiconductors with a small energy band gap give a high photocurrent and a low V_{OC} whereas wider energy band gap material will produce a high V_{OC} but a low I_{SC} . In order to get higher cell efficiency which is proportional to the output power, the energy band gap of the absorber material should lie within the range 1.0-1.7 eV [49].
- ii) The optical absorption coefficient α of the absorber layer should be high, in order to absorb most of the portion of the incident energy within the thin layer. For this reason direct band gap semiconductors are advantageous for making high performance solar cells (as in such materials α is high).
- iii) A “large” minority carrier diffusion length L is desirable to minimise the recombination of minority carriers. A larger diffusion length can be achieved by minimising the densities of crystalline defects and impurities. For efficient solar cells action: $L > 1/\alpha$.

- iv) The bulk resistivity of the absorber layer should be low to minimise losses in device operation arising due to series resistance.

2.11 Thin Film CuInSe₂ based Solar Cell Structures

The ternary compound CIS and its alloys are promising photovoltaic materials with material properties that can be adjusted for optimum solar cell performance. The material is a direct band gap semiconductor with high optical absorption and alloying with Ga produces Cu(In,Ga)Se₂ thin films [27].

There are basically two types of thin film solar cell structures:

- i) substrate configuration devices and
- ii) superstrate configuration devices structures

In the substrate configuration cell fabrication takes place in a sequence-back contact, absorber layer, buffer layer, window layer, top contact grid.

In superstrate configuration the fabrication sequence is in reverse order i.e. transparent conductive oxide (TCO)-coated glass/window layer/buffer layer/absorber layer/back contact.

The up and down block arrows in the figure 2.14 show thin film solar cell production order according to layer deposition sequence.

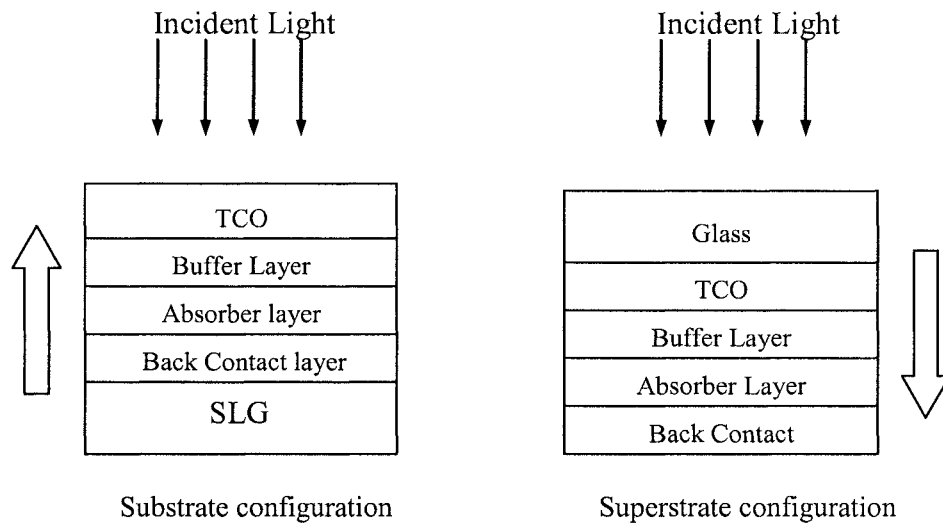


Figure 2.14 Thin film solar cell structures.

2.12 Losses in Real CuInSe₂ Photovoltaic Solar Cells

The photovoltaic cell efficiency is limited by many factors that primarily depend on incident photon absorption and utilisation of these photons in the photovoltaic process. Various layers are required to be deposited on the absorber layer in order to make the cell operational and to improve the cell performance. The loss of efficiency in a CIS-based thin film solar cell, however, is due to some structural, material and electrical properties of the cell [47, 50]. As shown in figure 2.15, starting from the top of the substrate CIS-based cell:

- i) The current collecting grid (Ni-Al metal contacts) is opaque for incident light and therefore this reduces an effective cell area for the entry of incident photons introducing ~ 4% loss.
- ii) Some of the incident photons that penetrate through the metal grid are reflected and are not absorbed. In case of CIS-based solar cells, this “reflection loss” it can be minimised by depositing an ARC of MgF₂.
- iii) The TCO is known as the window layer and the CdS layer as the buffer layer in order to distinguish between these two layers in solar cell. These absorb some of the incident photons if $h\nu > E_g$ (window layer) or E_g (buffer layer).
- iv) Some of the incident photons (with $h\nu > E_g$ (absorber layer)) are not absorbed in the depletion region due to a short minority carrier diffusion length in the absorber layer. The significant loss can be seen by analysing the quantum efficiency data in the long-wavelength region obtained for that particular cell. This is known as “bulk recombination loss”.
- v) $R_S \neq 0$: this reduces FF and J_{SC} and therefore device efficiency.

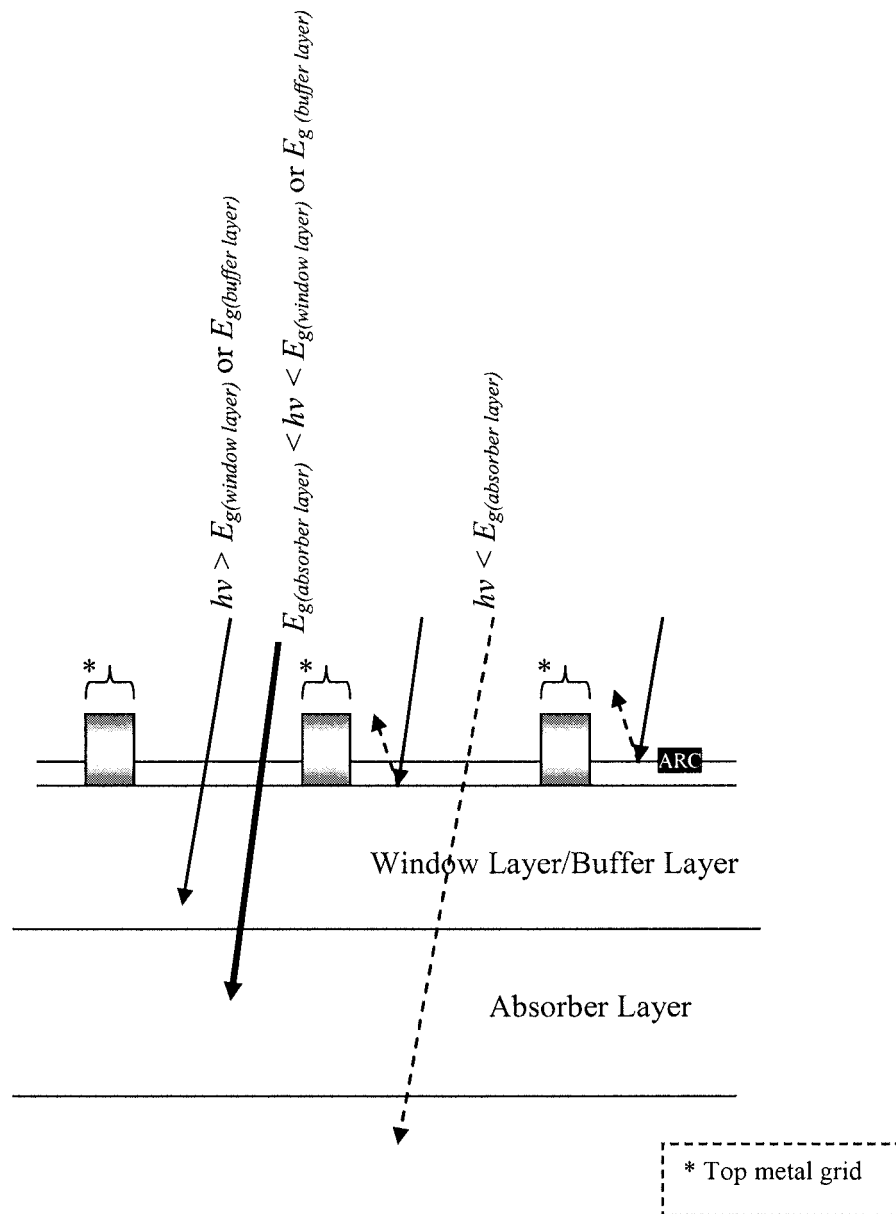


Figure 2.15 Reflection and absorption of incident photons in CIS-based thin film solar cell.

- vi) $R_{Sh} < 100 \Omega \text{ m}^{-2}$: if $R_{Sh} > 100 \Omega \text{ m}^{-2}$ its effects can be ignored. However if $R_{Sh} < 100 \Omega \text{ m}^{-2}$ the device efficiency is significantly reduced.

Bibliography- Chapter 2

- B. G. Streetman and S. Banerjee, *Solid state electronic devices*, Prentice Hall Series in Solid State Physical Electronics, Nick Holonyak, Jr., Series Editor, 5th Edition, (2000).
- J. Nelson, *The physics of solar cells*, Imperial College Press (2003).
- K. Chopra and S. Das, *Thin film solar cells*, Plenum publication (1983).
- L. D. Partain, ed. *Solar cells and their applications*, Wiley series in microwave and optical engineering, John Wiley & Sons, Inc., (1995).
- R. H. Bube, *Photovoltaic materials* - Series on Properties of Semiconductor Materials, Imperial College Press, (1998).
- S. M. Sze, *Semiconductor devices - Physics and Technology*, John Willey & Sons, (1985).

CHAPTER 3

LITERATURE REVIEW

3.1 Properties of CuInSe₂-based Absorber Material

CuInSe₂ (CIS) has the tetragonal chalcopyrite structure. This is represented as each I (Cu) or III (In) atom having four bonds to the VI atom (Se). This means that each Se atom has two bonds to the Cu atoms and two bonds to the In atoms. The strength of the I-VI and III-VI bonds are different and therefore the ratio c/a is not exactly equal to 2. In the literature, c/a is reported as being equal to 2.01 in CIS [51]. The Cu-In ratio variation leads to a high concentration of electrically active native defects and this result in large changes in carrier density. Hence a deviation from a unity value of Cu/In ratio determines whether the conductivity is n or p -type [47]. The Cu/In ratio in the precursor is an important factor for the absorber layer preparation in CIS thin film solar cells because their morphology and optoelectronic and structural properties have been found to be dependent on it [52]. Cu/In ratios higher than 0.95 have been shown to result poor cell performance due to unwanted Cu-related secondary phases present in the absorber material which leads to significantly lower shunt resistance [51]. Moreover, Cu-depleted films produced using an excess supply of Se form p -type material while Cu-rich films selenised in deficient Se supply would be expected to form n -type layers because the Se vacancy (V_{Se}) acts as a dominant donor in n -type chalcopyrite material and the Cu vacancy (V_{Cu}) acts as a dominant acceptor in Cu-poor p -type material [9]. However, the Cu-rich phase plays an important role during absorber film growth, it tends to yield grain sizes in excess of 1 μm whereas an In-rich composition results in smaller grain structured films [53].

Optical properties and grain boundary effects related to CIS single crystal as well as thin films were reported by Kazmerski *et al.* [54]. They found the difference

between the energy bandgap of single crystals (0.96 eV) and thin films (1.02 eV) to be due to nonuniformity in the composition of polycrystalline CIS absorber films. The optical properties of thin films were found to be dominated by the structure of the polycrystalline material such as rough surfaces and the presence of secondary phases at the grain boundaries [55]. Two μm -thick single-phase CIS thin films that exhibited a strong orientation along the prominent (112) peak have been found to have a bandgap above 0.95 eV and an optical absorption coefficient (α) near to 10^5 cm^{-1} [56]. The energy band gap of CIS can be widened, up to 1.7 eV by alloying with Ga and up to 2.7 eV by alloying with Al. There is a variation of the lattice constants a and c with energy band gap for CIS alloyed with Ga or Al substitution of In (Fig. 3.1) [30, 32].

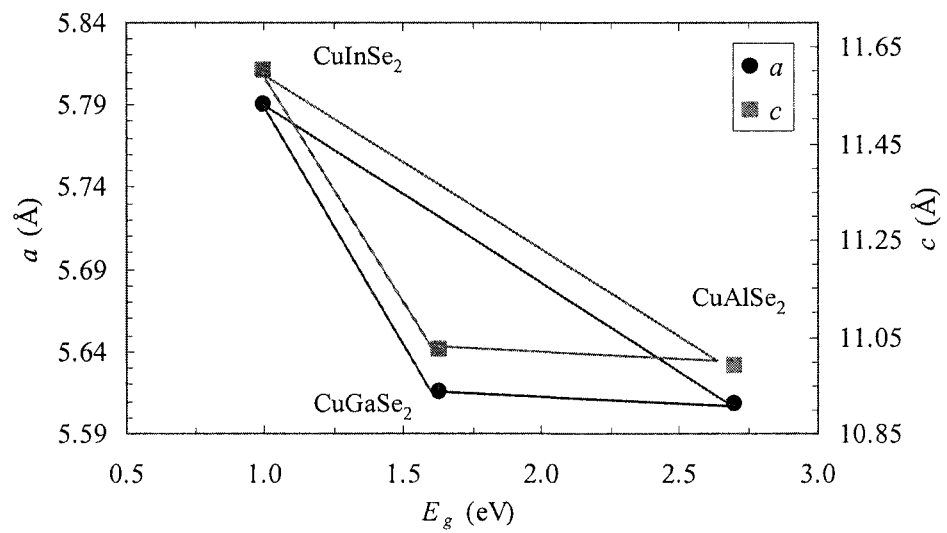


Figure 3.1 Alloying with Ga or Al changes energy band gap and lattice constants a and c [30].

3.2 Historical Development of CuInSe₂-based Thin Film Solar Cells

3.2.1 Single crystal CuInSe₂ material

In 1953, Hann *et al.* reported growing single crystal CIS [57]. In 1956, Austin *et al.* also reported the preparation of a polycrystalline ingot of CIS which was grown by the zone melting of pure Cu, In and Se [58]. It was however found that the polycrystalline ingot had many cracks. Austin *et al.* suggested that the reason for the poor quality of the ingot was due to differential thermal expansion between the *a* and *c* lattice axes in the chalcopyrite crystal structure.

In 1975, Wagner *et al.* reported the fabrication of a CIS based heterojunction device structure produced by the vacuum evaporation of *n*-type CdS onto single crystal *p*-type CIS [59]. These early devices had conversion efficiencies of approximately 5%. The CIS crystals were produced by melting a stoichiometric mixture of elements using a temperature of 980°C. The CIS of *p*-type was produced from the originally *n*-type crystal by annealing the boule at a temperature of 600°C in a Se atmosphere for 24 hours. The main purpose for the development of this heterojunction was to use it as a near-infrared radiation detector. In 1975, they produced CdS/CuInSe₂ solar cells with efficiencies of 12%. This was measured on a clear day in New Jersey (~ 92 mW/cm² solar intensity). At the time only three photovoltaic materials: Si, GaAs/Ga_xAl_{1-x}As and InP/CdS had demonstrated efficiencies > 10% and this paper stimulated work worldwide into developing thin film CIS solar cells [60]. In May 1975, Kazmerski *et al.* reported the growth and electrical properties of single crystals of another I-III-VI₂ chalcopyrite material, CuInS₂ [61]. Two deposition methods were reported, both based on thermal evaporation. The first method was based on a single source method and the second

involved a two source arrangement. They found the two-source method more controllable for sulphur incorporation into the films.

3.2.2 Polycrystalline CuInSe₂ thin films

In 1976, Kazmerski *et al.* reported the fabrication of polycrystalline thin film CdS/CuInSe₂ heterojunction solar cells [62]. The efficiencies of the solar cells produced were in the range 4-5%, measured under 100 mW/cm² tungsten-halogen illumination. The CIS was grown by the vacuum evaporation method. By 1981, a 10% efficient CuInSe₂/CdS thin film solar cell was produced by Mickelsen and Chen at the Boeing Aerospace company using a three-source co-evaporation method [23, 63]. The Boeing method involved the deposition of a CIS bilayer. The first CIS layer of low resistivity deposited was Cu-rich and this was followed by the deposition of an In-rich layer of higher resistivity. The total thickness was 2.6 μm. Since then the Boeing deposition method has become one of the established methods for producing CIS thin films. Different research groups such as the Institute of Energy Conversion (IEC) at Delaware, the National Renewable Energy Laboratory (NREL) (formerly Solar Energy Research Institute) at Colorado, Avancis GmbH (formerly Shell Solar GmbH-formerly, Siemens Solar-formerly, ARCO Solar [64]) and the University of Stuttgart at Germany have continued research into optimisation of the three-source evaporation method and improvement in output of the solar cells. In that same year, researchers at Boeing were able to increase the efficiency to 11.9%, for a cell area of approximately 1 cm², by improving the antireflection coating [65].

In 1984, Thornton *et al.* investigated the use of reactive direct current (DC) magnetron sputtering to produce CIS thin films [66]. The film synthesis method involved the deposition of Cu and In precursor layers using magnetron sputtering and

then reacting the metallic layers with H_2Se gas to synthesise CIS. Solar cells produced using this material had efficiencies up to 4%. In 1985, Ermer *et al.* fabricated CdS/CuInSe_2 solar cells in which the absorber was produced by room temperature DC magnetron sputtering from Cu_2Se and In_2Se_3 hot pressed targets, to form a precursor layer; this was followed by an anneal to synthesise the CIS [67]. They performed initial experiments using separate elemental Cu, In and Se targets, but found that the Se flux was difficult to control and also the Se poisoned the Cu and In targets. The window layers used in such devices were fabricated by the vacuum evaporation of 250 nm of high-resistivity undoped CdS followed by 2 μm of In-doped CdS. The top contacts were made using In/Ag grids. A SiO_x antireflection layer was evaporated onto the CdS layers to complete the devices. The best device fabricated using this technique had an efficiency of 6.1% (cell area, 4 cm^2). The major limitation to this type of fabrication approach was the instability of the In_2Se_3 sputtering target.

ARCO Solar instigated CIS development efforts in the early 1980s, inspired by Boeing's achievement in producing cells with efficiencies $> 10\%$. In 1985, Potter *et al.* at ARCO Solar, were able to increase cell efficiencies to $> 11.2\%$ (cell area, 4 cm^2) (Fig. 3.2) [68]. The fabrication method for the CIS layer was a two stage growth process in which Cu-In precursor layers were sputter deposited onto Mo-coated SLG substrates. This was followed by an anneal in H_2Se at an elevated temperature of 400-450°C to synthesise the CIS. The improved efficiency was attributed to the use of much thinner CdS than previously used (thickness < 500 nm) which allowed more light to penetrate to the junction region [68]. In 1988, ARCO

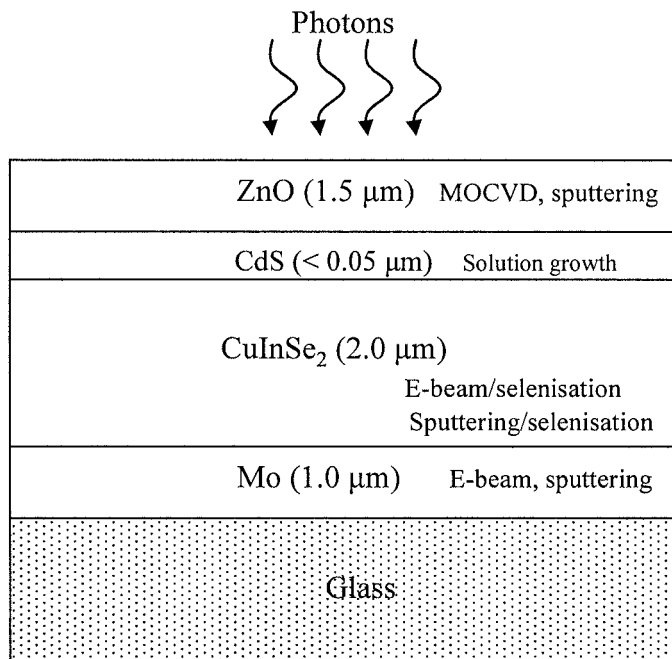


Figure 3.2 Cross-sectional view of the CdS/CuInSe₂ solar cell developed by ARCO Solar [69].

Solar developed CIS cells with efficiencies up to 14.1% (cell area, 3.5 cm²) [70]. They also synthesised an absorber layer by the selenisation of stacked metal layers using H₂Se. The fabrication method approach was based on the sequential deposition of Cu, In and Se elements, rather than the elements being deposited simultaneously. Although this increased the number of steps, it allowed higher rate depositions. The main disadvantages of this production method were the use of highly toxic H₂Se gas and the lack of reproducibility which resulted in a low production yield. The former problem was partially resolved by Eberspacher *et al.* [71]. They found that adding Se to the precursor metal Cu-In stack resulted in less H₂Se being needed to carry out the selenisation process.

In 1988, researchers at Northumbria University (formerly, Newcastle upon Tyne Polytechnic), UK, reported a novel patented method for the production of CIS films [72, 73]. This method involved the formation of stacked structures consisting of alternate elemental layers of In, Se and Cu, deposited in sequence onto Corning 7059 glass, by vacuum evaporation. The stacked structures were less than 0.5 µm-thick and consisted of 440 Å of In, followed by 920 Å of Se, followed by 200 Å of Cu. This sequence was repeated twice or more to get the required thickness. The deposited layers were annealed *in situ* at 500°C for 30 min in order to synthesise chalcopyrite CIS thin films. The CIS films obtained were *p*-type and had an energy band gap of 1.05 eV. The electrical and optical properties of CIS films synthesised were suitable for use in thin film solar cells and the method was also suitable for large scale, low cost production [73].

Since 1990, due to progress of ARCO Solar and Boeing companies in CIS technology, several research groups in USA, Europe and Japan were motivated to begin work on CIS based thin film solar cells.

In 1990, Kapur and Basol published a report on the key issues including cost estimates for producing CIS PV modules using the two-stage method in order to make the technique suitable for large scale, low-cost manufacturing [74]. At the International Solar Electric Technology (ISET) research centre, they developed a two stage process, based on the electrodeposition of stacked layers of Cu/In which were then by selenised using a H₂Se/Ar atmosphere, at 400°C, to form CIS. The CIS layers formed however had poor adhesion to the Mo back contact layer due to stresses caused by the expansion in volume of the Cu/In films during CIS formation. ISET recommended using the sputtering technique to avoid this problem and also suggested replacing the toxic H₂Se gas with elemental Se. The best cell produced had efficiencies up to 12.4% for an active area of 1 cm² [75].

In 1991, Siemens Solar Industries (formerly, ARCO Solar), fabricated CIS modules with efficiencies exceeding 10% [76]. However, the main challenge remained the improvement of process yield for CIS modules, so that they could progress toward large scale manufacturing.

Several other types of production methods for CIS thin films were explored by different research groups around the world such as electrodeposition, screen printing and the sintering method (SPSM) [77, 78]. These methods were investigated because they are low cost process, non-vacuum processes, with good material utilisation and good prospects for large area processing. In 1987, a non-vacuum type one-step electrodeposition process was reported for producing photoactive CIS thin films [77]. It was found that the CIS thin films grown by electrodeposition possessed the chalcopyrite structure with good adhesion to the Mo-coated glass substrates. These cells had an open circuit voltage of 240 mV, a short circuit current density of 3.2 mA/cm² and a fill factor (FF) of 0.4. In late 1988, Japanese researchers at

Matsushita Industries prepared CIS films using SPSM which was a non-vacuum and inexpensive method [78]. In this method a screen printing paste of CIS material was prepared by grinding together Cu, In and Se powders in a ball mill. An appropriate binding agent propylene glycol was added to form a paste of CIS for the screen printing. The paste was screen printed onto borosilicate glass substrate and the printed film then sintered in a N₂ atmosphere at 700°C.

In 1993, a world record efficiency of 15.4% was reported [79]. This cell had the structure ZnO/CdS/CuInSe₂/Mo/SLG and the CIS was produced using the co-evaporation method. However the cell was measured under an ELH lamp (American National Standards Institute code for a tungsten-halogen electric lamp [80]) which was rich in the red part of the spectrum and this result was disputed by AbuShama *et al.* [24].

In 2005, NREL reported a 15.0% CIS solar cell (cell area, 0.403 cm²) measured under standard test conditions (AM1.5 Global spectrum, 1000 W/m² at 25°C) [81].

3.2.3 Cu(In,Ga)Se₂ thin films

CIS has an energy band gap of 1.0 eV which is smaller than the optimum energy band gap of 1.4 eV, needed for PV energy conversion. Because of the small energy band gap it is not possible to achieve an open circuit voltage larger than 0.6 V [82]. A solution to increasing open circuit voltage is to add gallium (Ga) to CIS to form Cu(In,Ga)Se₂ (CIGS) thin films. The quaternary compound CIGS can be tuned to an energy gap between 1.0 eV to 1.7 eV by altering the Ga/(Ga+In) ratio in the selenised thin film.

In 1987, Chen *et al.* described the production of CIGS thin films and subsequently thin film ZnCdS/CIGS solar cells [83]. The CIGS material was produced by the simultaneous vacuum evaporation of the elements Cu, In, Ga and Se to form the quaternary compound. They followed a process similar to the two layer 'Boeing' process that had been used to deposit CIS thin films. The first Cu-rich layer (2 μm -thick) was grown using a substrate temperature in the range of 400°C to 450°C. A second 1 μm Cu-poor second layer was then deposited with a slight increase in temperature to 550°C. Different amounts of Ga were incorporated into the films by changing the evaporation rates of the appropriate sources. A range of cells (area, 1 cm^2) were made by varying x from 1.0 (CuGaSe_2) to 0.25 (25% Ga content in CIGS) and depositing a $\text{Zn}_{0.12}\text{Cd}_{0.88}\text{S}$ window layer. The FF was significantly reduced with the increase in Ga content. A value of $x = 1$ gave an open circuit voltage 0.68 V with an efficiency of 2.71%. In contrast, only 25% Ga content gave an open circuit voltage (V_{OC}) value of a 0.51 V, FF of 0.66 but a conversion efficiency value greater than 10%.

Similar work on CIGS was carried out by Dimmler *et al.* at the University of Stuttgart, Germany and they yielded cell efficiency up to 5.8% for CuGaSe_2 (CGS), 9.3% for CIS and 3% for a $\text{CuIn}_{0.56}\text{Ga}_{0.44}\text{Se}_2$ thin films [84].

In early 1990, Klenk *et al.* demonstrated that for Cu-rich CIGS a Cu_{2-x}Se phase is formed at the surface which is harmful to the photoactive properties of the thin film [85]. The absorber films were prepared by evaporation method and treated with 10% potassium cyanide (KCN) solution in order to remove the Cu_{2-x}Se phase at the surface. The performance of the solar cell was improved when the CIGS absorber films had been etched in KCN.

In 1993, Stolt *et al.* at the Royal Institute of Technology, Sweden, reported a solar cell ZnO/CdS/CuInSe₂ with an efficiency of 14.8% [86]. Although they claimed the CIS absorber was produced using the co-evaporation process, they had actually added 0.1% Ga throughout the film. It was possible to achieve higher efficiency because of improved properties of the absorber and the heterojunction by performing modifications to the fabrication process. These modifications included using soda-lime glass (SLG) substrate instead of sintered alumina. This resulted in CIS with larger grains and with a higher degree of $\langle 112 \rangle$ texture. The CdS layer used in these devices was deposited using chemical bath deposition (10-20 nm-thick). The cells were also annealed in air at 200°C for few minutes before taking the J - V measurements. The solar cells had $V_{OC} = 513$ mV, $FF = 0.716$ and $J_{SC} = 40.4$ mA/cm² (area, 0.262 cm²).

➤ **Role of Na during absorber growth**

The influence of the SLG substrate on the morphology and microstructure of CIS based absorber was investigated by Hedström *et al.* [79]. For this study, they deposited CIS on different substrates including SLG, borosilicate glass, sapphire and alumina, uncoated and coated with Mo. X-ray diffraction (XRD) measurements were carried out on these samples and they concluded that the strongest (112) orientated CIS films were associated with SLG substrates. In the surface and depth analyses performed on the films using X-ray photoelectron spectroscopy (XPS) and secondary ion mass spectroscopy (SIMS), elemental Na was detected in the samples which were deposited on SLG. In addition, there was an improvement in photovoltaic properties of CIS and CIGS cells fabricated on SLG substrates. Since then several

research groups have been investigating the effects of “Na ions” on the structural and electronic properties of CIS and CIGS films.

Inspired by Swedish researchers’ work into the role of Na, researchers at Siemens AG and the University of Stuttgart, Germany performed several experiments with and without Na incorporation into CIS based absorber layers [87]. The objective was to quantify the impact of Na on grain morphology and cell performance. The Na was deliberately incorporated in the films by depositing a layer of NaSe in between the Mo back contact and Cu-In-Ga precursor layers. The advantages of the presence of Na were a larger grain morphology of the CIGS and an improvement in cell performance.

3.3 Major Research Groups and Companies Working on CuInSe₂-based Thin Films

3.3.1 Co-evaporation from elemental sources

The process that has yielded the highest performance CIGS cells can be tracked back to Boeing's bilayer process. US researchers at NREL have reported the world record, 19.9% efficient, CIGS thin film solar cells based on NREL's patented three stage co-evaporation method [27, 88-90]. In the first stage, an (In,Ga)₂Se₃ precursor layer is deposited onto SLG using a substrate temperature of 300°C. The layer contains 90% of the total In and Ga needed later to form a CIGS absorber layer that is Cu-poor. The proportion of evaporated elements Ga and In in the flux is in the ratio of approximately 1:3. The substrate temperature is then increased to 560°C and elemental Cu is evaporated in an environment containing excess Se. For the third stage the substrate temperature was maintained at 560°C and the remaining 10% of Ga and In (Ga:In = 1:3) was evaporated. Excess Se was added during cooling of the sample from 560°C to 350°C. The overall thickness of the resulting absorber film was approximately 2.5 μm. This approach of absorber synthesis offers many advantages in control of film morphology, defects, orientation, band gap grading throughout thickness of the layer and stoichiometry control. This type of deposition method, however, is difficult to implement on an industrial scale.

In a recent publication, Ramanathan *et al.* compared the properties of the highest performance devices produced by the three stage method with those fabricated by other methods in order to identify areas for improvement [91]. They

suggested using thinner layers of CIGS to minimise the use of In, which is expensive and not abundant, to directly reduce the cost of absorber layer production. The efficiencies were in the range 16-17% for cells made using the thinner absorbers.

Researcher workers at Ångström Solar Centre, Uppsala University in Sweden, followed the Boeing recipe to deposit the CIGS layers by co-evaporation from open boat sources containing elemental Cu, In, Ga and Se [92]. The aims were to produce CIGS layers which were stable, low cost, and had low environmental impact. They also reported an efficiency of 16.6% for a CIGS mini-module (area, 100 cm²) [93]. In addition, significant progress was made towards reducing the cost of CIGS in the development of thinner absorbers of thicknesses in the range 0.8-1 µm. The baseline CIGS deposition process was modified by evaporating pure CGS at the bottom of the CIGS layer (near the Mo back contact surface) followed by Ga/In-grading of the absorber layer. This was to create a back surface field (BSF) which helps to reduce the recombination losses at the back contact. In this way, the thin film CIGS solar cells were produced with efficiencies up to 15% [94].

The Institute of Physical Electronic (IPE) at the University of Stuttgart, working in collaboration with the ZSW research centre has developed a high quality process for the production of high efficiency CIGS solar cells. In 2006, continued research efforts by research workers at IPE and ZSW made it possible for Würth Solar Company in Germany, to set up a 15 MW_p CIS production plant [95]. They have reported conversion efficiencies up to 19.3% for cell area up to 0.5 cm². The CIGS deposition process used was the three stage NREL co-evaporation technique described earlier [96].

Shafarman and Zhu from the Institute of Energy Conversion (IEC) at University of Delaware, USA, concluded that for given substrate temperature, there

is no relationship between grain size and device performance [97]. The CIGS films were deposited by physical vapour deposition using multi-source elemental evaporation.

Rudmann *et al.* have grown CIGS on the Mo-coated SLG substrate using the “bi-layer” recipe, in which a Cu-rich layer was deposited as the bottom layer followed by the deposition of an In-rich layer. The overall film grown was Cu-poor in composition. They reported the CIGS solar cell parameters; efficiency of 14.4%, FF of 72.8%, V_{OC} of 655 mV and J_{SC} of 30.3 mA/cm² (cell area, 0.585 cm²) [98, 99].

Japanese research workers at Matsushita Electric Industrial Company Limited reported producing a CIGS cell with an efficiency over 18%. They prepared CIGS absorber films by a three-stage physical vapour deposition method. They described the deposition sequence as: in the first stage, the evaporation of a In-Ga-Se precursor onto a Mo-coated glass substrate using a substrate temperature of 350°C; “in the second stage, the evaporation of a Cu-Se precursor, to form a Cu-rich composition, using a substrate temperature of 500°C; in the third stage the addition of an In-Ga-Se flux using a substrate temperature of 500°C, in order to form a slightly (In,Ga)-rich CIGS films” [100, 101].

3.3.2 Selenisation of sputter deposited metallic precursor layers

The two-stage process of CIS-based absorber layer formation involves the deposition of metallic precursor layers by magnetron sputtering, followed by selenisation of the precursor layers at an elevated temperature in a Se atmosphere created by H₂Se gas or elemental Se.

The process of ‘sputtering’ is a well established deposition technique used in the semiconductor and thin film coating industries. There are several distinguishing

features of magnetron sputtering such as uniform and cost-effective deposition of thin films over large areas [102]. In addition, the advantage of the sputtering technique is its higher degree of material utilisation (75%) as compared to that achieved using the thermal method (35%) in evaporation [74].

Showa Shell in Japan (using a process licensed from Siemens Solar Industry), fabricated $\text{Cu}(\text{In,Ga})(\text{S,Se})_2$ (CIGSS) thin film modules by a two stage method using In/Cu-Ga/Mo stacked precursors and H_2Se gas. The Cu-In-Ga precursor layers were deposited by magnetron sputtering followed by selenisation in H_2Se gas. A sulphurisation process was then used to introduce sulphur. They improved the deposition process and the process control technologies to enable processing of substrate sizes of 3600 cm^2 or larger. The highest efficiency reported was 13.4% for a $\text{Zn}(\text{O,S,OH})_x$ buffer/ $\text{Cu}(\text{In,Ga})(\text{S,Se})_2$ with a module size of 3600 cm^2 [103].

The CIS based module fabrication process of Avancis GmbH, Germany (a joint venture between Shell Solar GmbH and Saint-Gobain, the glass manufacturing company) avoided the use of highly toxic H_2Se gas in the selenisation process [64].

The CIS production method involves:

1. the deposition of the Cu-In-Ga precursor layers using magnetron sputtering,
2. the deposition of a Se layer on top of the precursor layer using a thermal evaporation,
3. rapid thermal processing (RTP) of the Se capped precursor layers in an environment containing both Se and S.

Avancis produced a CIGSS module with an efficiency of 13.5% for a CIGSS module (area, $30 \times 30 \text{ cm}^2$) and an efficiency of 13.1% for a $60 \times 90 \text{ cm}^2$ module [104].

The main advantages of this method are its suitability for a large area deposition and improved environmental safety by avoiding the use of H_2Se .

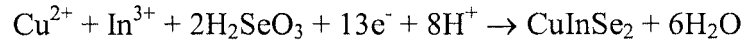
The highest efficiency reported for a CIS based cell is 19.9% (active area, 0.419 cm²). This was based on an absorber layer produced using the three-stage co-evaporation process [27]. However on the larger area both co-evaporation and sputtering yielded about the same efficiency. The world record efficiency is currently for the CIGSS modules produced by Showa Shell [105].

3.3.3 Electrodeposition

The electrodeposition (ED) technique is well suited for large-scale industrial applications due to the relatively low capital cost of the equipment required.

Bhattacharya *et al.* have reported a 15.4% efficient CIGS device produced using electrodeposited precursors [106]. The precursors were deposited by preparing a bath containing 0.02-0.05 M CuCl₂, 0.04-0.06 M InCl₃, 0.01-0.03 M H₂SeO₃, 0.08-0.1 M GaCl₃ for the source of Cu, In, Se and Ga respectively, and 0.7 M LiCl dissolved in water. The ED process was accomplished using a three-electrode (Pt-reference electrode, Pt gauze-counter electrode and the Mo/glass) cell and by applying a constant potential of 1.0 V for the purpose of electroplating. Although this is classed as an ED process, an additional layers of CIGS was deposited onto the electrodeposited CIGS films using a physical vapour deposition (PVD) technique using a substrate temperature of 560°. This process was based on a hybrid approach and therefore the main advantage of using non-vacuum method was lost.

French research workers reported work based on electrodeposition of the precursor film followed by thermal annealing to synthesise CIGSS thin films [107]. The solution was prepared by dissolving the precursor elements in an aqueous acidic bath and then co-depositing at the Mo/glass electrode. The following ideal cathodic reaction related to ternary CIS is given as



They extended their process to prepare quaternary (CIGS) as well as pentenary (CIGSS) alloys. Their best device on a laboratory scale had an efficiency of 10.6% for a device area of 0.1 cm² and 6-7% efficiencies for 30×30 cm² area cells.

3.3.4 Spray pyrolysis technique

Reddy and Miles have grown thin films of CuGa_xIn_{1-x}Se₂ using a spray pyrolysis method [108]. In this technique, an ionic solution containing the constituent elements of compounds such as copper chloride, gallium trichloride, indium trichloride and selenourea were sprayed over the SLG substrate with the substrate temperature maintained in the range 100-400°C. They found that CIGS layers grown at temperatures in the range 300-350°C were stoichiometric and single phase in composition.

3.4 CuAlSe₂ and Cu (In, Al)Se₂ Absorber Layers

Solar cells fabricated using CIS and CIGS absorber films are promising candidates for low cost photovoltaic applications. Several efforts are being carried out by researchers to reduce production cost of the good quality absorber films (which takes a significant portion of the entire module production cost), such as improving device performance to yield maximum efficiency, minimising material usage through depositing thinner films and depositing films over a larger area. Although the highest efficiencies have been achieved using CIGS, there is some concern with the lack of abundance of Ga and the very high market price of pure In material used in these devices. In order to address these problems, the replacement of Ga with Al would help to minimise the production cost due to the abundance and relatively low cost of Al. The quaternary compound semiconductor CuIn_{1-x}Al_xSe₂ (CIAS) can be produced with variable band gap by varying the amount of Al in thin film. In figure 3.3, the variation of energy band gap versus composition are plotted for both CIGS and CIAS using the equations 3.1 and 3.2 that can be found in the literature [30, 109]:

$$E_g(\text{CuIn}_{1-x}\text{Ga}_x\text{Se}_2) = 1.010 + 0.459x + 0.167x^2 \quad (3.1)$$

$$E_g(\text{CuIn}_{1-x}\text{Al}_x\text{Se}_2) = 1.000 + 1.080x + 0.130x^2 \quad (3.2)$$

[where $x = X/(\text{In}+X)$; X is Ga or Al]

In 1988, Niemi and Stolt fabricated CuAlSe₂ (CAS) thin films by the process of co-evaporation for the purpose of use in thin film solar cells [110]. The fabrication process included the evaporation of elements Se and Cu and an Al/Cu alloy (Al 90 at.% and Cu 10 at %) using resistively heated boats onto Corning 7059 glass substrates. The substrate temperature was maintained at 450°C during the deposition.

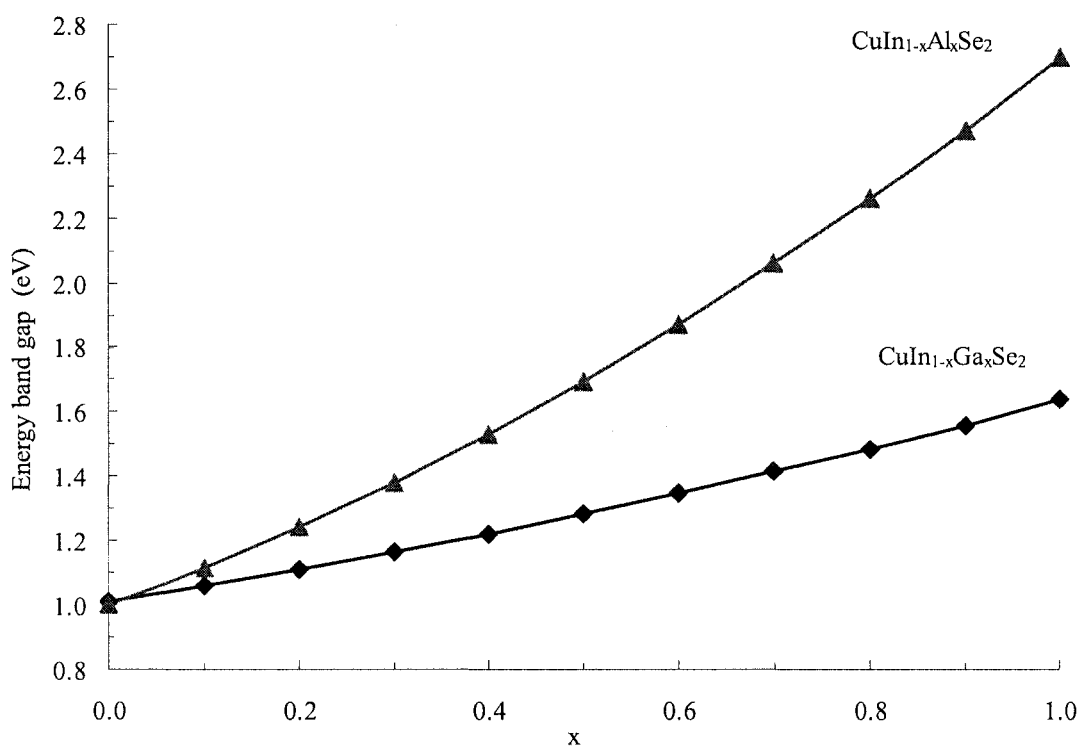


Figure 3.3 Energy band gap variations in absorber films with content x [$x = X/(\text{In}+X)$; where X can be Ga or Al] [30, 109].

Excess Se was supplied during the deposition to compensate for any Se loss in the thin films deposited. They synthesised material with *p*-type conductivity for all the CAS thin films.

Another type of experiment was carried out to prepare CAS thin films by the selenisation of sequentially deposited Cu/Al/Cu...Al/Cu layers [111]. The method involved, first the deposition of Cu and Al metallic layers onto the SLG substrates by alternate thermal evaporation using two separate tungsten crucibles. The significant difference between this process and that mentioned earlier is that Cu and Al elements were evaporated separately instead of using an Al/Cu alloy. The substrate was on a rotating substrate holder in order to form the alternate Cu and Al layers. Finally a topmost layer of Cu was deposited to prevent Al oxidation in open air. They selenised the Al/Cu/Al...Al/Cu sample in a vacuum sealed Pyrex tube for 24 hours at a temperature of 550°C. The energy band gap of the CAS thin film was of 2.67 eV. However, most of the films produced were poor as they had crystallised with large disordered grain boundary domains. There was concern about reproducibility of good quality material.

Reddy and Raja have investigated the effect of the Cu/Al ratio on the optical, structural and electrical properties of CAS thin films [112]. They synthesised CAS films using the three-source co-evaporation technique. The Cu and Al elements were evaporated in the stoichiometric ratio, while the Se evaporation rate was twice that needed to achieve stoichiometry; the substrate temperature was held at 400°C. In XRD analyses they have found three types of films: Cu-rich, near-stoichiometric and Al-rich films. The secondary phase in the Cu-rich films was Cu₂Se and the remaining two films were single phase. The energy band gap and the resistivity were increased with Al content in the films.

In 1990, Gębicki *et al.* produced bulk semiconductor CIAS crystals with x in the range between 0-1. The pure elements were supplied using a chemical transport method in which iodine was the transport agent [113]. In order to form the chalcopyrite structure for every composition, the sample was heated in a temperature gradient of 720-820°C for about 10 days. The variations in lattice constants a and c with the composition were recorded. These were found to obey Vegard's law in both cases.

In 1998, Itoh *et al.* reported the preparation of CIAS by depositing a stack of In(Al)/Cu/Se/Cu/Al(In) using vacuum evaporation and then heating the stack in vacuum [114]. The final top layer was an In cap to prevent Al oxidation. Then annealing of the stacked multilayer in vacuum was performed inside the sealed glass tube at 600°C for 2 hours. The selenised film was approximately 1 μm -thick. The resistivity and energy band gap of the films were found to increase with Al content. In addition, non-linear changes in lattice constants a and c were reported with increased Al content.

US researchers, from the IEC at Delaware, produced single phase CIAS thin films using multisource elemental evaporation in which the elements Cu, In, Al and Se were co-evaporated onto SLG or Mo-coated SLG substrates [115]. During the deposition, the substrate temperature was maintained in the range between 450-500°C. They have found that films deposited at temperatures $> 500^\circ\text{C}$ adhered poorly on glass as well as the Mo-coated glass substrates. Several depositions were carried out to obtain thin films with $x = 0-0.53$. The energy band gap was reported to vary over the range 1.0-1.74 eV with an increase in x . For the first time, they have reported the solar devices produced using CIAS absorber films; an efficiency of 11% was obtained for $x = 0.26$. Two years later the same research group reported a device

efficiency of 16.9% for a CIAS solar cell with absorber of thickness 2.0-2.5 μm and band gap 1.16 eV [32, 116]. The increase in device performance was achieved due to significant improvements in device fabrication process such as addition of the thin Ga layer (5 nm) by sputtering onto the Mo-coated SLG substrate. The bottom thin layer of Ga improved the adhesion of the absorber film to the Mo back contact for temperatures $> 500^\circ\text{C}$.

Reddy and Raja reported the production of CIAS thin films (with $x = 0.7$) by a 4-source co-evaporation method with the aim of using such layers in a tandem solar cell structure [117]. These films were single-phase, near stoichiometric and were *p*-type conductivity ($\rho = 140 \Omega.\text{cm}$).

Korean researchers have grown CIAS thin films by the selenisation of metallic Cu, In and Al precursor layers in a Se atmosphere [33]. This deposition method is similar to the two stage deposition process for CIS thin films. This method consisted of DC sputtering of Cu, In and Al to deposit metallic precursor layers onto Mo-coated SLG substrates; this was followed by selenisation of these layers in a Se environment, firstly at 300°C and then at 530°C . The films obtained had the chalcopyrite crystal structure. However the scanning electron microscopy (SEM) images revealed a bi-layer morphology and there were many voids in the layers. A range of deposition sequences were used in order to get uniform layers, but in all cases they observed bi-layer structured films that had poor adhesion to the substrate.

In table 3.1, a summary of deposition techniques used for CIS-based absorbers and solar cells or mini-module or module output parameters reported by research organisations around the world are represented.

Research group/company	Absorber deposition technique	Absorber material (CIS / CIGS / CIAS/ CIGSS)	Thickness (μm)	Energy band gap (eV)	Solar cell parameters					Reference
					V_{oc} (V)	J_{sc} (mA/cm^2)	FF (%)	η (%)	Cell/module area (cm^2)	
NREL, USA.	Co-evaporation	CIGS	~2.2	~1.14	0.690	35.5	81.2	19.9	0.419	[27]
	Co-evaporation	CIS	~2.8	~0.96	0.491	40.58	75.15	15.0	0.403	[80]
	Electrodeposition + PVD	CIGS	-	~1.15	0.666	30.51	75.56	15.4	0.418	[105]
IEC, Delaware, USA.	Co-evaporation	CIAS	~2.0-2.5	~1.16	0.621	36.0	75.5	16.9	0.470	[32, 115]
Angstrom Solar Centre, Uppsala University, Sweden.	Co-evaporation	CIGS	-	-	2.463	33.35	75.1	16.6	16	[92]
IPE/ ZSW/ Würth Solar Company, Germany.	Co-evaporation	CIGS	~2.8	-	0.711	34.7	77.1	19.0	0.5	[95]
Avancis GmbH, Germany.	Sputtering (SEL) + Selenisation (RTP)	CIGSS	-	-	54.6	1.78	66.7	13.1	5400	[67, 103]
Showa Shell, Japan.	Sputtering + Selenisation	CIGSS	-	-	31.17	2.153	68.9	13.4	3459.3	[102]

Table 3.1 Summary of CuInSe₂-based absorber layer deposition techniques and solar cell parameters reported by leading researchers around the World.

3.5 Deposition of the Back Contact Molybdenum Layer

Molybdenum (Mo) is used as a back contact layer in CIS based solar cells because of its low contact resistance, and it also exhibits insignificant material diffusion into the absorber layer during device processing. A variety of metals such as Pt, Au, Ni, W, Ta, Cr, Nb, V, Mn and Ti have been tested by research workers [118, 119]. Of these metals, the Pt, Au, Ni, Cr, V, Ti and Mn showed significant diffusion into the CIS based absorber layer with annealing at higher temperature or reaction with Se. There is little literature on the use of W, Ta, Nb and V as the back contact for CIS based solar cells. During processing, the Mo back contact layer is required to keep its properties such as conductivity and adherence to the substrate. The structure of the Mo layer is also thought to play a role in controlling sodium diffusion while the film is being produced, which gives good crystallinity and improvement in solar cell efficiency [9]. In general, Mo has been used as refractory metal for protective coatings and high temperature applications due to its outstanding mechanical properties, such as high melting point, mechanical hardness and high thermal stability [120].

Various techniques have been used to deposit Mo layers, including DC/RF magnetron sputtering, chemical vapour deposition, ion-beam assisted deposition, electron beam (e-beam) evaporation and laser ablation deposition [119, 121]. However, in general for CIS based thin film solar cells, the Mo layer has been deposited using e-beam evaporation or magnetron sputtering onto SLG substrate. The back contact deposited using these techniques yields comparatively inexpensive, inert layers which are conformal to the substrate even at temperatures in the range between 500-600°C.

➤ **Mo deposited by e- beam evaporation and magnetron sputtering**

Gullén and Herrero investigated the electrical and structural properties of e-beam evaporated Mo films as a function of the deposition process conditions in order to obtain high-quality material at particular process settings [122]. According to this study an evaporated Mo film thickness $> 0.7 \mu\text{m}$ gave sheet resistance values $< 1 \Omega/\text{square}$. The average lattice spacing in the direction normal to the plane of the Mo film varied with deposition rate. Also for higher deposition rates the films surface structure become less porous and more compact.

Fisher *et al.* reported an investigation into the effect of Mo morphology on the performance of CIGS thin films [123]. They compared structural, morphological and electrical properties of Mo back contact layers on Al_2O_3 substrates deposited by magnetron sputtering and by e-beam evaporation methods. The sputter deposited films were found to have porous and fibrous grains, whereas the e-beam evaporated layers had dense, compact and small grains. However the Mo films with fibrous surface morphology were reported as being beneficial for the growth of high quality CIGS thin films; this is attributed to controlled out-diffusion of Na from the substrate through the Mo microstructure [124, 125]. Electrical characterisation using four point probes measured an average sheet resistance of $0.66 \Omega/\text{square}$ for the sputter deposited Mo films and $5.7 \Omega/\text{square}$ in case of the e-beam evaporated Mo films. The fabricated CIGS devices using the e-beam evaporated Mo back contacts had lower efficiencies than those produced using the sputtered Mo films.

In magnetron sputtering systems, Mo films deposited at low argon gas (sputtering gas) pressure were found to have dense microstructure while those deposited at high pressures exhibited a porous microstructure with significant intragranular voids. The denser microstructure has been found to reduce Na

diffusion compared to that through a porous structure. The Mo surface is roughened when the sputtering gas is incorporated during deposition. The electrical resistivity of the Mo films was found to increase with the sputtering gas pressure. The variation in pressure is also found to introduce stress in the films, compressive stress at low pressure and tensile stress for high pressures. These, stresses in the back contact affect the properties of the absorber film and may result in poor adhesion to the back substrate material [118, 126, 127].

Researchers at NREL fabricated 1 μm -thick Mo using a 'bilayers' recipe in order to achieve stress free, non-porous, low resistivity and adherent back contact layers [118]. The Mo bilayer consisted of sputter deposition of a thin layer at a high pressure followed by the deposition of the remaining layer using a low pressure.

For improvement in a solar device performance, it is required to deposit the back contact Mo layer with low resistivity and with a fibrous but not porous surface microstructure with good adherence to the substrate and with very little or no stress and an optimum thickness ($\sim 1 \mu\text{m}$). The magnetron sputtering has been proved useful deposition technique to achieve all the necessary properties of Mo films.

3.6 Buffer Layers

Cadmium Sulphide (CdS) is used as the buffer layer for the best CIS based devices i.e. it is used as the *n*-type semiconductor to form a heterojunction with the *p*-type CIS absorber layer. One of the critical steps in device processing is the deposition of the CdS buffer layer to form high-efficiency CIS based solar cells. Several deposition techniques have been employed to deposit CdS thin film, such as chemical bath deposition (CBD), sputtering, closed-space sublimation and thermal evaporation [9, 128-130]. However, improvements in device performance for CIS devices have been attributed to using the CdS layer deposited by the CBD method. The CBD method is also useful for large-area deposition with comparatively lower cost [131]. The optimum thickness for the CdS layer is < 50 nm to maximise optical transmission of incident light to the junction region [132]. The CdS layer is also found to modify the surface chemistry of the CIS and to protect the absorber layer against sputtering when depositing the ZnO window layer. In particular the CdS layer improves the lattice match between the absorber and window interfaces reducing the density of interface states in the junction region. CdS is a II-VI semiconductor of wurzite (hexagonal) or zinc-blend (fcc) crystal structure and energy band gap of 2.20-2.45 eV depending on the crystal structure [9, 133, 134]. However, CdS is considered environmentally unsafe and therefore alternative materials are being investigated to replace it with a Cd-free buffer layer. Some candidates under consideration in the literature include: ZnS, ZnSe, Zn(O,S), (Zn,In)Se, In(OH,S) and In₂S₃ [135, 136]. Recently, Zimmermann *et al.* reported a 14.8% efficiency of CIGS mini-module with Cd-free Zn(O,S) buffer layer deposited by atomic layer deposition (ALD) [137].

3.7 Window Layers and Front Contacts

The highest performance CIS-based devices have been produced using a bilayer of ZnO window layer on top, prior to depositing the contact grid. This consists of depositing a thin layer of intrinsic ZnO (i-ZnO) onto the CdS buffer layer, followed by a thin Al doped ZnO (ZnO:Al). The high-resistivity i-ZnO layer (thickness in the range 50-100 nm) and the ZnO:Al layer, (thickness in the range 100-1500 nm) are usually sputter deposited [28]. The purpose of the very thin undoped ZnO layer is to block shunting paths in the very thin CdS layer, which degrades the V_{OC} of a device [138]. The ZnO:Al layer is to reduce the lateral resistance of this part of the device. An alternative TCO layer is indium doped tin oxide (ITO) which is deposited by RF magnetron sputtering system. ITO material is increasingly in demand in the optoelectronic industries for applications such as liquid crystal display flat screens for televisions, due to relatively low resistivity and high transmissivity to visible light. ITO delivers beneficial features essential for TCO integration as window layer in solar cells [139].

For the front contact grid, the main requirements are a large melting point in order to avoid diffusion during the cell processing and low resistivity to produce a very low series resistance [140]. A common choice is to use Ni-Al contacts which are deposited by co-sputtering from Ni and Al targets, through a contact mask onto the surface of the ZnO:Al.

CHAPTER 4

EXPERIMENTAL PROCEDURE

4.1 Device Processing of CuInSe₂-based Thin Film Solar Cells

Figure 4.1 shows the flow chart of the fabrication of CuInSe₂ (CIS) and CuIn_{1-x}Al_xSe₂ (CIAS) thin film solar cells with equipments used and processes mentioned in a square bracket.

4.1.1 Substrate cleaning

The properties of deposited films on the glass substrate can be affected by cleanliness of the substrate. It is necessary to remove any dust or foreign particles, organic impurities and glass particles from the surface of the glass substrate before depositing any layer on it.

Standard soda-lime glass (SLG) substrates with dimensions 76 mm × 26 mm × 1 mm were used in cell development process. The substrates were pre-cleaned super premium microscope glass slides purchased from VWR. The first step in processing involved cleaning the substrate using an established procedure. The established cleaning procedure is described as follows [141].

First, an individual substrate identification code was written by hand in the top left hand side corner using a diamond scribe on the back of the substrate (the growth surface was unscribed). The substrates were then fully immersed in a beaker containing 5% volume of Decon-90 detergent solution in de-ionised (DI) water, and then cleaned for 10 minutes in an ultrasonic bath. This step was essential to remove dust and glass particles and organic impurities. The substrate was then rinsed thoroughly in plenty of DI water and treated in an ultrasonic water bath to remove any traces of detergent. The substrate was then immersed in iso-propyl alcohol

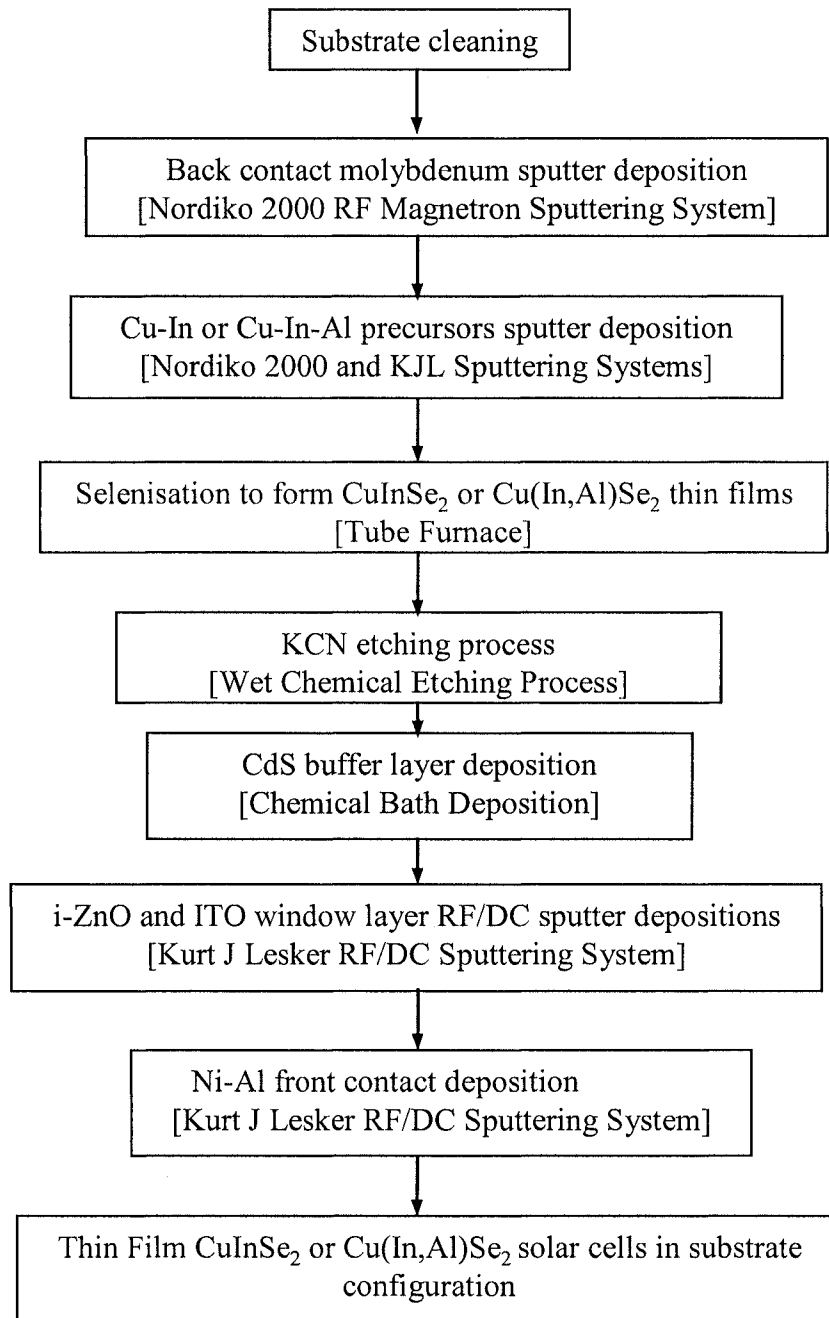


Figure 4.1 The flow chart of fabrication of CuInSe_2 and Cu(In,Al)Se_2 thin film solar cells with available equipment used and processes mentioned in a square bracket.

(IPA) (99.995%) for 10 minutes with ultrasonic bath treatment. The slides were quickly dried using a dry nitrogen jet and then placed in a slide container. Finally cleaned SLG slides were loaded into the deposition chamber.

4.1.2 The sputtering process

Argon (Ar) is the most common a sputtering gas which provides a medium in which a glow discharge can be started and maintained. For glow discharge sputtering, direct current (DC) or radio frequency (RF) type of generators are used.

When the glow discharge starts in the main sputtering chamber, a positive ion is incident on the surface of a solid material, the 'target', to be deposited on the substrate. The following phenomena may occur (Fig. 4.2):-

- The incident ion on the target surface may be reflected, possibly being neutralized in the process.
- Ejection of a secondary electron from the target surface may happen due to the impact of the ion.
- The incident ion may become buried in the target.
- The ion impact may also cause for structural rearrangements in the target material.
- The ion impact may set up a series of collisions between target atoms and in this way it results in the ejection of one of these atoms by momentum transfer. The process of dislodging target atoms is known as sputtering [142].

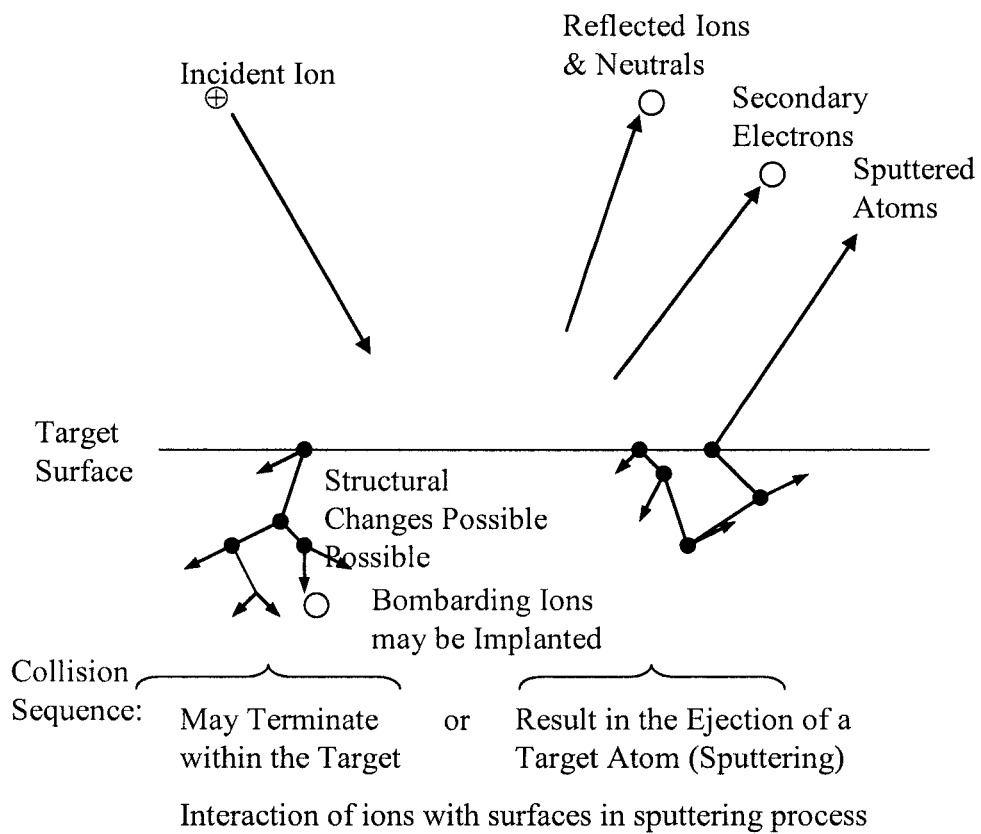


Figure 4.2 The principle of the sputtering process.

4.1.2.1 Effects of process parameters on the sputtering process

❖ Argon gas pressure

Sputtered atoms from a solid target may collide with a gas atom before reaching the substrate. The rate of collisions will increase with increasing pressure. The result of the collisions is to scatter sputtered atoms, in some cases back towards the target, and hence decrease the deposition rate. With increasing pressure, deposition results in a less line-of-sight and more a diffusion process.

❖ Argon gas flow

It is advantageous to use the highest Ar gas flow in order to sweep impurities out of the sputtering chamber. In addition this improves the properties of thin films. Increasing flow incorporates more gas atoms which help to sustain the glow discharge.

4.1.2.2 Essential process steps before actual sputter deposition

❖ Sputter etching of substrates before deposition

The sputter etching of substrates prior to film deposition is a necessary process to remove organic contaminants and oxides already over the surface. This can be done by introducing a small amount of O₂ gas along with Ar which reacts with the impurities and forms oxides. Then a sputter etch stage in Ar can be used to remove these oxides over the substrate surface.

❖ Presputtering of targets (target cleaning)

Presputtering of the target is required to remove impurities or surface oxides from the target surface. It also equilibrates the target surface prior to film deposition for the changed process parameters such as target power, gas pressure and gas flow. During this process a shutter is closed to avoid any deposition on the substrates.

4.1.2.3 DC and RF magnetron sputter depositions

In a DC sputtering system, a glow discharge is formed in a desired gas pressure with a high-impedance DC power supply. But DC sputtering deposition is only applicable in the case of conducting targets.

In an RF sputtering system, an RF potential on the cathode enables conducting as well as insulating materials to be sputtered. At a typical RF frequency (13.56 MHz), electrons oscillating in the discharge plasma acquire sufficient energy to continue ionising collisions and thus sustain the plasma even with a lower voltage. The RF generator is connected to the target assembly via an impedance matching network. The matching network, which includes a variable-shunt capacitor, a variable-series capacitor and a fixed inductor, helps to maintain a constant output impedance of the generator. It does this despite the much higher impedance of the glow discharge.

In the sputtering process at low pressures, the primary electron mean free path (mfp) is longer and therefore ions are produced away from the target or near the chamber wall and their probabilities of being lost to the walls are higher. However, at higher pressures, the flow of sputtered atoms in the direction of the substrate is reduced by collision scattering. This causes the deposition process to be less efficient. In order to increase the ionisation efficiency, by confining the primary electrons to the vicinity of the cathode, a magnetic field parallel to that cathode surface is applied. This type of arrangement is defined as the magnetron mode and the sputtering system is called a magnetron sputtering and can be either RF or DC [143].

4.1.2.4 Magnetron sputtering deposition systems

4.1.2.4.1 Nordiko 2000 RF magnetron sputtering system

The Nordiko 2000 RF magnetron sputtering system (Fig. 4.3 and 4.4) can be used to deposit material from metals and/or insulators. The system has an arrangement to attach six inch (15.24 cm) diameter targets to three electrodes by means of a circular clamping ring and backing plate. In this work, the three targets were Mo, Cu and In. The system was in the sputter-down configuration with a substrate table positioned below the targets. This arrangement is used to avoid the target surface contamination due to debris of deposited material. The distance between the targets and substrate table was fixed to 10 cm. The substrate table speed was held constant 1 rotation per minute (rpm). It was useful to rotate the substrate table for complete intermixing of elements to form alloys. The two RF Plasma Products Inc., RF 10, 1000 W RF generators were capacitively coupled to a target electrode via the impedance matching network. Each target was connected to a separate RF circuit so that all three targets could be powered simultaneously. The target power in the range 0-1000 W (Mo and Cu) and in the range 0-500 W (less than 200 W for In) can be defined according to the requirements. The impedance matching circuit was used to match the generator impedance to the target. The bias voltage can be applied to the substrate during the process. The main chamber was evacuated to high vacuum ($< 5 \times 10^{-6}$ Torr) using an oil diffusion pump (backed with a rotary pump) and was maintained at that pressure setting except during processing. The main chamber could be filled with appropriate gases controlled by mass flow controllers through any of the three inlets.

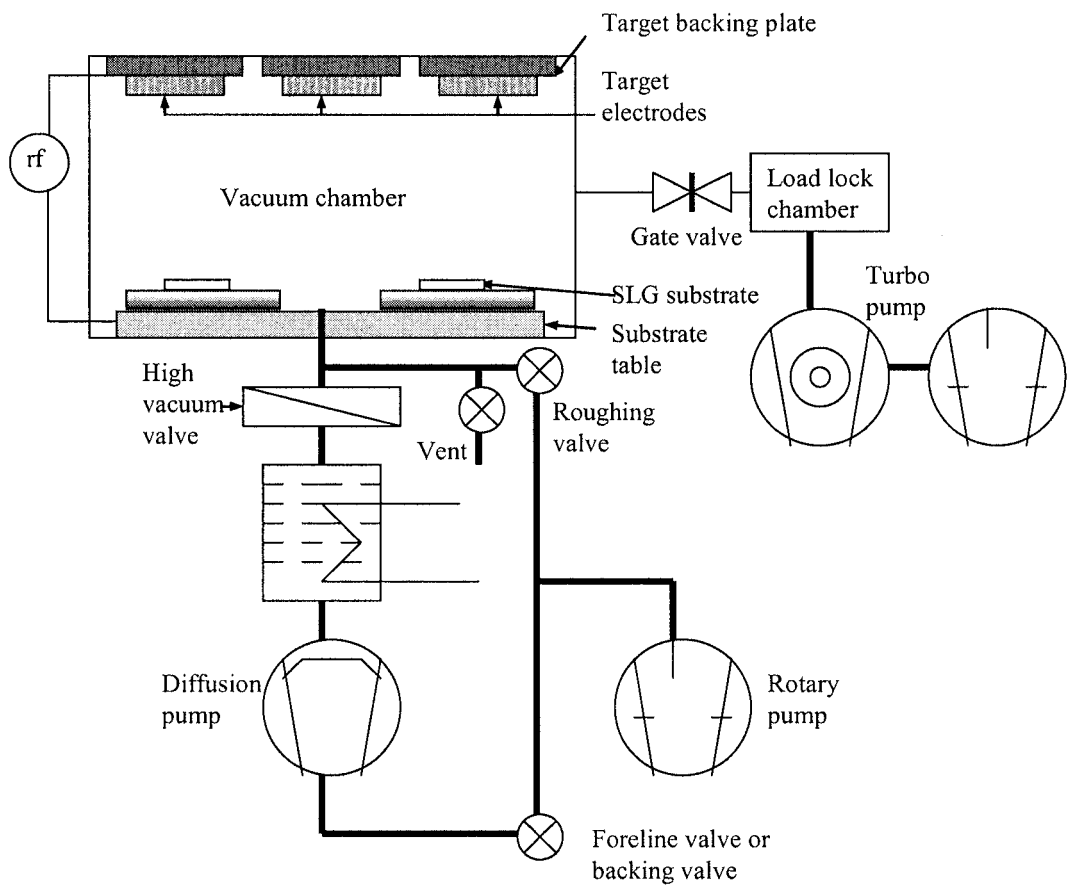


Figure 4.3 Schematic diagram of Nordiko 2000 RF magnetron sputtering system.

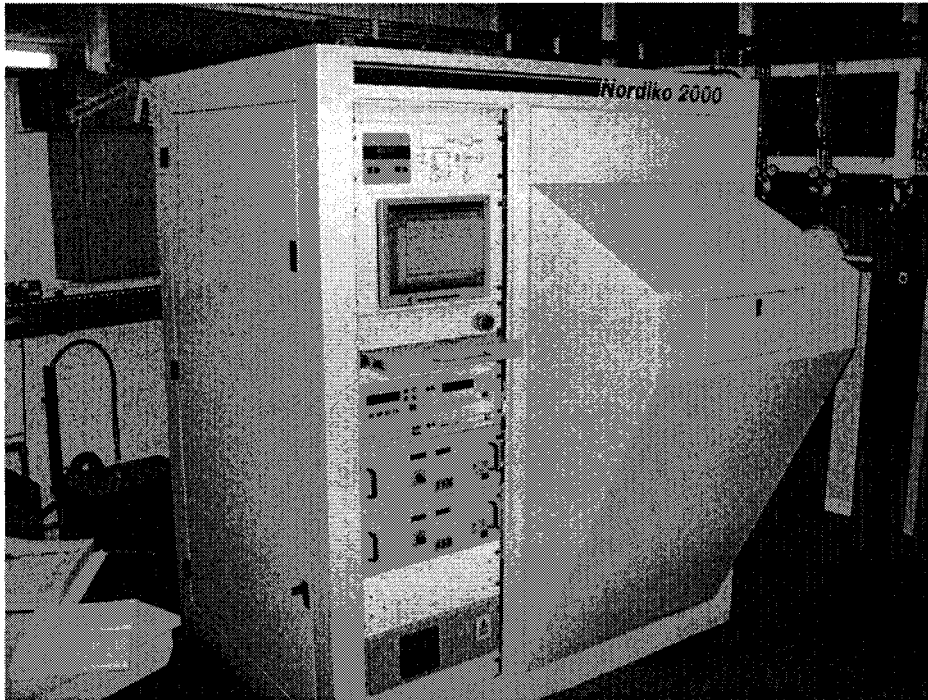


Figure 4.4 Photograph of the Nordiko 2000 RF magnetron sputtering system.

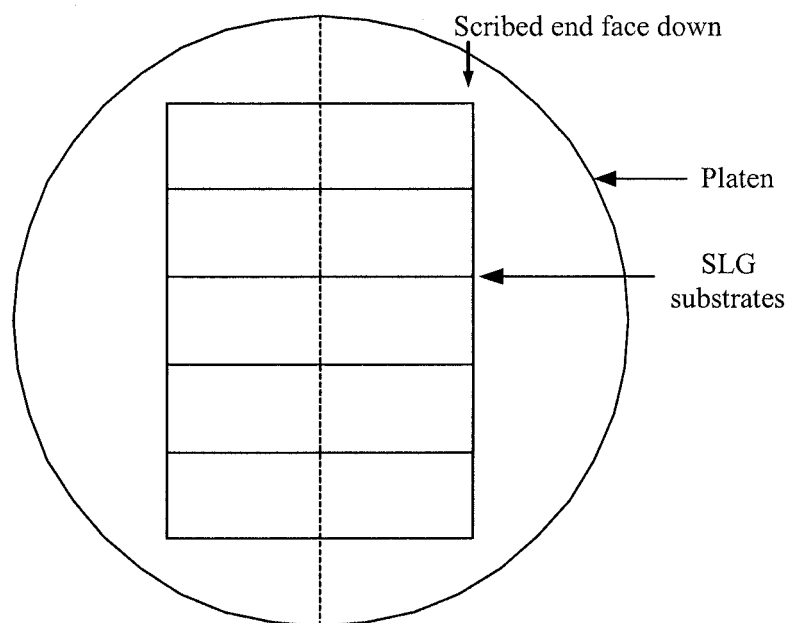


Figure 4.5 The arrangement of SLG substrates on the platen.

The two gases Ar and O₂ were used during this work. During the process, the pressure inside the main chamber was controlled with the help of Ar gas flow (range between 0 and 100 sccm) and butterfly valve throttle settings (5-100%). The substrates were placed on a circular platen according to a defined layout as shown in figure 4.5 and then loaded inside the chamber via a load-lock system. In this way, the four platens could be loaded inside the chamber one at a time. The main chamber was opened to atmosphere only for some purposes for example to clean the chamber, backing plates, substrate table and shutter, to change or adjust target and to do any maintenance.

Prior to the actual deposition the substrate cleaning and the pre-sputtering of targets (target cleaning) was carried out with the shutter closed.

4.1.2.4.2 Kurt J Lesker magnetron sputtering system

In a Kurt J Lesker (KJL) sputtering system (Fig. 4.6), three targets each of 3” (7.62 cm) in diameter can be fitted, of which one can be connected to a RF generator via a matching network and remaining two can be connected to DC generators. The maximum power value of the two DC generators was 1500 W and that of the RF generator was 600 W. In this work, Cu and In targets were connected to DC generators and an Al target was connected to the RF generator. In addition ZnO, ITO and Ni targets were used during cell processing. This system could also be used to deposit material by e-beam evaporation. The KJL system used sputter up configuration with the four substrate holders mounting assembly above the inclined targets. Each of four substrate holders can accommodate three full microscopic slides and therefore a maximum twelve slides can be deposited in a single run. There was a facility inside the main chamber to heat substrate uniformly to a maximum 250°C.

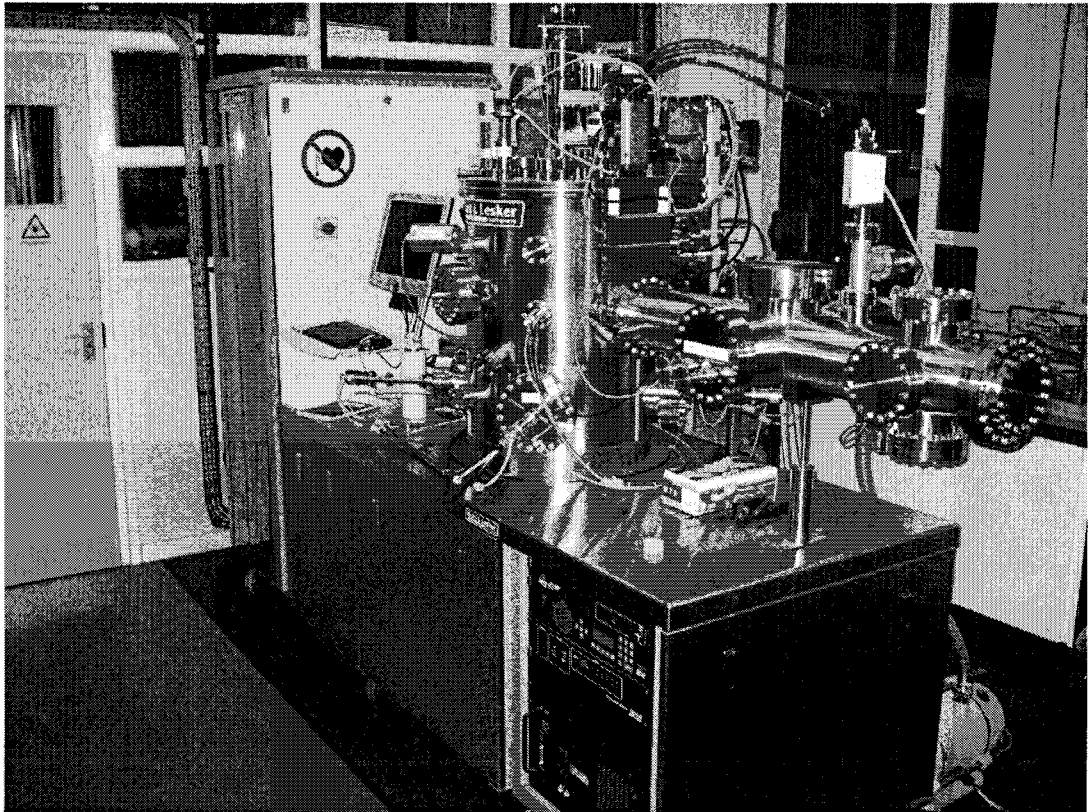


Figure 4.6 Photograph of the Kurt J Lesker magnetron sputtering system.

The substrates could be rotated at maximum rate of 10 rpm. The base pressure was maintained down to 1.4×10^{-7} mbar using a cryopump. The KJL system also has a load lock system to load the substrates into the chamber. The deposition process was carried out by following similar steps to those for the Nordiko 2000 sputtering system.

4.1.3 Selenisation process

The selenisation process is the conversion of the metallic precursor layers (Cu-In and Cu-In-Al) on glass or Mo/glass substrate in a selenium atmosphere into an absorber material such as CIS or CIAS.

In the selenisation process, the initial task was to coat the precursor sample with the Se layer i.e. Se cap layer, by thermal evaporation using a small thermal evaporator chamber. The Se capped precursor layer and half width Se coated glass slide were placed in a graphite box which can accommodate a full microscopic slide. The excess source of Se was supplied by the Se coated half slide (face up) below the Se capped precursor sample. The Se rich environment was required to counter balance the loss of Se from the sample surface during the selenisation process.

The actual selenisation process was carried out in a tube furnace (Fig. 4.7) fitted with a quartz tube and with a graphite box inside. The tube furnace can be heated to a maximum of 600°C temperature. The two gas inlet ports were connected to fill the tube with argon or hydrogen mixed nitrogen (5% H₂) gas. The schematic diagram of the tube furnace and magnified view of the graphite box with the sample position is shown in figure 4.8 (top). In the past, the temperature profile of the central zone of the tube furnace was plotted which is presented in figure 4.8 (bottom). It suggests that the graphite box was placed near a central hot zone.

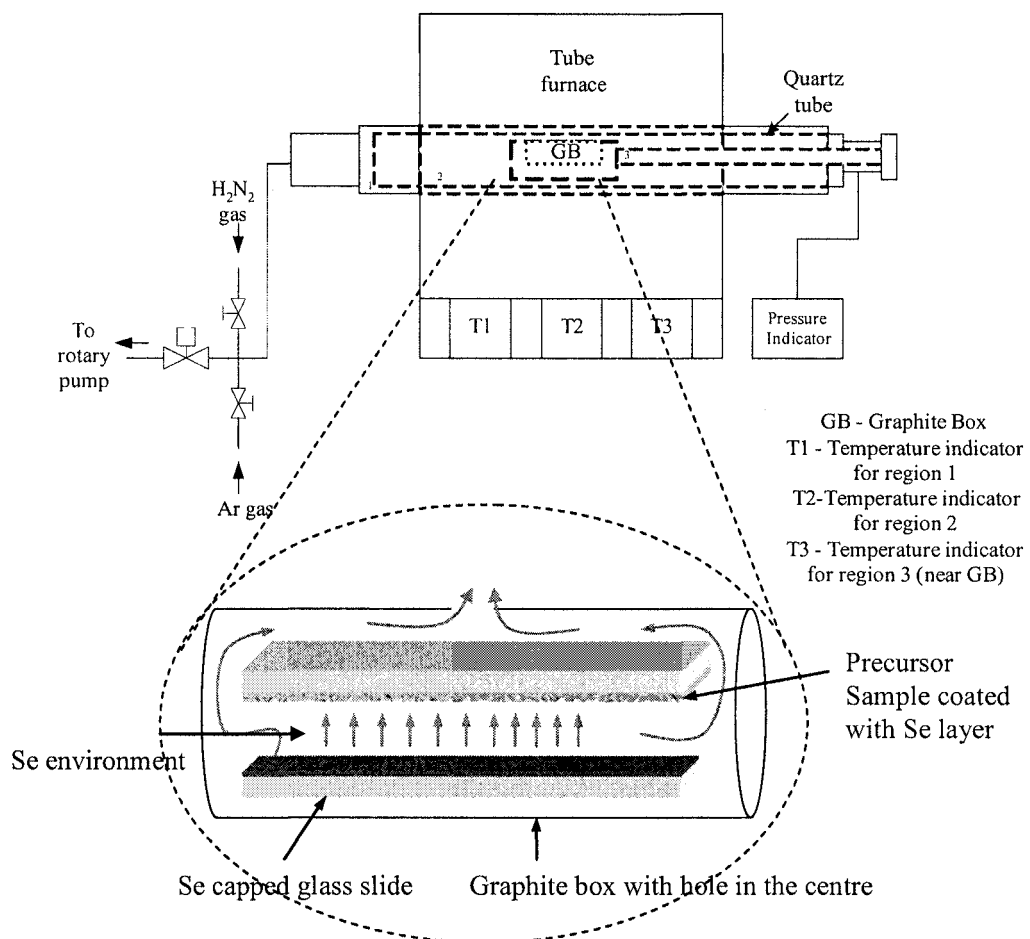


Figure 4.7 Schematic diagram of tube furnace and magnified view of a graphite box with the sample.

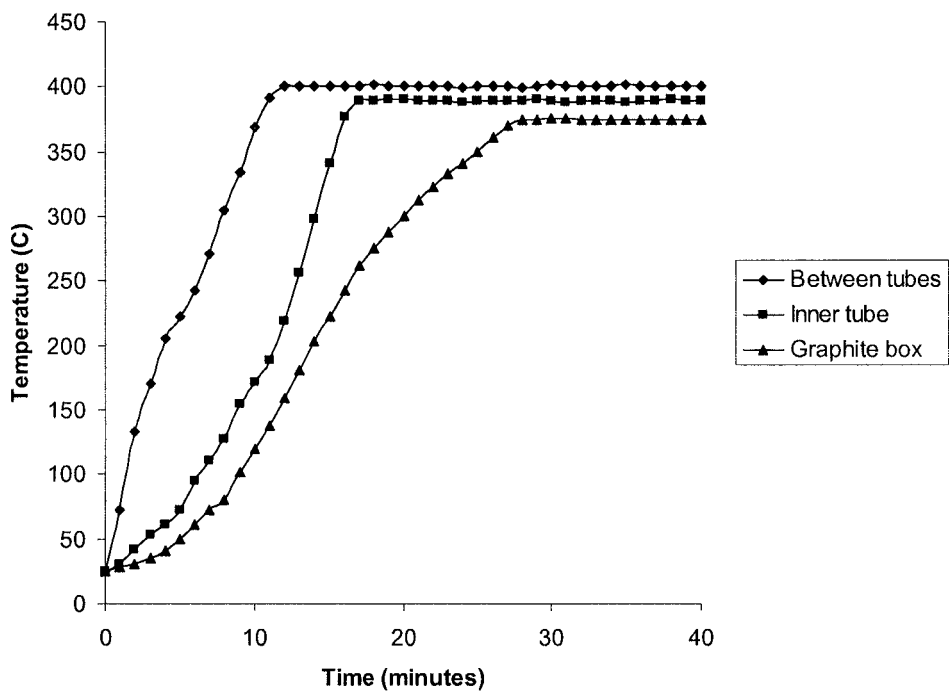


Figure 4.8 Photograph of the tube furnace with the graphite box inside the tube (top) and temperature profile of the central zone of the tube furnace (bottom) [144].

The tube furnace was first evacuated to a pressure approximately 1.4×10^{-2} mbar in order to minimise the water vapour and oxygen before commencement of selenisation process and then it was filled with pure Ar gas (99.995% purity) up to a desired pressure and then sealed. The required temperature was set by the temperature controller T1, by taking into account the difference between temperatures T1 and T3. A small hole was drilled at the centre of the graphite box lid in order to allow excess Se vapour to escape.

The Se environment was created in the graphite box by heating or annealing the sample in argon pressure range 0.5-10 mbar at a temperature ranging 250-550°C.

4.1.4 The etching process using KCN solution

During development of CIS thin film solar cells, prior to the deposition of the CdS buffer layers, an absorber thin film was etched in a 10 weight% (wt.%) KCN solution at a room temperature for 90 s to remove unwanted Cu_{2-x}Se at the absorber surface [85].

4.1.5 CdS buffer layer deposition

In CIS substrate solar cells, the cadmium sulphide (CdS) layer was deposited by chemical bath deposition (CBD) to form the heterojunction with the CIS absorber layer. The work described in this section is related to the deposition of CdS buffer layers on absorber thin films by the CBD method.

CdS thin films were deposited on good quality photoactive CIS absorbers on Mo-coated glass of approximately $38 \times 26 \text{ mm}^2$ size. The deposition (Fig. 4.9) was carried out from an aqueous basic solution with pH approximately 10, which contained 0.2M CdCl_2 , 0.4M NH_4Cl , 1.5M thiourea and 7.5 ml of NH_3 in 160 ml of

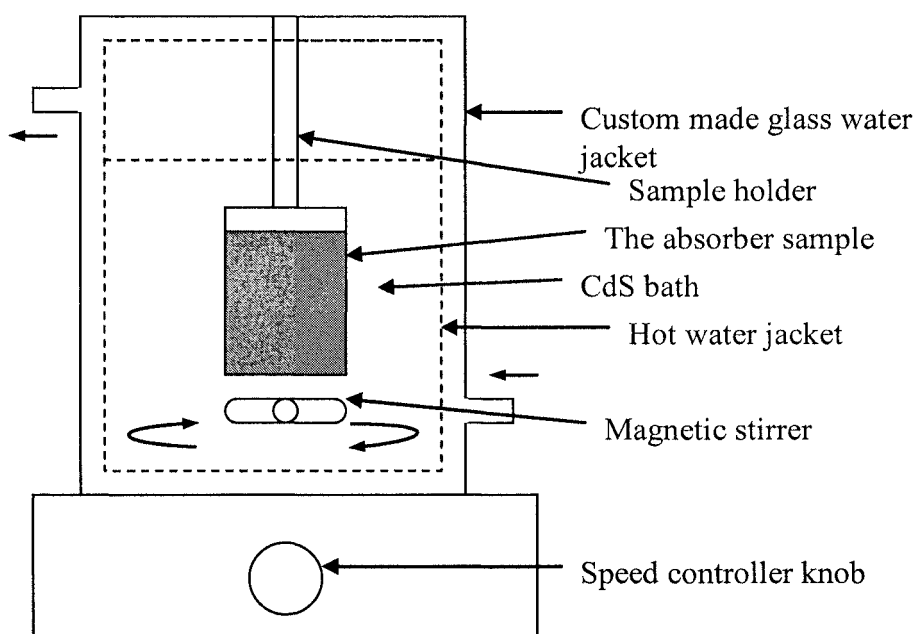
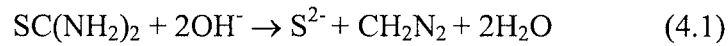


Figure 4.9 Schematic diagram of CBD setup.

DI water. During the deposition, the bath was maintained under constant stirring at a temperature of 65°C. CdCl₂ salt and thiourea were used for source of Cd and S ions, respectively. In this process, sulphur ions (S²⁻) are freed into the bath solution by the hydrolysis of thiourea (reaction 4.1) and cadmium ions (Cd²⁺) as written in reaction 4.2.



CdS film growth on the substrate initialises as per reaction 4.3 between Cd and S ions.



4.1.6 Window layer depositions

The window layer depositions were carried out in a KJL sputtering system.

- i) The energy band gap of the window layer should be as wide as possible to allow most of the photons to penetrate the absorber layer. Most of the window layer made up with bandgap in the range 3-4 eV.
- ii) Together with the transmissivity of the window layer a low value of resistivity is essential to reduce the device series resistance. High energy band gap materials give higher value of resistivities which can be reduced by doping with a suitable material, for example, Zn based window layers are doped with elements from IIIrd group such as Al, Ga or In. There is a trade-off between transmissivity and resistivity to yield optimum window layers.

4.2 Material Characterisation Methods

4.2.1 X-ray diffraction technique

When an X-ray beam with a wavelength approximately equivalent to the interatomic or intermolecular distance is incident on a material, an interaction with the material atoms causes diffraction of the beams, which is called X-ray diffraction (XRD). XRD is a well known non-destructive technique to analyse thin films, powders and alloys in material science [145]. It yields crystal structure information such as crystalline phases and orientation and atomic arrangement. This technique is a non-vacuum based and hence quicker analysis method. From XRD data, important information can be extracted such as lattice parameters, grain size and preferred orientation (texture analysis) of polycrystalline material and strain in the thin films [146]. With the aid of specialised techniques and additional accessories, more information can be obtained for example, film thickness, crystalline phases under influence of heat (hot stage method) and defect imaging and characterisation. Each material is composed of atoms or molecules generally arranged at an equidistance of 0.1 to 0.5 nm [145]. The XRD pattern generated for a particular sample is compared to that produced by analysing a powder sample of the same material. Each material has its own standard diffraction pattern which is helpful to identify phases present in the produced sample. The diffraction patterns for almost all sorts of materials (elements, compounds and alloys etc.) are fed into the database created by an international committee, the Joint Committee on Powder Diffraction Standards (JCPDS) which has been replaced by International Centre for Diffraction Data (ICDD).

➤ **Working principle of X-ray Diffractometer**

The working principle of the XRD instrument is based on Bragg's Law. When a beam of X-rays is incident on polycrystalline material or any type of material or thin film, it interacts with the sample and is diffracted (Fig. 4.10). In case of constructive interference of waves, the geometry as shown in the figure 4.10 gives expression,

$$n\lambda = PQ + QR$$

$$\text{As } PQ = QR$$

$$\sin \theta = \frac{PQ}{d} \quad \dots\dots [\because PQ = QR]$$

$$n\lambda = 2 \cdot d \cdot \sin \theta \quad (4.4)$$

where n = order of diffraction.

λ = Wavelength of incident X-ray.

d = spacing between atomic planes hkl in the crystalline material.

θ = angle of incidence with respect to diffracted atomic plane hkl .

This expression derived Bragg's law of diffraction with n is substituted equal to 1,

$$\lambda = 2 \cdot d_{hkl} \sin \theta_{hkl} \quad (4.5)$$

The crystallographic structure of different types of thin films were analysed by XRD using a Siemens Diffractometer D5000 with Cu $K\alpha$ radiation (1.5406 Å). During scanning mode instrument was operating at 40 kV and 40 mA.

As shown in figures 4.11 and 4.12, the sample was mounted on a fixed sample holder in a horizontal position. The X-ray tube and detector are moved in a circular path such that incident and diffracted beam makes an equal angle with surface of the sample. X-rays are generated in an X-ray tube and the beam was

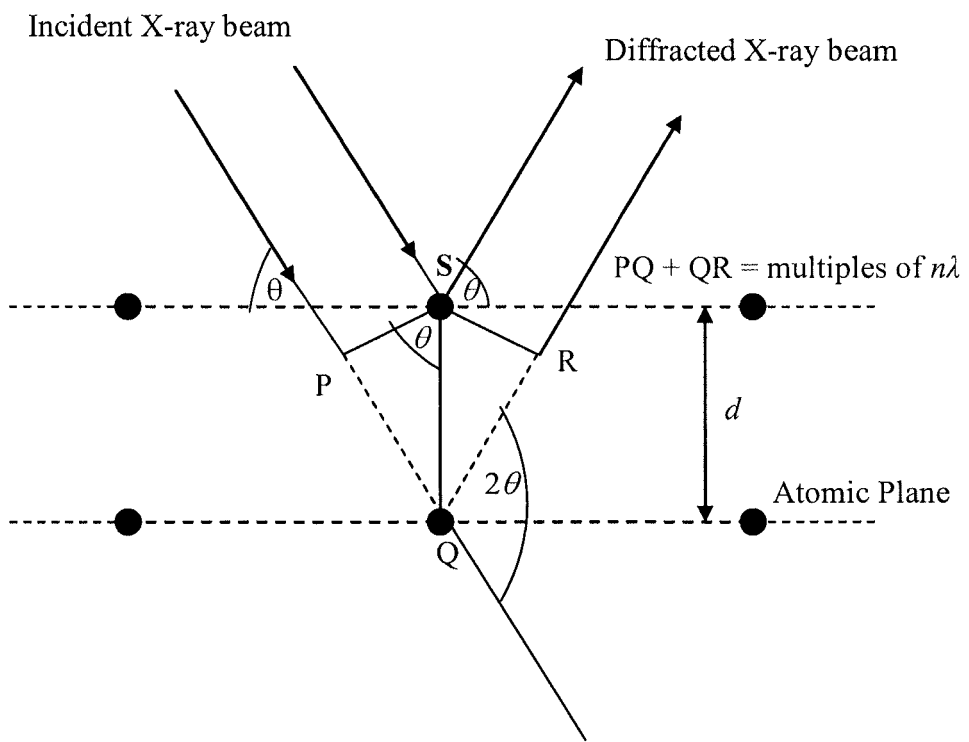


Figure 4.10 Working principle of X-ray diffractometer.

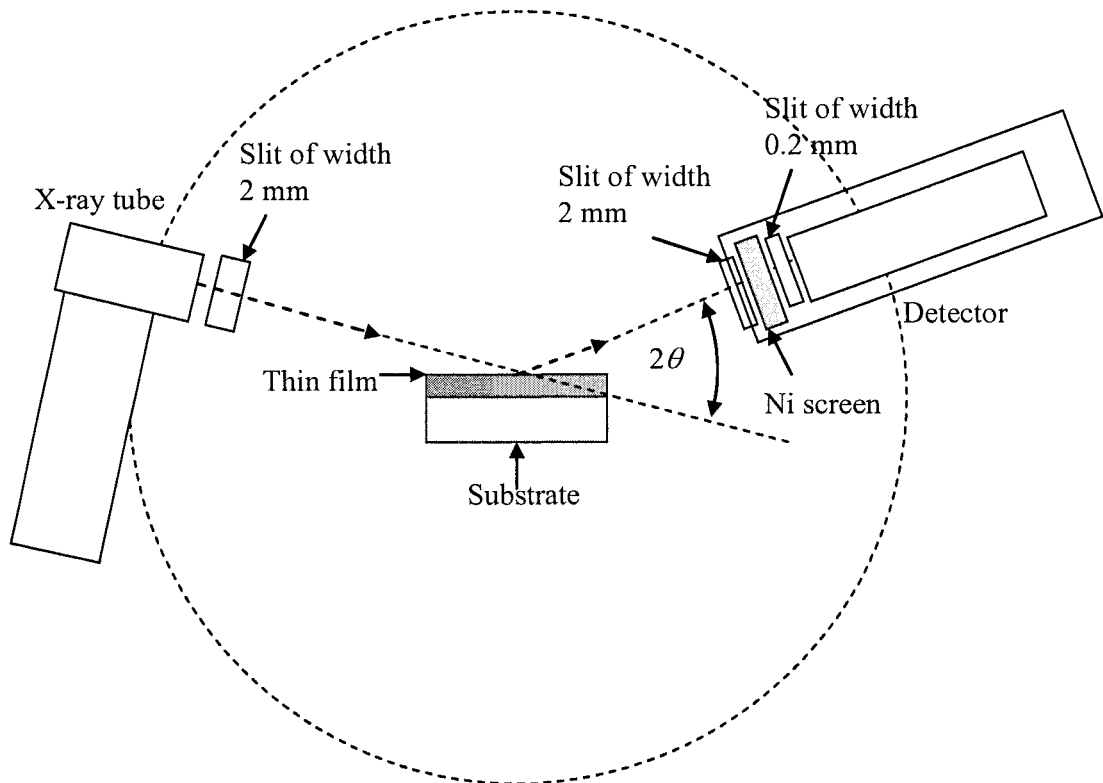


Figure 4.11 Simplified diagram of the XRD instrument in the θ - 2θ configurations.

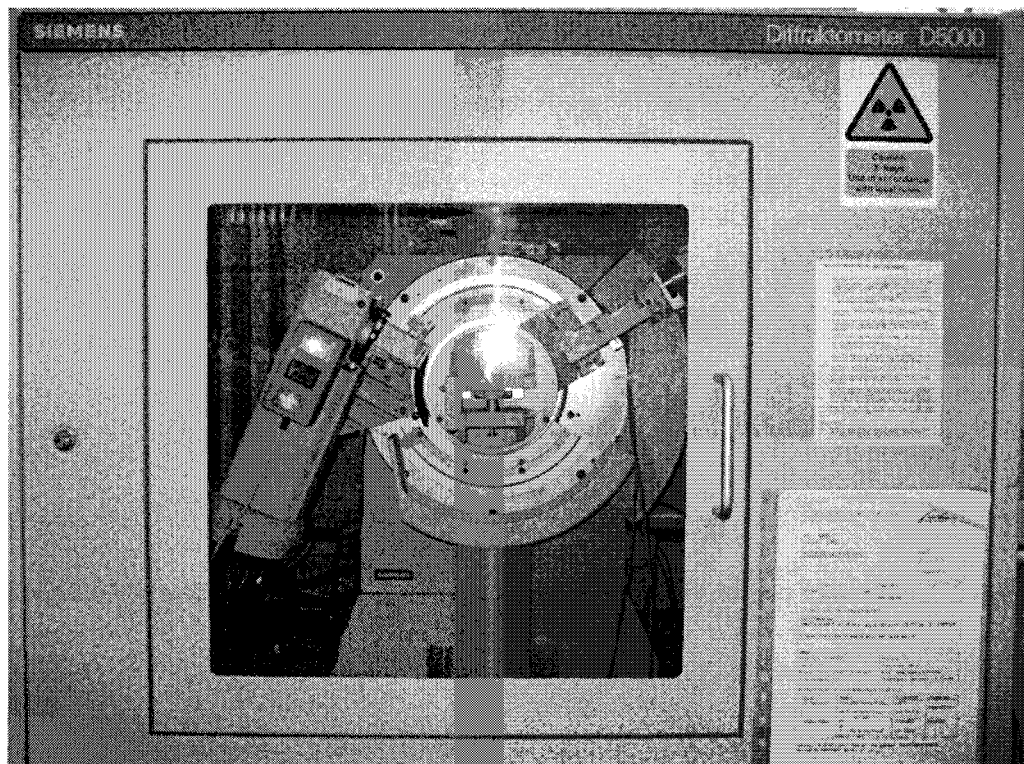


Figure 4.12 Photograph of the Siemens D5000 X-ray diffractometer.

collimated using a slit of 2 mm width and then incident over a small surface area of the sample. The diffracted beam at an angle of 2θ is detected. The diffracted beam was narrowed using slits of widths 2 mm and 0.2 mm and then passed through a Ni screen ($K\beta$ filter) in order to remove characteristic Cu $K\beta$ radiation in the diffracted signal and finally incident on a detector [147].

XRD measurements were performed in 2θ range between 10° - 90° with step of 0.01° per second in order to detect phases present in thin films.

➤ **Calculation of Lattice Parameters of Mo and CIS thin films**

Molybdenum has a cubic crystal structure. Therefore it is only necessary to calculate lattice constant a .

From Bragg's law (equation 4.5) the lattice spacing d_{hkl} was determined by inserting value of θ for a hkl reflection on the 2θ scale.

$$\lambda = 2 \cdot d_{hkl} \sin \theta_{hkl}$$

In case of Mo structure, d_{hkl} was calculated using the following mathematical expression [146]. The main peak (110) of Mo was used to determine hkl and to substitute in the equation 4.6.

$$d_{hkl} = \frac{a}{\sqrt{h^2 + k^2 + l^2}} \quad (4.6)$$

But for CIS and CIAS materials, due to their tetragonal crystal structures, d_{hkl} was calculated using the following mathematical expression [146].

$$d_{hkl} = \frac{a}{\sqrt{h^2 + k^2 + l^2 \left(\frac{a}{c}\right)^2}} \quad (4.7)$$

The strength of I-VI and III-VI bonds in a chalcopyrite crystal structure are different, and therefore the ratio of lattice constants c/a is not exactly equal to 2. The

lattice constants a and c were determined from hkl chalcopyrite peaks (220)/(204) of CIS and CIAS thin films. But in case of CIS, c/a is approximately to be considered equal to 2.01 [51].

➤ **Determination of full width at half maximum**

XRD is a useful technique to identify crystallinity of thin films by evaluating reflection peak width i.e. full width at half maximum (FWHM) (Fig. 4.13). A narrower peak indicates better crystallinity of the sample. There is also a relationship between peak width and thickness of thin film. Decrease in film thickness gives a wider diffraction peak [146].

➤ **Determination of strain in the thin films**

Strain present in the as-deposited or processed thin films can be estimated with the aid of diffraction peak position and width. The method to determine lattice strain is depicted in figure 4.14. The strain in the films can be calculated using the following formula [148].

$$\text{Strain (\%)} = \frac{a_l - a_0}{a_0} \times 100 \quad (4.8)$$

where a_0 is the reference value of lattice constant for the film and a_l is a lattice constant of the as-deposited or processed film. For Mo, $a_0 = 3.1469 \text{ \AA}$.

➤ **Texture and crystallographic orientation of thin films**

The average orientations of all the grains may be randomly distributed or they may tend to incline along the particular direction. This characteristic of polycrystalline material or thin film is termed as preferred orientation or texture. The powder diffraction data was used to calculate texture coefficient (C_{hkl}) of a particular hkl peak.

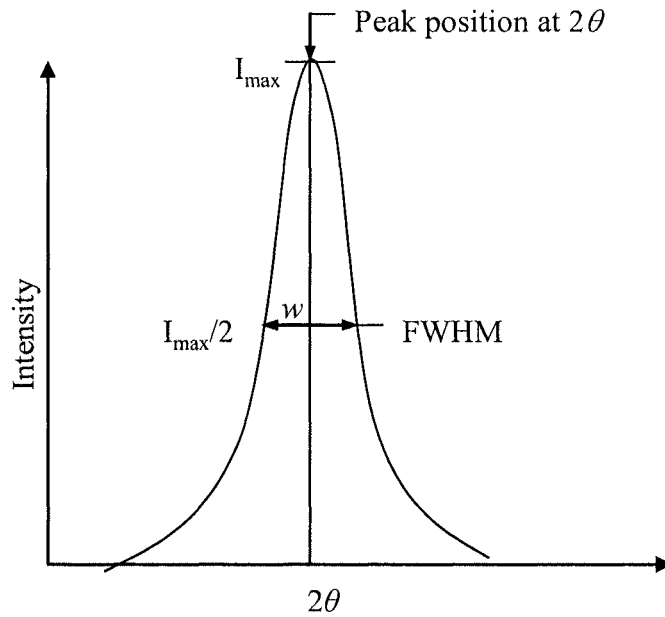


Figure 4.13 Diffraction peak width at FWHM.

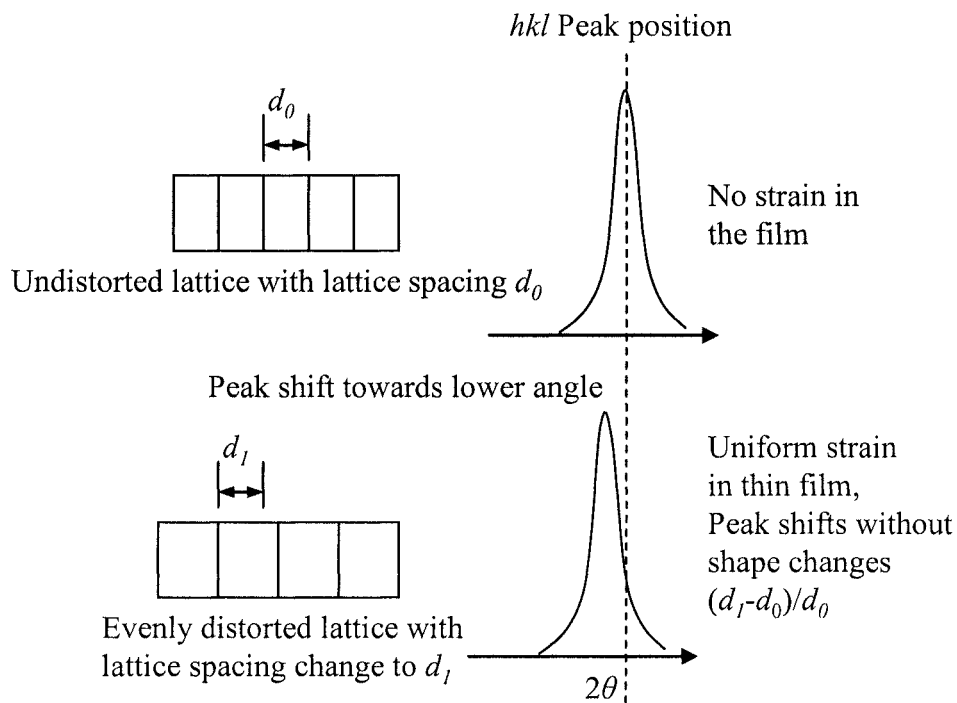


Figure 4.14 Effect of lattice strain on peak position.

It can be written as [149]

$$C_{hkl} = \frac{\frac{I_{hkl}}{I_{ro,hkl}}}{\frac{1}{n} \sum \frac{I_{hkl}}{I_{ro,hkl}}} \quad (4.9)$$

where I_{hkl} is the intensity of a particular hkl peak and $I_{ro,hkl}$ is intensity of the standard (reference) of peak (completely random sample). The texture coefficient of any peak under investigation varies in the range 1 for randomly oriented sample to n for a sample having complete preferred orientation.

The preferred orientation of thin film is expressed from standard deviation σ of all C_{hkl} values of reflections and is given as [150]

$$\sigma = \sqrt{\sum \frac{1}{n} (C_{hkl} - 1)^2} \quad (4.10).$$

For the samples of different thickness or surface roughness, lower or higher σ values are better indications for randomly or completely orientations respectively.

4.2.2 Scanning electron microscopy and energy dispersive X-ray spectroscopy

The surface morphology of the films was characterised using a FEI Quanta 200 instrument (Fig. 4.15) fitted with an Oxford Instrument's scanning electron microscope (SEM). The composition of the films was determined using the same instrument fitted with an energy dispersive X-ray spectroscopy (EDS) capability of FEI (Phillips) Instrument. The surface analysis also allowed investigation of grain structure, size and arrangements. The cross-sectional image of thin films was acquired to estimate thickness of the deposited layer and to observe features at interfaces between layers.

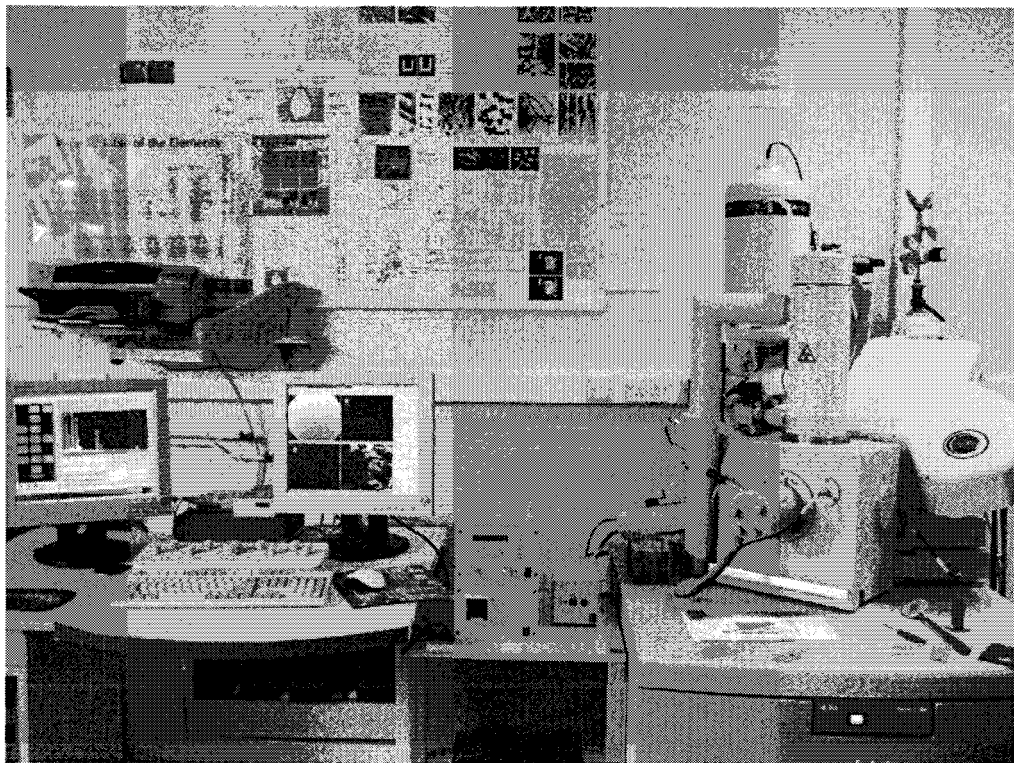


Figure 4.15 Photograph of the FEI Quanta 200 (EDS) and Oxford Instrument (SEM) systems.

When the primary electron beam hits the sample surface, the electron beam interacts with the sample within a bulb shaped volume. The penetration depth and shape of beam varies with the accelerating voltage of the primary beam and with the structure of the sample. The penetration depth can be written in terms of the radius (R) of sphere in nm, the incident primary electron energy (E) in keV and the density (δ) of absorbing material in g/cm³ and can be expressed as [144, 151],

$$R = \frac{4120}{\delta} E^{(1.265 - 0.0954 \ln E)} \quad (4.11)$$

Various kinds of electrons are generated after beam interaction takes place as shown in figure 4.16 but for EDS analysis only emitted X-ray radiation was taken into account for compositional analyses [152]. The EDS analyser was attached with SEM instrument to obtain quantitative material composition data. EDS is a useful technique for compositional analysis of as-deposited, grown and processed thin films in very short time. In this work, all compositional analysis data was represented in atomic percentage (at.%) only. SEM and EDS measurements were performed at 20 kV. The SEM was used to acquire surface and cross-sectional images of different selected samples for instance Mo back contact layer, metallic precursors Cu-In and Cu-In-Al layers, CIS and CIAS thin films. The EDS quantitative compositional analysis was performed on metallic precursors Cu-In and Cu-In-Al layers, CIS thin films. The EDS accuracy is estimated to be better than $\pm 5\%$. Unfortunately, the determination of composition of the CIAS absorber was not possible because it required the use of the Se- K line. But separation between the Se- L and Al- K lines was less than the resolution of the Si(Li) detector used in the measurements.

Due to incompatibility of the EDS instrument, it was not feasible to know the composition of elements (Cu, Al, In and Se) present in the selenised films.

Primary electron beam 20 kV

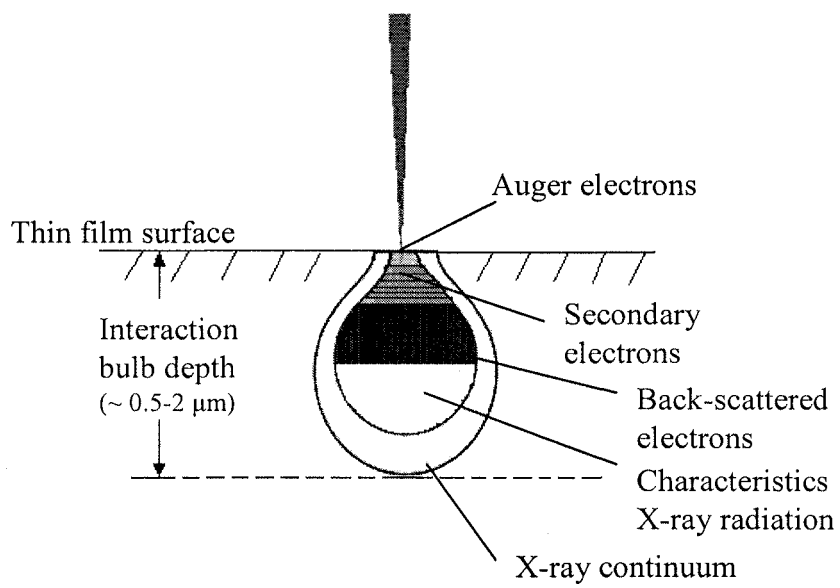


Figure 4.16 Electron beam interactions with thin film in EDS analysis.

In case of CIAS films, compositional analyses of selenised Cu-In-Al metallic precursors are not presented. To improve image quality, the samples were usually sputter coated with a gold film of thickness $\sim 10\text{-}30$ nm prior to capture of surface and edge images [153].

4.2.3 Optical spectral measurements (transmittance and reflectance)

The percentage transmittance (T%) and reflectance (R%) were measured using a Shimadzu UV-VIS-NIR Solidspec3700 spectrophotometer (Fig. 4.17) [154].

In this spectrophotometer, the T% of the selenised thin film on the glass substrate was measured by balancing the light beam through SLG to 100% transmittance over the wavelength range 500 to 2000 nm. The R% of the films on glass as well as on the Mo layer was acquired using an integrating sphere which was equipped with the three detectors covering the wavelength range 830-3700 nm.

The transmittance/reflectance measurements were performed to determine the absorption coefficient (α) of the absorber layer, using the equation [155]

$$\alpha = \frac{1}{t} \ln \left[\frac{(1-R)^2}{T} \right] \quad (4.12).$$

where t = film thickness.

The equation 4.12 determines an approximate value of the absorption coefficient. It does not take account of reflective losses in thin films and makes transmittance measurement independent of the film surface.

The energy band gap (E_g) of the semiconductor material was determined by getting the intercept of the curve to the X-axis in the plot $(ah\nu)^2$ versus $h\nu$.

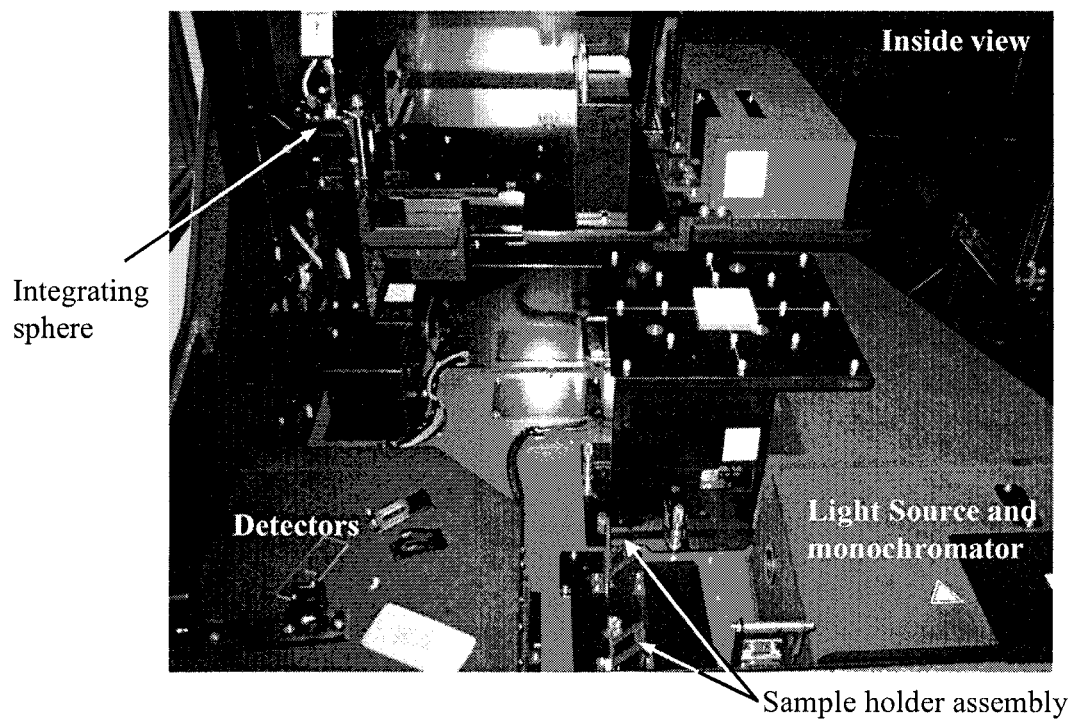


Figure 4.17 Photograph of the Shimadzu Solidspec3700 spectrophotometer in the laboratory.

4.2.4 Secondary ion mass spectroscopy

Secondary ion mass spectroscopy (SIMS) is a very useful tool to get information regarding surface and depth profiling of elements, species and impurities present in the thin film. When a surface of the sample (Cu-In, Cu-In-Al, CIS or CIAS layers on SLG or Mo-coated glass substrates) was bombarded by energetic primary ions, the energy of the primary beam was transferred to the atoms in the sample by a collision. The process of serial collisions between the atoms in the material caused different types of phenomenon, some collisions return to the surface and result in the emission of atoms and atom clusters, some of which were ionised while leaving the surface and can be detected with a mass spectrometer (Fig. 4.18) [156].

The samples analysed in a bench-top MiniSIMS instrument (Fig. 4.19) produced by Millbrook Instruments Limited with energetic 6 keV gallium ions (Ga^+) were used as the primary ion beam. The MiniSIMS system can be pumped down to an approximate pressure value of 5×10^{-7} mbar and working pressure is around 1×10^{-6} mbar [157].

The CIS or CIAS absorber sample of dimensions approximately $0.4 \times 0.4 \text{ cm}^2$ was used with reasonably uniform surface structure. The focussed primary ions beam impinges on the sample surface and scans over raster area $100 \times 100 \text{ }\mu\text{m}^2$. In depth profiling, the primary ion beam removes a significant amount of material and forms a crater. But the shape of the crater was not perfectly rectangular i.e. the walls of the etched crater are slanting and it may create noise in the secondary ion spectrum by adding signal from this sloping area of exposed material. To minimise this effect, an electronic “gate” technique was applied to the detector. In this way, when the primary ion beam is in the flat centre of the etched crater and marginally away from

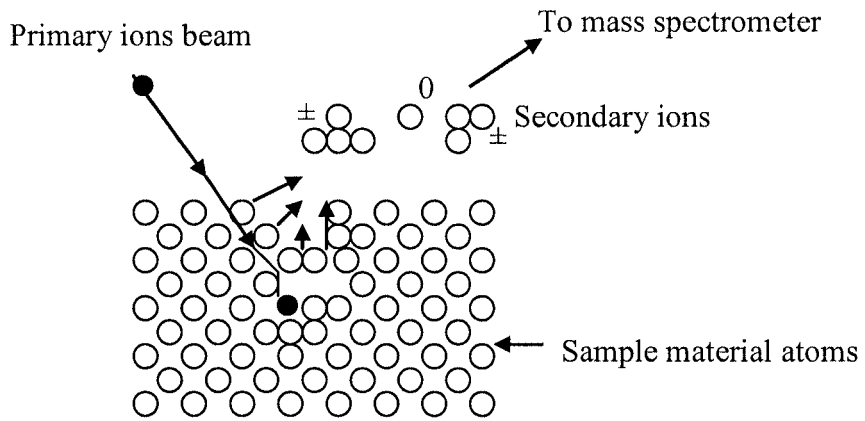


Figure 4.18 Basic working principle of SIMS instrument.

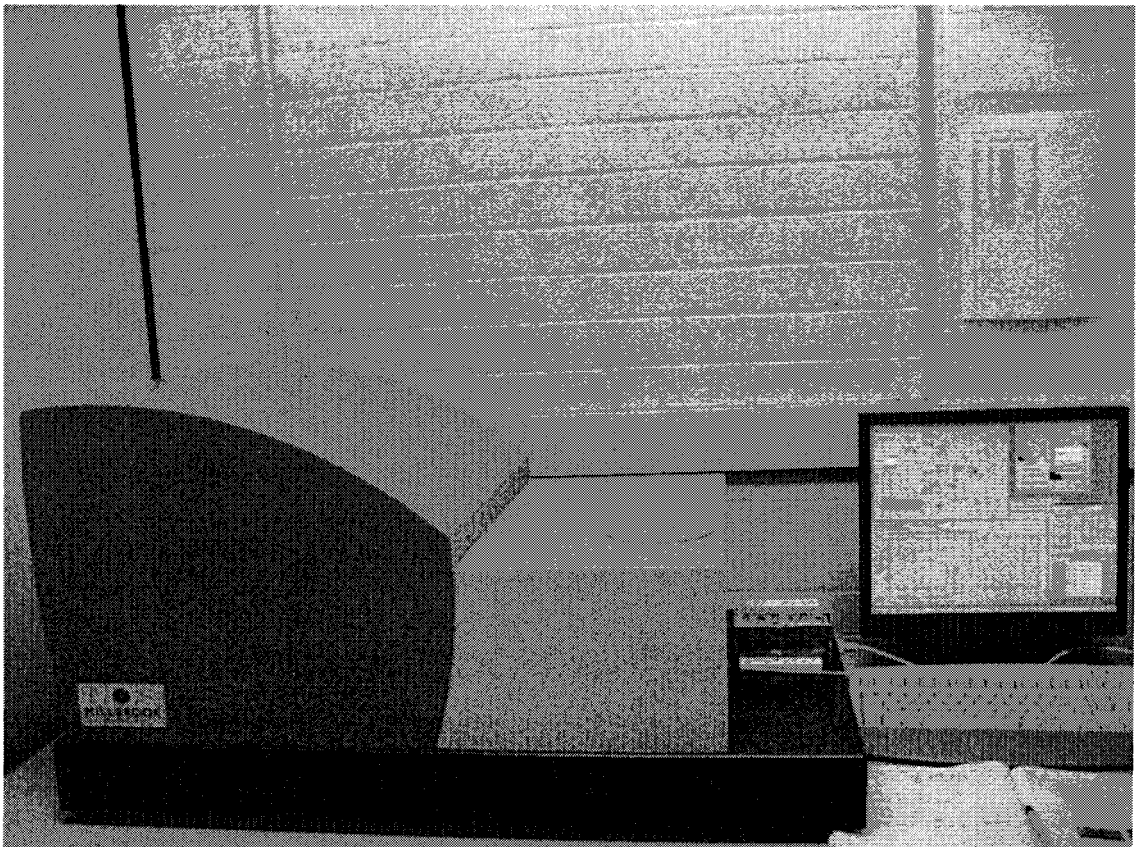


Figure 4.19 Photograph of a bench-top MiniSIMS instrument.

the walls, the electronic gate opens and the detector picks up the true signal and vice versa. Therefore, all analyses were performed with a gate size of 10%. The emitted material consisted mainly as neutral fragments and ~ 1% are emitted in the form of charged particles which are both positive and negative secondary ions. Those emitted secondary ions were collected and then separated through a quadrupole mass filter according to mass-charge ratio and finally detected as single ion in the secondary mass spectrometer. Both positively and negatively charged secondary ions can be represented separately on the secondary mass spectrum.

Mostly, the samples were analysed in MiniSIMS for the purpose of acquisition of depth profiling of elements (Cu^+ , In^+ , Al^+ , Mo^+ and Se^-), Na^+ and O^- . Only the qualitative distributions of these elements within the precursor layers and absorber films are presented as there was no reference sample was measured. Therefore it is not relative in terms of composition but more in relation to the signal. The signal level differs for each element and oxidation or matrix state. For instance the signal level for Cu in the as-deposited Cu-In precursor layers can not be compared with same element (Cu) signal in CIS sample.

4.2.5 Atomic force microscopy

The roughness and grain structure of CIS thin film surfaces were observed by atomic force microscopy (AFM). In AFM measurements, the scanning tip is held in close proximity to the surface to be analysed. The spacing between the tip and the surface of the sample is in the order of a few angstroms (tens to hundreds angstroms). This type of AFM is called a non-contact AFM. The AFM cantilever is vibrated near the sample surface. An interatomic force called the van der Waals force between the tip and the sample surface causes the cantilever to bend, or deflect. It

depends upon the distance between the tip and the sample surface [158]. A laser is focussed on the top of the cantilever and reflection is detected in a photodiode, which is sensed by a position sensitive detector (Fig. 4.20). The piezoelectric scanner kept the sample moving in the z-direction to maintain a constant force and the x and y directions for scanning the sample surface. The feedback signal is fed to the cantilever to avoid any possibility of tip breakage due to crash with large grain or uneven surface. The surface image is produce on the computer screen.

The AFM measurements were performed on the surface of thin films such as precursor Cu-In layers and CIS using a Digital Instrument Dimension 3100 manufactured by Veeco (Northumbria University) and Topometrix explorer microscopes (Durham University), respectively. The size of scanning area varied according to the type of sample.

4.2.6 Four-point probe method

The resistivity of thin films on a glass substrate was measured using the four point probe method.

The four point probe method as depicted in figure 4.21, consisted of two current carrying outer probes and two inner voltage measuring probes. All four probes were separated from each other by an equal distance s which is very small or negligible as compared to dimension d of thin film. A small current I from a constant-current Keithley225 source was passed through the outer probes and the voltage the between two inner probes was recorded using a Keithley175 auto ranging digital multimeter.

For a thin film on the SLG substrate which may be of Mo, CIS, CIAS or TCOs materials, the resistivity ρ , is given by,

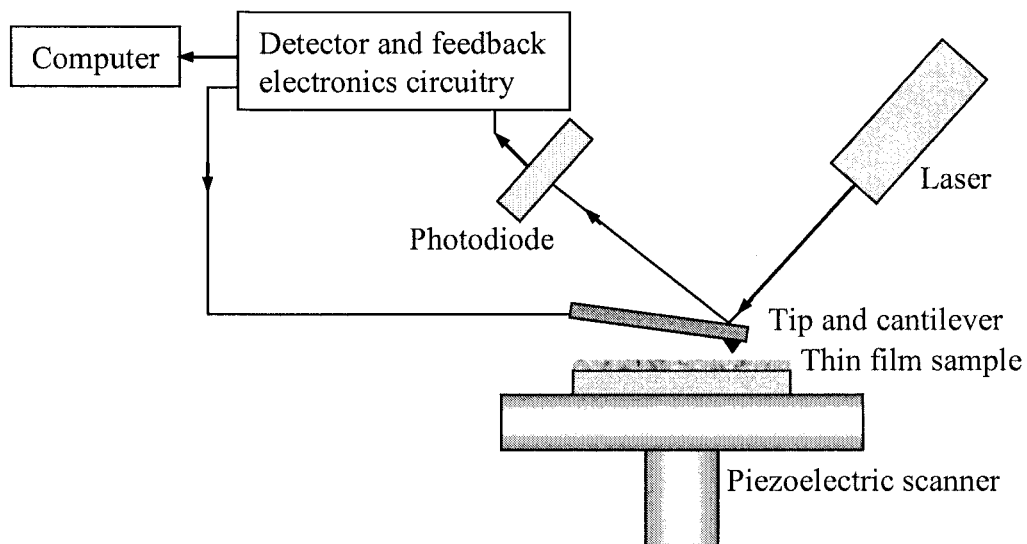


Figure 4.20 Schematic diagram of AFM instrument.

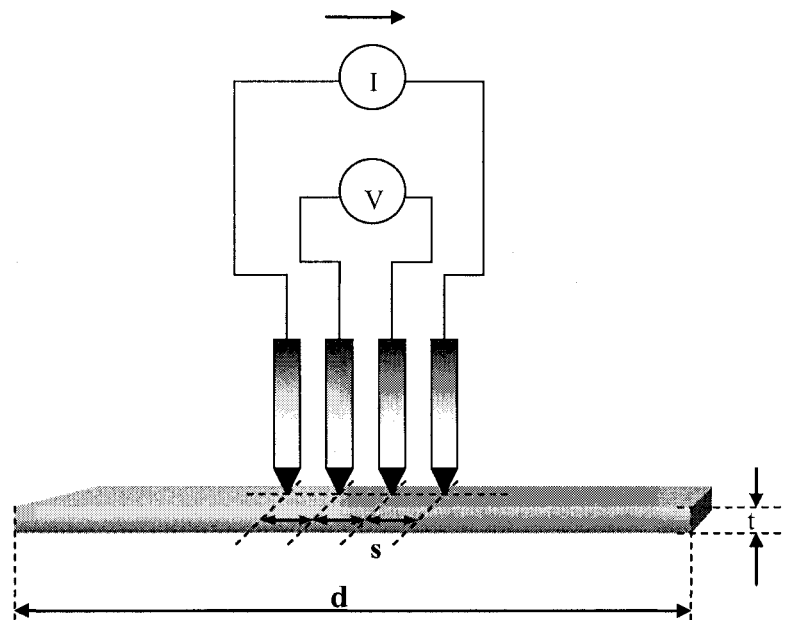


Figure 4.21 Schematic diagram of four point probe method for resistivity measurement.

$$\rho = \frac{V}{I} \cdot t \cdot CF \quad \Omega.cm \quad (4.13)$$

In this equation CF is the ‘correction factor’ which is taken as 4.54 because $d/s > 20$ [35]. The resistivity equation is given as [159]

$$\rho = 4.54 \cdot \frac{V}{I} \cdot t \quad \Omega.cm \quad (4.14).$$

The resistivity measurements were performed with probes placed in the central area of the thin films.

Several measurements were taken on different places of the same sample and an average was taken until unless there was not a significant amount of variation in the readings.

4.3 Solar Cell Characterisation Methods

4.3.1 Current density versus voltage measurements

Current density versus voltage measurement (J - V) measurement is one of the important electrical methods for solar cell characterisation. The purpose of J - V measurements is to assess the quality of the absorber material incorporated into thin film solar cell, in order to improve the cell performance. In addition J - V measurements on processed solar cells offered feed-back, whether properties of produced CIS thin films were useful to yield maximum cell efficiency.

The fabricated devices were characterised by current-voltage (I - V) measurements under AM1.5 (100 mW/cm² at temperature of 25°C ± 1°C) standard test conditions. The solar simulator was custom made by TS Space Systems and is of class A, AM1.5 and calibrated using a spectro-radiometer, to measure spectrum and standard cell or pyrometer to measure cell irradiance. The solar cell was illuminated by the solar simulator while the electronic load swept the cell voltage from a reverse-bias condition, through the third J - V quadrant up to V_{OC} . The recorded I - V data was presented in a text file format using provided computer software and was exported in Microsoft Excel file format for further analysis. From the J - V graph, numbers of useful solar cell parameters- V_{OC} , J_{SC} , FF and solar cell efficiency (η) were extracted. The R_{sh} and R_s values were calculated by measuring the slopes of the lines which are tangent to the curves at V_{OC} and J_{SC} as shown in figure 4.22 [160].

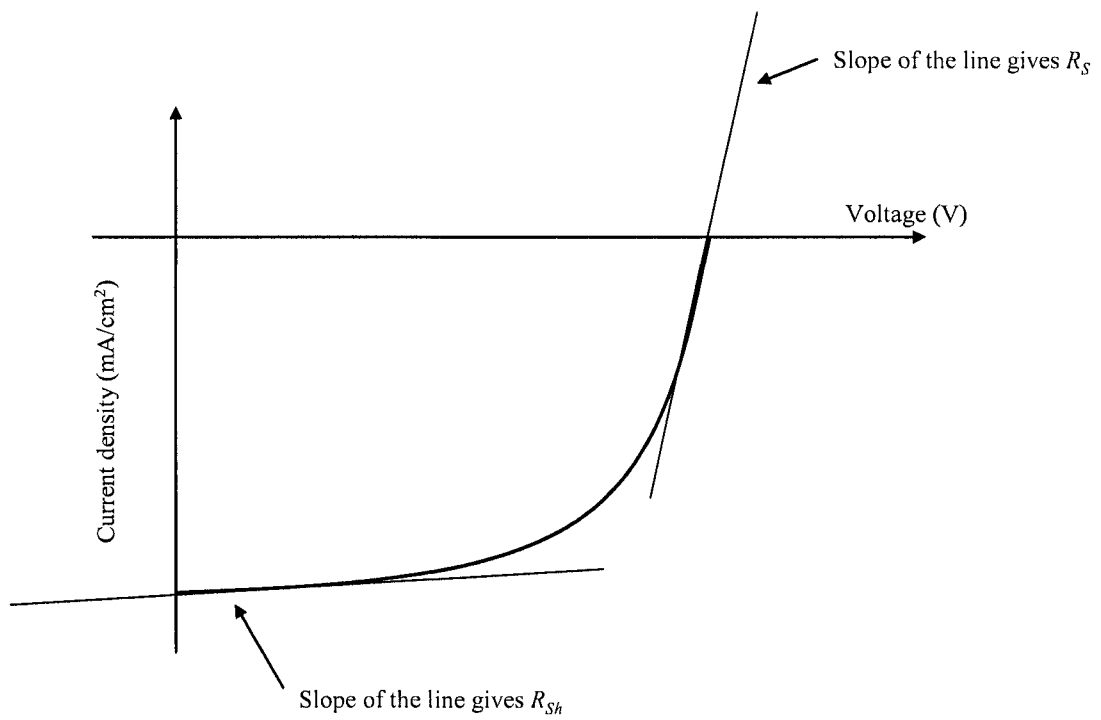


Figure 4.22 Series (R_S) and shunt (R_{Sh}) resistance calculations by using J - V characteristic of solar cell.

4.3.2 Incident photon-to-photocurrent conversion efficiency

measurements

When light is incident on a junction formed between a semiconductor and a liquid electrolyte (semiconductor/electrolyte junction) and incident photon energy ($h\nu$) exceeds the energy band gap (E_g), electrons get excited from the valence band to the conduction band. Sub-band gap response may also be expected due to excitation of electrons and holes from surface or bulk traps to the energy bands with the absorption of lower energy photons. Incident photon-to-photocurrent conversion efficiency (IPCE) measurements involved quantitative measurement of the ratio of the electron flow in the external circuit to the number of incident photons. IPCE is also called internal quantum efficiency. The equation for the photoresponse of an ideal semiconductor/electrolyte junction under reverse bias condition can be written as [161]

$$IPCE = \frac{i_{photo}}{qj_0}; \text{ where } j_0 = \text{incident photon flux} \quad (4.15).$$

The measurement set up (Fig. 4.23) consisted of three electrodes- solar cell (WE-working electrode), Ag/AgCl (RE-reference electrode) and platinum foil (SE-secondary or counter electrode) immersed in a Europium liquid electrolyte to form semiconductor/electrolyte junction. Light from a high-pressure xenon lamp (UV/visible region) is passed through a monochromator and chopper and then it is incident on the sample (absorber film or thin film solar cell). The wavelength of the incident light is selected by a grating monochromator. The photocurrents of low signal from background (dark) currents are distinguished with the use of the mechanical chopper and lock-in amplifier assembly. The output photocurrent is displayed on a computer screen and also given feedback to monochromator. The

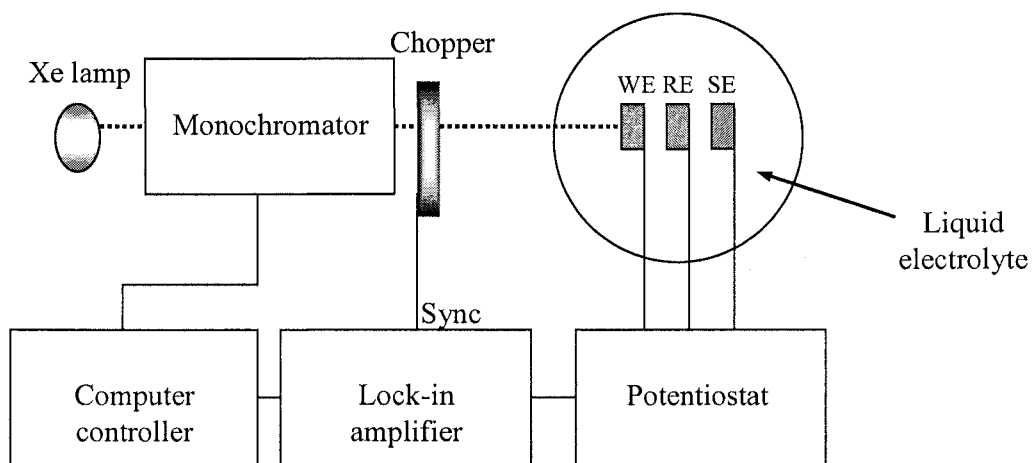


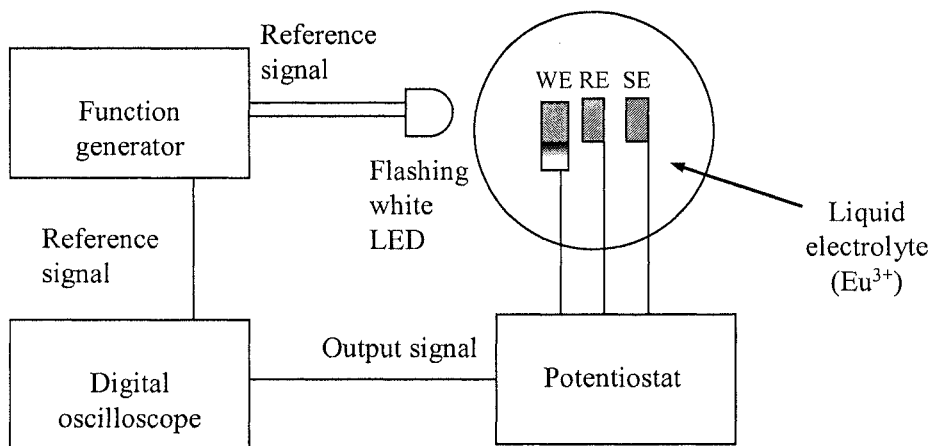
Figure 4.23 Experimental setup for IPCE measurement.

falling signal edge at higher wavelength region can be used to estimate the energy bandgap of the absorber material [162].

The complete solar cells were fabricated to test the quality of absorber material and therefore IPCE measurements were also performed on selected completed cells to get internal quantum efficiency. IPCE measurements were also carried out on absorber layers and part processed cell structures at Bath University.

4.3.3 Photoactivity testing of the absorber layer

The photoactivity property of the absorber layer was checked by a photoelectrochemical experimental set up as shown in figure 4.24. This technique was transferred to Northumbria University from Bath University. The experimental set up consisted of three electrodes: a small part of the CIS/Mo/SLG or CIAS/Mo/SLG samples with Mo layer exposed on top for contact purpose. Ag/AgCl (RE-reference electrode) and platinum foil (SE-secondary or counter electrode) immersed in a Europium (Eu^{3+}) liquid electrolyte to form semiconductor/electrolyte junction. Light from a white LED incident on sample was kept flashing in a ON (2 s)-OFF (1 s) cycle selected by using Si photodiode and a function generator. This reference signal was also fed to channel 1 (Ch 1) of a digital oscilloscope. In the potentiometer a knob was adjusted such that a value to get 10 V corresponds to 1 mA on the oscilloscope. The output signal from the potentiometer was fed to channel 2 (Ch 2). If the absorber layer is photoactive the Ch 2 showed some kind of photo-response with respect to the reference as shown in figure 4.25. The non working (dead material) showed no response i.e. flat signal. Mostly all absorber layers were KCN etched before testing for photoactiveness.



- WE - Working electrode (CIS/Mo/SLG or CIAS/Mo/SLG)
- RE - AgCl/Ag electrode
- SE - Platinum

Figure 4.24 Schematic diagram of photoactivity testing set up for the absorber layers.

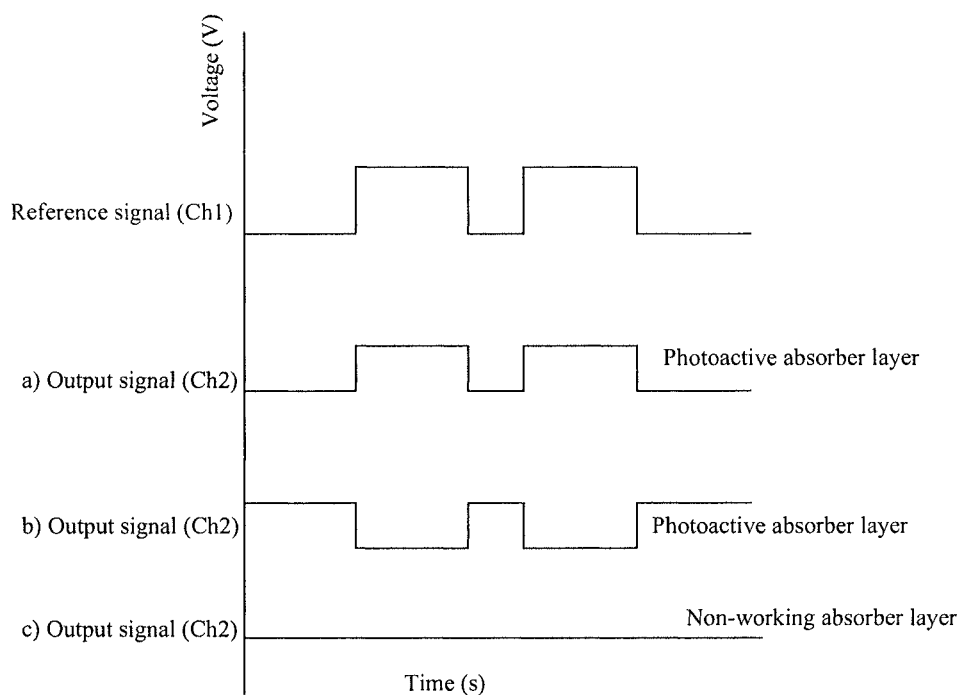


Figure 4.25 The waveform shows photoactive ((a) and (b)) or non-working (c) types of the absorber layers.

Bibliography - Chapter 4

- B. Chapman, *Glow discharge processes-sputtering and plasma etching*, A Wiley-Interscience Publication, (1980).
- B. D. Cullity, *Elements of X-ray diffraction*, 2nd Edition, Addison-Wesley Publishing Company Inc., (1978).
- J. C. Vickerman, A. Brown and N. M. Reed, *Secondary ion mass spectrometry-principles and applications*, Oxford Science Publications, (1989).
- J. C. Vickerman, *Surface analysis-The principal techniques*, John Wiley & Sons, (1997).
- J. Vossen and W. Kern, eds. *Thin film processes*, Academic Press Inc. (London) Ltd., (1978).
- M. T. Postek, K. S. Howard, A. H. Johnson and K. McMichael, *Scanning electron microscopy- A student's handbook*, Michael T. Postek, Jr. and Ladd Research Industries Inc., (1980).
- R. Howland and L. Benatar, *A practical guide to scanning probe microscopy*, Park Scientific Instruments, (1997).

CHAPTER 5

RESULTS

AND

DISCUSSION

5.1 Molybdenum as a Back Contact Layer

The deposition conditions required to produce particular material properties can be generally similar between different types of sputter processing. However, the detailed control of properties is dependant on the details of the individual deposition system and requires optimisation for each.

The main objective of the work presented in this section was to deposit thin films of molybdenum (Mo), as a back contact for $\text{CuIn}_{1-x}\text{Al}_x\text{Se}_2$ (CIAS) thin films, on soda-lime glass (SLG) substrates to provide a uniform, minimum stress, pinhole-free structure with minimum sheet resistance and good adhesion. To achieve this, the main task was to investigate and optimise the sputter deposition process parameters i.e. mainly the working gas pressures and flow. The Mo bilayer structures were also investigated and presented in this section.

In the Nordiko 2000 radio frequency (RF) magnetron sputtering system, the general deposition settings for the Mo experimental work are summarised in table 5.1. From the assessment (appendix I, Fig. A) it was found, that the deposition system enabled control of argon (Ar) gas flow between 10 and 90 sccm and pressure between 2.5 and 100 mTorr and therefore the investigation of the Mo was carried out within these limits.

5.1.1 Effect of argon sputtering gas pressure and flow on structural and electrical properties of the Mo films

Molybdenum was deposited at four different sputtering pressures maintained in the main chamber by varying Ar flow rate but fixed throttle valve position (throttle

Process Parameters	Settings
Power applied to Mo target	300 W
Target-to-substrate distance	~ 10 cm
Substrate table rotation speed	1 rpm
The main chamber base pressure	$< 5 \times 10^{-6}$ Torr
Substrate etching (cleaning) period	~ 30 min
Target pre-sputtering period	~ 20 min
Deposition period to achieve Mo film of thickness in between 700 and 750 nm	90 min

Table 5.1 Summary of sputter deposition settings established during Mo film depositions.

valve setting 27%). The values of the Mo film growth rate and the sheet resistance for the different pressures are summarised in table 5.2. The variation of Mo film growth rate and resistivity versus Ar gas pressure for the films deposited at four different pressures is shown in figure 5.1. According to this, the growth rate varies in a convex manner, after an initial rapid increase in growth rate with increasing pressure, the rate of increase reduced after 5 mTorr. The change in Mo film growth rate was slower at 7.8 mTorr (N54) to 10 mTorr (N55) than 2.6 mTorr (N56) to 5.3 mTorr (N58).

The sheet resistance was measured on four locations of the same sample along the central line of the longer axis. The resistivity was calculated taking an average of the measurements to compensate variations in the individual measurements. The resistivity trend is linear with variation in Ar gas pressure. The Mo films sputter deposited at lowest Ar pressure have the lowest resistivity in comparison with those deposited at highest Ar pressures.

All Mo films exhibited good adhesion on SLG as determined by the Scotch tape test method [163].

Figure 5.2 (a) shows the XRD pattern of the Mo layers in the range 10° - 90° on the 2θ scale obtained from the Bruker AXS software. From X-ray diffraction (XRD) characterisations all the Mo films exhibited preferred orientation along the [110] plane for all the working gas pressures. Shifts in position of the prominent Mo peak (110) on the 2θ scale with respect to the standard value 40.516° [164] were observed (Fig. 5.2 (b) and table 5.3). The XRD pattern shows the variation of the full width at half maximum (FWHM) of the Mo (110) peak with sputtering pressure as plotted in figure 5.3 (a). It can be observed that films deposited at low pressures have narrower FWHM than the film sputter deposited at the highest pressure.

Batch	Ar gas flow (sccm)	Ar gas pressure (mTorr)	Mo film thickness (nm)	Growth rate ($\text{\AA}/\text{s}$)	Sheet Resistance (Ω/\square)	Resistivity ($\mu\Omega.\text{cm}$)
N56	10	2.6	700	1.30	0.25	17
N58	30	5.3	735	1.36	0.41	29
N54	50	7.8	745	1.38	0.60	40
N55	80	10	750	1.39	0.61	48

Table 5.2 Table of the average values of Mo film growth rate, sheet resistance, resistivity according to Ar flow and pressure settings.

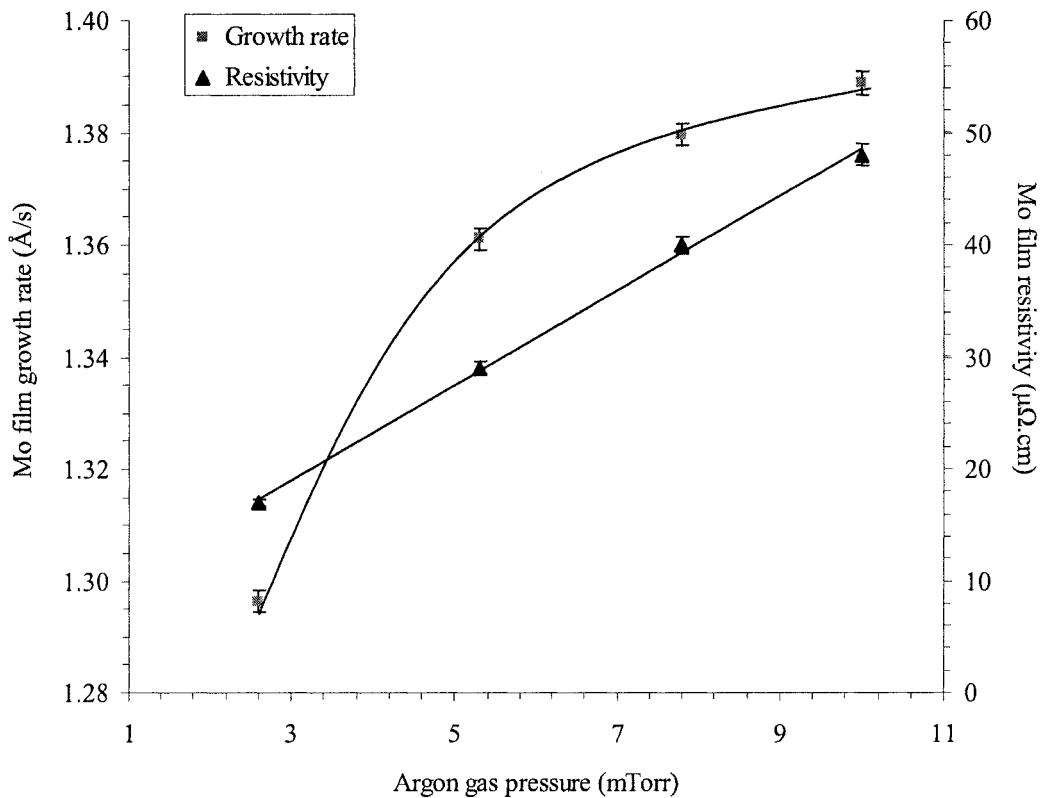


Figure 5.1 The plot of Mo film growth rate and resistivity with pressure variations inside the main chamber.

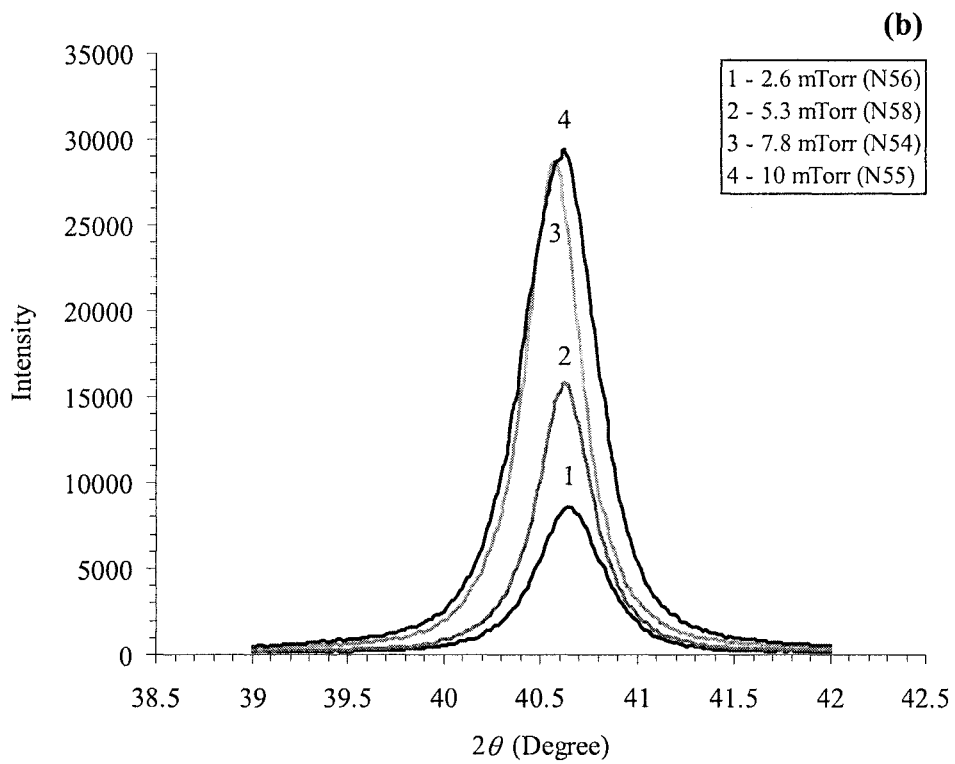
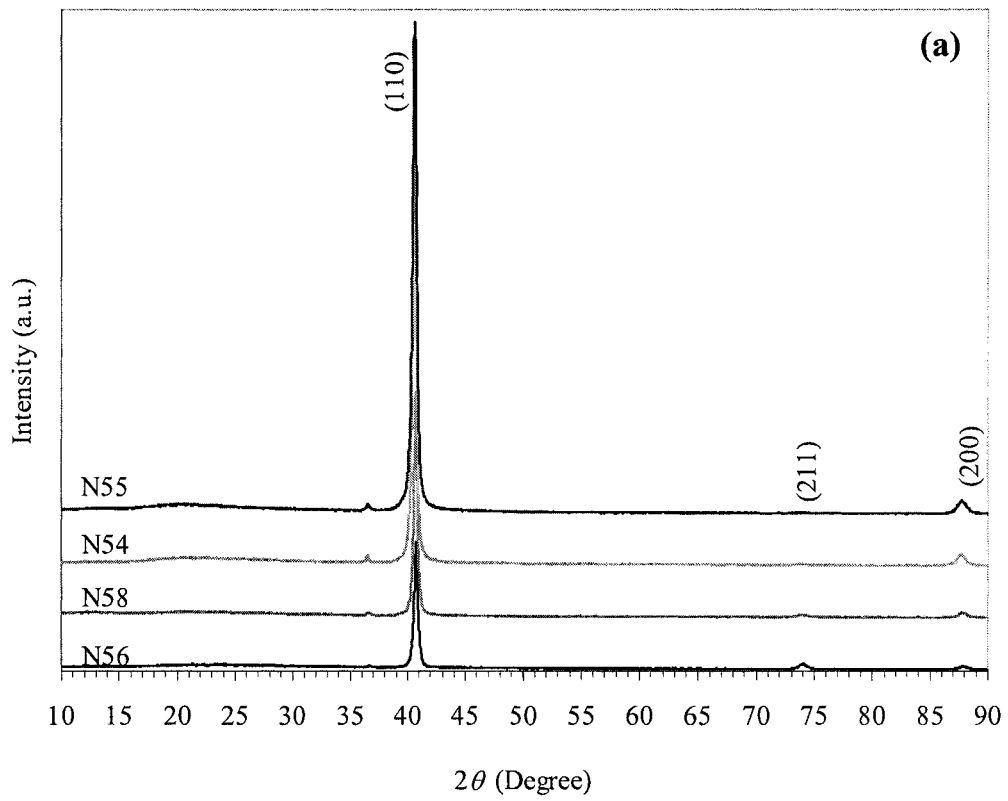


Figure 5.2 XRD patterns of the Mo layers (a) in the range 10-90 degrees and (b) the main Mo (110) reflection for various Ar pressures.

Batch	Ar gas flow (sccm)	Ar gas pressure (mTorr)	XRD data analyses				
			Mo(110) peak position on 2θ scale (Degree)	Mo(110) peak intensity (Counts)	Mo(110) Peak FWHM width (Degree)	Lattice spacing $d(110)$ (Å)	Lattice constant a (Å)
N56	10	2.6	40.66	4249	0.33	2.2099	3.1253
N58	30	5.3	40.63	7793	0.45	2.2187	3.1377
N54	50	7.8	40.58	14319	0.39	2.2213	3.1414
N55	80	10	40.62	14766	0.65	2.2192	3.1384

Table 5.3 XRD data of the Mo films for different Ar pressure and flow settings.

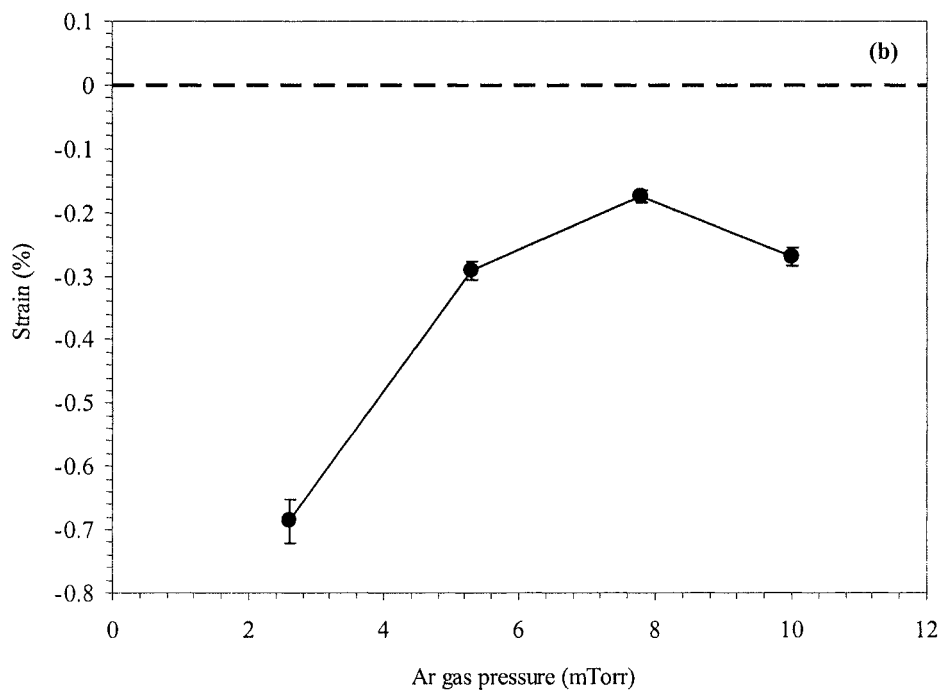
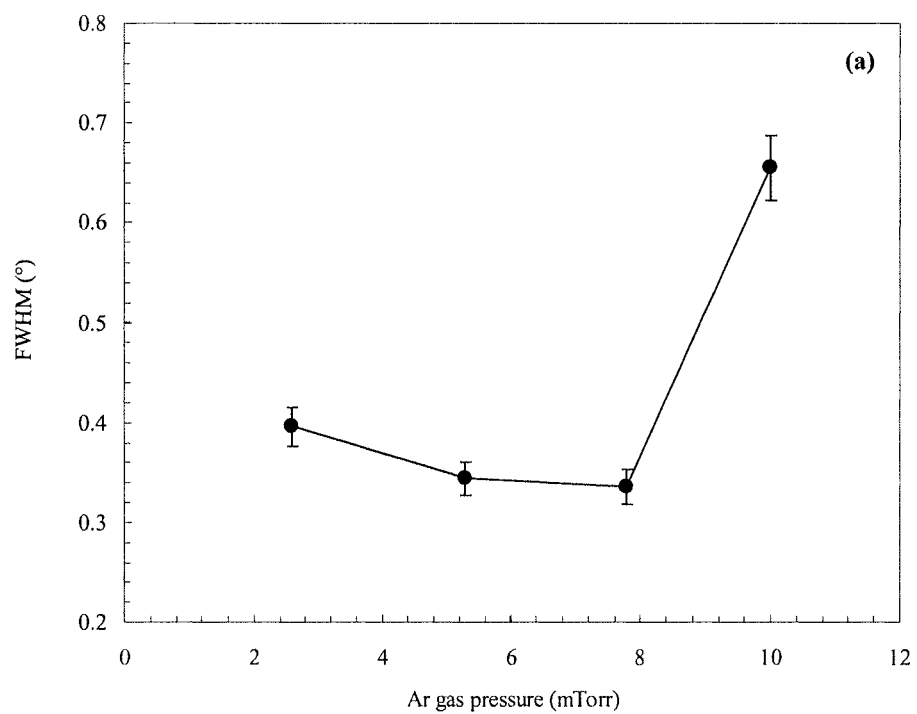


Figure 5.3 The plots of (a) FWHM variation of the Mo main (110) peak and (b) percentage strain on as-deposited Mo films as a function of Ar pressure inside the main chamber.

All the films had experienced strain which caused stress of varying magnitude. For the first three values, it shows increase in strain with pressure and the fourth reading decreased with increasing pressure as shown in graph in figure 5.3 (b).

The effect of Ar flow and sputtering pressure process parameters on surface microstructure of the Mo thin films is depicted in scanning electron microscopy (SEM) images as shown in figure 5.4. In these images, surface morphology reveals differences in surface grain microstructure according to pressure variation. The Mo films deposited at pressures higher than 2.6 mTorr have fibrous surface morphology with elongated grains.

Generally, all the Mo films produced have a dense columnar structure as shown in figure 5.5. Two sputtering process parameters, flow and corresponding Ar pressure both were shown to have an effect on film growth and stress present in the film. So to study the effect of an individual parameter, gas flow or pressure, on the Mo films another approach was implemented.

5.1.2 Effect of argon sputtering gas flow on structural and electrical properties of the Mo films

In order to investigate the effect of Ar gas flow on deposited film properties, the pressure inside the main chamber was held constant and gas flow was varied in the range 10-90 sccm with small changes in throttle valve settings. Three sets of different constant pressures 2.7 mTorr (Batch-N135 and N141), 60 mTorr (Batch-N138-N139) and 100 mTorr (Batch-N136-N137) were maintained in the deposition chamber.

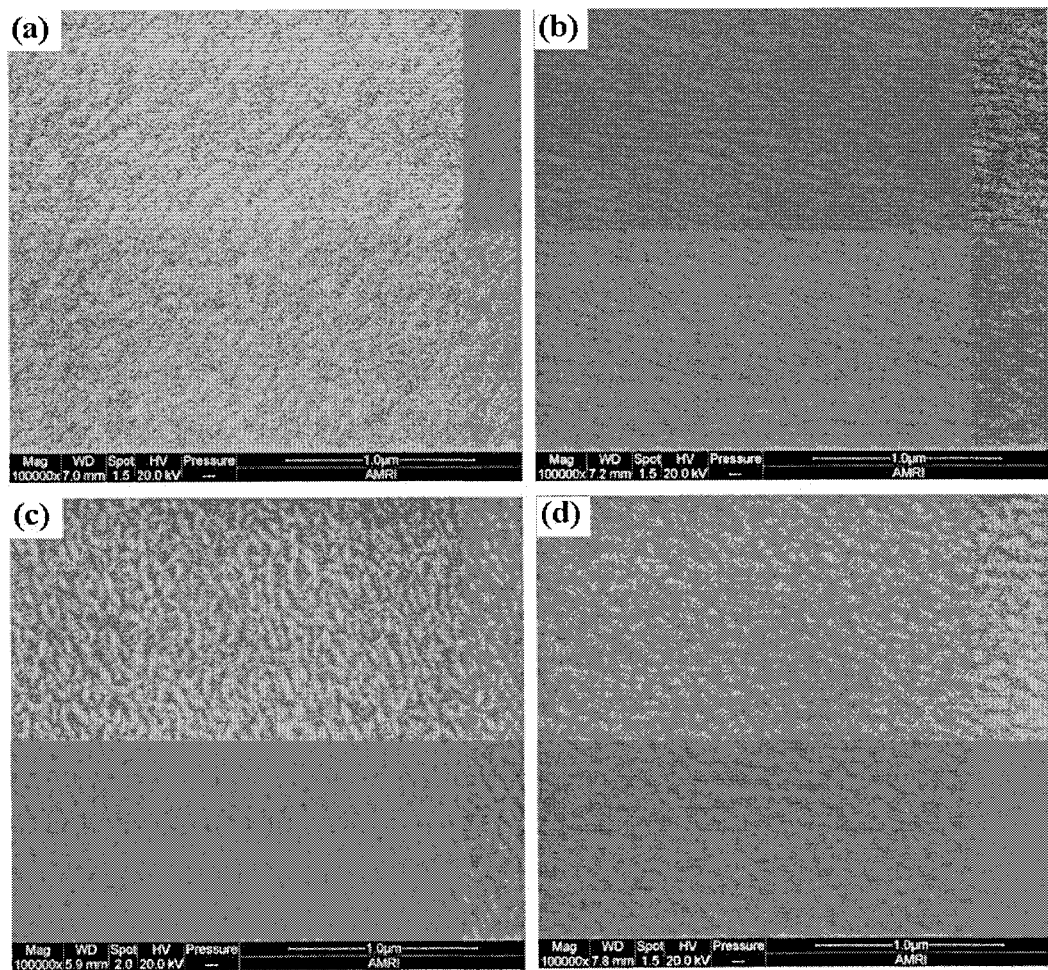


Figure 5.4 SEM surface images of Mo thin films for various Ar pressures; (a) 2.6 mTorr, (b) 5.3 mTorr, (c) 7.8 mTorr and (d) 10 mTorr.

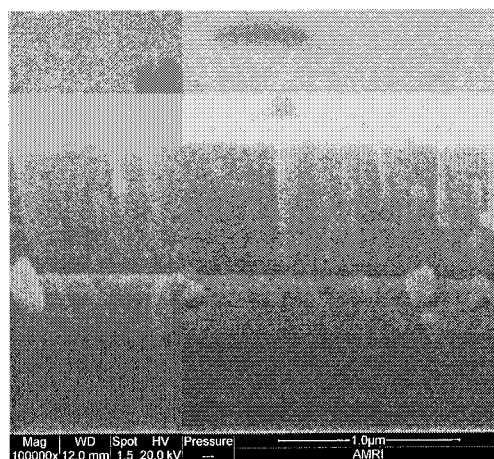


Figure 5.5 SEM cross-sectional image of the Mo thin film on the SLG substrate (Sample-N58C).

As shown in figure 5.6 (a) for lowest pressure 2.7 mTorr, the growth rate of the film increased according to flow but it dropped for 45 sccm. It should be noted that the sputtering system was found unreliable to maintain pressure 2.7 mTorr at the flow rates less than 10 sccm and higher than 50 sccm. Therefore the figure shows only three points plotted for 2.7 mTorr. The growth rate at 19 and 30 sccm was little changed (difference $\approx 0.5 \text{ \AA/s}$) and similarly in between growth rates at 30 and 45 sccm (difference $\approx 0.3 \text{ \AA/s}$). At higher pressures, 60 and 100 mTorr, the trends are almost horizontal i.e. growth rate measured constant with different flow settings. At lower pressure, the growth rate was higher but there is no definite trend.

Resistivity measurements revealed (Fig. 5.6 (b)) significant differences between films deposited at lowest pressure and at higher pressure settings. Films deposited at lowest pressure have resistivity in the range 11-18 $\mu\Omega\text{.cm}$. Films sputter deposited at higher pressure were found to have resistivity within broad range 32-95 $\mu\Omega\text{.cm}$. At high pressure settings, the lowest resistivity was found to be 32 $\mu\Omega\text{.cm}$, although there was not any definite trend in the data.

XRD measurements performed on these films detected variations in FWHM width and the position on the 2θ scale with respect to standard value of the Mo prominent (110) peak. FWHM values were plotted in a graph and shown in figure 5.7 (a). At pressure 2.7 mTorr, the line connecting three points is almost horizontal and parallel to Ar gas flow scale (horizontal axis). Similarly, at pressure 60 mTorr, four points were plotted suggesting a linear relationship. However, at the highest pressure of 100 mTorr there was no particular trend suggested by the plotted points. For the lowest Ar flow (10 sccm), the FWHM width has shown the highest value amongst the readings.

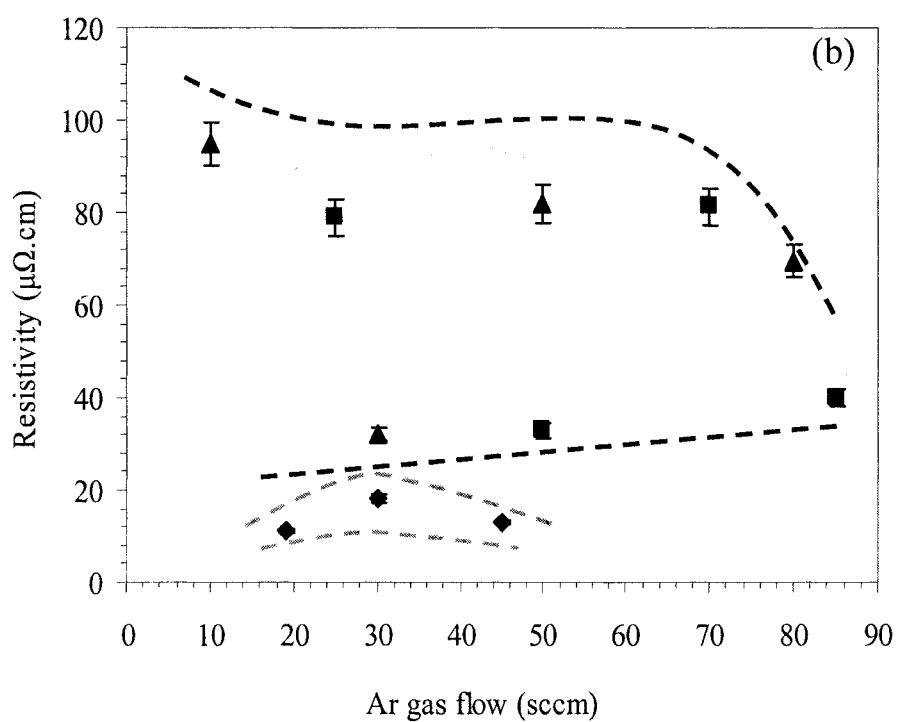
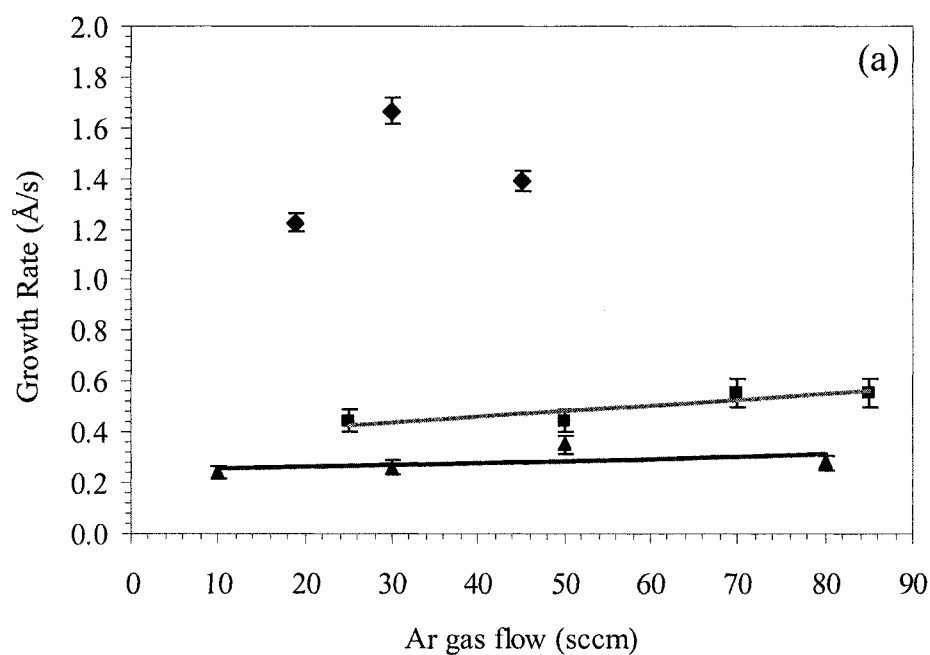


Figure 5.6 Variations in the Mo film (a) growth rate and (b) resistivity with Ar gas flow in the main chamber (\blacklozenge 2.7 mTorr, \blacksquare 60 mTorr and \blacktriangle 100 mTorr). (The dashed line shows the span (an envelop) of the variations in the values).

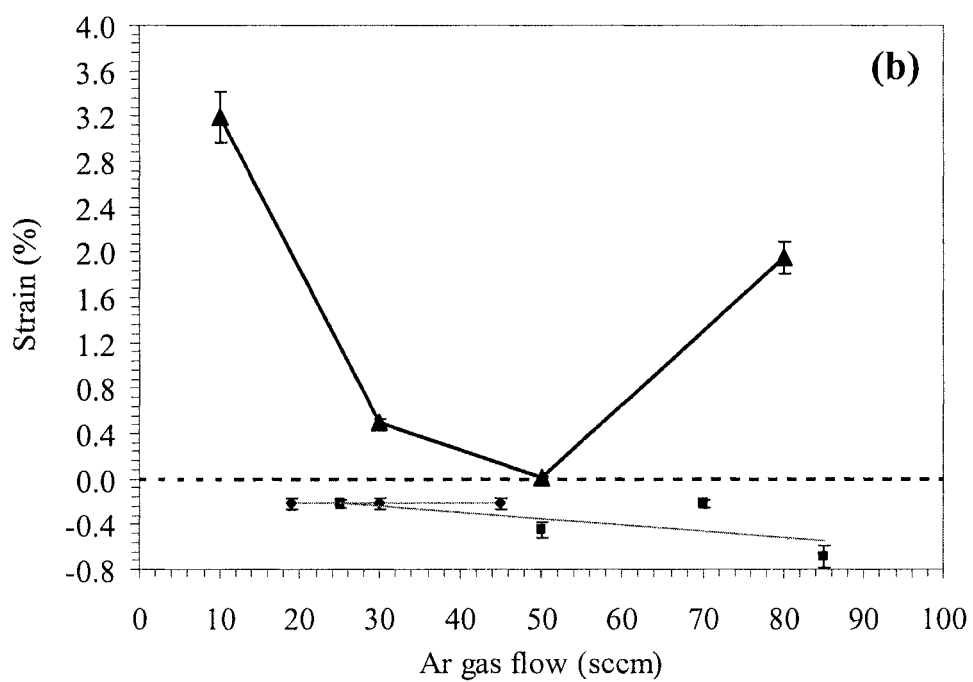
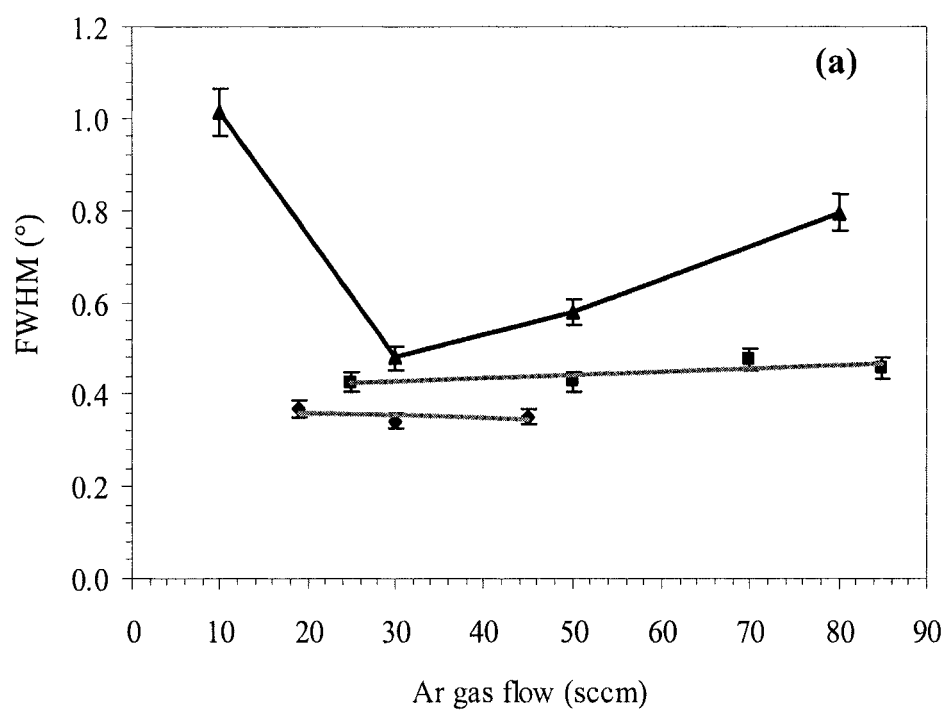


Figure 5.7 The graphs of the Mo films (a) FWHM width of the prominent (110) peak and (b) percentage strain versus Ar gas flow (◆ 2.7 mTorr, ■ 60 mTorr and ▲ 100 mTorr).

Strain in the film varied (Fig. 5.7 (b)) according to Ar gas flow for different pressure settings. At the highest pressure, the strain values have shown a large amount of variation between first and second readings, whereas the second, third and fourth readings increase in a linear manner.

The films deposited at pressures of 60 and 100 mTorr were found to have many pinholes for all ranges of flow settings. The surface SEM image of one of those films is shown in figure 5.8.

5.1.3 The Mo bilayer deposition

In this section the Mo bilayer was sputter deposited in which the bottom first thin layer was deposited at high pressure in the range 55-76 mTorr followed by the second layer deposited at low pressure (in the range 5.1-5.5 mTorr).

The sputtering procedure for the Mo bilayer deposition was similar to single layer deposition except Ar pressure varied (by varying Ar flow and throttle valve settings) and different deposition time in accordance to the variation in target power settings in the range 200-500 W.

The Mo bilayer thicknesses and resistivity values with deposition conditions are summarised in table 5.4. Lowest resistivity was measured to be 10.7 $\mu\Omega$.cm for a Mo bilayer of thickness 960 nm. It shows significant decrease in resistivity of films in comparisons with single layer deposition. The adhesion to the substrate was good but significant numbers of pinholes were observed in these layers.

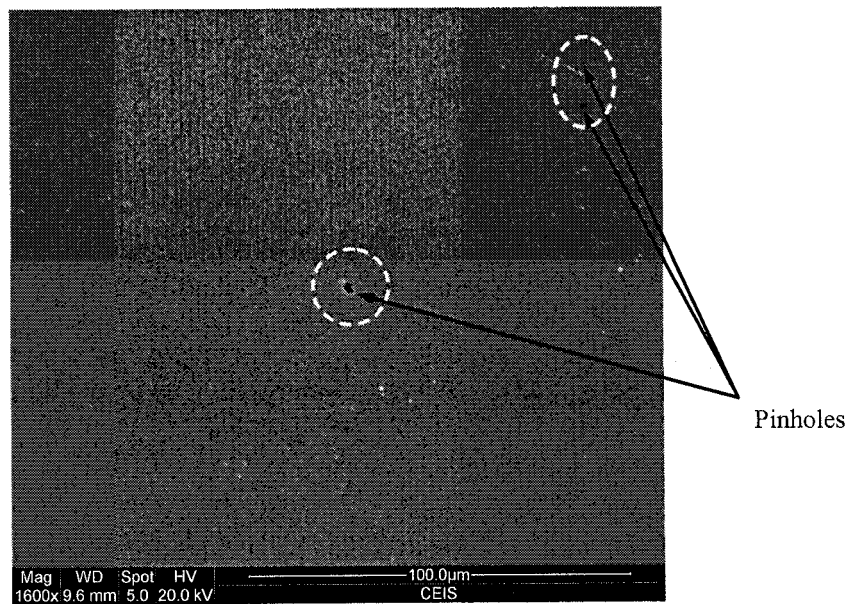


Figure 5.8 The SEM surface morphology image of one of the Mo layers (Sample-N137Q) sputter deposited at higher pressure (100 mTorr) shows many pinholes.

Sample	Mo target power (W)	Ar flow (sccm)	Throttle valve setting (%)	Ar pressure (mTorr)	Deposition time (min)	Mo single layer thickness (nm)	Mo bilayer thickness (nm)	Sheet resistance ($\mu\Omega/\text{sq.}$)	Resistivity ($\mu\Omega\cdot\text{cm}$)
N61	200	100	15	55	90	300	900	0.42	25
	400	30	27	5.5	45	600			
N62	300	100	15	52	100	300	950	0.33	19
	400	30	27	5.1	60	650			
N65	400	100	15	76	60	250	960	0.27	10.7
	500	30	27	5.1	45	710			

Table 5.4 Thickness and resistivity values obtained in Mo bilayer depositions for different process parameters.

5.1.4 Discussion

The investigation of the effect of Ar gas flow and corresponding pressure on growth rate of the Mo films (of the batches N56, N58, N54 and N55) gave a non-linear trend. Lower gas pressures of 2.6 and 5.3 mTorr were achieved with the help of lower Ar gas flow values of 10 and 30 sccm, respectively. Therefore, it may be directly interpreted as a smaller number of gas atoms incorporated in the main chamber as compared to that for high pressures, 7.8 and 10 mTorr, with high flow rates 50 and 80 sccm. Lower resistivities of 17 and 29 $\mu\Omega\cdot\text{cm}$ were measured for Mo films deposited at pressures 2.6 and 5.3 mTorr, respectively. Significantly higher film resistivity values of 40 and 48 $\mu\Omega\cdot\text{cm}$ at pressures of 7.8 and 10 mTorr, respectively, were measured. The scattering of Mo atoms may be due to the number of Ar gas atoms incorporated in the main chamber at high flow rate. The film became porous due to scattering of sputtered species. This caused increase in the film resistivity [118]. The Mo films deposited at lower pressures were found to have densely packed microstructure but the films were porous in structure at higher pressure. XRD measurements performed on these films have shown a shift in the prominent Mo (110) peak position and subsequent variation in $d(110)$ and lattice constant a . It suggests that the average lattice spacing in the direction normal to the plane of the Mo film varies with Ar gas flow and corresponding pressure. At a relatively low pressure of 2.6 mTorr the grown Mo films have revealed densely packed elongated grain microstructure. For pressures higher than 2.6 mTorr, the films have fibrous surface morphology.

The effects of Ar flow with constant pressure settings on the properties of the Mo film were presented. In general a higher growth rate was found at a low pressure setting (2.7 mTorr) than the value for higher pressure settings (60 and 100 mTorr).

Although growth rate varied significantly with flow at low pressure setting, the results are entirely consistent with a scattering effect. At the higher end of the pressure range, the deposition process becomes less a line-of-sight process. Therefore a depositing material atom experiences more scattering as more gas atoms were incorporated in the main chamber for nearly constant operating pressures and they become less energetic as they approach to the substrate. At a low pressure setting (2.7 mTorr) for three different Ar gas flow, resistivity values of those films were found to be in the lower range 11-18 $\mu\Omega\cdot\text{cm}$. At higher pressure settings, 60 and 100 mTorr, the higher resistivity values in the range 32-95 $\mu\Omega\cdot\text{cm}$ were measured. At pressures of 2.7 and 60 mTorr, the films experienced tensile stress of constant value. While at the high pressure setting of 100 mTorr, these films have experienced compressive stress of varied values.

The Mo bilayers for different pressures were deposited in three different batches (N61, N62 and N65). The lowest resistivity of 10.7 $\mu\Omega\cdot\text{cm}$ was obtained for the Mo bilayer of sample N65. This Mo bilayer of thickness 960 nm was deposited as an initial single Mo thin layer of 250 nm-thick deposited for high pressure of 76 mTorr, followed by the second Mo layer of 710 nm-thick deposited for low pressure of 5.1 mTorr.

Several samples of the Mo single and bilayers were tried to test adhesion of the Cu-In precursor layer and subsequent thin films. The single layer performed well as the back contact during processing of thin films in terms of adhesion of thin films on the Mo layer and also adhesion of Mo on the SLG substrates. In the case of bilayers it was found that the absorber films on the Mo bilayer were peeled off in most of the cases and thus produced the worst thin films. In this case at this time the Mo bilayer performed very poorly and thus effectively was not suitable to use as a

back contact for CIAS thin films solar cells. Therefore the Mo single layer was chosen to use as a back contact layer for solar cells.

In summary, the sputter deposited Mo films obtained with increased Ar gas pressures (in the range 2.6-10 mTorr) by varying flow settings (in the range 10-80 sccm) had found increased growth rates in the range 1.30-1.39 Å/s, and linear increase in the resistivity values in the range 17-48 $\mu\Omega\cdot\text{cm}$. These films had fibrous surface morphologies (except the Mo films of batch N56, which had dense surface morphology) and adhered well to the SLG substrate. The results of the investigation of the effect of Ar gas flow on the Mo film indicated that the films had the resistivities in the wide range 11-95 $\mu\Omega\cdot\text{cm}$ with growth rates in the range 0.24-1.67 Å/s at different pressure settings (2.7, 60 and 100 mTorr), a significant variation in percentage strain in the film at highest pressure settings (100 mTorr). Only those films which were sputter deposited at higher pressure settings, (60 and 100 mTorr) were found to have pinholes. In the Mo bilayer experiment, the lowest resistivity of 960 nm-thick Mo bilayer was measured to be 10.7 $\mu\Omega\cdot\text{cm}$. These layers performed poorly in several trials of the conversion of the precursor layers into thin films.

Research workers at NREL and at the University of Denver reported the low resistivities in the range 10-15 $\mu\Omega\cdot\text{cm}$ for sputter deposited single layered 1 μm -thick Mo films [118]. These films were poor in adhesion and stressed (compression), although deposited at a low Ar pressure range of 0.2-2 mTorr. Also they found that the Mo films sputter deposited for pressures in the range 5-20 mTorr had higher resistivity in the range 50-250 $\mu\Omega\cdot\text{cm}$, good adherence to the glass substrate and were tensile stressed. Then they investigated the Mo bilayer deposition process in which the first layer was deposited at higher pressure of 10 mTorr followed by the

second layer deposited at lower pressure of 1 mTorr which yielded a total layer of 1 μm in thickness. These films have lowest resistivities in the range 12-15 $\mu\Omega\cdot\text{cm}$ and well adhered to the substrate. These films are being used as a back contact layer in NREL's high efficiency (World record cells) Cu(In,Ga)Se_2 (CIGS) thin film solar cells. The Mo bilayers described in this thesis yielded resistivity in the range 10.7-25 $\mu\Omega\cdot\text{cm}$. These layers had good adhesion to SLG with significant numbers of pinholes. The lower resistivity values 17 and 29 $\mu\Omega\cdot\text{cm}$ were recorded for the single layered Mo films sputter deposited at pressures 2.6 and 5.3 mTorr, respectively. These layers had pinhole free surface morphology. The resistivity values obtained for the Mo bilayer in this work were relatively near to that reported by NREL workers. However, only the single layer was good enough with low resistivity, pinhole free and good adherence to the substrate.

The significant decrease in the Mo film growth rate at higher pressures (60 and 100 mTorr) can be explained by the sputtering theory. In the sputtering process decrease in the film growth rate may be related to shorter mean free path and the deposition process becoming less of a line-of-sight process [142]. A similar kind of phenomenon may have taken place at higher pressures that decreased the Mo film growth rate.

Dependency of the Mo film resistivity on Ar gas pressure can be explained according to work reported by Scofield *et al.* [118]. According to their investigations, they found an increase in resistivity with Ar gas pressure. The lowest resistivity they achieved was 10.8 $\mu\Omega\cdot\text{cm}$ for the pressure 0.2 mTorr whereas when they increased the gas pressure to 20 mTorr the Mo film exhibited a resistivity of 250 $\mu\Omega\cdot\text{cm}$. In the case of the sputter deposited Mo films at pressures in the range 2.6-100 mTorr

(taking into consideration all pressure values mentioned in the Mo section in this thesis) similar behaviour was observed. The lowest resistivity ($17 \mu\Omega\cdot\text{cm}$) measured for the Mo film was obtained at a pressure of 2.6 mTorr, and the highest resistivity ($95 \mu\Omega\cdot\text{cm}$) at the highest pressure 100 mTorr.

The existence of types of stresses in the sputter deposited Mo films according to sputtering pressure settings was observed and reported by several research groups [118, 126, 163, 165, 166]. According to NREL workers, all the Mo films had experienced strain which caused compressive stress of varying magnitude [118]. The type of stress (tensile and compressive) experienced on the Mo films was determined using XRD data and plotting percentage strain versus sputtering pressure, according to work reported by Khatri and Marsillac [148]. In the sputtering deposition, the angle of the arriving atoms or species to the substrate was highly dependent on variations in Ar gas pressure [166]. Therefore whatever stresses occur in the sputter deposited Mo films are due to sputtering gas pressure. In relation to the work described in this thesis, the stress present in the Mo films may be due to pressure and that caused shift in the prominent Mo (110) peak with respect to the standard peak position on the 2θ scale in the XRD measurements. However the Mo films deposited at very high pressure (100 mTorr) experienced stress (which could be seen by observing bending of cover slips by naked eye) which is similar to that described by researchers around the World.

The variation in FWHM width of the prominent Mo (110) peak with process parameter (e.g. sputtering pressure) suggests that the film crystallinity varies accordingly. The narrow peak means the film has good crystallinity. Yoon *et al.* found that the Mo films deposited at low pressures have higher crystallinity than those deposited at relatively high pressures according to variations in FWHM width

of the Mo (110) peak [127]. Scofield *et al.* also found in their investigation that the FWHM width of the Mo (110) peak increased with increasing sputtering pressure [118]. These investigations support the hypothesis presented in this thesis that the significant variations in FWHM widths (comparatively higher values than obtained in case of pressures below 60 mTorr) with high sputtering Ar gas pressures (60 and 100 mTorr) tend to produce films of poor crystallinity in the Mo.

The main purpose of the investigation of the sputtering process was to deposit the back contact Mo layer which was of substantially good quality layer. Therefore low resistivity of $\sim 29 \mu\Omega\text{.cm}$, conformal, pinhole free and reasonably thick (thickness in the range 700-800 nm) Mo films were obtained with Mo target power 300 W, Ar pressure approximately 5 mTorr, Ar flow 30 sccm and deposition period 90 min. These Mo films were used as the back contact layer for further work on CIAS thin film solar cells. Some of the process parameters (flow and deposition time), Mo film thickness and sheet resistance values for the Mo work which are reported by the research workers across the World and presented in this thesis (highlighted) are listed in table 5.5.

At this stage, the investigation of the Mo deposition process produced Mo films of reasonably good quality which acted as the basis for subsequent experimental work.

Sputtering deposition technique	Pressure (Flow)	Mo Single or Bilayer	Mo film Thickness	Deposition time (Growth rate)	Average sheet resistance (Resistivity)	Reference
DC magnetron sputtering	10 mTorr- First layer; 1 mTorr- Second layer	Bilayer	1000 nm	First layer 3 min + Second layer 17 min	0.12-0.14 Ω/\square (12-14 $\mu\Omega.\text{cm}$)	[118]
RF magnetron sputtering	4 mTorr	Single layer	560 nm	60 min	1.12 Ω/\square (62.72 $\mu\Omega.\text{cm}$)	[167]
DC magnetron sputtering	8.6 mTorr	Single layer	-	6-26 min	- (9 $\mu\Omega.\text{cm}$)	[168]
DC magnetron sputtering	30 mTorr	Single layer	300 nm	(High power cycle)	5.77 Ω/\square	[169]
Pulsed direct magnetron sputtering	7.5 mTorr	Single layer	750 nm	(32 $\text{\AA}/\text{s}$)	0.65 Ω/\square	[123]
RF magnetron sputtering	- (80-140 sccm)	Single layer	1000 nm	20-70 min	0.1-0.2 Ω/\square	[170]
RF magnetron sputtering	5.3 mTorr (30 sccm)	Single layer	735 nm	90 min (1.36 $\text{\AA}/\text{s}$)	0.41 Ω/\square (29 $\mu\Omega.\text{cm}$)	In this thesis.

Table 5.5 The research work reported by research groups (working on CuInSe_2 -based thin film solar cells) around the World on the Mo layers deposited using a sputtering technique.

5.2 CuInSe₂ Absorber Layers

This section presents the results obtained from deposition of copper-indium (Cu-In) precursor layers on a good quality Mo back contact layer and conversion of precursor layers into CuInSe₂ (CIS) ($x = 0$ in CIAS) thin films.

The purpose of the work presented in this section was to optimise the binary Cu-In precursor layers and to establish process conditions, including conversion of these layers to produce good quality and photoactive CIS absorber films. The development of CIS solar cells were for two main purposes; a) to investigate the reduction of absorber film thickness (which directly reduces material cost) and b) to provide the basic technology to introduce a substitute for In and to replace gallium (Ga) in CIGS for wider energy band gap (E_g) (to optimise single junction cell and to provide upper cell for a multijunction device).

The flow diagram in figure 5.9 shows the sequence of deposition of the component layers and processing required to complete a thin film CIS solar cell [171].

5.2.1 The Cu-In precursor layers

The Cu/In ratio plays a major role in determining the properties of CIS absorber layers. In the sputtering process, the main process parameters such as Cu and In target power settings and deposition time were adjusted to produce slightly Cu or In-rich precursor layers on a Mo-coated glass substrate. Other parameters such as gas pressure, rate of gas flow, substrate table rotation speed and throttle settings were fixed unless otherwise stated.

Several batches were deposited in a dynamic mode (i.e. the sputtering table

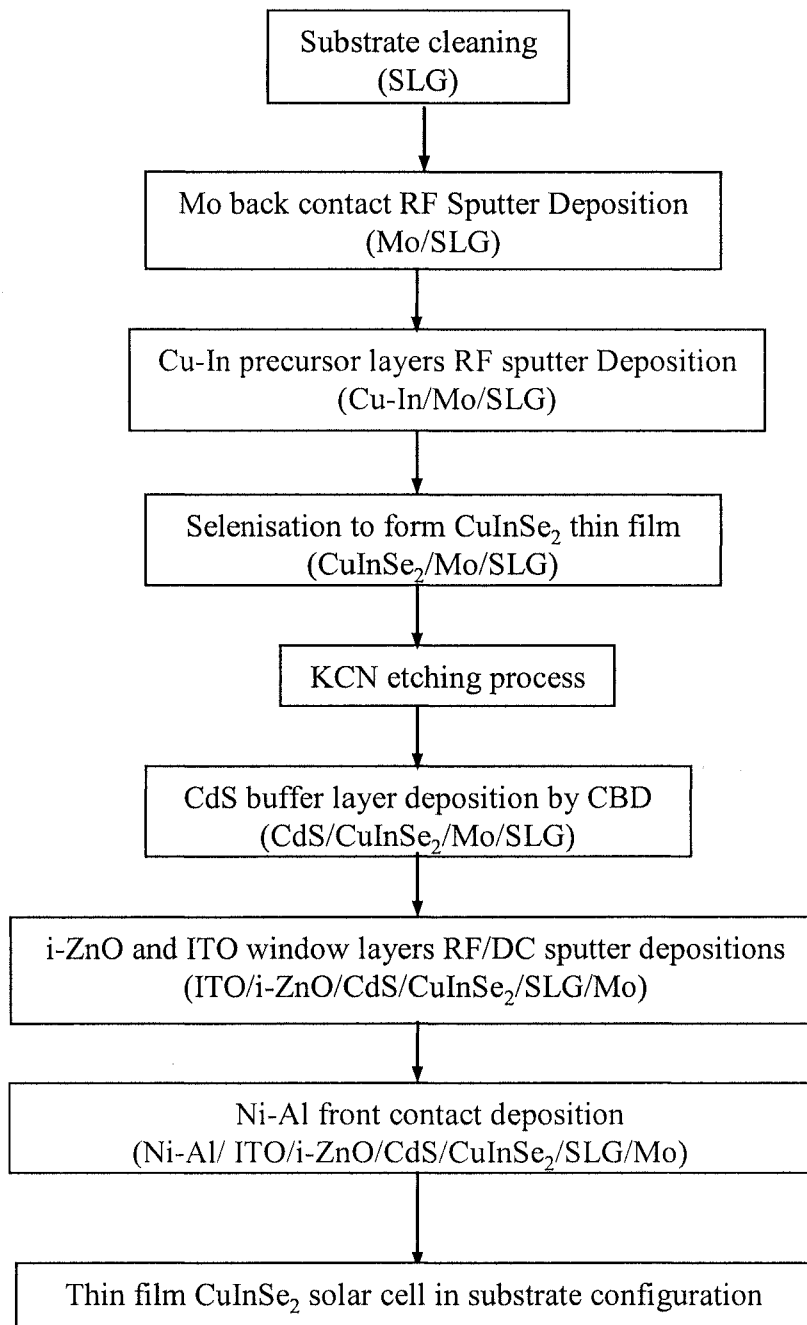


Figure 5.9 Flow chart diagram of CuInSe₂ thin film solar cell processing.

was rotating in order to keep substrate rotating during the deposition) to investigate the influence of film growth rate on the properties of the as-deposited precursor layers. In order to deposit a homogeneous mixture of Cu and In metals it was essential to rotate the substrate so as to deposit alternate thin layers of Cu-In on SLG. In this experiment, the composition was varied by varying the Cu target power between 45-60 W with the In target power fixed at 80 W and deposition time 480 min.

Energy dispersive X-ray spectroscopy (EDS) was used to measure the compositions (in atomic % (at.%)) of these layers and the results are summarised in table 5.6 and in the graph shown in figure 5.10. When the power applied to the In target is constant Cu/In composition varies fairly linear with Cu/In power ratio. This is property of sputtering in general that can be used accurately to control film composition.

The film growth rate was calculated and estimated to be approximately 0.33 Å/s.

Several sputter depositions were carried out to adjust the composition of the precursor Cu-In layers to slightly Cu-rich and hence to investigate growth rate. The deposition time was reduced to 120 min with In target power of 120 W and Cu target 60 W. The Cu-In precursor layer composition was slightly Cu-rich (Cu 51 at.% and In 49 at.%, Fig.5.12 (a)), which was supported by XRD as shown in figure 5.11, had a thickness of approximately 800 nm. The prominent peak of the $\text{Cu}_{11}\text{In}_9$ phase was formed with an additional CuIn_2 phase. No single elemental Cu or In was detected in the diffraction spectrum. This shows the appropriate formation of Cu-In alloy by intermixing of elements without intentional substrate heating. The SEM image of surface morphology of the as-deposited Cu-In precursor layer on the Mo-coated glass

Batch	Cu Target Power (W)	Cu (at.%)	In (at.%)
N48	45	46	54
N50	48	47	53
N51	49	49	51
N49	50	53	47
N47	60	60	40

Table 5.6 EDS results of the precursor layers in at.% of Cu and In with variation in power applied to Cu target for fixed In target power of 80 W.

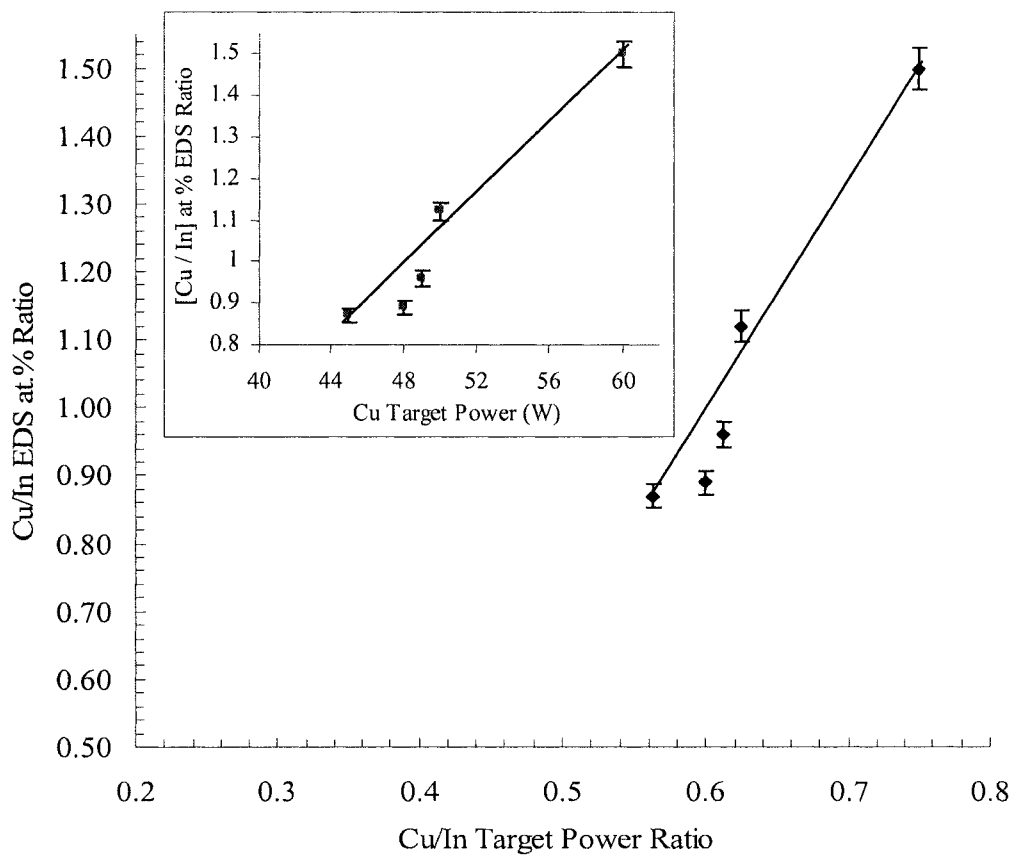


Figure 5.10 EDS at.% Cu/In ratio variation with Cu/In power ratio (The inset shows Cu target power settings).

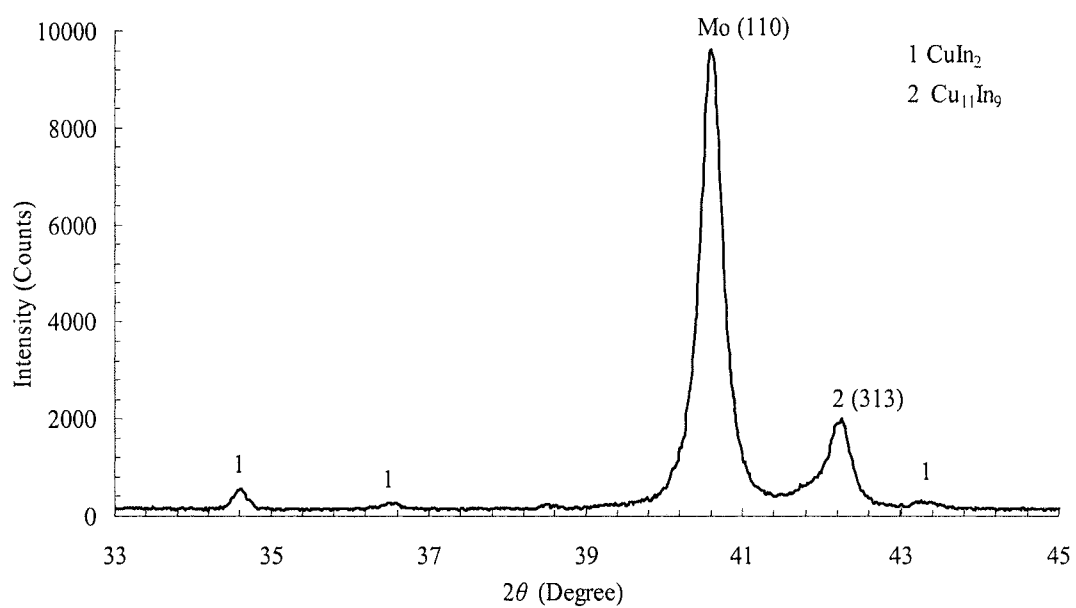


Figure 5.11 The XRD pattern of the sputter deposited Cu-In precursor layers (Sample-N94) on the Mo-coated glass substrate [There is no *hkl* information available for CuIn₂ reflection (peak 1) in PDF database software].

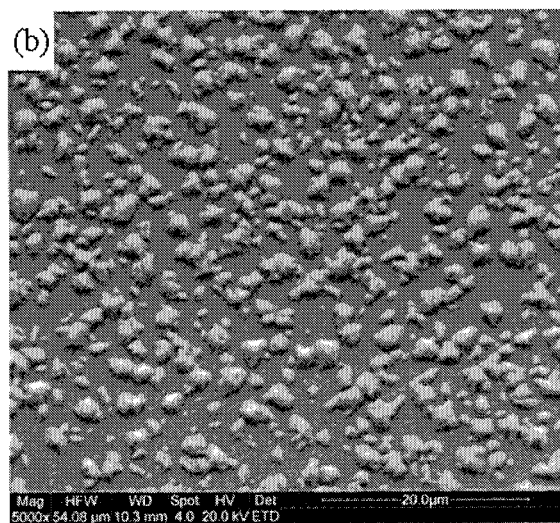
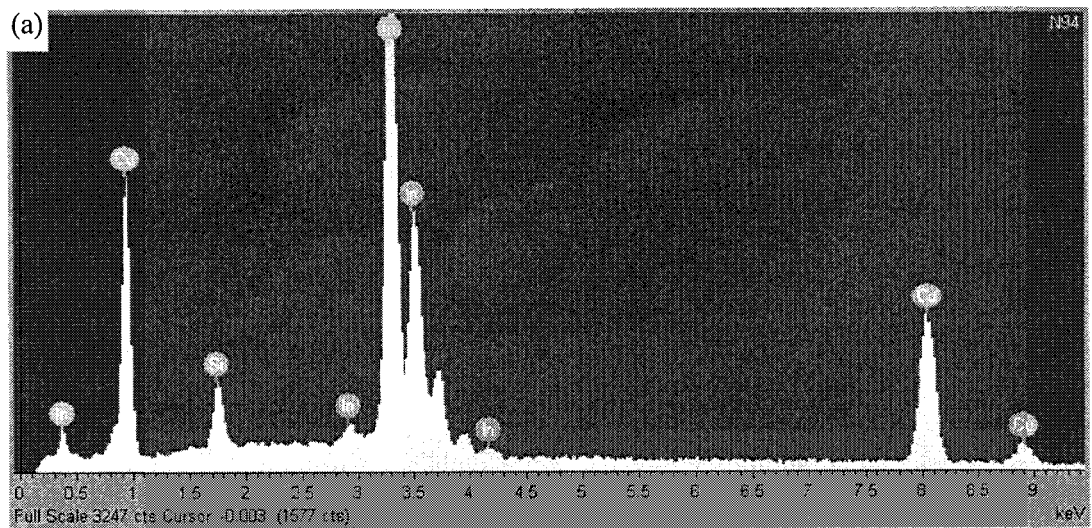


Figure 5.12 (a) The EDS spectrum and (b) the SEM surface image of the sputter deposited Cu-In precursor layers (Sample-N94) on the Mo-coated glass substrate.

substrate is shown in figure 5.12 (b). It reveals a rough surface structure that may be due to In-rich phases.

5.2.2 Selenisation of sputter deposited Cu-In precursor layers

The Se (of purity 99.999 %) material was evaporated onto surface of the precursor layer and onto the cleaned SLG ($76 \times 13 \text{ mm}^2$) using a resistively heated tantalum source in a separate chamber. The Se capping typically had a thickness in the range 1-2 μm . Commencement of the selenisation process was the same as discussed before (section 4.1.3) as a method to produce CIS thin films. Initial conversion experiments were carried out to investigate the morphology and crystallographic characteristics of converted films in accordance with the tube furnace and graphite box geometry. The temperature profiles for single-step and two-step selenisation process in a graphite box are shown in figure 5.13.

Annealing of the Cu-In layers at different temperatures

Annealing experiments for different process temperatures were carried out to investigate the crystalline phases present and the surface morphology. The Ar gas pressure of 2 mbar, duration 30 min and sample preparation method were kept fixed. The Cu-In precursor layer was slightly Cu-rich (Cu 51 at. % and In 49 at.%) in composition and 600 nm-thick.

The XRD patterns for films selenised at different temperatures are depicted in figure 5.14 and phases detected in the selenised films are listed in table 5.7. It can be seen that binary selenised phases are mainly formed at 250°C and 350°C. Copper selenides binary phases at both temperatures were identified to be CuSe_2 and Cu_{2-x}Se , while indium selenides were identified as In_2Se_3 and InSe .

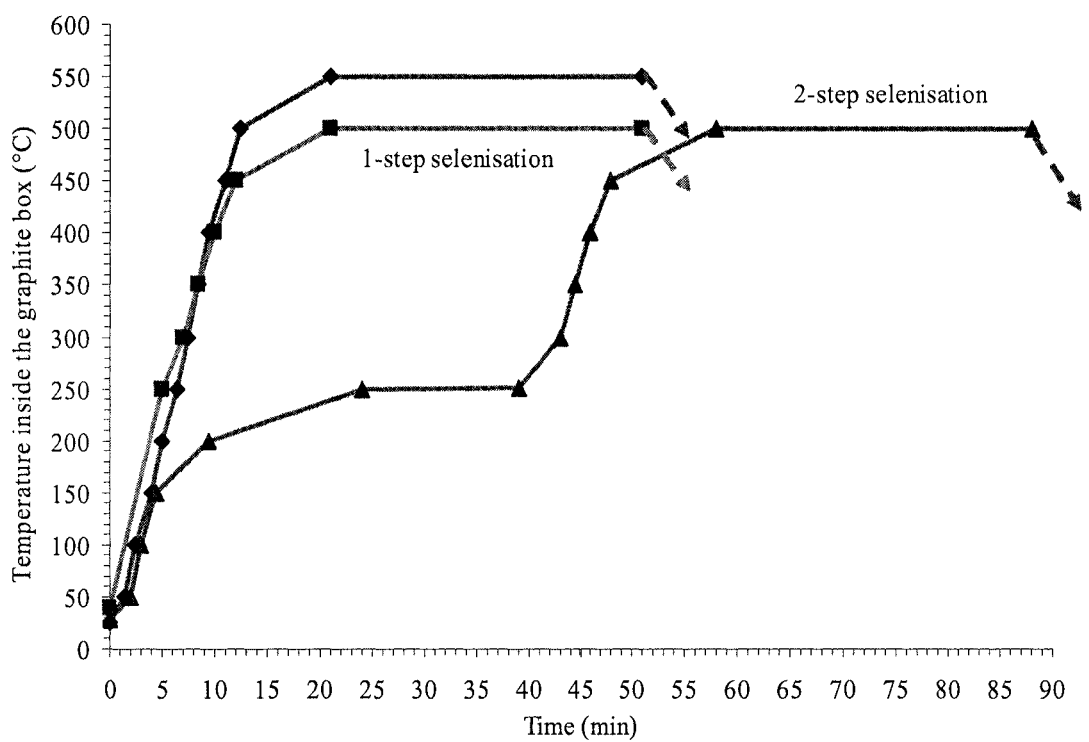


Figure 5.13 Temperature profiles for single- step and two-step selenisation process in a graphite box. (The dashed line with arrow represents start of cooling process).

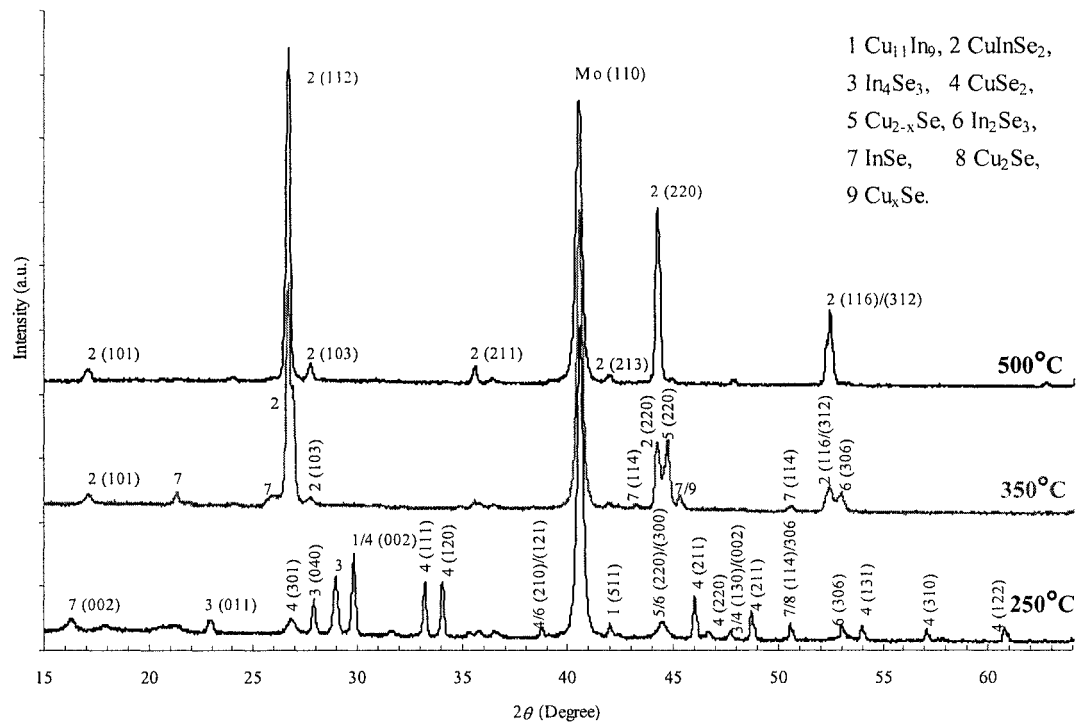


Figure 5.14 XRD spectra of films selenised at different temperatures; 250°C (Sample-N161J1), 350°C (Sample-N161J2) and 500°C (Sample-N161J3).

Annealing Temperature (Sample ID)	Metals (Cu/In alloy)	Phases present in the selenised films		Compositional analysis		
		Binary selenides	Ternary selenides	Cu (at. %)	In (at. %)	Se (at. %)
250°C (N161J1)	C ₁₁ In ₉ , CuIn ₂	InSe, In ₄ Se ₃ , CuSe ₂ , In ₂ Se ₃ , Cu _{2-x} Se, Cu ₂ Se	-	41.84	11.04	47.12
350°C (N161J2)	C ₁₁ In ₉ , CuIn ₂	InSe, CuSe ₂ , In ₂ Se ₃ , Cu _{2-x} Se, Cu _x Se	CuInSe ₂	40.51	16.9	42.59
500°C (N161J3)	C ₁₁ In ₉ , CuIn ₂	CuSe ₂	CuInSe ₂	28.51	24.36	47.13

Table 5.7 Summary of data obtained using XRD and EDS techniques on the selenised CuInSe₂ films at different temperatures.

The composition (Table 5.7) of these films was measured by EDS. At 250°C, the composition of In (approximately 11 at.%) present in the film was less as compared to the compositions of Cu and Se (Cu/In \approx 3.8). The In content in the films was measured as a function of the rise in temperature. At a temperature of 350°C, the Cu/In was calculated as approximately 2.4. The CIS film converted at 500°C was measured to be of Cu/In approximately 1.17 (Cu-rich).

The SEM surface images of films selenised at 250°C, 350°C and 500°C are shown in figure 5.15 and they showed clearly the change in surface topology and topography with increase in temperature. At a temperature of 250°C, the surface showed rectangular plate-like elongated structures. At a temperature of 350°C, the surface of the films possessed grain-like structures and at temperature of 500°C these became more angular shapes of average size in the range between 2-3 μm .

XRD, EDS and SEM data suggests that the temperature of 500°C (Ar pressure 2 mbar and duration 30 min) was required to convert the precursor Cu-In layer into the CIS absorber films with a prominent CIS (112) peak in the XRD graph and large grains.

Several selenisation processes were carried out to achieve the required properties in the CIS films to work as the absorber in the solar cell. This also confirmed the repeatability and reproducibility of the CIS films for particular precursors.

After several trials the single step (at temperature of 500°C) was found to yield better conversion of precursor layers into CIS. The XRD of a good quality thin film structure is shown in figure 5.16. All peaks were found to belong to the ternary CIS phase with different Miller indices (hkl). It suggested complete conversion of the precursor layers into CIS material.

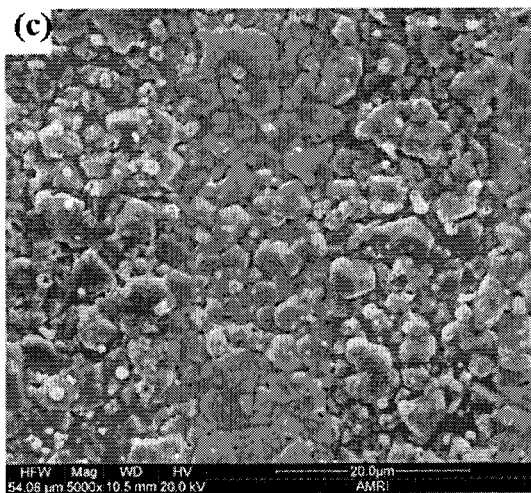
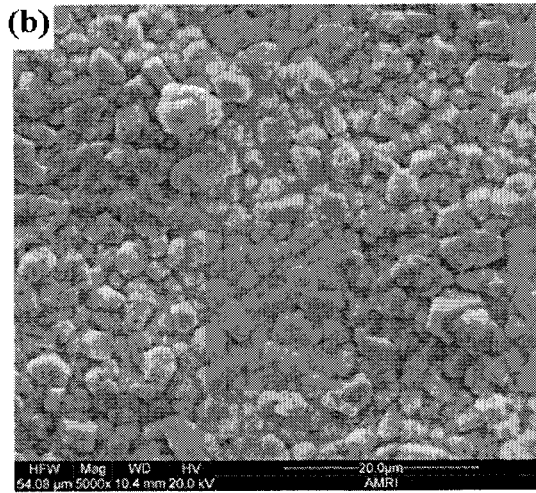
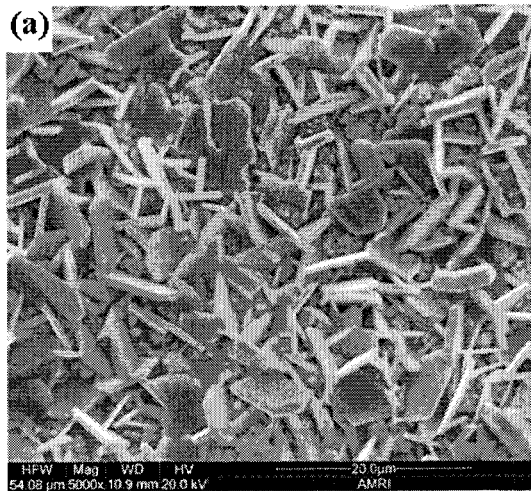


Figure 5.15 SEM images of surface of the films selenised at different temperatures; (a) 250°C (Sample-N161J1), (b) 350°C (Sample-N161J2) and (c) 500°C (Sample-N161J3).

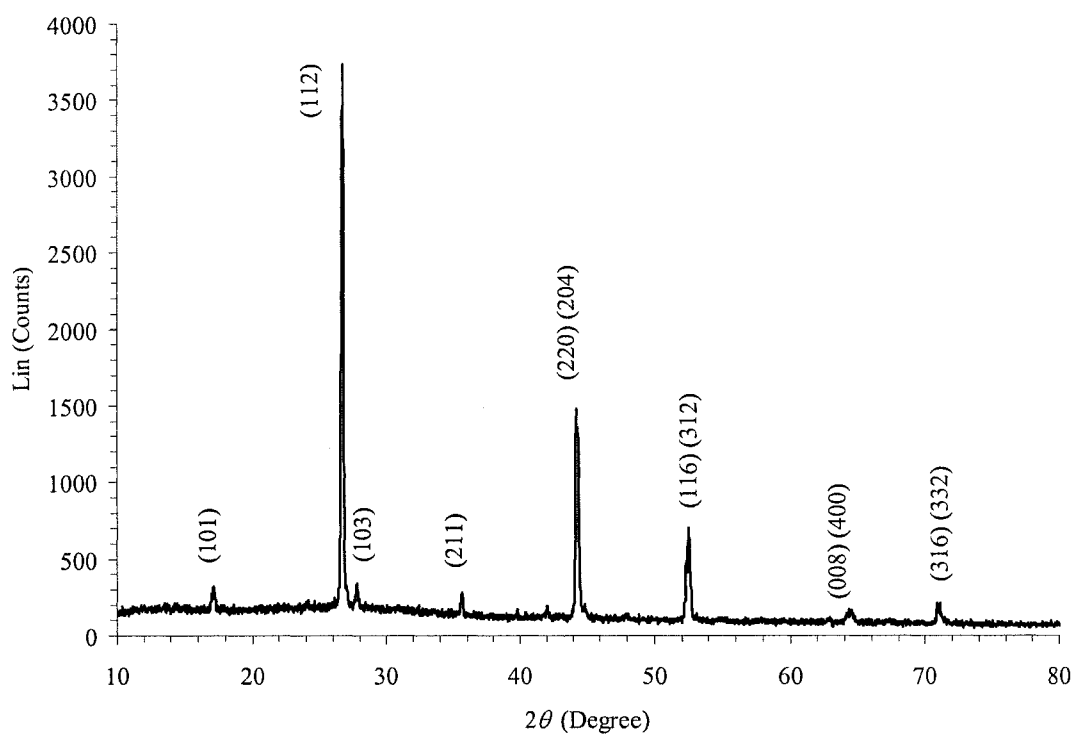


Figure 5.16 XRD of CIS thin films on glass substrate produced by using the Se cap layer (Sample-N53H).

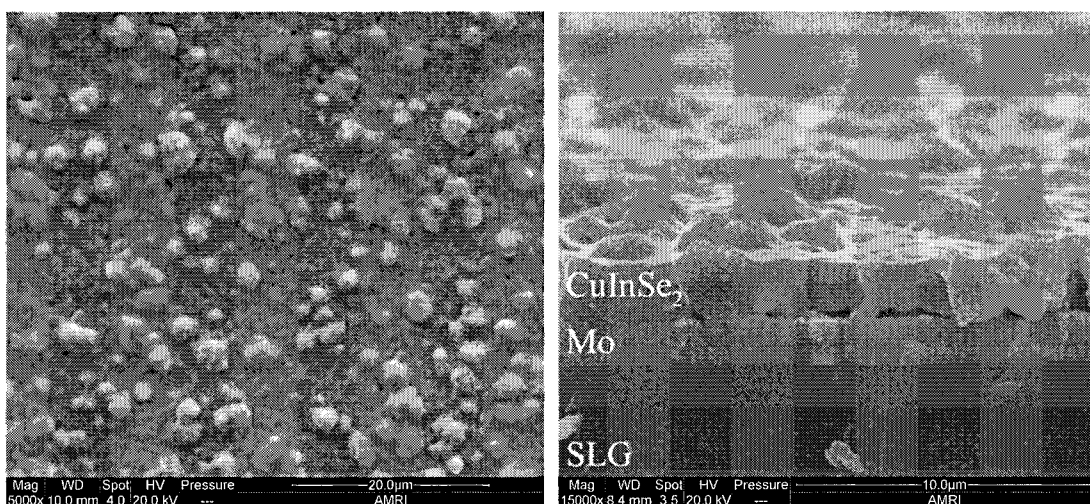


Figure 5.17 SEM images of the surface (left) and cross-sectional view (right) of the CIS thin film on Mo coated glass substrate selenised at 500°C [Sample-N53H].

The SEM images (Fig. 5.17) of the converted layers exhibited a dense crystal structure on the Mo-coated glass substrate. The cross-sectional SEM image shows large grains of CIS absorber of height equivalent to the absorber thickness of approximately 2 μm .

5.2.3 Conversion of thinner layers of Cu-In precursors into CuInSe_2 absorber films

In this section the influence of Cu-In precursor layer thicknesses on the morphological and optical properties of the CIS thin films was investigated. The precursor layers were deposited with thicknesses in the range 90-400 nm (Table 5.8). The actual sample or batch names are listed in appendix II. The metallic Cu-In layers were subsequently selenised in Ar atmosphere, under excess Se, at 500°C to form CIS thin films. The thicknesses of the films were in the range 400-1600 nm.

XRD patterns of the selected Cu-In precursor layers of different thicknesses are shown in figure 5.18. According to it the dominant phases present in the layers are $\text{Cu}_{11}\text{In}_9$ and CuIn_2 . There was no peak corresponding to elemental Cu or In indicating good intermixing for layers deposited without deliberate substrate heating. Again it was confirmed that sputter technology proved to be useful in achieving homogenous, well mixed and high quality precursor layers without requiring any heating facility in the chamber.

The compositional (at.%) Cu/In ratio (Table 5.8) of the precursor layers measured using EDS was in the range 0.96-1.13. All compositions of the precursor layers were Cu-rich except for sample A (slightly In-rich).

Sample	Cu-In thickness (nm)	CuInSe ₂ thickness (nm)	Compositional analyses		XRD Data analyses for CuInSe ₂ thin films							
			Cu-In	CuInSe ₂	Texture coefficients						Preferred orientation σ	
			Cu/In	Cu/In	Se/(Cu+In)	C ₁₁₂	C ₂₁₁	C ₁₀₁	C ₁₀₃	C ₃₀₁		C _{220/204}
A	90	400	0.96	0.85	1.21	0.5	1.4	3.0	0.0	0.0	0.4	1.2
B	130	500	1.12	0.98	1.27	1.7	3.3	0.0	0.0	0.0	1.1	1.2
C	200	800	1.04	0.96	1.22	0.7	1.0	2.2	1.1	0.0	0.5	0.7
D	240	900	1.10	1.02	1.34	0.8	1.4	2.9	0.0	0.0	0.7	1.0
E	340	1000	1.13	0.96	1.04	0.6	1.0	2.1	1.2	0.0	0.5	0.8
F	400	1600	1.09	0.96	1.07	0.6	0.8	1.4	1.1	1.2	0.4	0.4

Table 5.8 EDS and XRD data analyses of the Cu-In precursor layers and CuInSe₂ thin films with different thicknesses.

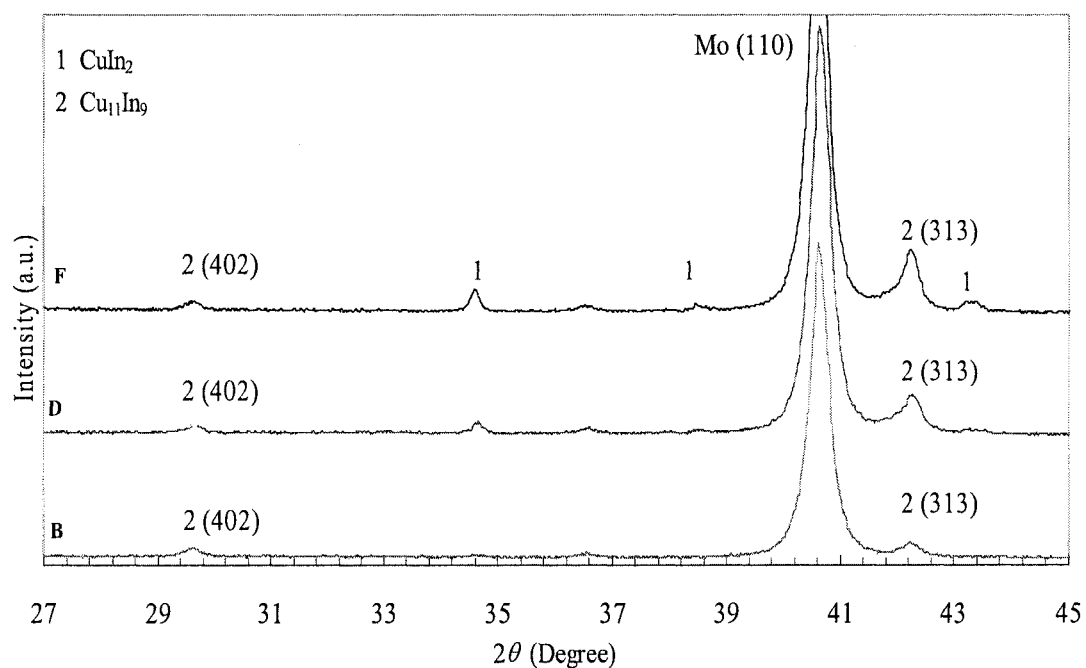


Figure 5.18 XRD graph of the different thickness Cu-In precursor layers of the samples B (130 nm), D (240 nm) and F (400 nm) [There is no *hkl* information available for the reflection CuIn₂ (peak 1) on the PDF database software].

The SEM and the three dimensional atomic force microscopy (AFM) images of the surface structure of the precursor layers of samples B, D and F are shown in figure 5.19. There was an increase in quantity of In-rich features on the surface with the sample thickness. The surface roughness monotonically increased with thickness from 6.9 nm for a 130 nm thin film to 25.2 nm for a 400 nm-thick film.

Figure 5.20 shows secondary ion mass spectroscopy (MiniSIMS) depth profiles of $^{23}\text{Na}^+$, $^{63}\text{Cu}^+$, $^{113}\text{In}^+$ and $^{98}\text{Mo}^+$ species for precursor layer D (240 nm-thick). Traces of the metallic species Cu and In are uniform throughout the thickness of the layer except near the surface, the apparent deviation near the surface is due to instrument limitations. Similarly the Na signal is also uniform and close to the background level of detection.

XRD patterns for selected films selenised at 500°C of three different thicknesses are shown in figure 5.21. All the peaks can be identified and belong to the Mo substrate and to the chalcopyrite phase of CIS. XRD data was used to calculate texture coefficient (C_{hkl}) and degree of preferred orientation (σ) (Table 5.8) [172]. The thicker films are more randomly orientated as indicated in figure 5.22 and according to it there is a decrease in preferred orientation with thickness of the films. In the XRD pattern additional peaks such as (101), (103) and (301) are detected for thicker films.

The compositions of the CIS films are presented in a table 5.8. There was no particular variation in the composition of the films with variation in thickness. However, all films were found to have excess Se in the compound.

The surface morphology of thin films was investigated by using SEM and is shown in figure 5.23. It reveals increase in grain size according to thicknesses.

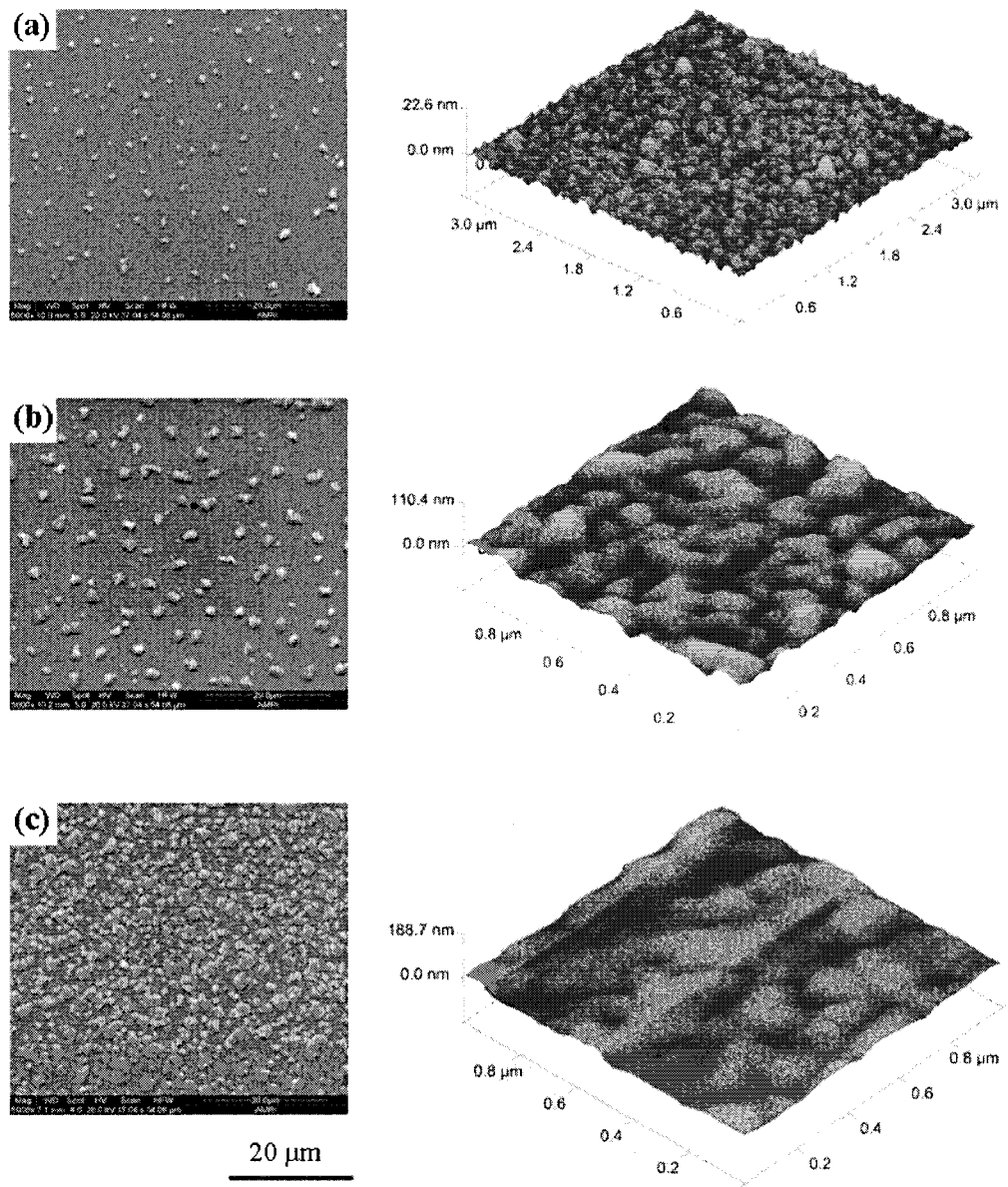


Figure 5.19 SEM (left) and AFM (right) surface images of the Cu-In precursor layers of different thicknesses of samples (a) B (130 nm), (b) D (240 nm) and (c) F (400 nm). [AFM images were taken using a Veeco instrument at Northumbria University].

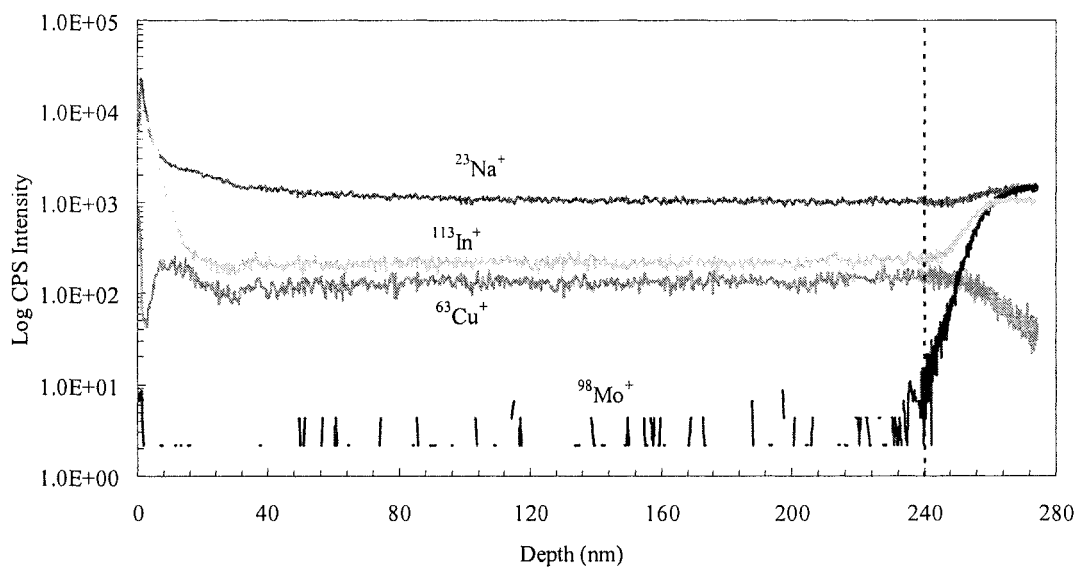


Figure 5.20 MiniSIMS depth profile of the Cu-In precursor layer of the sample D (240 nm) (The dashed line shows CuIn/Mo interface).

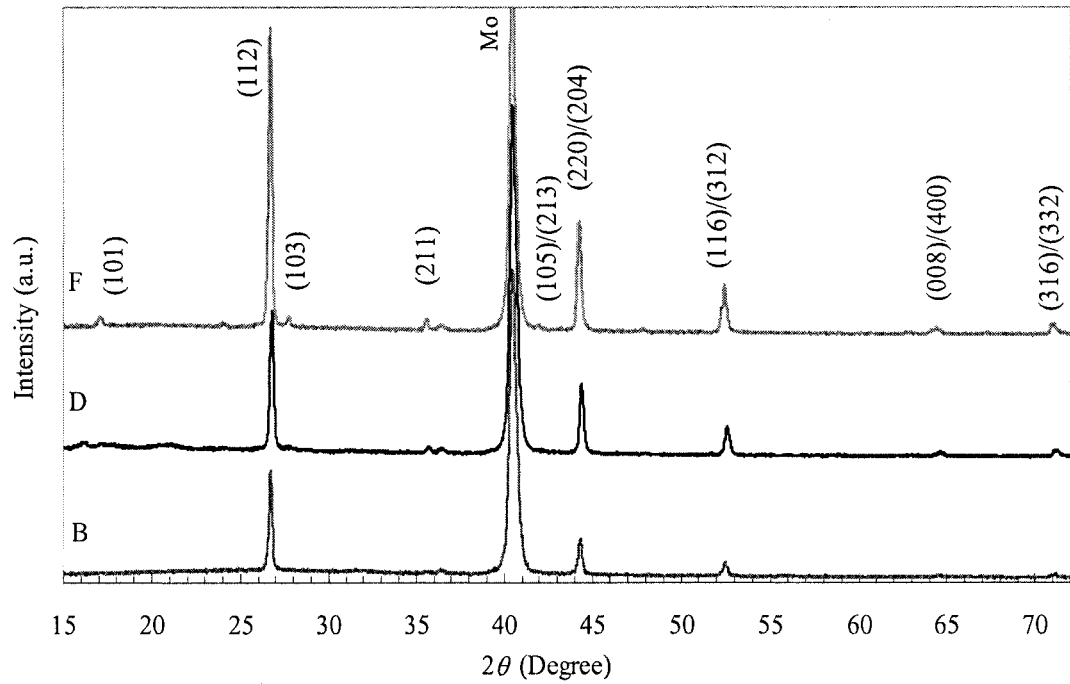


Figure 5.21 XRD pattern of the CIS films of the samples B (500 nm), D (900 nm) and F (1600 nm).

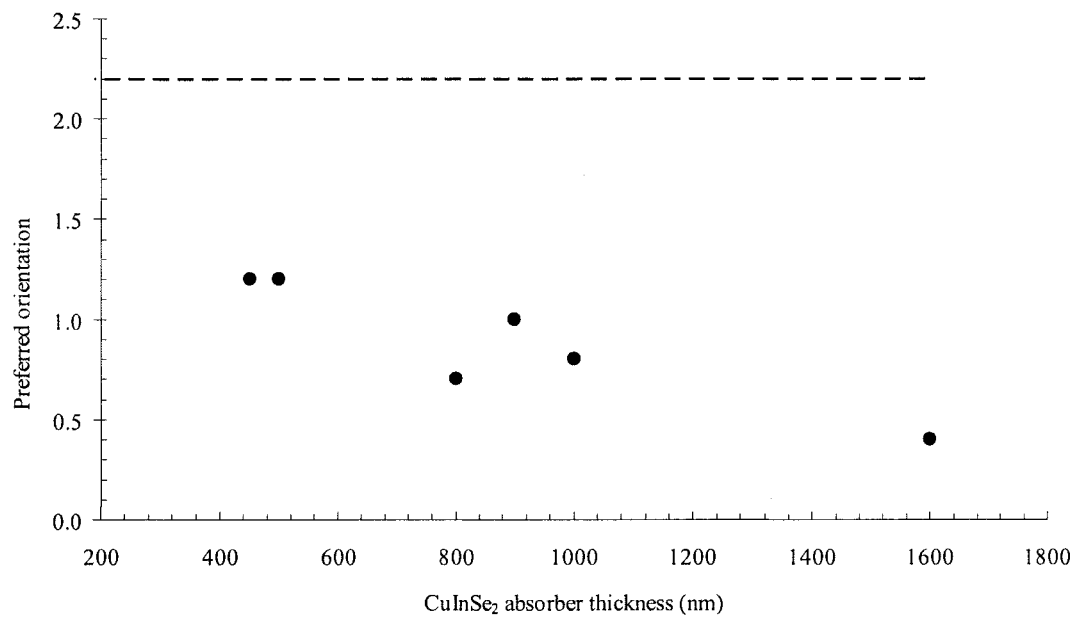


Figure 5.22 Preferred orientation variations with CIS absorber film thickness.

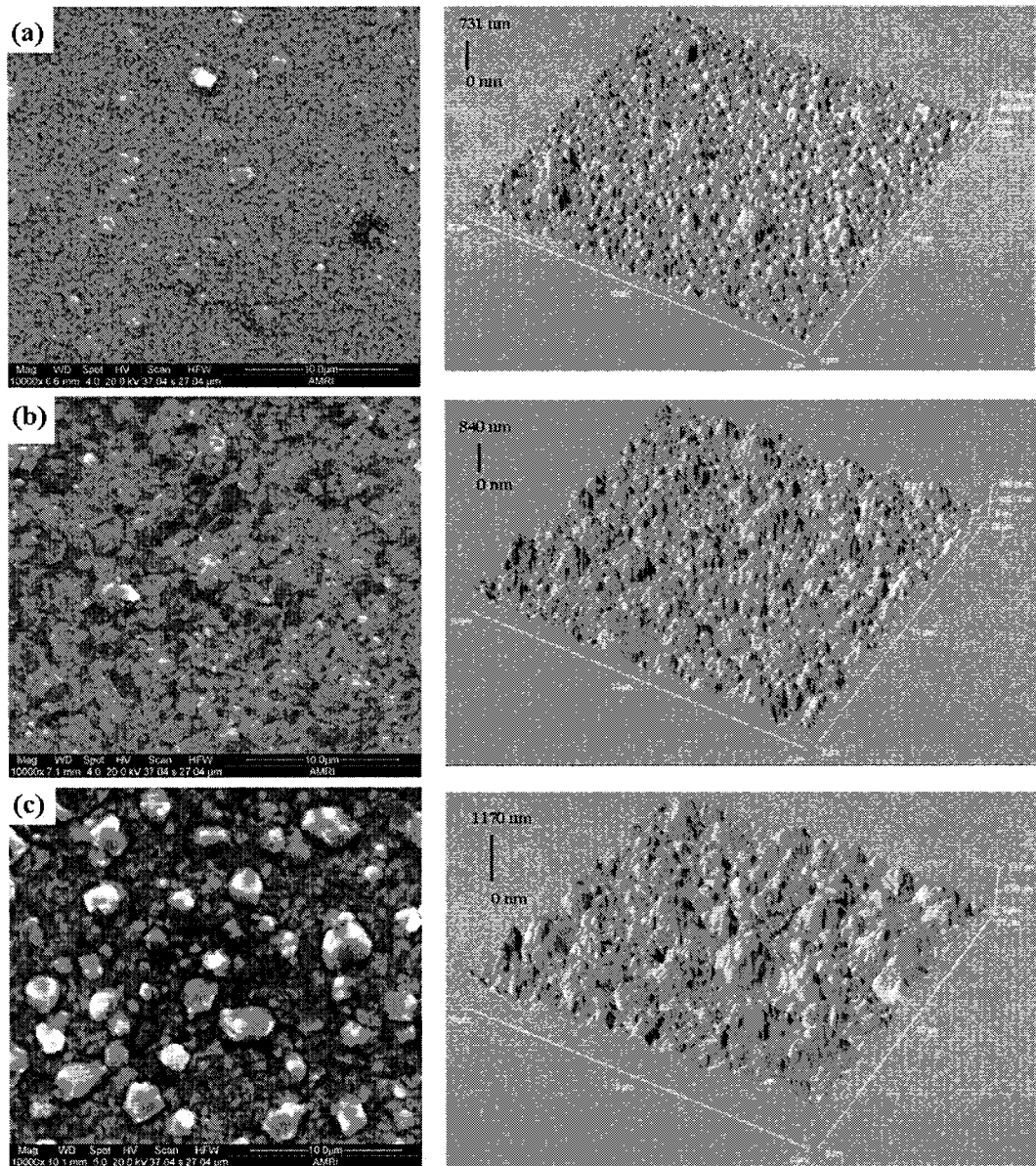


Figure 5.23 SEM (left) and AFM (right) surface images of the CIS thin films of samples: (a) B (500 nm), (b) D (900 nm) and (c) F (1600 nm). The AFM images are for a $20 \times 20 \mu\text{m}$ field of view. [AFM images were taken using Topometrix explorer instrument based at Durham University (Supergen project consortium member)].

AFM scanning over a 20 μm surface area was carried out on the samples B, D and F and the output results are shown in figure 5.23. The degree of surface roughness was observed and estimated using the available software with an AFM instrument. The root mean square roughness values are 90, 123 and 201 nm for samples B, D and F, respectively. This indicates that the surface roughness increases monotonically with film thickness. It is considered desirable to have absorber film surface to be smooth in order to deposit a uniform CdS buffer layer.

The absorber film thickness of 500, 900 and 1600 nm were found to have the average grain sizes 430, 650 and 1700 nm, respectively. The lateral grain size was measured using a software package Soft Imagine System GmbH version 3.2 which was available with Oxford instrument. The grain size was found to increase with the absorber thickness but it is not a linear trend as shown in figure 5.24.

Depth profiles (Fig. 5.25) of $^{113}\text{In}^+$ and $^{80}\text{Se}^-$ were acquired for a 1600 nm thick CIS film (sample F) using the MiniSIMS system. The profiles of the metallic species (including $^{63}\text{Cu}^+$ (not shown here)) are uniform throughout the film thickness. The $^{113}\text{In}^+$ profile is non-uniform near the surface (approximately 0-300 nm deep from the surface of the film) which may be due to a slight In loss near to the surface of the film. Na out-diffusion from the glass can be considered the cause of the variation in Na depth profile, which shows a higher signal by one order of magnitude at the CIS/Mo interface. Near the CIS/Mo interface the precursor profiles decreased and therefore it is concluded that the higher Na signal is a real high concentration region and not an artefact.

The CIS films B, D and F were scanned in the light of wavelength range 500-1600 nm in the spectrophotometer. The graphs of normalised percentage transmittance and reflectance versus wavelength of those films are presented in

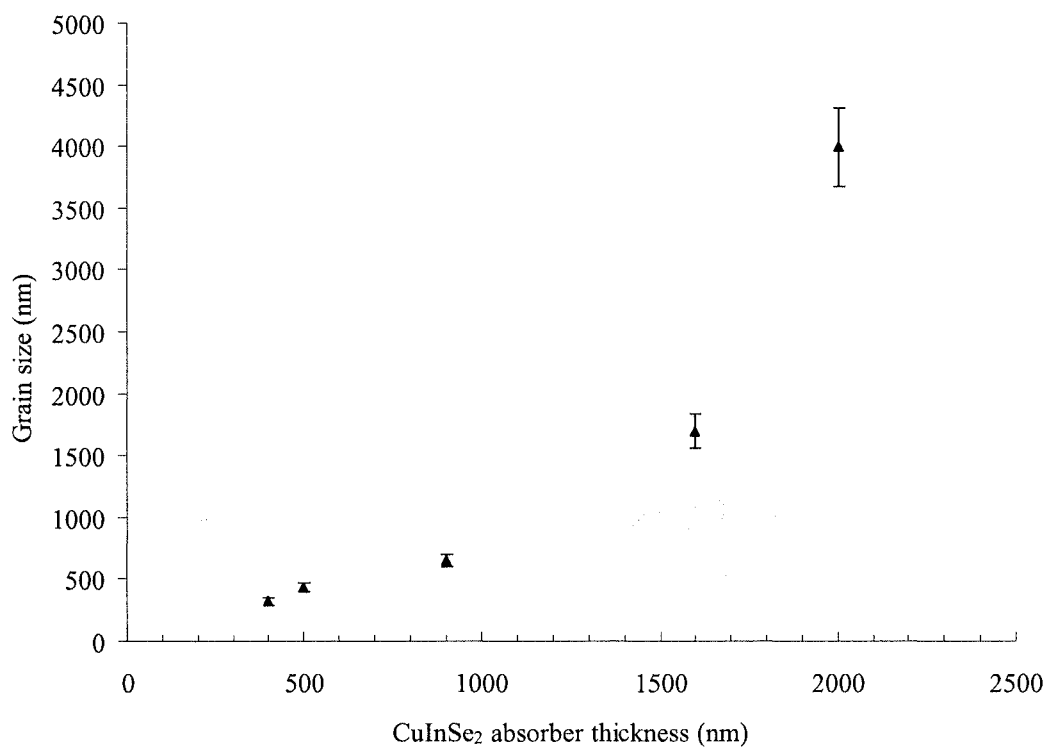


Figure 5.24 Grain size variations with the CIS absorber film thicknesses.

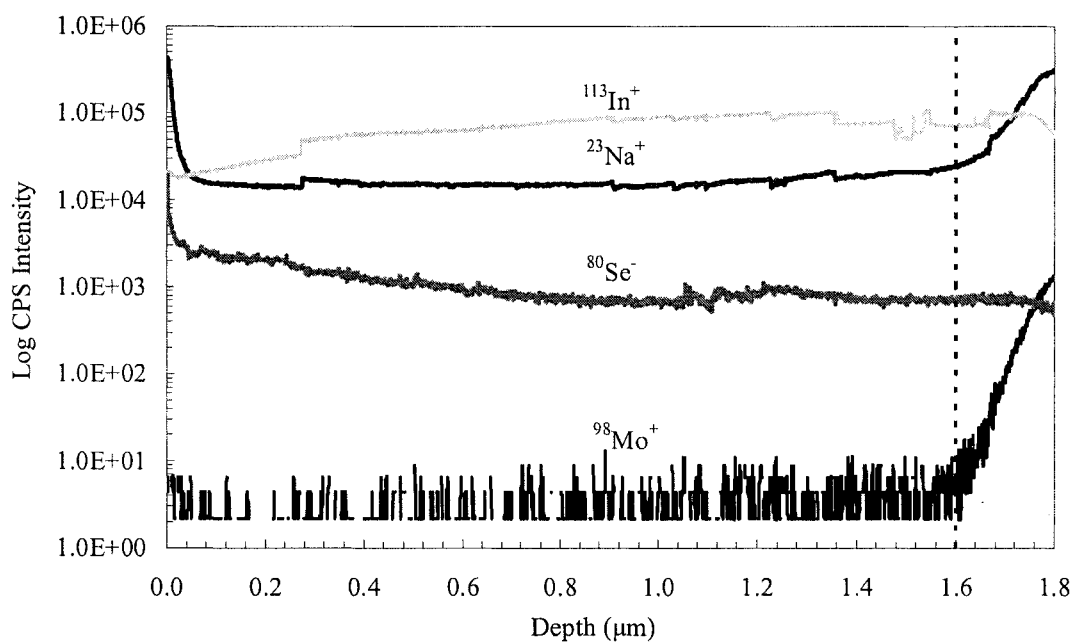


Figure 5.25 MiniSIMS depth profile of CIS thin film of sample F (1600 nm) [The dashed line shows the CIS/Mo interface].

figure B in the appendix I. Absorption coefficient (α) and energy band gaps (E_g) of these direct semiconductor materials were calculated using the expression:

$$\alpha h \nu = A(h \nu - E_g)^{1/2}$$

Where, h is Planck's constant, ν is the frequency of incident light and A is a constant.

The plot of $(\alpha h \nu)^2$ versus $h \nu$ for different thickness CIS films is shown in figure 5.26.

Energy band gaps within the range 0.90-0.94 eV were measured and little variation in the optical properties of films from ultra-thin to thinner absorbers was observed.

These CIS films were photoactive with p -type conductivity found by the photocurrent experiments. This indicated that these absorber layers were useful for processing further to incorporate in the solar cell structure.

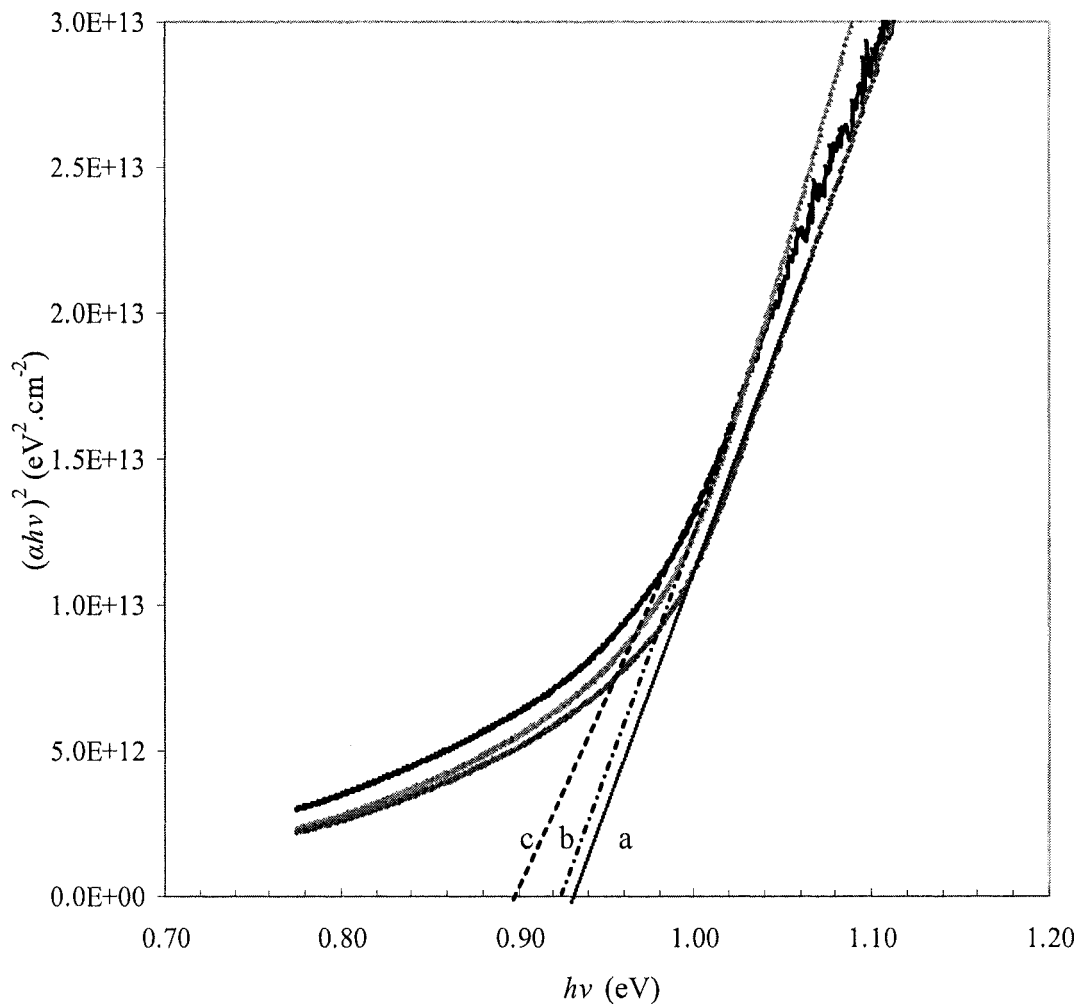


Figure 5.26 Energy band gaps of the CIS films on the glass substrates of thicknesses; $a = 500$ nm (sample B), $b = 900$ nm (sample D) and $c = 1600$ nm (sample F).

5.2.4 Discussion

In this work, precursor Cu-In layers of the required composition were achieved by keeping the power of one target (In) fixed and varying the power of the other target (Cu). This demonstrated that during sputtering the material composition can be effectively controlled by varying target powers. XRD of the precursor layers showed that the prominent phase was $C_{11}In_9$ with an additional $CuIn_2$ phase.

The results of annealing of the precursor Cu-In layers at different temperatures were analysed. At a low temperature of 250°C, the melting of In and Se was started and the reaction between In and Se and Cu and Se was just begun. However, EDS data confirmed that there was a loss of In (11 at.%) at 250°C due to its melting point at 156°C [173]. The increase in In content with temperature (16.9 at.% at 350°C and 24.36 at.% at 500°C) due to the mixing of In with Cu and Se atoms. The film annealed at 500°C was slightly Cu-rich with appropriate composition (Cu 28.51 at.%, In 24.36 at.% and Se 47.13 at.%) according to CIS structure. The additional Se was supplied from the Se environment created in the graphite box.

The XRD spectra showed many peaks of binary phases ($CuSe_2$, Cu_2Se and In_2Se_3) and prominent Mo reflection (110) suggesting that the temperature of 250°C was not sufficient to form single phase ternary compound CIS material. At 350°C, the ternary CIS phase and some binary phases were detected. This suggests that most of the Se incorporation into the Cu-In precursor layer took place at temperatures between 250°C and 350°C. As the temperature increased, the binary phases disappeared and a ternary phase became prominent. At temperatures higher than 250°C, the formation of CIS phase was considered to be due to a reaction between copper selenides and indium selenides. When the precursor layers were selenised at

500°C, the prominent (112) reflection (peak position 26.6° on the 2θ scale) of CIS material was detected.

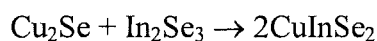
EDS and XRD results were supported by analysing surface morphology using the SEM technique. The surface morphology showed significant differences between the samples selenised at 250°C and 350°C and at 250°C and 500°C. The plate-like features in the film selenised at 250°C suggest that the reaction took place only on the surface of the samples probably between In and Se. As the temperature increased to 350°C, Se started to diffuse into the precursor layer and reacted with Cu and In. It is attributed to the formation of binary phases (CuSe_2 , Cu_2Se and In_2Se_3) and a small amount of CIS material. At 500°C, the Se completely diffused into the absorber and reacted with binary compounds to form a ternary single phase CIS. This experiment confirmed that a temperature of least 500°C was required for complete selenisation of the precursor layers.

In summary, annealing of the Cu-In precursor layers (slightly Cu-rich in composition) at temperature 500°C for 30 min in a Se environment was enough to form good quality CIS films.

Similar experiments and subsequent results have been reported in the literature to explain reaction mechanism for formation of the CIS chalcopyrite phase.

The formation of the Cu-In precursor layer composition with certain metallic phases is an essential step in order to prepare high quality CIS film. For instance the $\text{Cu}_{11}\text{In}_9$ phase is required ensuring the proper mixing of the elements in the precursor layer [174, 175]. Menna *et al.* reported the alloy phases of $\text{Cu}_{11}\text{In}_9$ and CuIn_2 in the precursor layers deposited by RF sputtering at substrate temperature between 24°-75°C [176]. This supports the explanation for the results of XRD of the Cu-In precursor layers (slightly Cu-rich) which showed $\text{Cu}_{11}\text{In}_9$ and CuIn_2 phases.

The results of annealing of precursor layers at temperatures, 250°C, 350°C and 500°C demonstrated that a high temperature of 500°C was needed to form CIS films. According to Reddy *et al.* at temperature 500°C the reaction between copper selenides and indium selenides took place at the same time as Se incorporation to compensate for losses (evaporation) [177]. This accelerated the formation of chalcopyrite CIS phase and binary phases become insignificant in the converted films. A simple chemical reaction to explain the incorporation of Se while reacting with Cu and In to form selenised ternary phases is given in the literature [178] as follows



The analyses of the results (by EDS, XRD and SEM) from annealing experiments were consistent with the explanations from literature regarding reaction between Cu, In and Se at temperature 500°C to form CIS thin films.

The influence of thinner layers of Cu-In precursors on the structural and optical properties of CIS absorber film was investigated. XRD pattern for the precursor layers (slightly Cu-rich) showed essential phases $\text{Cu}_{11}\text{In}_9$ and CuIn_2 . The surface roughness of these precursor layers increased with thickness. This may be due to the formation of In-rich islands which were also observed in surface SEM images. MiniSIMS data of the precursor layer confirmed that there was proper mixing of Cu and In layers. In addition out-diffusion of Na from SLG through the Mo layer was detected.

The XRD data of the absorber films suggested complete conversion of the thinner layers of precursors into the CIS thin films. The films became more randomly oriented with thickness. The SEM surface images of these films have shown increase in grain size with thickness. AFM results confirmed increase in surface roughness

with thickness that might be applicable in this work to prove the relationship between thickness and grain size of the films. The MiniSIMS depth profile of selected converted film has shown insignificant variation in Se trace (reasonably uniform) from the surface to the CIS/Mo interface however, the initial drop in In signal suggests a slight In loss near the film surface. This indicated uniform diffusion of Se throughout the precursor layer and thus a uniform conversion of the precursor layers into the chalcopyrite material. Depth profile for Na (count rate higher than 1×10^4) which was out-diffused from the Mo-coated SLG substrate may have helped in enhancing the absorber grain sizes. The energy band gaps of the CIS films were found to be in the range 0.90-0.94 eV.

In summary, the precursor layers of different thicknesses had well mixed sputter deposited metallic elements with overall slightly Cu-rich compositions. They showed an increase in surface roughness with increasing thickness. The CIS films produced from these precursor layers were completely converted with increased surface roughness and grain size according to increase thickness. The CIS films had found direct energy band gaps (in the range 0.90-0.94 eV) which were in close agreement with those reported in the literature (actual values in the range 0.95 and 0.97 eV, respectively) [24, 179]. These films were found to be suitable as good quality absorbers (photoactive and *p*-type conductivity) to include in the solar cell structures.

In this work, the increase in In-rich islands caused an increase in the surface roughness of the thinner precursor layers, which can be explained with phenomenon reported by Japanese researchers. Nakano *et al.* observed the higher surface mobility of In atoms and their tendency to amalgamate and to grow with increase in

deposition period [180]. These islands were formed by the segregation of excess In atoms.

One of the precursor layers (sample D) was found to be slightly Cu-rich in composition and with uniform distribution of the metallic elements which may be due to sputter deposition in a dynamic mode (substrates rotating).

When thinner layers of precursors were heated at 500°C in an excess Se environment to form CIS thin films, the grain size was measured and found to be increased with thicknesses. This agreed with the results reported by Mitra *et al.* who investigated effect of thickness on grain size in nickel films [181]. In addition the surface roughness also increased with the thicknesses of thin films. Negami *et al.* found in their investigation that grain size of co-evaporated CIGS thin films decreased with decreasing absorber thickness; however, the surface became rough due to sharp smaller grains [182]. They also reported that the thicker thin film was smoother in surface morphology. The reduction in absorber thickness ($\sim 0.5 \mu\text{m}$) resulted in increased surface roughness which caused a shunting problem (shunt conductance) in solar cells [182, 183]. Interestingly, the absorber surface roughness was decreased with reducing thickness in the work described in this thesis. This may be advantageous in this type of CIS production method (sputter depositions of the precursor layers followed by the selenisation) over a co-evaporation method. The controlled amount of out-diffusion of Na from the glass substrate is beneficial for enhancing grain growth. In this work, Na was found to be out-diffused from the Mo-coated glass substrate as demonstrated by the MiniSIMS depth profile of the precursor layer and the CIS thin film. Hedström *et al.* found an improvement in cell performance which was fabricated on the SLG substrate with detection of Na in SIMS depth profile in CIS based absorber [79]. Probst *et al.* reported the advantages

of the presence of Na which are larger grain morphology of CIGS and an improvement in cell performance [87]. Since then, the effects of Na are still being investigated mainly for CIGS by several research groups around the World. The purpose of presenting Na related literature is that in this work (described in this thesis), Na detection in the precursor layer and absorber film may be related to the morphology of the good quality Mo layer that helped in out-diffusion of a controlled amount of Na from the glass substrate. Although there was no evidence to specify the amount or concentration of Na detected in the samples (as MiniSIMS was not calibrated for this element), it confirmed the presence of Na in the samples. The energy band gap values (in the range 0.90-0.94 eV) and photo activeness of these absorber films indicated that the thinner absorber films were useful to incorporate in solar cell structure (particularly lower cells in a multijunction solar device).

This work demonstrated that there was a potential to reduce the cost of production of absorber films by minimising material usage due to reduction in the precursor layer thickness and corresponding absorber CIS thin films.

The main conclusion that can be drawn from the results of the CIS thin films produced from thinner absorber layers is that the absorber films were of good quality and useful to add as absorbers in solar cell structures.

5.3 CuInSe₂ Thin Film Solar Cells

In this section, selected CIS absorber layers, with different thicknesses (samples B, D and F), were incorporated into solar cells. Thin film CIS solar cells were fabricated in substrate configuration of structure Ni-Al/ITO/i-ZnO/CdS/CuInSe₂/Mo/SLG.

5.3.1 Fabrication of CuInSe₂ thin film solar cells

In the process of fabrication of CIS solar cells, prior to CdS deposition, the absorber layer was treated with a KCN solution in order to remove Cu-Se phases (Cu_xSe, Cu_{2-x}Se) (section 4.1.4). The cadmium sulphide (CdS) layer was deposited by a chemical bath deposition (CBD) method to form the heterojunction with the CIS absorber layer. CdS thin films were deposited on selected photoactive CIS absorbers on Mo-coated glass substrates of size approximately 38×26 mm² (section 4.1.5). The deposition period was 6 min to yield the CdS layer of estimated thickness approximately 100 nm. Immediately after the deposition the sample was removed from the bath and rinsed with DI water in order to remove excess CdS particles from the deposited surface.

The solar cells were prepared by depositing intrinsic ZnO (i-ZnO) layer and indium tin oxide (ITO) window layer which acts as a transparent conductive oxide (TCO) layer using a metallic mask (Fig. 5.27). The ITO layer was approximately 280 nm thick with resistivity $1.4 \times 10^{-4} \Omega \cdot \text{cm}^2$. The graph of percentage transmittance (T%) versus wavelength for CdS, i-ZnO and ITO layers is shown in figure C in the appendix I section. The buffer and window layers transmitted 85-90% of light in the

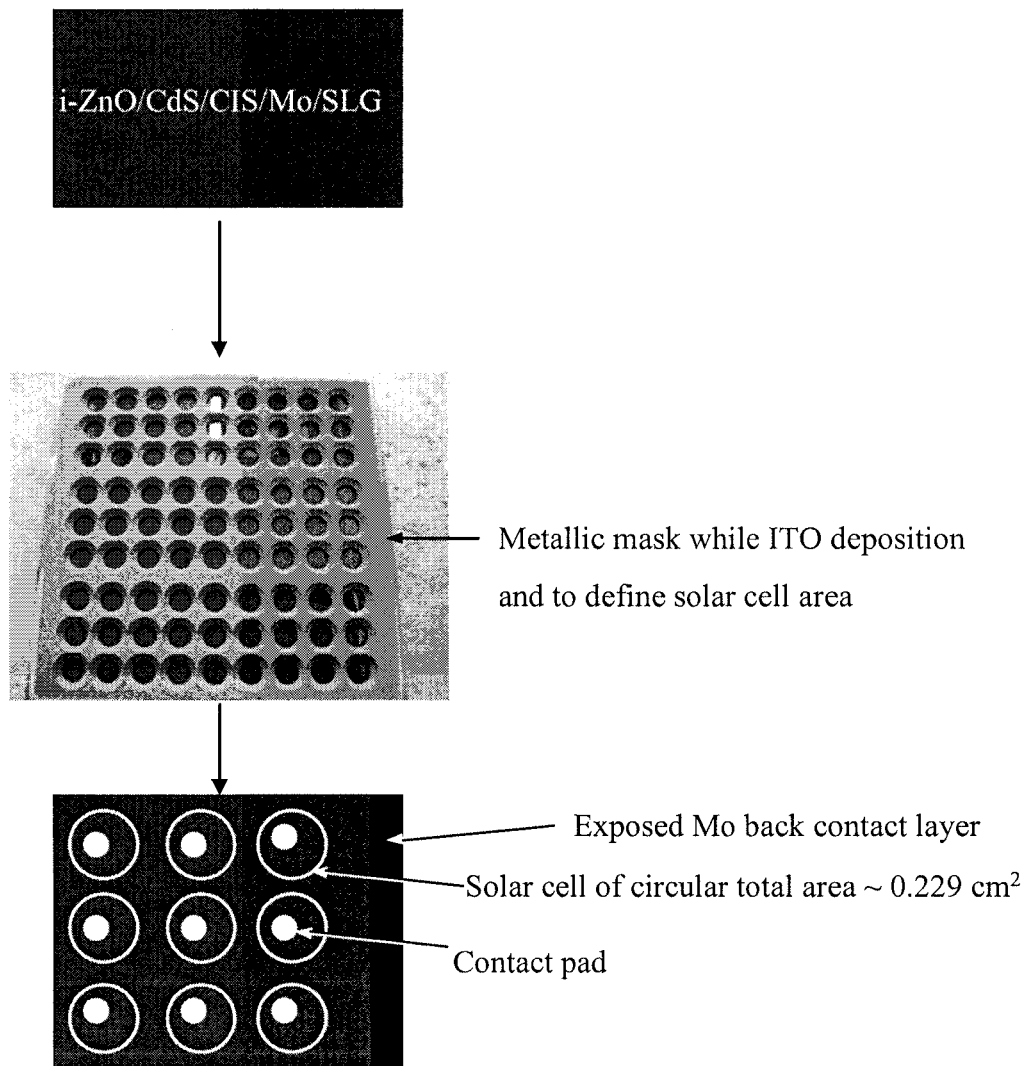
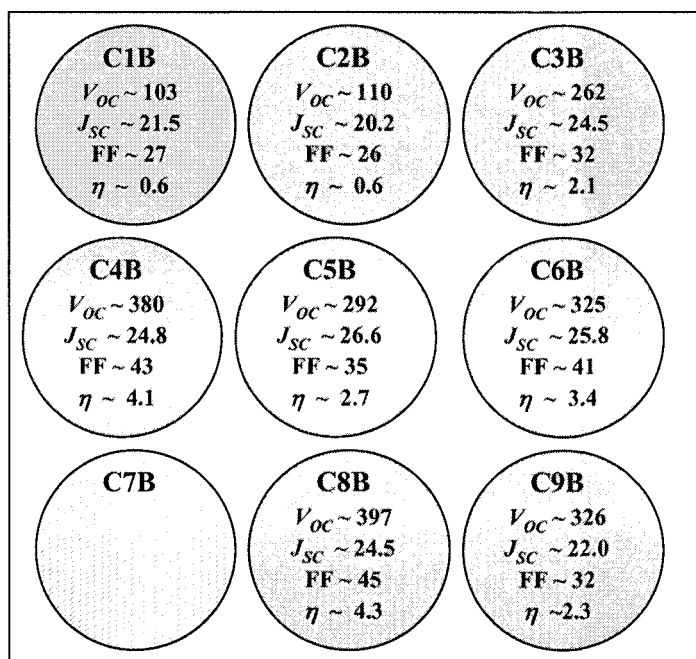


Figure 5.27 Photograph shows the final stages of CIS fabrication process (not to scale).

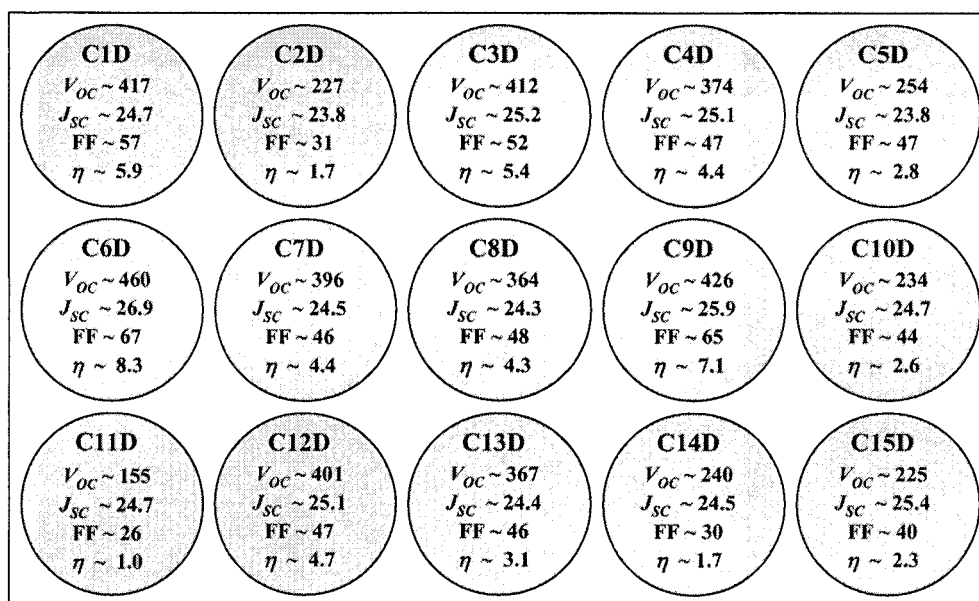
range 400-1200 nm. The energy band gap of ITO was found to be 3.4 eV (Fig. D in appendix I). The front contact layer was deposited using RF sputtering. The fabrication of the solar cell was completed with circular cell of diameter ~ 0.54 cm and area 0.229 cm². The Ni-Al front contacts were also sputter deposited on the fabricated solar cell which had structure ITO/i-ZnO/CdS/CIS/Mo/SLG by using a separate metallic mask (not shown in figure) with circular holes of diameter 2 mm. The Ni-Al metal front contact covered an area approximately 0.0314 cm² which was approximately 14% of the total cell area.

5.3.2 *J-V* characteristics of solar cells made from thinner absorber films B and D

Illuminated *J-V* characteristics of the CIS solar cells fabricated using a 500 nm (sample B) and 900 nm (sample D) absorber films were measured under simulated (AM1.5, 100 mW/cm²) conditions at 25°C. All cells (C1B-C9B of sample B and C1D-C15D of sample D as shown in Fig. 5.28) were measured for the cell parameters such as open circuit voltage (V_{OC}), short circuit current density (J_{SC}), fill factor (FF) and the cell conversion efficiency (η). The solar cells C8B and C6D of the sample B and D were found to have highest output values, respectively. According to calculations from the *J-V* characteristics (Fig. 5.29) of these cells, output parameters of cell B and D were obtained as η of 4.3% and 8.2%, FF values of 46% and 67%, V_{OC} of 398 mV and 460 mV and J_{SC} of 23.8 mA/cm² and 26.9 mA/cm², respectively. In sample D, the solar cell C9D was also found to have high output parameters- η of 7.1%, V_{OC} of 426 mV, J_{SC} of 25.9 mA/cm² and FF of 65%.



Sample B



Sample D

V_{oc} in mV
 J_{sc} in mA/cm²
 FF in %
 η in %

Figure 5.28 Distributions of output parameters (V_{oc} , J_{sc} , FF and η) in the CIS thin film solar cells of the samples B and D with cell location (not to scale). (The shaded area of the cell C7B indicates non-working cell).

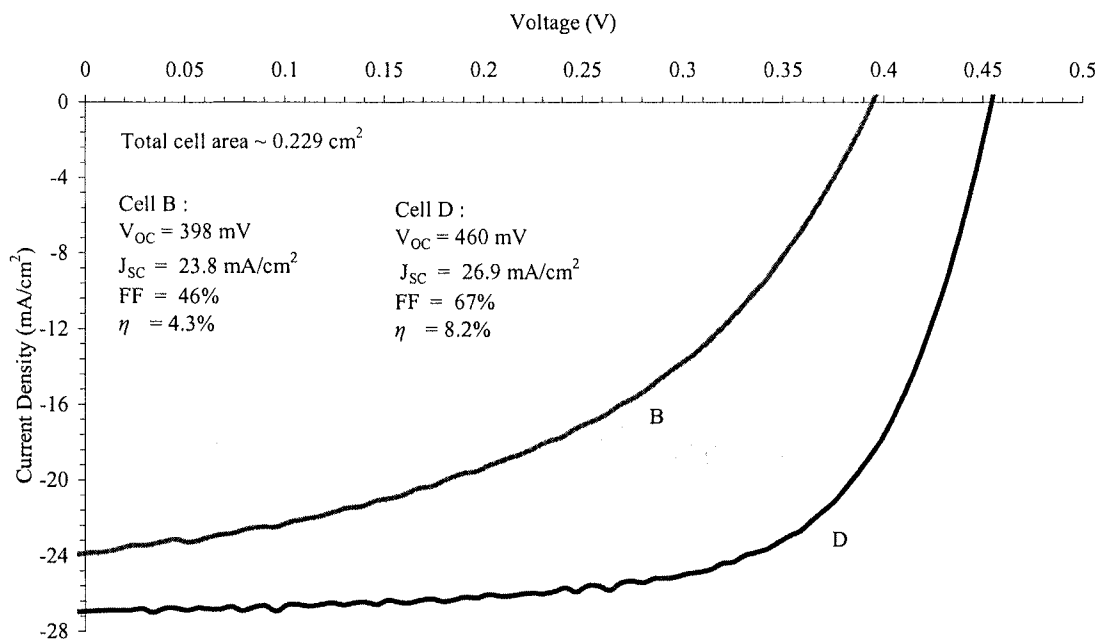


Figure 5.29 *J-V* characteristics for solar cells included absorber layers B (500 nm) and D (900 nm) of different thickness.

The cell performance over the entire substrate (dimension approximately 76×26 mm) was not uniform. It should be noted that the cell of sample F did not have the same optimised CdS buffer layer as cell of samples B and D and therefore was not included in the J - V plots. However the highest cell (total area ~ 0.229 cm²) conversion efficiency using absorber film of the sample F was calculated as 5.1%, FF of 51%, V_{OC} of 378 mV and J_{SC} of 26.1 mA/cm².

5.3.3 Incident photon to photocurrent conversion efficiency

measurement

The graph of incident photon-to-photocurrent conversion efficiency (IPCE) as a function of wavelength for the cells is shown in figure 5.30. The sample F spectrum demonstrated a maximum IPCE of 80% as compared to 66% for the sample B. The IPCE spectrum of the sample B has shown a less steep drop-off at longer wavelength. The energy band gaps of the samples B and F were calculated as 0.96 and 0.99 eV, respectively. These band gap values were slightly different than those (0.90-0.94 eV) values estimated earlier from optical spectral measurements. (The IPCE measurements were part of collaboration with Bath University and measured there by Bath researchers).

5.3.4 Discussion

In this section the characterisation using J - V and IPCE provided an insight into CIS cells made using thin absorber layers.

Variations in the solar cell output parameters (V_{OC} , J_{SC} , FF and η) were noticed from one cell to another fabricated on the same absorber layer on the Mo-

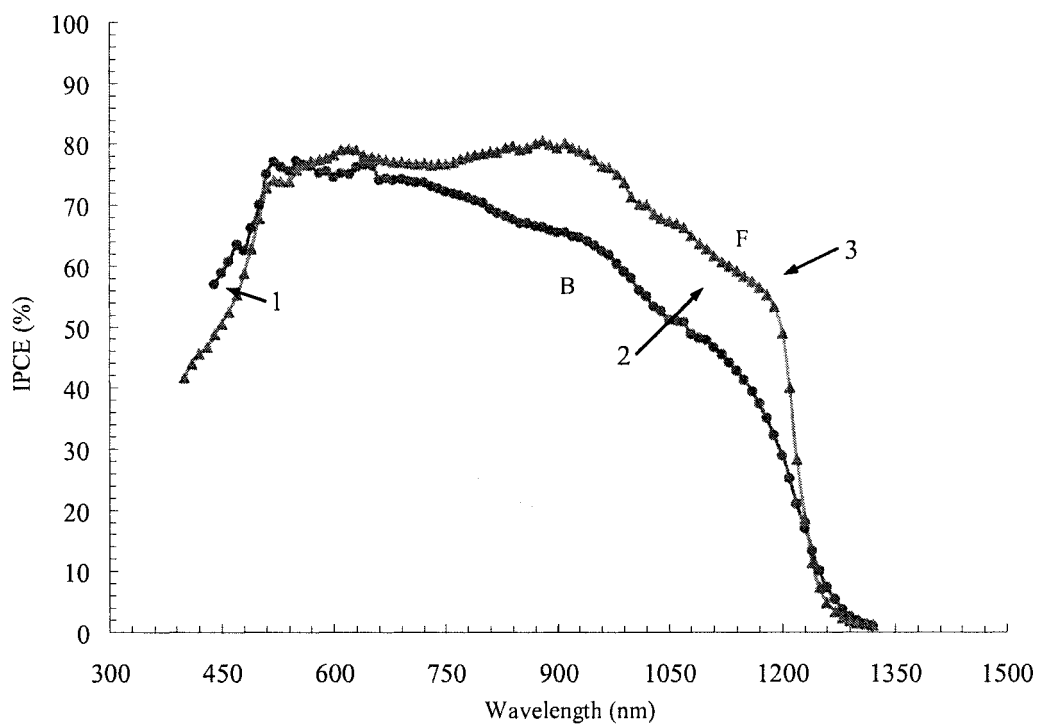


Figure 5.30 IPCE spectra for solar cells of the absorbers B (500 nm) and F (1600 nm). (Numbers with arrows are showing regions of possible losses in IPCE).

coated substrate. This could be due to a number of possible reasons such as non-uniform CIS film, pinholes in some regions, non-conformal CdS layer on the absorber and defects in the layers. The non-uniformity over the absorber layer was indicated by variations in the cell parameters. These output results imply that there was significant variation in uniformity and reproducibility of the absorber layer. However it was clear that all cells were giving output which indicates that the absorber layer of half or more than half the slide (area $\sim 76 \times 26 \text{ mm}^2$) was photoactive. The solar cell efficiencies of 4.3% and 8.2% achieved using these thinner absorbers of thicknesses 500 nm and 900 nm, respectively, were reasonably higher and also it showed steadily increasing efficiency with the thickness of the absorber layers. The performance of cell B was limited mainly due to a very thin absorber layer that caused incomplete photon absorption. The contact resistance and physical properties of the absorber and buffer layer contributes losses in the form of R_S and R_{Sh} , respectively. The R_S and R_{Sh} values (calculated as explained in section 4.3.1) for the cell B are $4.8 \Omega \cdot \text{cm}^2$ and $66 \Omega \cdot \text{cm}^2$ and for the cell D are $2.7 \Omega \cdot \text{cm}^2$ and $363 \Omega \cdot \text{cm}^2$, respectively. In ideal conditions, R_S must be less than $0.5 \Omega \cdot \text{cm}^2$ and R_{Sh} must be at least $M\Omega \cdot \text{cm}^2$ of the solar cell area [160].

Referring to the IPCE spectra (Fig. 5.30) for the thinner CIS samples with regions displayed by numbers, the optical absorption losses (explained by referring to a paper presented on device measurements and analysis by Hegedus and Shafarman [184]) in several layers in the solar cell include:

Region 1: Loss in this region (λ in the range 450-520 nm) could be due to absorption in the CdS buffer layer. The energy band gap of CdS is 2.4 eV and this causes loss in quantum efficiency for $\lambda < 517 \text{ nm}$ (for sample F). This loss increases with the CdS

layer thickness. The electron-hole pairs generated in the buffer layer are not collected. However, the solar cells B and F were fabricated for different CdS deposition conditions. Moreover, the cell F did not have the same optimised buffer layer. In addition structural defects, such as pin holes and non-uniformities in the buffer layer, tend to increase absorption losses in both types of solar cell.

Region 2: The larger mismatch between the spectra for cells B and F is probably due to incomplete collection of photo-generated carriers in the absorber layer. This is attributed to the difference in the thicknesses of B and F absorbers, 500 nm and 1600 nm, respectively.

Region 3: Incomplete absorption in the absorber layer close to the CIS bandgap. The solar device B has an ultra thin absorber layer which is thinner than $1/\alpha$, (where α is the absorption coefficient just above the energy band gap). This significant loss could be minimised by employing bandgap grading or light trapping mechanisms.

Unfortunately, there was no IPCE measurement carried out on sample D. However, the buffer layer mainly affects V_{OC} and FF and therefore inclusion of cell F along with cell B in figure 5.29 was valid. Strong loss in carrier generation is seen as indicated by lower IPCE.

In summary, the solar cells (total cell area, 0.229 cm^2) were fabricated using thinner absorber of thicknesses 500 nm and 900 nm which yielded highest efficiencies of 4.3% and 8.2%, FF values of 46% and 67%, V_{OC} of 398 mV and 460 mV and J_{SC} of 23.8 mA/cm^2 and 26.9 mA/cm^2 , respectively. IPCE of the cell B indicated that the significant loss in the output performance of the latter cell may be due to incomplete photon absorption in ultra thin absorber film.

AbuShama *et al.* reported NREL's highest efficiency CIS solar cells (confirmed total area = 0.403 cm^2). They obtained a 15.0% efficient CIS solar cell

with absorber thickness 2.7 μm [81]. In this thesis, the solar cell D has measured $\sim 94\%$ of V_{OC} (491 mV), $\sim 66\%$ of J_{SC} (40.58 mA/cm²) and $\sim 90\%$ of FF (75.15%) of this most efficient reported cell. It means less than 40% of NREL's absorber thickness resulted in $\sim 55\%$ cell efficiency of their highest performing CIS solar cell. In the I - V measurements described in this thesis, it was observed that a shadow from the tip of the measuring probe in contact with the cell (Fig. 5.31) covered the cell area between in the range 15-20%. The highest efficiency of 8.2% was underestimated by substituting the total cell area of 0.229 cm² in the calculations. Therefore by considering shadowing losses due to probe and contact grid the active area will be in the range between ~ 0.182 - 0.193 cm² and efficiency will be in the range between 9.7-10.3%.

Several leading research groups around the World demonstrated higher solar cell efficiencies using thinner (thickness ≤ 1 μm) CIGS absorber films. The comparisons of the output parameters of the highest efficient CIS and CIGS of different thicknesses reported by NREL and a Swedish group at Uppsala University with those described in this thesis is listed in table 5.9. Ramanathan *et al.* reported a 17.1% efficient cell which was fabricated using a 1 μm -thick CIGS absorber film [185]. They improved the absorber film structure by employing band gap grading. They also demonstrated lower values of efficiencies of 12.6% and 9.1% for solar cells with absorbers of thicknesses 0.6 and 0.4 μm , respectively. The Swedish group at the Uppsala University fabricated devices of efficiencies 15.0% and 12.1% using CIGS films of thicknesses 1.0 μm and 0.6 μm , respectively [94]. In the device fabrications, they used modified CIGS films by a creating back-surface field (BSF) of a thin layer of CuGaSe₂ at the bottom of the films. Figure 5.32 shows a comparison between J - V characteristics (normalised current density) of the high

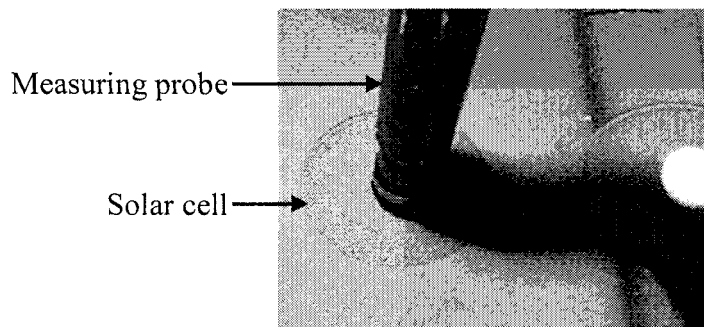


Figure 5.31 Photograph shows shadowing loss due to the measuring probe in contact with solar cell in the I - V measurement. (Photo courtesy - Dr. I. Forbes).

Material (CIS or CIGS)	Film thick- ness (μm)	E_g (eV)	V_{oc} (mV)	J_{sc} (mA/cm^2)	FF (%)	Solar cell/device area (cm^2)	η (%)	Reference
CIS	2.7	-	491	40.58	75.15	0.403 [Total area]	15.0	[81]
CIS*	2.5	-	513	40.4	71.6	0.262 [Active area]	14.8	[86]
CIS	-	1.04	515	41.2	72.6	0.380 [Total area]	15.4	[9, 24]
CIGS	1.0	-	678	31.9	79.2	0.409 [Device area]	17.1	[185]
CIGS	1.0		690	28.8	75.5	0.5 [Total area]	15.0	[94]
CIGS	2.2	-	690	35.5	81.2	0.419 [Device area]	19.9	[27]
CIS***	0.9	0.94	460	26.9	67	0.229 [Total cell area]	8.2 (9.7- 10.3%)**	In this thesis

* Ga ~ 0.1 at.% was added throughout the thickness of the absorber films.

** Efficiency was calculated for the estimated active cell area (0.182-0.193 cm^2) after considering shadowing loss.

*** The solar cell design (grid coverage, resistance of metal and use of ARC) was not optimised.

Table 5.9 Comparison of the solar cell parameters reported by NREL and the University of Uppsala groups with those described in this thesis.

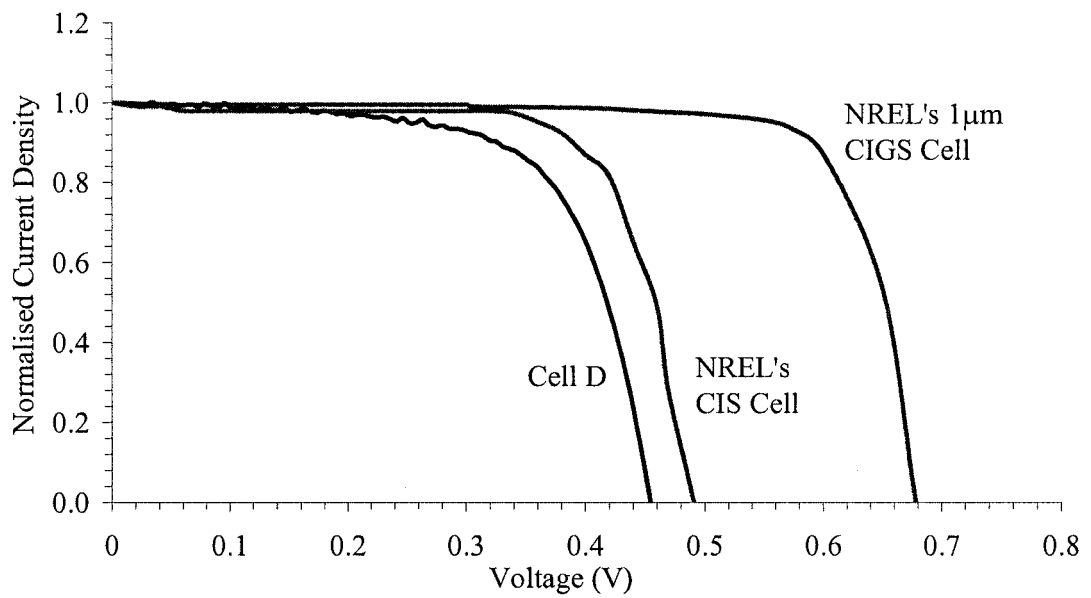


Figure 5.32 Comparison between J - V characteristics of the solar cell fabricated in this work (cell D) and NREL's highest efficient CIS and CIGS solar cells with 1 μm -thick CIGS absorber layer (Reproduce data from [24] and [185]).

efficiency solar cell produced in this work (CIS-based solar cell D), NREL's highest efficient CIS cell and high efficiency CIGS solar cell with 1 μm CIGS absorber layer. According to table 5.9 and figure 5.32, the efficiency of over 10% of the solar cell with 0.9 μm -thick CIS absorber film has been considered as a promising output. The reduction in absorber thickness is one of the strategies to minimise absorber material cost and hence production cost of the solar cell. This method of cost reduction creates many challenges. One of these is the decrease in the amount of light absorption which is also applicable to the solar cells presented in this section and also found in the literature [94]. The poor values of J_{SC} calculated in the solar cells B and D could be attributed to incomplete light absorption due to reduction in thickness. This type of problem has been addressed by both NREL and the Uppsala University groups in their high performing CIGS devices with thinner absorber films. As mentioned earlier they increased the light absorption capacity of the films by employing band gap grading by grading the Ga through the thickness of CIGS films and by introducing the BSF of a very thin CGS layer (50 nm) near the CIGS/Mo interface, respectively [94, 185]. This can be applied to CIS absorber film by employing band gap grading in the thickness of the absorber. However in the two stage method (selenisation of the sputter deposited precursor layers, sections 4.1.2 and 4.1.3) the grading will only be possible during sputter deposition of precursor layers (Cu-In). Other methods to increase J_{SC} include light trapping mechanisms and reducing reflection of the light (by depositing an anti-reflection coating (ARC) of MgF_2 as there was no ARC in these cells). Avoiding contact shadowing due to measuring probe arrangement could be possible to minimise the losses in the measurements. The introduction of a BSF causes shortening of diffusion length and reducing recombination at the back contact will improve J_{SC} values [94].

In this work, the influence of the metallic Cu-In precursor layer thicknesses on the properties of thinner CIS thin films demonstrated that reasonably high performing solar cells can be produced. It has provided knowledge to identify the importance of absorber thickness reduction in relation to the cost-effective CIS solar cells production. In CIS Ga, which is less abundant and therefore also expensive, was not added. In addition the cost of production was further reduced by minimising usage of In which is also another highly expensive material. In this work although energy band gap grading and BSF approaches were not implemented, the sputtering might have inherently helped in formation of graded (Cu or In) precursor layers. Incorporation of thinner CIS absorbers (produced using precursor layers of thickness 240 nm) along with the optimised window layer yielded highest cell (total area $\approx 0.229 \text{ cm}^2$) efficiency of over 8% with approximately 900 nm-thick absorber film. These investigations of reducing precursor layers and corresponding absorber thickness will provide a lower energy band gap cell that will be suitable for the bottom cell in a multijunction solar device. The good quality ternary CIS absorber film provided a baseline for further development and investigation of CIAS absorber layers and their processing.

5.4 Thicker CuIn_{1-x}Al_xSe₂ Absorber Thin Films

The purpose of the work described in this section was to investigate the structural and physical properties of the Cu-In-Al precursor layers and CIAS thin films prepared by the selenisation of these layers. The results obtained from the Cu-In precursor layers and CIS thin films provided a baseline to establish process settings and conditions for preparation of CIAS thin films.

5.4.1 The Cu-In-Al precursor layers

In this subsection, the investigations of compositional and structural properties of the binary Al-In and ternary Cu-In-Al metallic precursor layers are presented. These precursor layers were deposited using sputtering technique using a Kurt J Lesker (KJL) system. The investigations of Cu-In precursor layers were presented in the earlier subsection that provided understanding for sputtering deposition of the layers. Hence information from Cu-In and Al-In layers was useful in depositing the Cu-In-Al and Cu-Al precursor layers on the Mo-coated SLG substrates.

5.4.1.1 Deposition of binary Al-In compounds

Four samples of varying Al-In composition were sputter deposited in a KJL system. The elemental composition of Al and In in the layers in at.% is shown in table 5.10 and was achieved by varying the RF power applied to the Al target and the direct current (DC) power applied to the In metal target. The thickness of the metallic Al-In layers was in the range 0.8-1.2 μm , measured by using a Talystep.

The XRD spectra for all the different Al-In samples are shown in figure 5.33.

Sample (Actual sample ID)	Target power ratio (Al/In)	Al (at.%)	In (at.%)	Al/In
Alln-1 (K154H)	0.78	10	90	0.11
Alln-2 (K150E)	2.89	40	60	0.67
Alln-3 (K151B)	5.00	60	40	1.50
Alln-4 (K178B)	11.25	80	20	4.00

Table 5.10 The Al-In samples with compositions in at.% measured by EDS.

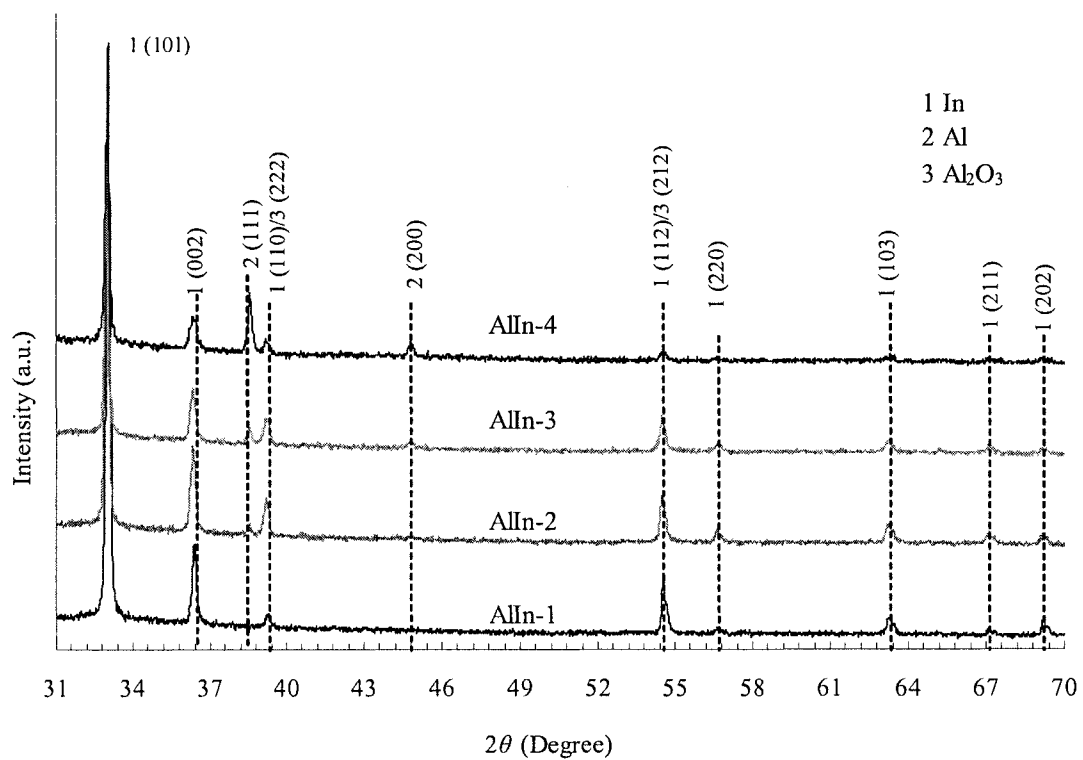


Figure 5.33 XRD spectra of sputter deposited Al-In layers on the glass substrates of different compositions (as given in table 5.10).

It can be seen that the prominent peak of In was detected in all types of samples at the position 33° on 2θ scale. In addition the Al peak was detected and its occurrence depends on the Al/In compositional ratio. For $\text{Al/In} \geq 0.67$, the Al peak intensity is found to be increased. The XRD scan (in the range 31° - 70°) of all samples showed no peak related to binary Al-In phases. The oxidised Al_2O_3 phase (at positions 39.3° , 54.7° and 56.82°) was observed and attributed to oxide formation in exposure to atmosphere. However, there is some uncertainty about these peaks as to whether they are due to Al_2O_3 or In.

Compositional analyses by EDS of these samples (AlIn-1 to AlIn-4) showed that they contained oxygen. The content varied between 5-10 at.% depending on the Al content of the layer and sample exposure to air. The EDS spectrum of one of the samples (AlIn-3) is shown in figure 5.35 (a).

The surface SEM images (Fig. 5.34) of the samples revealed a decrease in the number of In islands with increasing Al concentration. One of these samples AlIn-3 was studied in more detail by EDS. The EDS beam of circular scan area of diameter $2\ \mu\text{m}$ scanned on the islands and detected very In-rich composition (In ~ 90 at.%) compared to the smooth area in between the islands (In ~ 10 at.%). In the cross-sectional image (Fig. 5.35 (b)) of the sample AlIn-3, the height of these droplets was found to be of average $2\ \mu\text{m}$ which is well above the penetration depth (1 - $1.5\ \mu\text{m}$) of the electron beam used for the EDS analyses.

5.4.1.2 First set of Cu-In-Al precursor layers

The compositions of sputter deposited Cu-In-Al precursor layers on a Mo-coated glass substrate are tabulated in table 5.11. The original sample names are listed in an Appendix II. A $5\ \text{nm}$ Cu seed layer was deposited before depositing the

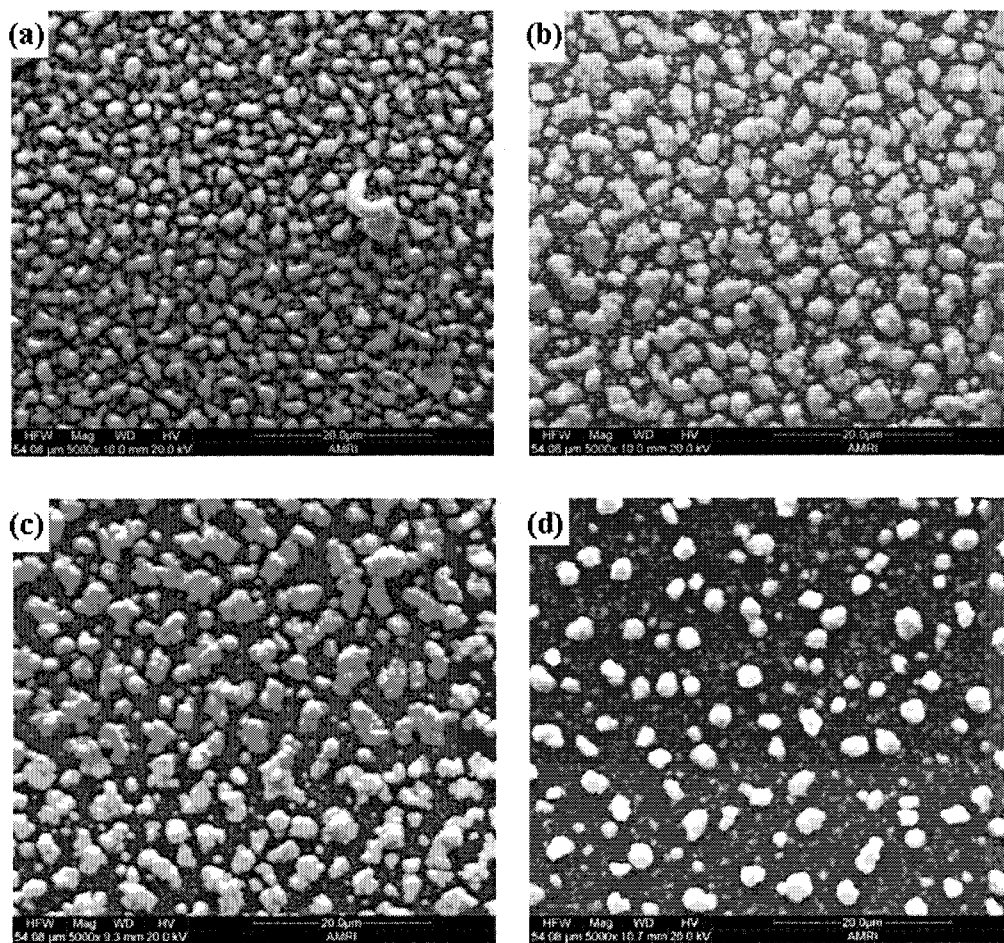


Figure 5.34 SEM images of surface morphology of sputter deposited Al-In layers (a) AlIn-1, (b) AlIn-2, (c) AlIn-3 and (d) AlIn-4.

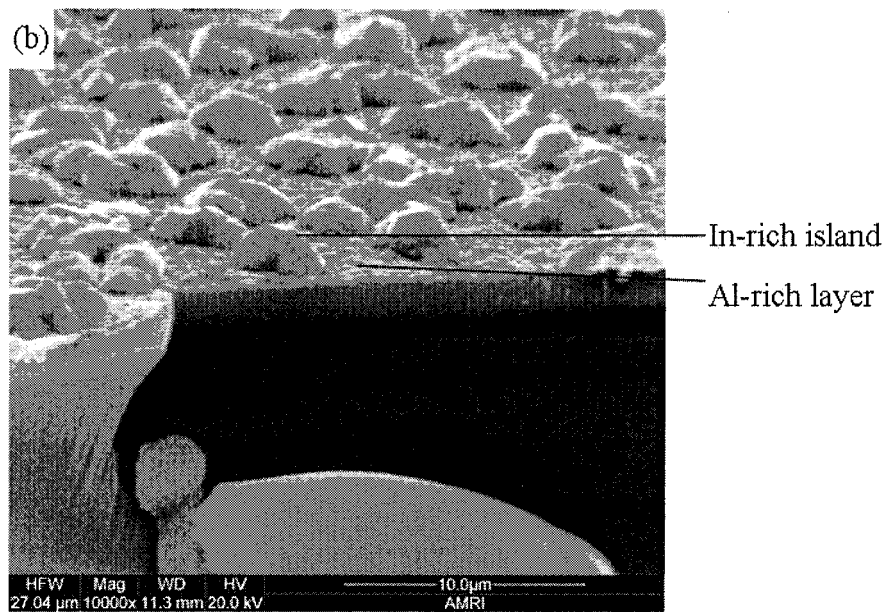
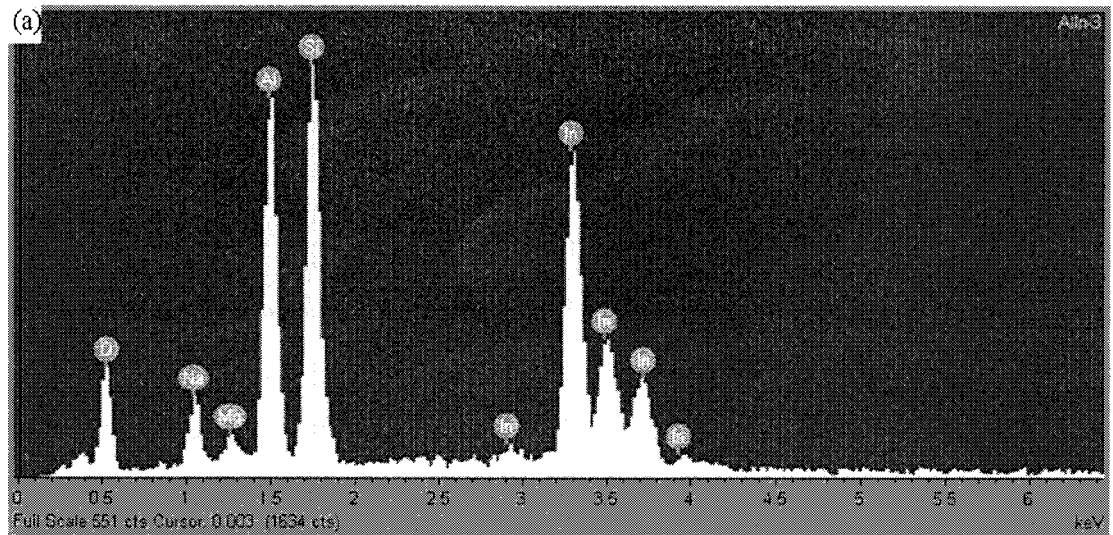


Figure 5.35 (a) The EDS spectrum and (b) the SEM picture of the cross-sectional view of the sample AlIn-3 on the SLG substrate.

Sample	Cu, In, Al Targets' Power Ratio		Precursor Composition					Precursor layer Thickness (nm)
	Cu/(In+Al)	Al/(Al+In)	Cu (at.%)	In (at.%)	Al (at.%)	[m = Cu/(In+Al)]	[n = Al/(In+Al)]	
KJL-A	0.50	-	54	46	-	1.17	-	900
KJL-B	0.62	0.38	58	35	7	1.38	0.17	2100
KJL-C	0.28	0.45	48	41	11	0.92	0.21	1000
KJL-D	0.25	0.84	44	18	38	0.78	0.68	1300
KJL-E	0.23	0.94	42	9	49	0.72	0.84	900
KJL-F	0.25	1.00	39	-	61	0.64	1.00	500

Table 5.11 EDS compositional analyses and thicknesses of the Cu-In-Al precursor layers with metal target power settings.

actual precursor layer. This was a necessary step to achieve good adhesion of the precursor layer on the SLG and Mo-coated SLG substrate. The XRD pattern for all precursor layers in conjunction with that of the Cu-In sample is shown in figure 5.36. Peaks of inter-metallic binary phases namely $\text{Cu}_{11}\text{In}_9$, AlCu_3 , AlCu_4 , Cu_2In , CuIn_2 and CuIn were detected. Information about XRD phases in the precursor layers with position of the peak on 2θ scale are given in table 5.12. The phases formed depends on the $[\text{Cu}/(\text{In}+\text{Al})]$ ratio. There was no binary phase of Al-In detected. The Cu-Al precursor layer contains mainly the CuAl_4 phase due to Al-rich content.

5.4.2 Selenisation of sputter deposited Cu-In-Al precursor layers

The selenisation processes were carried out on the Cu-In-Al precursor layers as listed in table 5.11. After initial trials, the selenisation steps were followed similarly to that for CIS production using Se capping except that the temperature of selenisation was raised to 550°C .

Figure 5.37 shows XRD patterns of selenised films prepared from the precursor layers of six different samples (Table 5.11). Information about XRD phases of the precursor layers and thin films with position of the peak on 2θ scale in degree are given in table 5.12. The absorber film KJL-A contained the most intense CIS (112) peak (at 26.7°) whereas the sample KJL-F has no such reflection. Each spectrum contained binary phases. Among those there are some binary phases with Al, for instance Cu_9Al_4 , Al_2O_3 and Al_2Se_3 . The main point of interest was the CIS (112) reflection which was used to monitor the effect of addition of Al on the position of this prominent peak. There is a shift in peak position of the sample KJL-B and KJL-C with respect to sample KJL-A toward higher values on 2θ scale as shown in figure 5.38. This was attributed to the Al content in the converted film but no PDF

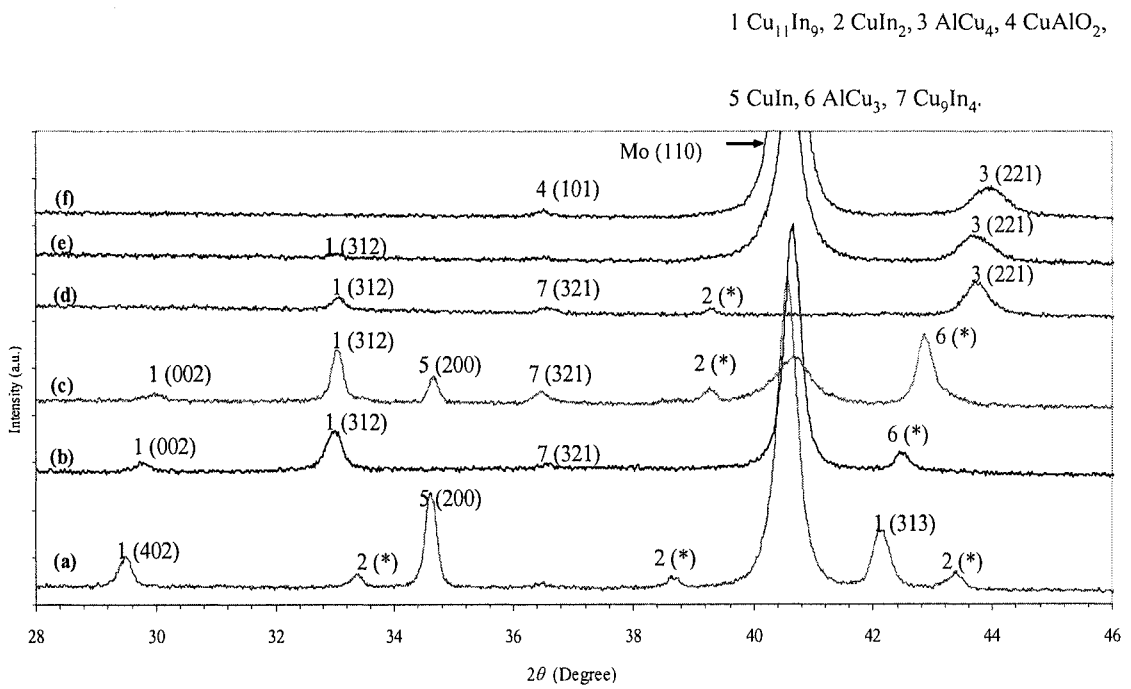


Figure 5.36 XRD patterns of the Cu-In-Al precursor layers (a) KJL-A, (b) KJL-B, (c) KJL-C, (d) KJL-D, (e) KJL-E and (f) KJL-F. [There is no *hkl* information available for the peaks labelled as (*) in PDF database software].

Sample	XRD phases detected in the precursor layers (position on 2θ scale in degree)	XRD phases detected in the absorber films (position on 2θ scale in degree)
KJL-A	$\text{Cu}_{11}\text{In}_9$ (29.5°, 33.5° and 42.2°), CuIn (34.6°) and CuIn_2 (38.7° and 43.4°).	In_xSe_y (24.2°, 36.7° and 48.0°) and CuInSe_2 (26.7°, 35.6° and 42.1°, 44.4° and 52.5°).
KJL-B	$\text{Cu}_{11}\text{In}_9$ (29.5° and 33.1°), Cu_9In_4 (36.7°) and AlCu_3 (42.5°).	In_xSe_y (24.2° and 47.4°), CuInSe_2 (26.7°, 35.7°, 42.5° and 52.5°), Cu(In,Al)Se_2 related phase (27.9°), InSe (28.6°), Al_2Se_3 (29.7°, 34.5°) and CuSe_2 (33.0° and 49.6°).
KJL-C	$\text{Cu}_{11}\text{In}_9$ (30.1° and 33.1°), CuIn (34.7°), Cu_9In_4 (36.7°), CuIn_2 (39.3°), and AlCu_3 (42.9°).	In_xSe_y (24.3°), CuInSe_2 (27.0°, 42.5° and 53.1°), Cu(In,Al)Se_2 related phase (28.2°), InSe (29.2°) and Al_2Se_3 (29.7°).
KJL-D	$\text{Cu}_{11}\text{In}_9$ (33.1°), Cu_9In_4 (36.7°), CuIn_2 (39.4°), and AlCu_4 (43.8°).	CuInSe_2 (27.0°, 36.7° and 44.4°), Cu(In,Al)Se_2 related phase (27.7°), InSe (28.5°) and CuSe_2 (33.1°).
KJL-E	$\text{Cu}_{11}\text{In}_9$ (33.1°) and AlCu_4 (43.7°).	In_xSe_y (23.0° and 47.5°), CuInSe_2 (26.7° and 44.4°), Al_2O_3 (25.2°), InSe (28.5°) and CuSe_2 (33.2°).
KJL-F	CuAlO_2 (36.6°) and AlCu_4 (44.1°).	Al_2O_3 (25.3°), CuSe_2 (28.5°), CuAlO_2 (36.52°) and Cu_9Al_4 (44.3°).

Table 5.12 XRD phases detected for the precursor layers and thin films of samples KJL-A to KJL-F.

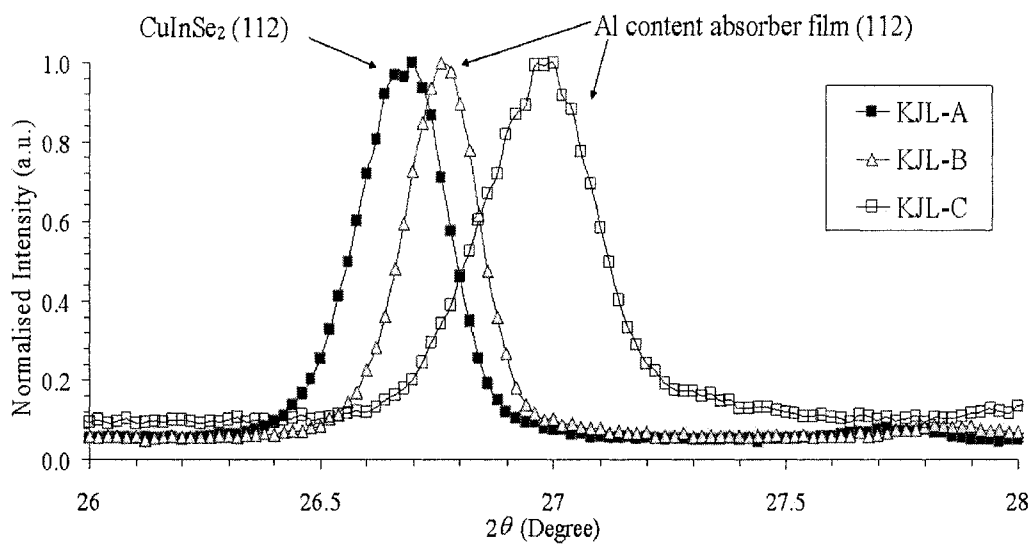


Figure 5.38 XRD of the main reflection (112) of CIS (no Al) and Al content absorber films.

file relating to CIAS phase was found in the ICDD database. However the peak position related to this phase was identified by referring to the literature [30]. Other samples KJL-D, KJL-E and KJL-F have no such prominent (112) reflections. Vegard's law was applicable to some extent to samples KJL-A, KJL-B and KJL-C. But no evidence suggested that there was complete mixing of Al in the absorber layer.

It was not possible to carry out EDS compositional analyses on the films selenised from precursor layers containing Al due to the proximity of the Al-K and the Se-L lines which can not be resolved (Instrument limitation).

Figures 5.39 and 5.40 show surface and cross-sectional SEM images of the absorber films according to variations in concentration $n = \text{Al}/(\text{Al}+\text{In})$ in the precursor layers in the range 0 to 1 (Table 5.11). The CIS absorber layer of sample KJL-A (Fig. 5.39 (a)) has a grain size of $1.9 \mu\text{m}$ (equal to the thickness) with large grains revealed in the surface image. The surface topology and topography of the sample KJL-B (Fig. 5.39 (b)) shows large grains of irregular shape however, the cross-sectional image clearly reveals a bilayer structure in which each layer was approximately $2 \mu\text{m}$ -thick. The surface and cross-sectional morphology (Fig. 5.39 (c)) of sample KJL-C shows a large grain size of approximately $2 \mu\text{m}$ with a close packed structure. SEM images (Fig. 5.40 (d) and (e)) of samples KJL-D and KJL-E reveals large disordered features on the Mo back contact. Sample KJL-F which consisted only of Cu-Al metallic precursor layers, was not converted into a CAS absorber structure. After selenisation, nothing happened on this sample as it was found with a similar shiny surface structure to the precursor layer. SEM images (Fig. 5.40 (f)) of this sample shows only Mo-coated glass with a precursor layer containing some material (probably of Se) on the film surface. Similar results were

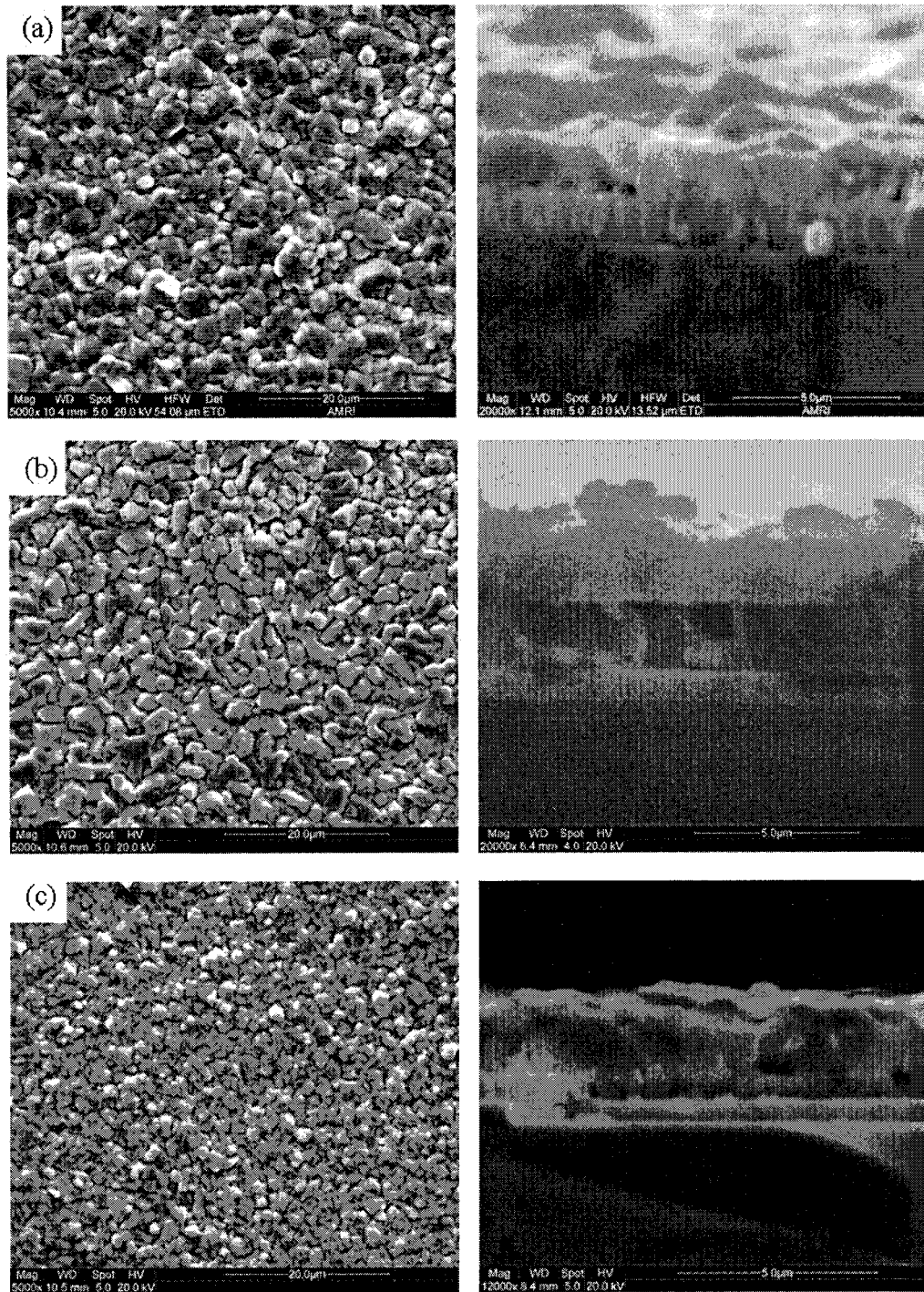


Figure 5.39 SEM surface (left) and cross-sectional (right) images of films selenised on Mo-coated SLG substrates; (a) KJL-A, (b) KJL-B and (c) KJL-C.

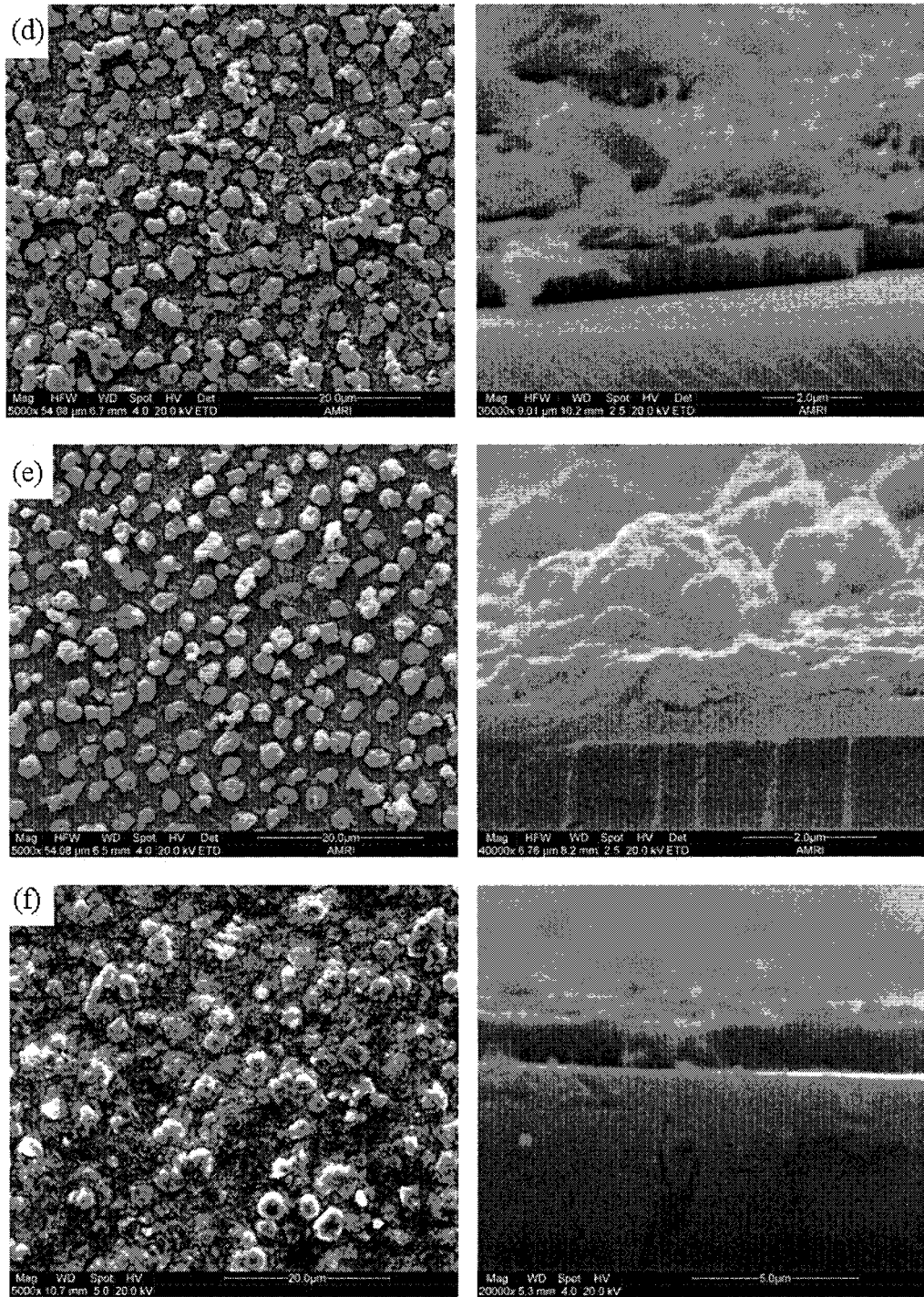


Figure 5.40 SEM surface (left) and cross-sectional (right) images of films selenised on Mo-coated SLG substrates; (d) KJL-D, (e) KJL-E and (f) KJL-F.

obtained from the selenisations on the Cu-Al samples from the same batch of KJL-F for the temperatures slightly higher than 550°C (560 and 570°C). The melting point of the SLG has prevented selenisation higher than a temperature of 570°.

The converted film of the sample KJL-C of original sample name N66D with $n = 0.21$ was found to be photoactive. MiniSIMS analysis was performed on this sample to investigate distribution of the metals In, Al and Na and Se with depth. The output of the MiniSIMS depth profile is shown in figure 5.41. The result shows an almost horizontal trace of $^{113}\text{In}^+$ profile which is uniform throughout the thickness of the absorber layer. Aluminium was not uniformly distributed throughout the absorber film but the concentration is higher at the surface and then decreased in the central part of the film. The Al profile shows an increase in the signal near the CIAS/Mo interface and indicates the accumulation or segregation of Al at the bottom of the layer. The Na signal was attributed to out-diffusion from the glass and exhibited a similar profile to that of Al. The Se ($^{80}\text{Se}^-$) signal is uniform with depth and implies that diffusion was complete throughout the absorber layer. The In was uniformly distributed in the absorber layer.

Sample KJL-C (N66D) was used as an absorber layer in fabrication of the solar cells.

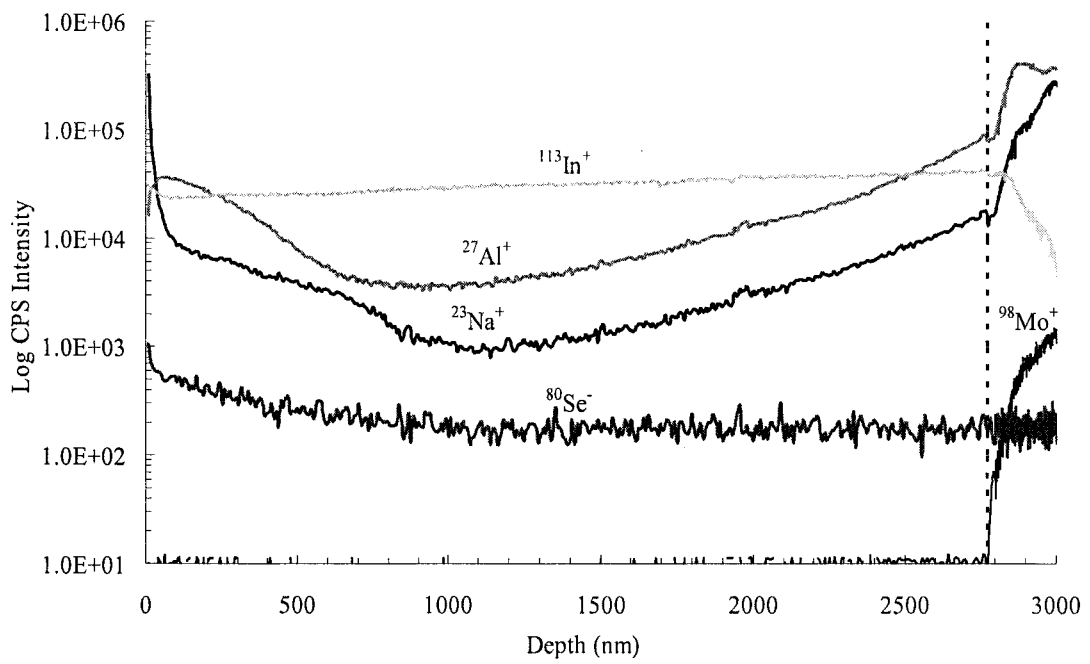


Figure 5.41 MiniSIMS depth profile of the absorber film prepared from the Cu-In-Al precursor layer of the sample KJL-C (N66D) (The dashed line indicates interface between the absorber film and the back contact Mo layer).

5.4.3 Fabrication of solar cells based on sample KJL-C (N66D) absorber layers

Films selenised from the precursor layers of the sample KJL-C (N66D) were found to be photoactive and well adhered to the Mo-coated glass substrate. Therefore solar cells were fabricated for the first time using this Al containing absorber film.

The solar cell fabrication was carried out as shown in figure 5.42. The solar cell structure was substrate configuration type of structure Ni-Al/ITO/i-ZnO/CdS/CIAS/Mo/SLG formed in the sequence: SLG as a substrate, sputter deposited the back contact Mo layer, CIAS absorber thin film by two stage method- sputter deposited Cu-In-Al precursor layer followed by selenisation in Se environment, the CdS buffer layer by CBD, sputter deposited i-ZnO and ITO (TCO) layers and the sputter deposited Ni-Al front contacts. The buffer layer and TCO window layers were deposited with similar properties obtained during CIS thin solar cells fabrication session. In the case of CIAS cell fabrication, a similar methodology which was followed during CIS cell fabrication was used.

The solar cells were measured for $I-V$ characteristics in which the highest efficiency cell was of $\sim 2\%$. However there was no clear evidence of incorporation of Al in the chalcopyrite structure to form quaternary CIAS phase. There was ambiguity for this absorber film about formation of CIS or CIAS. This was clarified by IPCE measurements performed on these cells at Bath University. Therefore $J-V$ characteristics curves for these cells are not presented.

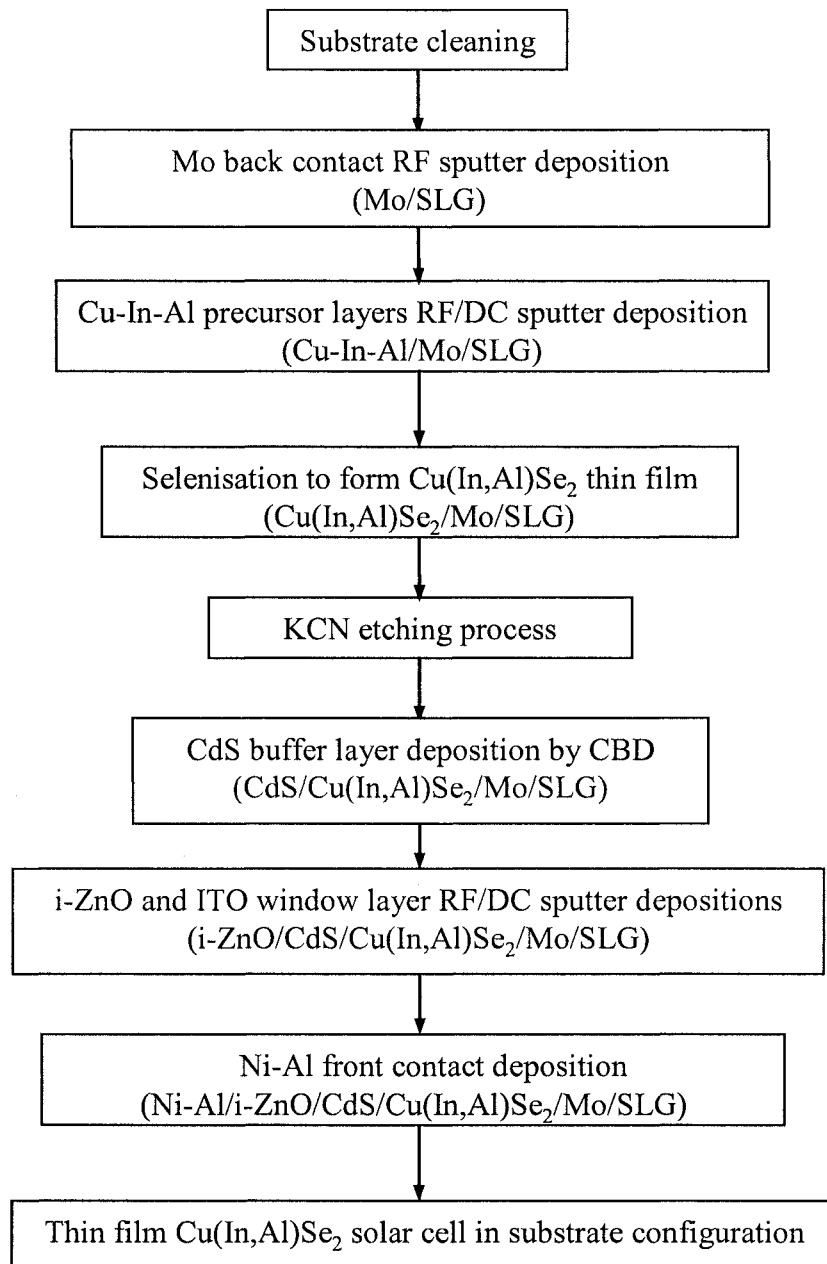


Figure 5.42 Flow chart diagram of CIAS thin film solar cell processing.

5.4.4 IPCE output of Cu(In,Al)Se₂ solar cells

The IPCE spectra (Fig. 5.43) obtained from the two working solar cells of the sample KJL-C (N66D), however, did not reveal significant band edge shift towards the lower side of the wavelength axis. The linear part of the higher end was extrapolated to the X-axis. The measurements which were carried out on both cells have shown exactly matching falling edge of the trace at longer wavelength. This estimated 1270 nm value corresponds to an energy band gap of 0.98 eV. This energy band gap is closer to that of the CIS absorber film (actual 1.04 eV). It may suggest that the absorber film was not showing optical characteristics of CIAS films.

5.4.5 Discussion

The purpose of the depositions of Al-In multilayers was to study and investigate structural and morphological properties of Al-In layers. The Al/In compositions were in the range 0.11-4.00. XRD pattern for these samples (AlIn-1 to AlIn-4) showed prominent In peaks and increasing Al reflection for increasing Al/In composition from AlIn-1 to AlIn-4, accordingly. The surface images also revealed roughly decreasing In islands with increasing Al content. This investigation clarified that there was no complete intermixing of Al and In in sputtering. The effect of sputter deposition parameters such as Al and In target power on the In island density is not well understood.

The first attempt to deposit the Cu-In-Al precursor layers with variations in Al content $n = \text{Al}/(\text{Al}+\text{In})$ in the range 0-1 yielded the precursor layers (thickness in the range 0.5-2.1 μm) of nearly required compositions, which were well-adhered to SLG and also Mo-coated SLG substrates. The Cu seed layer was found to be useful for adherence of layers. The formation of the Cu-Al related phases i.e.

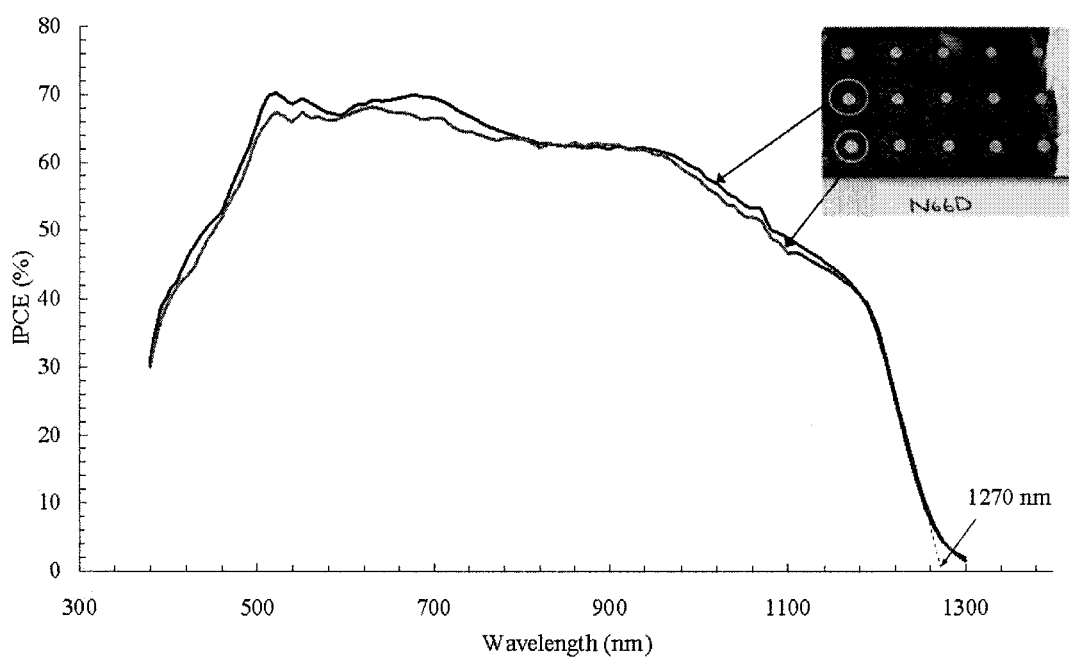


Figure 5.43 IPCE spectrum of the solar cells including the absorber film prepared from the Cu-In-Al precursor layer of the sample KJL-C (Sample-N66D).

AlCu_3 , AlCu_4 and CuAlO_2 were detected in the XRD graph of the Cu-In-Al and Cu-Al precursor layers, respectively. Hence in the Cu-In-Al precursor layers although it was found that the alloy formations of binary Cu-In and Cu-Al were possible, there was no information indicating phases of binary Al-In and ternary Cu-In-Al in these metallic layers.

The selenisation of different Cu-In-Al precursor layers containing Al yielded poor quality films (except KJL-C). The CIS thin film (KJL-A) had good surface and cross-sectional morphology and adhered well to the substrate. The SEM cross-sectional image of sample KJL-B revealed two layers of selenised films. This may be due to segregation of CIS and CIAS related phases as detected in XRD measurement. The film morphology became poorer and disordered with increasing Al in the precursor layers (samples KJL-D and KJL-E). After selenisation, the surface of the film KJL-F was found to be smooth and shiny (which could be seen by naked eye). This indicated that no reaction (diffusion) of Se took place with the Cu-Al layers. In these films, sample KJL-C was found to have uniform film colour (except along the edges) with compact grain arrangements and well-adhered to the Mo layer.

Depth profiling of the absorber film KJL-C confirmed that Al was not uniformly distributed even though In and Se were uniformly distributed throughout the thickness of the film.

The converted film KJL-C was found to be photoactive which suggested inclusion as an absorber in a solar cell structure. The IPCE spectra for the selenised KJL-C confirmed that the absorber material was of lower energy band gap of 0.98 eV which is near to CIS material. It was found from the investigations that there were several problems which need to be addressed from results obtained to produce CIAS films in first attempt. They were as follows:

- i) Poor adhesion of the absorber film to Mo/SLG.
- ii) Oxygen incorporation (formation of the oxidised layer).
- iii) Bilayer formation at the bottom of the film (segregation of Al-rich phases).
- iv) Poor surface features i.e. non-uniform absorber surface structure

The following could be possible reasons for poor absorber film formation:

- i) Prolonged exposure of the Cu-In-Al precursor layers to air. There was no capability to transfer the precursor layers directly into the selenisation compartment. It is likely that an oxide would be formed and this could have prevented conversion.
- ii) In addition thick precursor layers ($> 1 \mu\text{m}$) which may have hindered diffusion of Se atoms to form CIAS compound.
- iii) There may have been incomplete mixing of Cu, In and Al metals although the substrate was rotated similarly to Cu-In deposition process. The possible main reason was that there is immiscibility between Al and In as indicated earlier.

The XRD, EDS and SEM results obtained from the Al-In layers suggest that there was negligible solubility of In in Al which was found similarly also in a collaborative research work undertaken at Northumbria University [186]. Another supporting explanation is that mixing of Al-In metal is very difficult as Al and In tend not to mix with each other due to low affinity of the Al-In phase as compared to those of Cu-In and Cu-Al [187]. There is no literature available reporting Al-In relating work by research group (in the research area of CIAS thin films) around the World.

The adherence of the Cu-In-Al layers to the substrates (SLG and Mo/SLG) was improved by sputter depositing very thin Cu seed layers. In the literature it is

reported that a very thin layer (~ 5 nm) of Ga was deposited at the bottom of the precursor layer or absorber film to improve adhesion on the Mo-coated glass substrate [116]. In the case of work presented in this thesis, the Cu seed layer deposition was an alternative to Ga. This made it possible to save time by not having to replace any other material target (in this case Ga) in the sputtering chamber and maintained the aim of replacing Ga with Al.

The conversion of the Al containing precursor layers, KJL-B and KJL-D, into thin films attributed poor in surface and adherence. The KJL-F was found identical before and after selenisation except for a few spots on the shiny surface. XRD patterns for absorber films of KJL-B and KJL-C indicated (from the Al_2Se_3 phase) that Se diffused into the precursor layers which reacted with Al. According to Jost *et al.* the binary phase Al_2Se_3 is the only reported Al containing binary phase at 477°C [188]. The formation of Al_2Se_3 phase may have taken place at a temperature of about 477°C in samples KJL-B and KJL-D. The XRD of the sample F selenised from the Cu-Al precursor layers showed the presence of binary CuSe_2 and Cu_9Al_4 phases as per matched with standard reflection pattern in Inorganic Crystal Structure Database (ICSD) [189]. The cross-sectional SEM image of KJL-B film clearly revealed a two-layered structure in which each of the layers was ~ 2 μm -thick. A Korean research group synthesised CIAS films by sputter deposition of precursor layers followed by the selenisation process [33]. They also reported bi-layer morphology in CIAS thin films produced by three step method.

The investigation of IPCE data indicated lower energy band gap of 0.98 eV of Al containing absorber thin film. This showed even though Al was present in the films it did not form complete CIAS films. It means there must be segregation of Al-rich phases towards the back contact and CIS layer formed on top of it.

To investigate the influence of the thickness of the Cu-In-Al precursor layers and corresponding thin films, a subsequent set of precursor layers with thicknesses of $\leq 1 \mu\text{m}$, were sputter deposited.

5.5 Thinner CuIn_{1-x}Al_xSe₂ Absorber Films and Solar Cells

The results obtained from thinner CIS absorber films were promising in terms of the solar cells' output parameters. A similar experiment was carried out to synthesis thinner CIAS absorber films in order to investigate physical properties of thin films.

5.5.1 The thinner layers of Cu-In-Al precursors

In this section, a set of thinner layers of Cu-In-Al precursors of thicknesses $\leq 1 \mu\text{m}$ was sputter deposited with three different compositions listed in table 5.13. Several experiments such as annealing at two process conditions, temperature and pressure, were performed on these layers. Selenisation of these layers was carried out in a similar manner to that described earlier for the CIAS films.

The XRD performed on the precursor layers KJL-G and KJL-I shows an increase in AlCu₄ peak intensity with increase in Al in the precursor layers (Fig. 5.44). There was no phase of Al-In compound detected. The binary Cu₁₁In₉ and Cu₂In phases were also formed.

The SEM surface image of the precursor layer KJL-G is shown in figure 5.45. It reveals rough features of precursor films grown on the smooth surface. The balling-up of film may be due to de-wetting of the oxidised Mo film, in which the film breaks into droplets or globules of spherical ball shape.

MiniSIMS depth profiling for Cu, In and Al metals in the sample K181K with $n \approx 0.28$ (from the same batch of KJL-G) is shown in figure 5.46. Both positive Cu, In and Al species and negative O were detected and plotted. A typical MiniSIMS plot exhibited relatively high count rates of $^{27}\text{Al}^+$ and $^{115}\text{In}^+$, which is related to the

Sample (Original sample name)	Cu, In and Al Targets' Power Ratio		Precursor Composition					Thickness (μm)
	$\text{Cu}/(\text{Al}+\text{In})$	$\text{Al}/(\text{Al}+\text{In})$	Cu (at.%)	In (at.%)	Al (at.%)	$m = (\text{Cu}/\text{In}+\text{Al})$	$n = (\text{Al}/\text{Al}+\text{In})$	
KJL-G (N172G)	0.50	0.28	50	36	14	1.00	0.28	0.55
KJL-H (N171L)	0.71	0.27	51	26	23	1.04	0.47	0.6
KJL-I (N170R)	0.72	0.31	54	21	25	1.17	0.54	1.0

Table 5.13 The Cu-In-Al precursor layers of varying Al content.

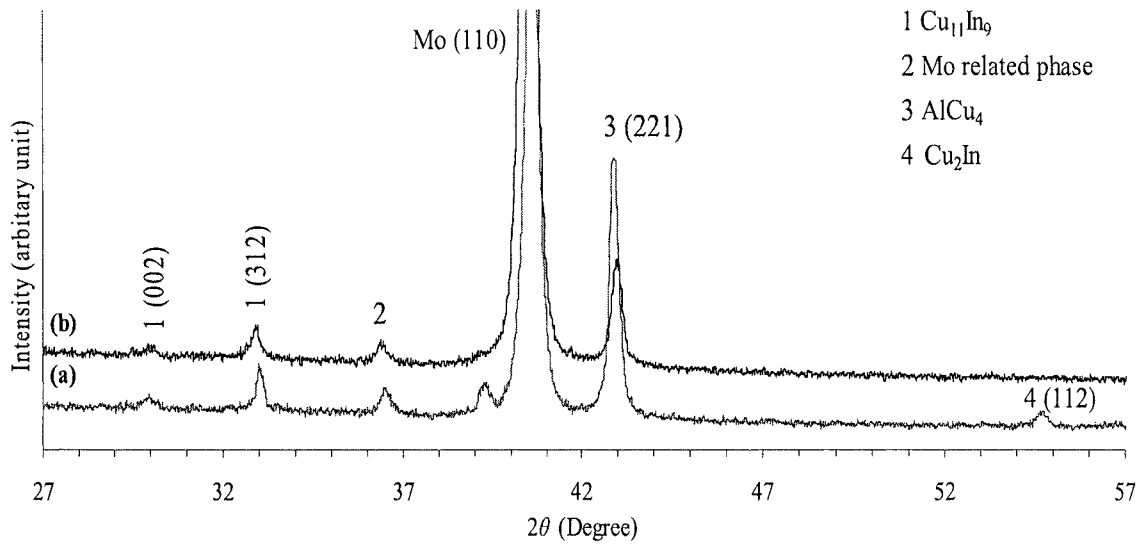


Figure 5.44 XRD patterns of the Cu-In-Al precursor layers on the Mo-coated SLG substrates; (a) KJL-G and (b) KJL-I [Note: Mo related phase indicates the peak related to Mo containing phase. However there is no *hkl* information available in PDF database].

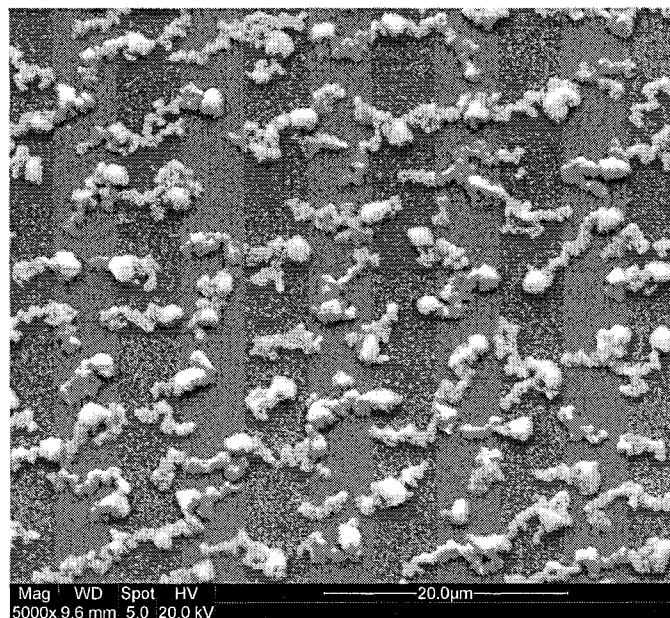


Figure 5.45 SEM image of surface morphology of the Cu-In-Al precursor layer with $n = 0.28$ (Sample: KJL-G).

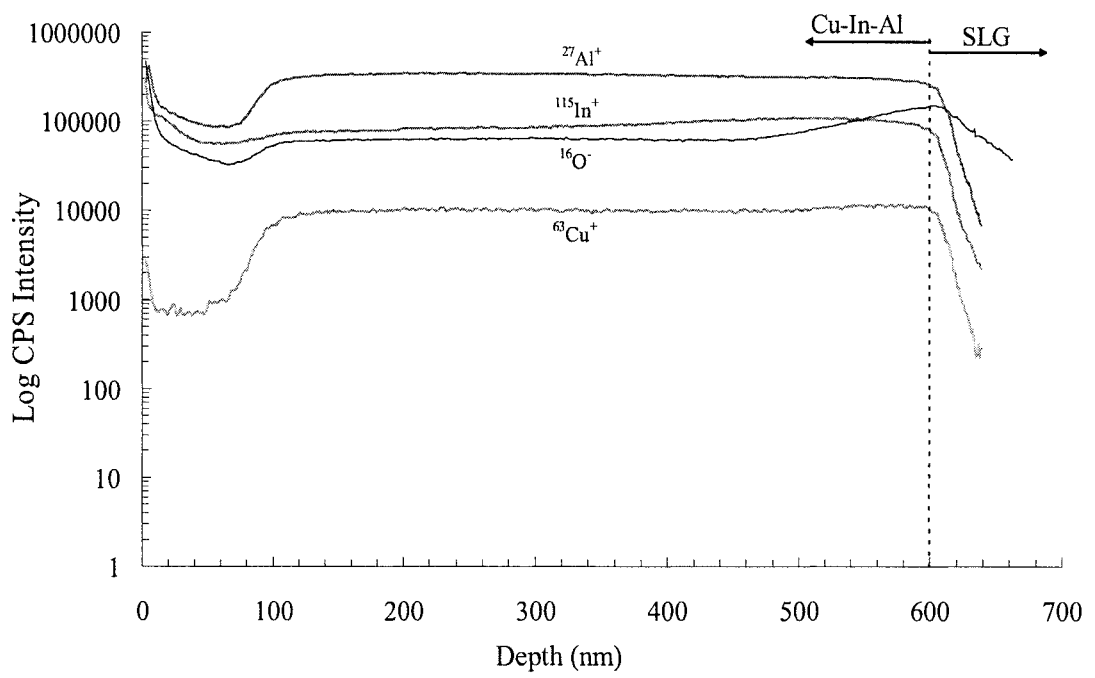


Figure 5.46 MiniSIMS depth profiling scan of the Cu-In-Al precursor layer of the sample K181K (equivalent to sample KJL-G) with $n \approx 0.28$.

high sensitivity of SIMS detector for these elements. In the beginning (depth from the surface of the layer ≈ 10 nm) Cu, In, Al and O signals have shown a high count rate. As can be seen the Cu, In and Al signals are fairly uniform in the depth range between 140-540 nm. The higher In signal near the surface (approximately up to 60 nm deep) can possibly be explained by the presence of the In cap layer which was there in order to prevent the oxide layer formation in air. The increased Cu signal at the bottom of the layer, i.e. near the Cu-In-Al layer/glass interface, is attributed to the very thin Cu seed layer as mentioned earlier. The $^{16}\text{O}^-$ impurity level increased near the surface and remained relatively uniform in the layer and then increased in the vicinity of the precursor layer/glass interface.

5.5.2 Annealing of the Cu-In-Al precursor layers for different temperatures and pressures

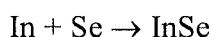
5.5.2.1 Annealing of the Cu-In-Al precursor layers for different temperatures

The Cu-In-Al precursor layers were annealed for different temperatures in order to find the optimum temperature range to obtain good quality quaternary CIAS thin films. The as-deposited Cu-In-Al precursor multilayer of sample KJL-I was coated with a Se cap layer prior to annealing at temperatures of 250°C, 400°C, 500°C and 550°C. The selenisation process conditions, Ar pressure of 5 mbar and process duration for 30 min (estimated from CIS experiment), were fixed for this experiment.

The XRD results of the converted films are shown in figure 5.47. At 250°C, a number of binary phases InSe, CuSe and AlCu_4 were detected. The binary phase AlCu_4 was not definitely confirmed but was found to be matched with the standard of PDF file. The reflection detected at 26.8° was of a selenised ternary phase that

might be incomplete CIS material. Therefore a lower annealing temperature 250°C was not sufficient to form single phase quaternary chalcopyrite CIAS material. This was done to look for the phases and enable monitoring of phase evolution for a low temperature.

The surface morphology of the film selenised at 250°C was a non-uniform, non-granular and loosely arranged structured revealed in SEM image in figure 5.48 (a). The surface of the selenised film was mostly covered by flat plate-like crystals and some round structures. Those kind of flat structures are considered due to an InSe prominent binary phase at 31.4° position as the melting points of In and Se are 157°C and 217°C, respectively.



When the precursor layer was annealed at 400°C the diffraction pattern was different from that obtained for 250°C. The main changes noted were an increase in the CIAS (112) prominent peak intensity at 26.8°, the disappearance of many binary phases and splitting of the (220/204) reflection at 44° which is characteristic of chalcopyrite material formation [174]. The main (112) peak is more prominent. Even though the XRD results were satisfactory, SEM shows the surface structure with spherical droplet-like structures and still there was no compact grain structure (Fig. 5.48 (b)). Therefore 400°C temperature was also found to be insufficient to form the CIAS absorber thin films.

At 550°C, according to the XRD data, the prominent CIAS (112) peak became more smooth and symmetrical. There were no additional small peaks associated with binary phases. The chalcopyrite structure was identified from the splitting of the peak (220)/(204) due to the tetragonal distortion where $c/a \neq 2$ [190]. The XRD diffraction patterns obtained for films selenised at 500°C and 550°C did

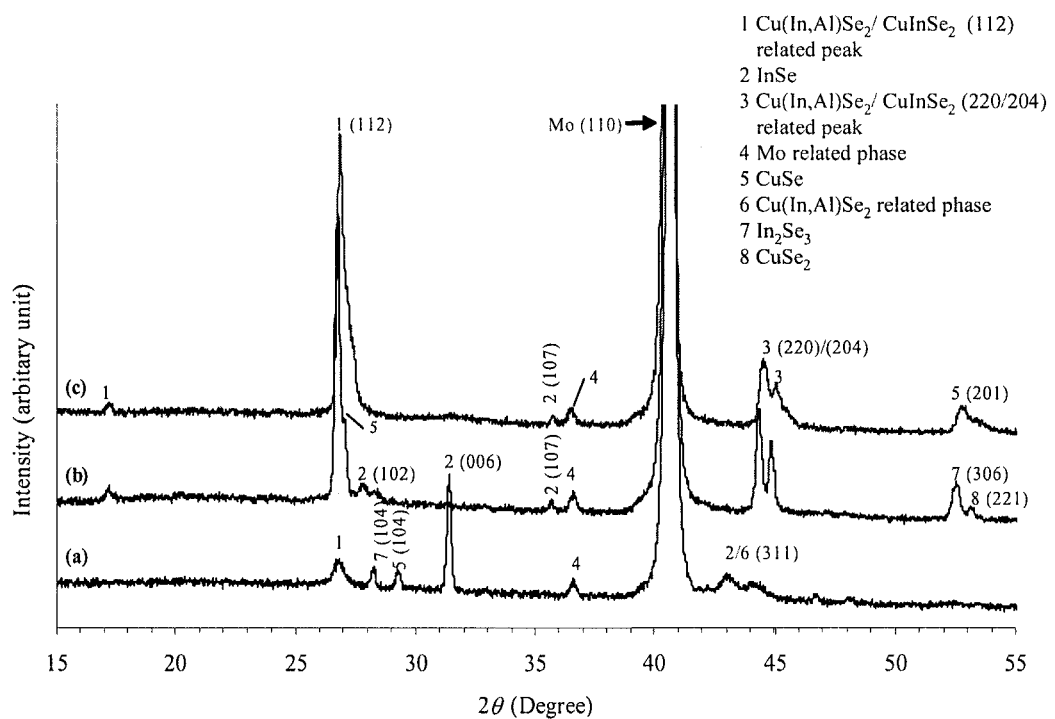


Figure 5.47 XRD pattern of the Cu-In-Al precursor layers (Sample KJL-I) selenised at different temperatures in a Se environment: (a) 250°C, (b) 400°C and (c) 550°C. [Note: Cu(In,Al)Se_2 related phase indicates the peak related to CIAS phase. However there is no hkl information available in the PDF database software].

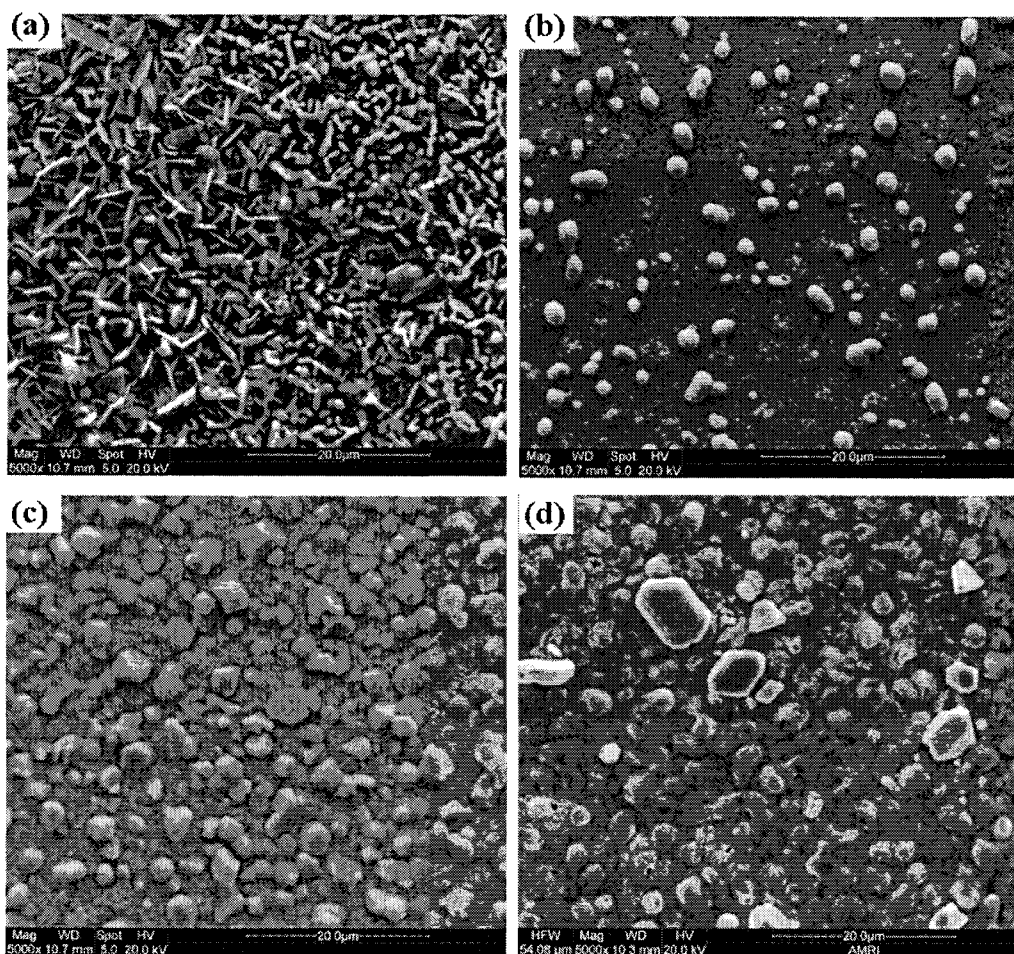


Figure 5.48 SEM surface morphology of the selenised films prepared from the Cu-In-Al precursor layers (Sample KJL-I) at different temperatures; (a) 250°C, (b) 400°C, (c) 500°C and (d) 550°C.

not show any clear differences.

The SEM micrographs shown in figures 5.48 (c) and (d) were taken for the surfaces of the samples selenised at 500°C and 550°C, respectively. The surface morphology at 500°C reveals large grains of circular or hexagonal structures; however, the surface structure was not compact. There were some smooth features in between the large grains. Moreover, the surface morphology of the sample selenised at 550°C was compact and with regular grains 2 µm approximately in size (there were also occasional very much larger grains with dimensions > 5-10 µm). The most appropriate selenisation temperature to form CIAS absorber film was found to be approximately 550°C for the Cu-In-Al precursor layers.

5.5.2.2 Annealing of the Cu-In-Al precursor layer at different Ar pressures

In the experiment of selenisation of the Cu-In-Al precursor layers at different temperatures, it was found that 550°C yielded the best results. The work reported in this section was aimed at investigating the effect of Ar pressure during selenisation. The precursor layers were annealed (temperature 550°C) at three different pressures; 1 mbar, 5 mbar and 10 mbar.

At 1 mbar, the SEM surface morphology was observed to be relatively smooth with a few tetragonal and polygonal shaped grains (Fig. 5.49 (a)). The underlying smooth layer can also be observed. When the layers were annealed at 5 mbar, the surface morphology was altered compared to that produced at 1 mbar. The converted film had many grains with sizes > 2 µm; the films also had a less smooth surface structure (Fig. 5.49 (b)). The absorber film adhered well on the Mo-coated glass substrate for 1 and 5 mbar. When the precursor layers were annealed at a higher pressure of 10 mbar the films peeled off and the Mo surface was exposed. On very

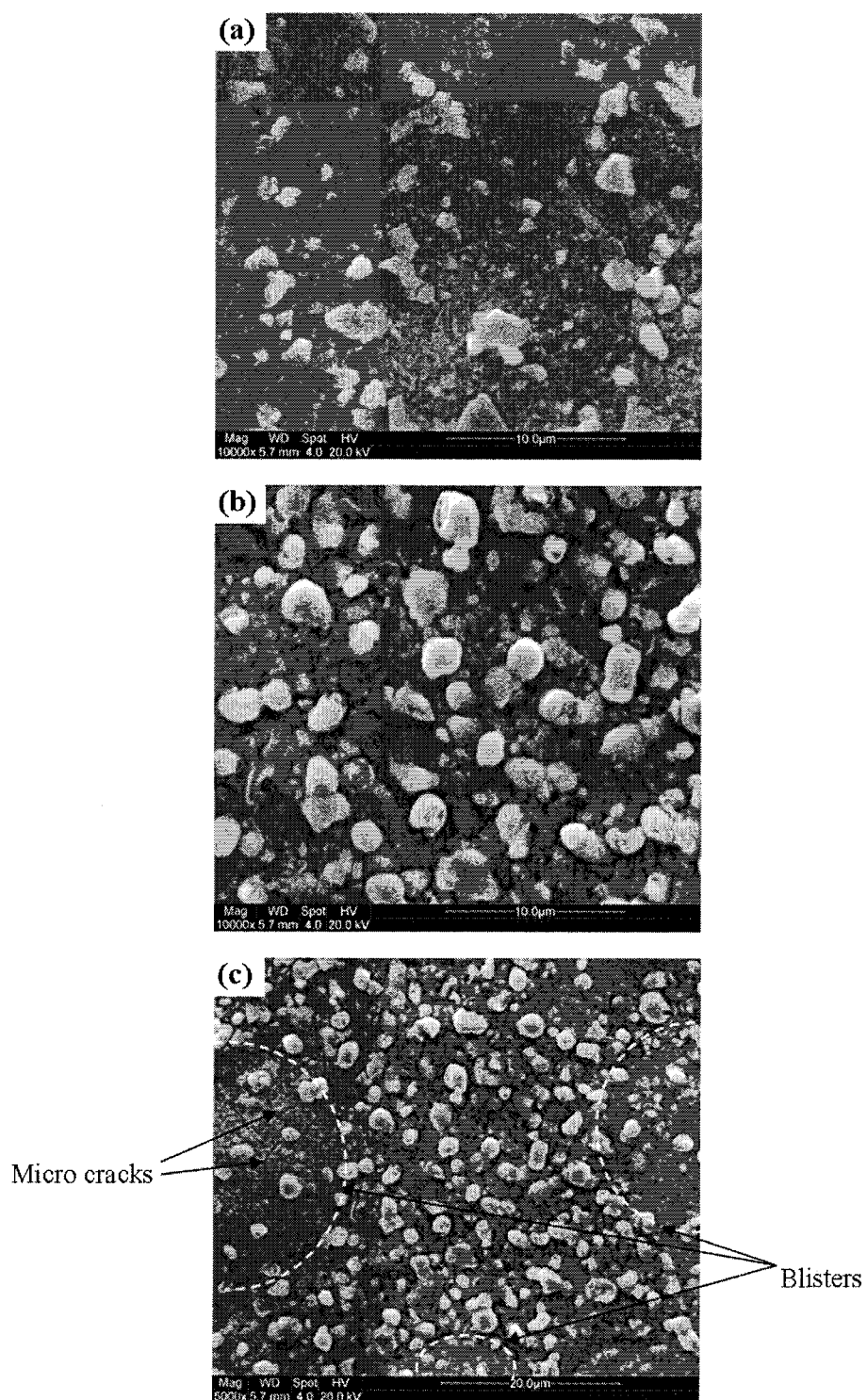


Figure 5.49 SEM surface morphology of the films selenized from the Cu-In-Al precursor layers (Sample KJL-I) for Ar pressures; (a) 1 mbar, (b) 5 mbar and (c) 10 mbar.

small areas the films remained attached to the Mo back contact. These areas were examined in greater detail under the SEM and the results are shown in figure 5.49 (c). Large blisters (outlined by white dashed lines) with micro-cracks and grains in between those blisters can be clearly seen. It was not possible to get any XRD result from the remaining films due to poor surface structure. However, it was confirmed that very high pressure caused poor adhesion of the film with several blisters and micro-cracks. This type of film structure was not appropriate for deposition of a buffer layer and fabrication of the complete solar cell.

It was confirmed that a pressure of 5 mbar and a temperature of 550°C were found to be suitable process conditions for the formation of CIAS thin films in a tube furnace.

5.5.3 Selenisation of the thinner layers of Cu-In-Al precursors

The selenisation process was conducted on the thinner Cu-In-Al precursor layers of the samples KJL-G, KJL-H and KJL-I on the Mo-coated SLG substrates at a temperature of 550°C, a pressure of 5 mbar and process duration for 30 min.

The XRD diffraction patterns of the main (112) reflections obtained for the films converted from different precursor layers are shown in figure 5.50. There was a shift in (112) reflection position with Al content: (26.80° for $n = 0.28$; 26.87° for $n = 0.47$ and 26.80° for $n = 0.54$). The peaks labelled as $x = 0$, $n = 0.28$ and $n = 0.47$ are symmetrical in shape. The reflection for $n = 0.54$ is not symmetrical and is also not shifted much compared to the reflections for $n = 0.28$ and $n = 0.47$. The values presented in the table 5.14 were obtained using the Bruker AXS software available with XRD instrument. It suggest that as the peak position shifts, the intensity and the FWHM width (Fig. 5.51) are decreased with increased Al content in the precursor

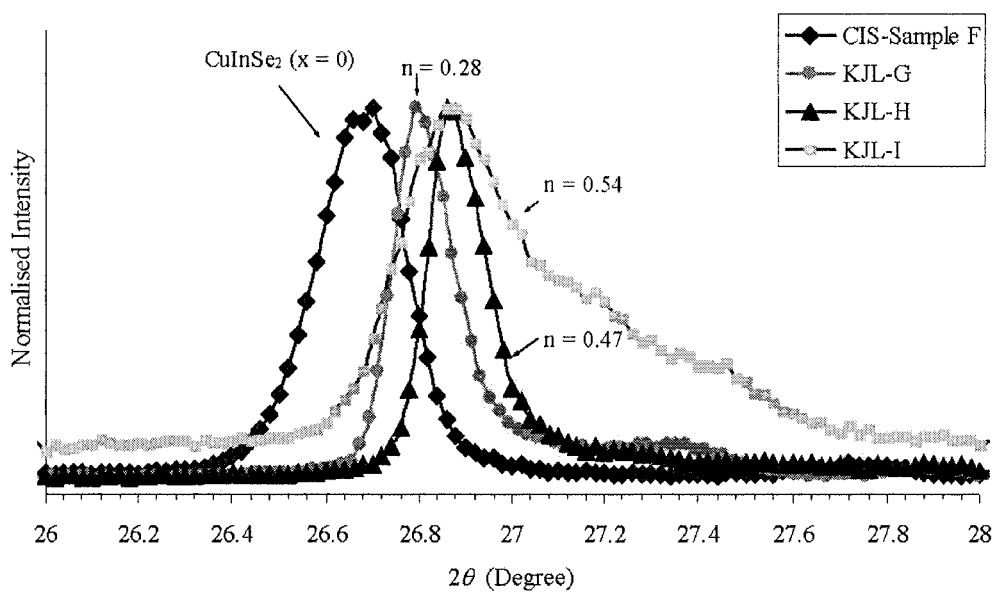


Figure 5.50 XRD patterns of the (112) reflections for CIS ($x = 0$) and CIAS films with increasing Al content (n) in the precursors.

The absorber films									
Sample	n = Al/(Al+In) in the precursor layers	XRD data analyses							Absorber thickness (μm)
		XRD details of prominent (112) peak				Lattice spacing (<i>d</i>) of (112) peak (\AA)	Lattice constant <i>a</i> (\AA)	Lattice constant <i>c</i> (\AA)	
		Peak position (Degree)	Peak intensity (Counts)	FWHM (Degree)					
F (CuInSe ₂)	-	26.68	10000	0.2800	3.3382	5.7810	11.5602	1.6	
KJL-G	0.28	26.80	8000	0.1600	3.3250	5.7621	11.5244	1.8	
KJL-H	0.47	26.86	7250	0.1604	3.3166	5.7564	11.5130	2.0	
KJL-I	0.54	26.87	3500	0.4800	3.3154	5.7520	11.5042	1.3	

Table 5.14 XRD analyses of CuInSe₂ and Cu(In,Al)Se₂ thin films.

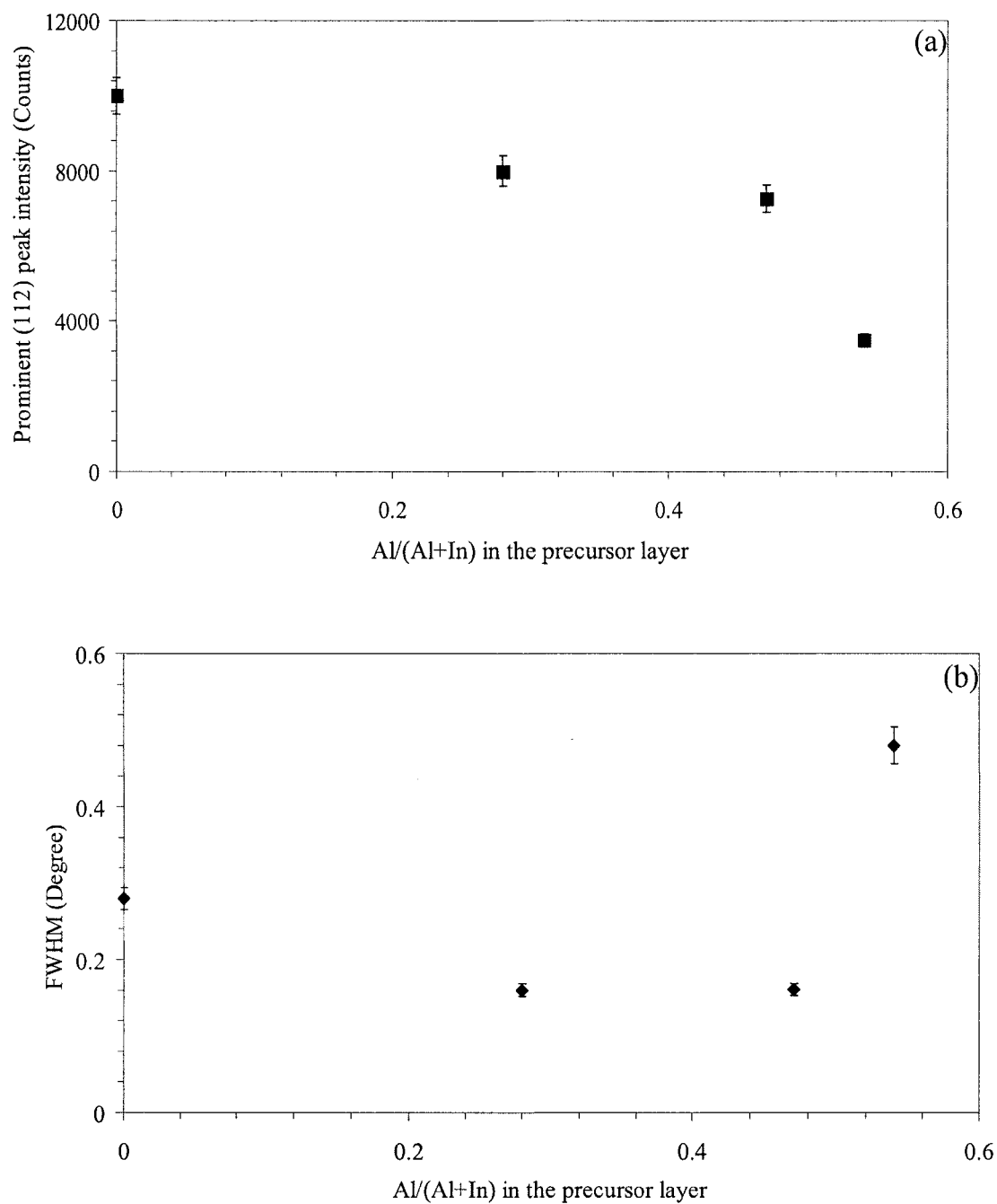


Figure 5.51 Variations in (a) intensity and (b) FWHM of the prominent CIS or CIAS (112) diffraction peak with n content in the Cu-In-Al precursor layers.

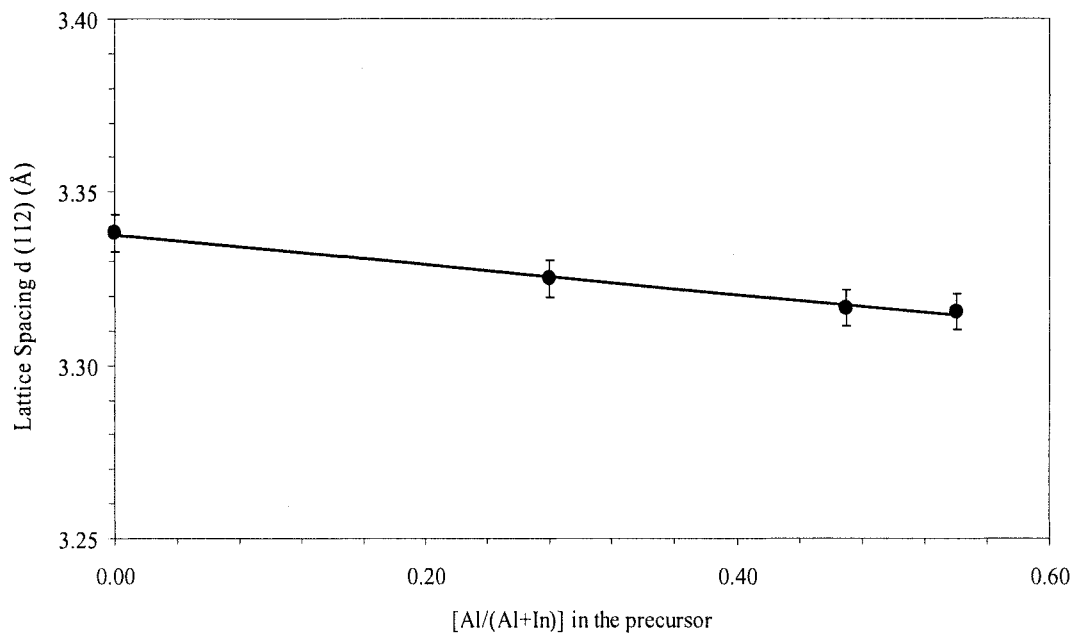


Figure 5.52 Variation in lattice spacing $d(112)$ of the selenised film with Al content in the precursor layer.

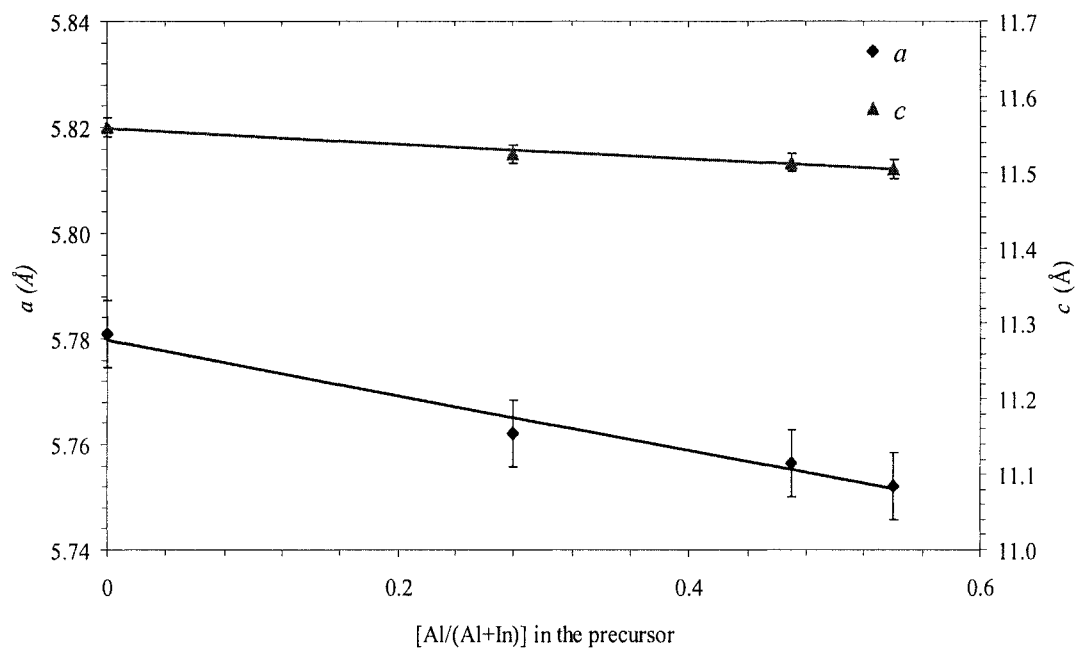


Figure 5.53 Lattice constants a (◆) and c (▲) of the films selenised from the precursor layers with variation in 'n = (Al/Al+In)' content.

layers. The lattice spacing $d(112)$ (Fig. 5.52) was calculated using the (112) peak position of each sample, with the Mo peak as a reference. However, it can be seen that the shift in the (112) reflection position, is less for sample KJL-I as compared to samples KJL-G and KJL-H. The FWHM of the (112) reflection became wider with an increase in Al in the precursor layers. There was a non-linear variation in lattice constants a and c with Al content (n) (Fig. 5.53).

The surface morphology and the cross-sectional SEM images of CIAS films with varying 'n' in the precursor layers are shown in figure 5.54. In the case of the bottom very thin (5-10 nm) Cu seed layer, a better result was obtained in terms of adhesion of films to the Mo layer and glass substrates. In addition, the significant grain structure was yielded with lower Al content as shown in figure 5.54 (a) and film adhesion on the Mo back contact was poorer with increasing Al content [31]. The cross-sectional image of the selenised film KJL-G showed large grains of 1.8 μm in size. There was also formation of the thin layer (thickness approximately 130 nm) between the back contact Mo layer and thin film. Samples KJL-H (Fig. 5.54 (b)) and KJL-I (Fig. 5.54 (c)) have shown poor quality of grain arrangement or no ordered grain arrangements with thickness 2.0 and 1.3 μm , respectively.

MiniSIMS (Fig. 5.55) was performed on the sample K181K ($n \approx 0.28$) selenised similar to the KJL-G thin film. The depth profile indicated a 1.9 μm -thick layer. The depth was measured from the free surface of the CIAS absorber layer. The MiniSIMS depth profile shows a change in Al content through the thickness. The Al signal is lower in the region between 100-500 nm and higher concentration towards the glass surface (1.0-1.3 μm depth). The depth profiles of elements $^{115}\text{In}^+$ and $^{80}\text{Se}^-$ were uniform with depth but $^{63}\text{Cu}^+$ trace is increasing near at the bottom part of the film i.e. near the glass surface. The Na present in the film is thought to be the result

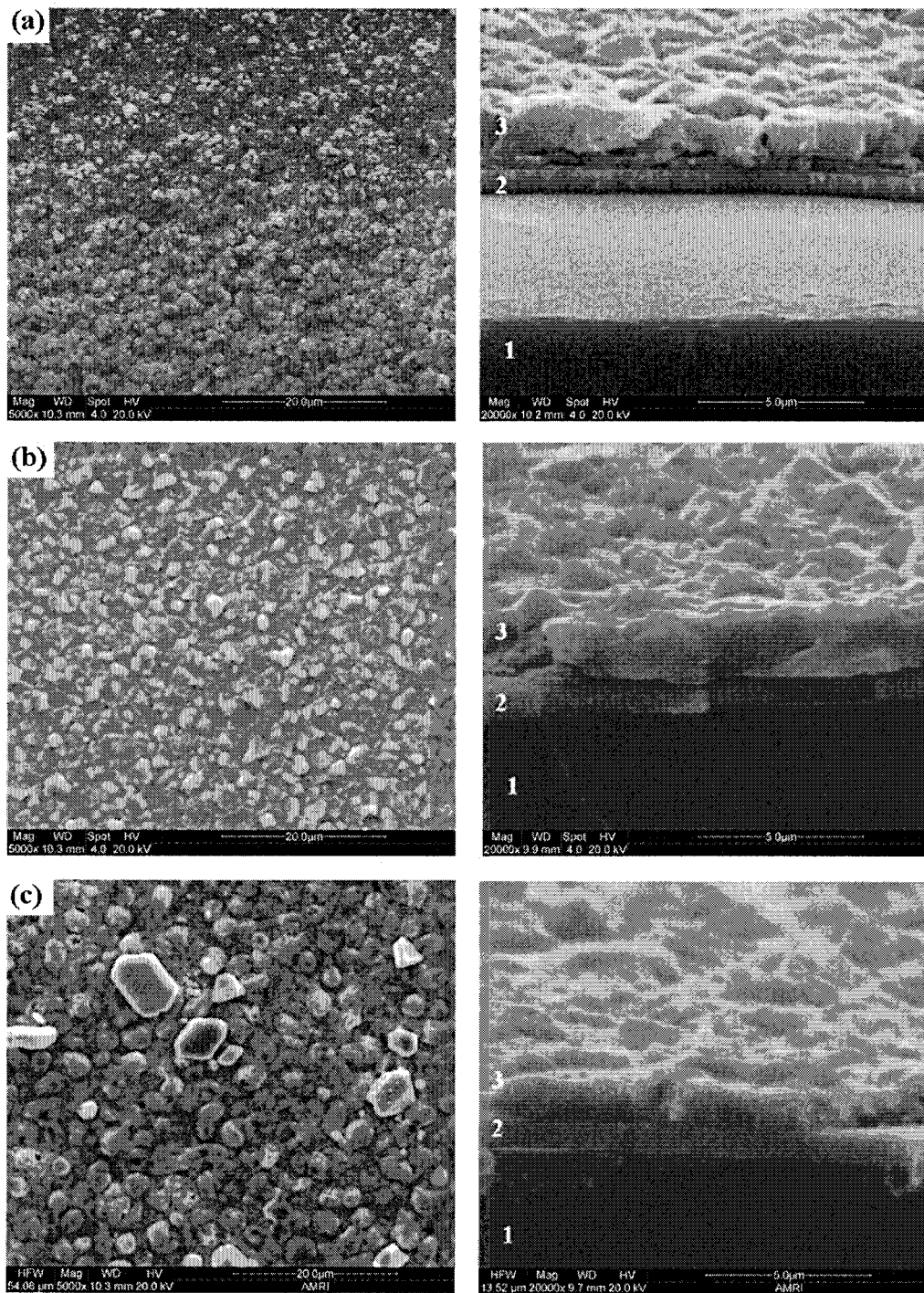


Figure 5.54 The SEM surface morphology (left) and the cross-sectional images (right) of the CIAS films; (a) KJL-G, (b) KJL-H and (c) KJL-I.

[Note: The number displayed in figure indicates: 1 – SLG substrate, 2 – The Mo layer and 3 – The absorber films].

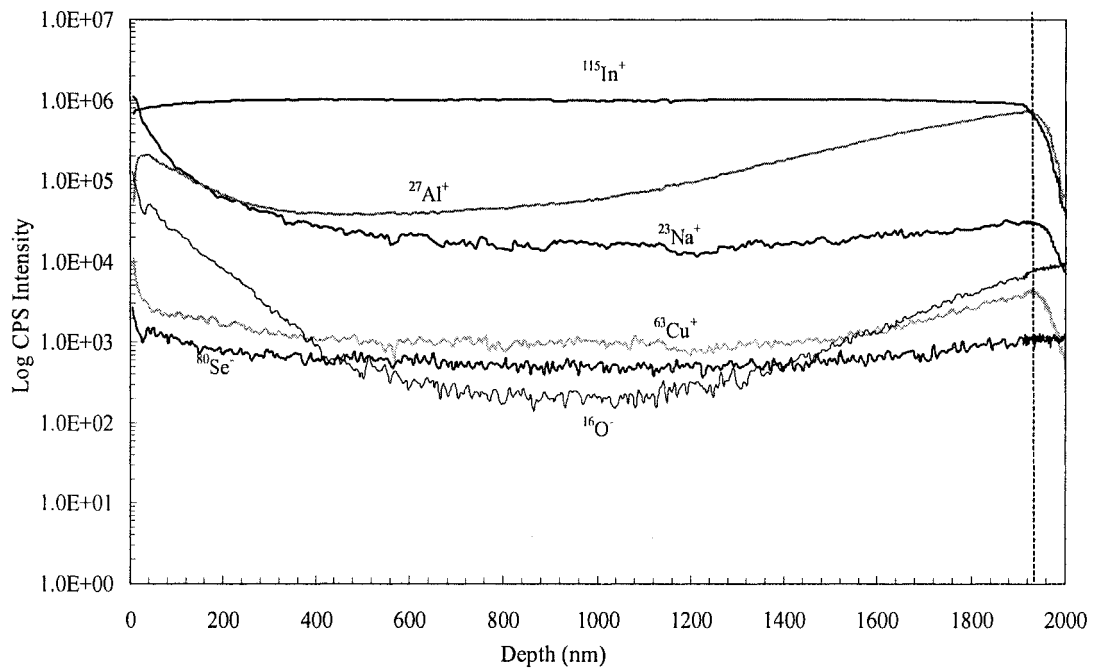


Figure 5.55 MiniSIMS spectra of the CIAS film on the glass substrate selenised from the Cu-In-Al precursor layer of the sample K181K (from the same batch of KJL-G ($n \approx 0.28$)) (The dotted line represents the CIAS/glass interface).

of the out-diffusion from glass during absorber film formation. However, any phase segregation (CIS and CIAS) that may have occurred during the formation of the absorber film. The oxygen (^{16}O) content in the film shows a higher signal profile near the surface and drops in the centre and again increases towards the CIAS/glass interface. The higher ^{16}O signal level near the surface is attributed to the formation of an oxide layer on the exposed surface.

The optical spectral measurements (transmittance) were performed on the absorber film K181K on the SLG substrate. The percentage transmittance versus wavelength graph of this film on glass substrate is shown in figure E in appendix I. The energy band gap of the absorber film was estimated by plotting a graph (Fig. 5.56) of $(\alpha h\nu)^2$ versus $(h\nu)$ and extrapolating absorption edges to the $h\nu$ axis. The curve shown in graph has two different optical transitions. When the linear portions of the curve extrapolated onto the energy bandgap ($h\nu$) axis, the two energy band gaps were found to be 1.10 eV and 0.98 eV. The higher energy band gap of 1.10 eV corresponds to the energy band gap of CIAS related thin film while the lower energy band gap is attributed to the presence of the CIS. The SEM image cross-section of this sample is displayed along with the graph and according to it a bilayer structure can be seen with formation of the thinner layer at the bottom of the thin film.

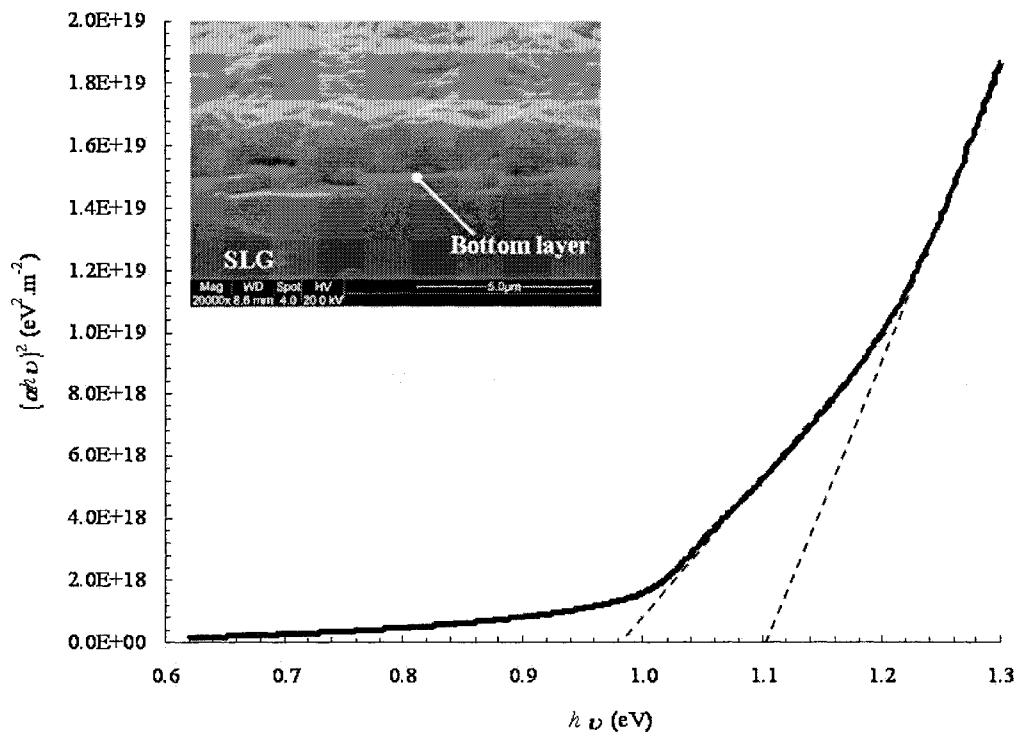
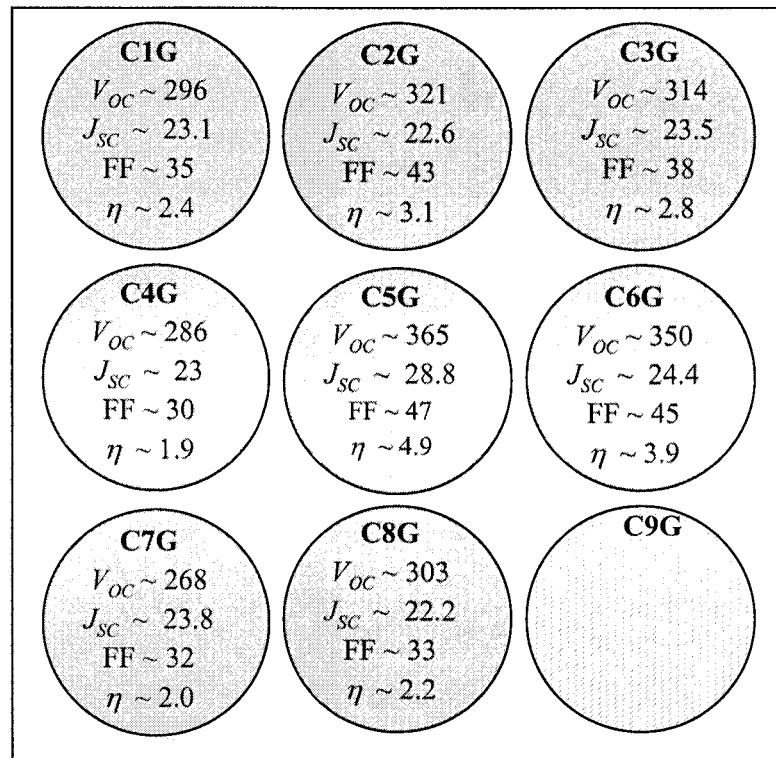


Figure 5.56 The plot of $(\alpha h\nu)^2$ versus $(h\nu)$ for the sample K181K CIAS film ($n \approx 0.28$ in the precursor layer) on the SLG substrate.

5.5.4 The solar cell fabrication using thinner CIAS absorber films

The absorber layers of the sample N172H4 (similar to KJL-G) selenised (in a collaborative work with Dr. Zoppi) using thin Al content precursor layer of composition $n \approx 0.28$ were processed further to fabricate solar cells. The fabrication process was the same as that discussed earlier for the absorber N66D. Figure 5.57 shows the solar cell parameters, V_{OC} , J_{SC} , FF and η , of the solar cells. The solar cell performance was non-uniform across the substrate. Illuminated J - V measurements were performed on all cells C1G to C9G. The best result, obtained for a CIAS solar cell C5G of an active area of $\sim 0.217 \text{ cm}^2$ (subtracting 0.023 cm^2 (contact pad area) from 0.240 cm^2 (total cell area)), is presented in figure 5.58. The CIAS cell (C5G) parameters were calculated from J - V curve under illumination. The cell conversion efficiency (η) was approximately 4.9% with $V_{OC} \sim 0.364 \text{ V}$, $J_{SC} \sim 28.2 \text{ mA/cm}^2$ and FF $\sim 47\%$.



V_{oc} in mV
 J_{sc} in mA/cm²
 FF in %
 η in %

Figure 5.57 V_{oc} , J_{sc} , FF and η distributions in CIAS thin film solar cells fabricated using absorber films of sample N172H4 (similar to sample KJL-G) (The solar cell C9G was found non-functional cell) (Not to scale).

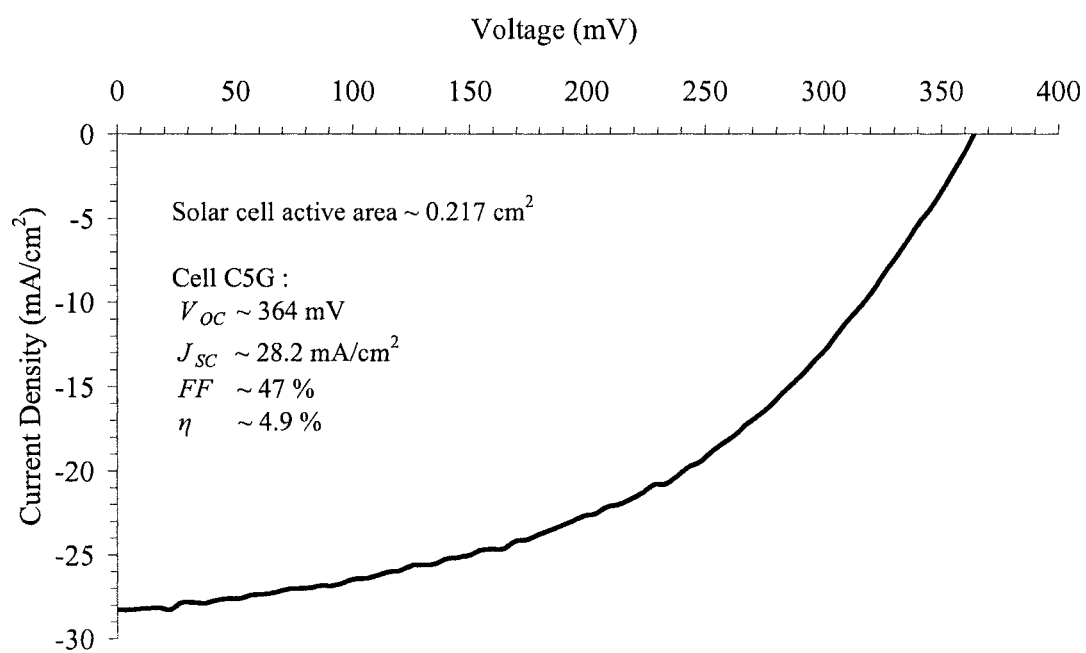


Figure 5.58 J - V characteristic for the CIAS thin film solar cell C5G fabricated using absorber films of sample N172H4 (similar to sample KJL-G).

5.5.5 Discussion

In this section, the thinner layers (thicknesses $\leq 1 \mu\text{m}$) of Cu-In-Al precursors were sputter deposited in a KJL deposition system. XRD results obtained from these precursor layers confirmed that there was mixing of Al and Cu due to the AlCu_4 phase detected. In addition there was mixing of Cu and In that formed $\text{Cu}_{11}\text{In}_9$ and Cu_2In phases. However there was no peak to indicate any mixed phase of Al and In.

The presence of Cu, In and Al metals in the precursor layer was studied by MiniSIMS depth profiling. From the depth profile data, the Cu, In and Al traces were consistent with sputter etch time which suggests a uniform distribution of these metals with depth in these layers.

From the experiment of annealing of the precursor layer KJL-I (Al 25 at.%) at different temperatures it was found that 250°C and 400°C were not high enough to form good quality thin films. This was concluded from the number of binary phases detected in XRD data. At 550°C , the XRD spectra exhibited a prominent (112) peak related to quaternary CIAS material. The SEM surface images of those films selenised at different temperatures (250°C , 400°C , 500°C and 550°C) clearly revealed differences in the surface morphology. Only at 550°C the surface morphology exhibited a compact structure with large grains. Therefore it was concluded that 550°C was the selenisation temperature required for the preparation of good quality absorber layers.

The precursor layer was also annealed under different Ar pressures (1 mbar, 5 mbar and 10 mbar at 550°C) in a Se environment. The surface morphology showed that the surface of the films selenised at 1 mbar was smooth. It is suggested that this could be due to poor Se diffusion in the precursor layer. The films produced at 10 mbar pressure had a very poor morphology and the films exhibited poor adhesion

with areas peeling off. The high pressure created due to the dense Se atmosphere may have damaged the films. The precursor layer selenised at 5 mbar pressure yielded better surface morphology with large grains. This film was found well-adhered to the Mo back contact layer.

In summary, the process conditions, temperature of 550°C, Ar pressure 5 mbar and duration 30 min, were used for the conversion of subsequent thin Cu-In-Al precursor layers to obtain good quality films.

The conversions of the thinner layers of Cu-In-Al precursors into thin films were carried out for the process conditions, temperature of 550°C, Ar pressure of 5 mbar and duration for 30 min. According to XRD data of these films, there was a variation in lattice constants a and c of absorber films with substituting element Al, obeying Vegard's law at some extent [191]. However, there was increase in non-linearity in lattice constants at higher n (Al/(Al+In) in the precursor layer). The lattice spacing $d(112)$ was decreased with n content in the precursor layer.

The cross-sectional images of these films converted showed a layer of few nanometres between the thick film (CIS or CIAS) and the back contact Mo layer. The films showed better crystallinity selenised from lower Al containing precursor layer (KJL-G) than that selenised from the precursor layer of higher Al content (KJL-I).

In MiniSIMS analyses of the absorber film, there was increasing Al signal towards the glass which may be interpreted by assuming an accumulation of Cu and Al towards the bottom of the absorber film (this can be correlated to a layer of a few nanometres found in the cross-sectional SEM images). The reason for the higher Cu signal might be due to the Cu seed layer during precursor layer deposition.

The optical energy band gap of the absorber film K181K was 1.10 eV, significantly higher than that of CIS material. It implies that Al had been incorporated into the absorber layer to some extent. However, the Al was not uniformly incorporated with depth in the film. The results are consistent with the formation of a 2-layer structured selenised film; the bottom layer was thought to be the result of a segregated phase (or accumulation of Al-rich phases).

The solar cell fabricated using the absorber film (N172H4) with the Al content, similar to sample KJL-G (Al 14 at.%, $n = 0.28$), had a similar buffer layer, window layer and front contact properties as that for CIS solar cells. The solar cell yielded an efficiency of 4.9% under illumination.

In summary, the conversions of the thinner layers of Cu-In-Al precursors of increasing Al content for the identical process conditions yielded different grain structures. The films with lower Al content were found to have better grain morphology than that for high Al content. XRD patterns for these films showed a shift in the prominent CIAS related (112) peak towards the higher values on the 2θ scale. However there was no evidence of composition of absorber films due to EDS instrument's incompatibility as described earlier. MiniSIMS depth profiles of the Al, in the sample before and after selenisation, demonstrated that although Al was found to be uniform in the precursor layer it became non-uniform (higher counts near the CIAS/glass interface) in the film. This suggested that accumulation of Al-rich phases was at the bottom of the film. The optical measurements on this absorber film estimated a higher band gap value of 1.10 eV. The solar cells fabricated using a photoactive absorber layer yielded highest cell efficiency of 4.9%.

The XRD patterns for thin films converted from thinner layers of Cu-In-Al have shown shifts in the prominent CIAS (112) peak towards high values on the 2θ

scale. It suggested that there was an alteration in the lattice structure of the chalcopyrite CIS compound by alloying with Al. This was attributed to variations in the lattice parameters, a and c [191]. However, these values for $n = 0.47$ and $n = 0.54$ indicated incomplete incorporation of Al [192]. According to $d(112)$ calculations and values reported in literature, the value of $x = \text{Al}/\text{Al}+\text{In}$ in the absorber film is estimated to be near to 0.2 for the film selenised from the precursor layer with $n = 0.28$ [115]. However, it did not apply to other films selenised from the precursor layers with $n = 0.47$ and 0.54 due to inconsistency with values reported. The broadening of the (112) peak FWHM width of the thin film selenised from the precursor layer with $n = 0.54$ could be due to poor crystallinity or due to the presence of binary phases [193].

Halgand *et al.* stated explanations for the presence of a very thin layer at the bottom of CIAS absorber layer. According to them, there is a migration of Al atoms to the grain boundaries. Another possibility could be the formation of CuAlSe_2 (CAS) and CIS mixture [194]. Korean researchers synthesised CIAS films by a two stage growth method i.e. sputter deposition of the precursor layers followed by the selenisation process. They reported incomplete incorporation of Al in films that caused formation of a CIS structure and accumulation of Al at the back contact in the form of intermetallic phases [33]. A similar process could have occurred in the absorber films described in this thesis that yielded a very thin layer near the CIAS/Mo interface.

The non-uniform distribution of Al in the CIAS film was also found in other similar CIAS films synthesised in the collaborative work. It was concluded that Al may be present in the films in the form of precipitates or segregates at the grain boundaries [195]. Minemoto *et al.* reported MiniSIMS profile studies of CIAS films

grown by the three-stage evaporation process [196]. They found an Al distribution located at 300-400 nm from the surface of CIAS film that was V-shaped and then almost a flat trace up to Mo surface.

The optical measurements for the CIAS film on the SLG substrate showed two energy band gaps of 0.98 and 1.10 eV. These values were attributed to bilayer cross sectional morphology of the film.

The photoactive CIAS absorber film converted from the Cu-In-Al precursor layer with $n \approx 0.28$ was used in fabrication of the solar cells. The output parameters of the highest efficiency solar cell (C5G of the active area 0.217 cm^2) were measured, $\eta \sim 4.9\%$, FF $\sim 47\%$, $V_{OC} \sim 364 \text{ mV}$ and $J_{SC} \sim 28.2 \text{ mA/cm}^2$. Marsillac *et al.* reported the highest efficiency solar cell based on CIAS absorber films which were synthesised by multisource elemental evaporation [32]. They achieved a highest cell efficiency of 16.9%, FF of 75.5%, V_{OC} of 621 mV and J_{SC} of 36.0 mA/cm^2 . There is no literature which reported thin film solar cells using CIAS absorber films produced by the method similar to that discussed in the work in this thesis.

The FF of the solar cell was significantly low ($< 50\%$). This was due to the high value of series resistance ($R_S \sim 5 \Omega \cdot \text{cm}^2$) which should ideally be $< 0.5 \Omega \cdot \text{cm}^2$. The shunt resistance ($R_{Sh} \sim 80 \Omega \cdot \text{cm}^2$) should also be $> 500 \text{ M}\Omega \cdot \text{cm}^2$, in order not to cause a drop in current through the cell. The resistance values were calculated according to method described in section 4.3.1. The lower shunt resistance could be due to several reasons such as the presence of pinholes in the absorber layer or poor adhesion of the layer on Mo or the porous nature of CdS buffer layer. The low cell conversion efficiency could also be partly due to incomplete absorber material conversion (phase segregation) and impurity defects resulting in the formation of electron-hole recombination centres in the cell. The cell performances were

promising considering that these results were for the first cell which was produced using Al containing thinner absorber film which was prepared by a two stage method, sputter depositions of precursor layers followed by selenisation in Se environment.

Summary of Discussions

In this thesis, the development of CIAS thin films for use in photovoltaic solar cells has been described. Initially the focus was given on depositing good quality (near to optimisation) back contact Mo layers on the SLG substrates. The good quality Mo layers were obtained by investigating the effects of sputtering Ar gas pressure and flow on the morphological and electrical properties of the Mo layer. The Mo bilayers were also deposited and investigated. The Mo single layers were found to be better than Mo bilayers in terms of adhesion of absorber thin films onto it. From investigations it was found that for the process settings, Ar pressure 5 mTorr, flow 30 sccm, deposition period 90 min and Mo target power 300 W, the Mo single layers were of good structural and electrical properties. Hence the back contact Mo layers used in the work described in this thesis were well adhered, conformal, low resistivity of $\sim 29 \mu\Omega\cdot\text{cm}$, pinhole free and reasonably thick in the range 700-800 nm. The single layers were in agreement with Mo bilayers reported by NREL group in terms of film structure and adhesion to the glass substrate. Although the low resistivity ($29 \mu\Omega\cdot\text{cm}$) obtained for the single Mo layer was higher than NREL's low resistivity range 12-14 $\mu\Omega\cdot\text{cm}$ for Mo bilayer, the single layer was good enough to use as back contact for CIS and CIAS thin film solar cells [118].

For the development of CIAS thin films the main objective was to optimise the base line process for the formation of high quality CIS absorber thin films ($x = 0$). It involved the RF magnetron sputter deposition of the Cu-In precursor layers and then conversion of these layers in a Se environment to form good quality CIS thin films on Mo-coated glass substrates. The required compositions of Cu-In layers were deposited by controlling the Cu and In metal target powers. The conversion of the Cu-In precursor layers for temperature 500°C using the Se capping method yielded good quality and adhesion of CIS films. The next objective was to reduce thickness of the absorber films by reduction in the thicknesses of the precursor layers. The investigation and characterisation of the influence of metallic Cu-In precursor layers of thicknesses in the range 90-400 nm on the properties of CIS thin films of thicknesses in the range 400-1600 nm demonstrated promising results. Surface roughness of the precursor layers and thin films were increased with thicknesses. This was attributed to increase in In-rich islands in precursor layers and increase in grain size in thin films with thickness, respectively. The Cu and In elements were well mixed and uniformly distributed in the precursor layers. The absorber films were converted completely with good grain morphology and chalcopyrite structure. The Na out-diffusion from the glass may have played important roles during conversion. The energy band gaps of the films were estimated in the range between 0.90-0.94 eV. The solar cells (total area $\approx 0.229 \text{ cm}^2$) fabricated using these thinner absorbers of thicknesses 500 nm and 900 nm yielded high conversion efficiencies of 4.3% and 8.2%, respectively. These efficiencies were recorded for the solar cells of un-optimised cell designs. These include grid coverage, resistance of metal and without ARC. The comparison of the cell output parameters with literature indicated promising results using the thinner 900 nm absorber films. Most work on thinner

absorber films are reported on the CIGS thin films [94, 185]. The output performance of this cell was limited due to incomplete light absorption and structural problems. However this work demonstrated that the solar cell fabrication could possibly be cost-effective due to less material usage of the expensive element In in the absorber films. The CIS related progress was useful to work further in developing CIAS thin films.

Initially sputter depositions of Al-In layers were carried out to study structural properties prior to actual Cu-In-Al precursor layers depositions. This study has revealed that there was immiscibility of Al into In due to low affinity of the Al-In phase as compared to that for Cu-In and Cu-Al. This was concluded from the characterisation and analyses of these layers using EDS, XRD, SEM techniques and literature relating to Al-In depositions [186, 187]. First trials of depositions of Cu-In-Al precursor layers were carried out with variations in $n = (\text{Al}/(\text{Al}+\text{In}))$ in the range 0-1. In the precursor layers (for $n > 0$) the phases detected relating to Cu-Al were AlCu_3 , AlCu_4 and CuAlO_2 . The conversion of these precursor layers yielded thin films of poor surface quality and material formation compared to CIS film. XRD data showed binary Al_2Se_3 and CIAS related phases in samples KJL-B and KJL-C. An Al distribution in thin film (KJL-C) was found to be non-uniform. This suggested incomplete conversion of the precursor layers into thin films. The solar cells fabricated using this absorber film yielded a cell conversion efficiency of $\sim 2\%$. The IPCE measurements have shown that the absorber film had an energy band gap of 0.98 eV, which is nearer to that for CIS thin films. Several problems were found which contributed to the poor quality of the thin films and poor output performance of the solar cells. These are the formation of an oxidised layer on the precursor layers, Al-rich phase segregation and poor surface features. From the investigations it

was found that the precursor layers were reasonably thick (up to 2.1 μm), therefore further work was focussed on depositing precursor layers of thicknesses $\leq 1 \mu\text{m}$.

The thinner layers of Cu-In-Al (thickness $\leq 1 \mu\text{m}$) precursors were sputter deposited with composition $m = \text{Cu}/(\text{Al}+\text{In})$ in the range 1.00-1.17 with Al content $n = \text{Al}/(\text{Al}+\text{In})$ in the range 0.28-0.54. XRD patterns for precursor layers had shown increasing AlCu_4 peak intensity with Al. Other binary $\text{Cu}_{11}\text{In}_9$ and Cu_2In phases were also found. It did not show any single elemental Cu, In or Al phase. It indicated proper intermixing of Cu-In and Cu-Al, however, there were no ternary Cu-In-Al and binary Al-In phases found to be formed. The elements were uniformly distributed in the precursor layers. Annealing of the Cu-In-Al precursor layers for different temperatures and pressures determined process conditions of 550°C and 5 mbar for 30 min duration to synthesise better quality films. These process settings were used in selenisation of thinner precursor layers. The converted films had better appearances and better adherence to the Mo-coated SLG substrates than films selenised from the earlier Al containing precursor layers. Characterisation of these films by XRD, SEM and MiniSIMS techniques provided more information in detail. The XRD patterns of the prominent (112) peaks relating to CIAS for thin films were found to be shifted to higher 2θ angle with reference to CIS film. Lattice parameters a and c were also changed which was attributed to Al content in the film, according to Vegard's law [191]. The crystallinity of the films became poorer with increasing Al in the precursors. This was observed in surface and cross-sectional images taken by SEM. In addition the cross-sectional images revealed formation of some kind of very thin layer at the bottom of thin film. MiniSIMS depth profile of the sample K181K ($n = 0.28$) suggested segregation of Al-rich phase at the bottom of the film (near to the surface of the substrate). The converted sample N172H4 which was from

the same batch of precursor layers with $n \approx 0.28$ was found to be photoactive. It was used in fabrication of solar cells. The output parameters of the most efficient cell (the active area = 0.217 cm^2) were measured to be $\eta \sim 4.9\%$, $\text{FF} \sim 47\%$, $V_{OC} \sim 364 \text{ mV}$ and $J_{SC} \sim 28.2 \text{ mA/cm}^2$. The solar cell conversion efficiency was reasonably good with absorber thickness less than $2 \text{ }\mu\text{m}$ and precursor layer of $0.55 \text{ }\mu\text{m}$ -thick. This demonstrated there will be a potential in reducing the absorber material cost by reducing CIAS thickness and hence using a smaller amount of In which is an expensive element and completely eliminating less abundant Ga. More work needs to be done in order to produce an absorber with uniformly incorporated Al. Korean researchers reported preparation of CIAS thin films by the similar method described in this thesis. However they have not reported fabrication of the solar device from CIAS absorber films [33].

The results obtained from thinner absorber films of CIAS demonstrated that the lower energy band gap CIS and wider energy band gap CIAS solar cells make suitable promising lower and upper components, respectively, for thin film multi-junction solar devices. This also makes it possible to progress towards achieving high efficiency device with a reduction in production cost due to minimising expensive In, eliminating less abundant Ga and introducing abundant and cheap Al.

CHAPTER 6

ENVIRONMENTAL **I**MFACTS OF

MATERIALS AND **P**ROCESSES

RELATED TO **C**_u**I**n**S**e₂ AND **C**_u(**I**n,**A**l)**S**e₂

THIN **F**ILM **S**OLAR **C**ELLS

6.1 Introduction

The manufacturing capacity of CuInSe₂ (CIS)-based thin film photovoltaic (PV) modules is expanding rapidly. They are predicted to have an output of 1 GW_p per annum between 2010 and 2020 [197]. The fabrication processes involve complex chemical reactions involving some toxic and flammable substances although in relatively small amounts. A large variety of materials may be used in manufacturing PV devices and there is some concern about the release of certain materials as by-products of normal or abnormal plant operations. Consequently there are strong environmental implications related to large scale production of CIS solar cells and utilisation of raw materials. The viability of CIS thin film solar cell technology to become a leading solar cell production technology depends on its acceptability to the general public and industry. Therefore, it is an important task to assess environmental implications of the materials and the related processes. Environmental assessment is also important in terms of growth of the solar cell technology in the European Union (EU) due to extensive legislation.

This chapter describes an environmental impact assessment of the materials used and related processes undertaken in the laboratory during the development of CIS based thin film solar cells.

CIS based solar cell structures used within the PV industry and the constituent materials and processes which have been used are shown in figure 6.1

All materials used to develop thin film CIS based solar cells described in this work are summarised in table 6.1. It includes the state of the material (solid, liquid and gas), the deposition process, role of the material in the process (not applicable if

n - type window layer	ZnO:Al (Sputtering)	ZnO:B (Sputtering)	ZnO:B (Sputtering)	ZnO:Al (Sputtering)
Buffer layer	CdS (CBD)	CdS (CBD)	Zn(S,OH) _x (CBD)	CdS (CBD)
p-type absorber layer	CIGS (Co-evaporation)	CIGSS (sputtering + selenisation/sulfurisation)	CIGSS (sputtering + selenisation / sulfurization) CIGS (sputtering + selenisation)	CIGS (Co-evaporation)
The back contact	Mo (Sputtering)	Mo (Sputtering) barrier	Mo (Sputtering) barrier	Mo (Sputtering) barrier
Substrate	SLG	SLG	SLG	Stainless steel foil
	ZSW / Würth Solar	Shell Solar Industry	Showa Shell Sekiyu	Global Solar

Figure 6.1 The constituent layers in CuInSe₂ based solar cells manufactured by major companies (Reproduced from [95, 198-200]).

Material (In the form of)	Deposition Process	Role in thin film solar cell development	Hazardous Identifications and related Health Hazards		Comments [reference]
Soda-lime glass (SLG) substrate cleaning					
Decon90 (Organic solvent)	-	Cleaning liquid for glass	Irritant	Prolonged skin contact may cause dermatitis. Ingestion may cause gastrointestinal irritation with nausea, vomiting and diarrhoea. Inhalation may cause respiratory tract irritation.	[197].
Iso propyl alcohol (Liquid)	-	To make water free substrate surface	Highly flammable	Irritation with pain and stinging with skin contact. Irritation to eyes. Ingestion causes several stomach problems such as gastrointestinal irritation with nausea, vomiting and diarrhoea. Vapours from IPA may cause drowsiness and dizziness.	[198].
Nitrogen gas (Oxygen free)	-	To dry glass slides	Non- flammable	Only inhalation in High concentration may cause death and asphyxiation i.e. suffocation due to lack of supply of oxygen. Causes loss of mobility and unconsciousness.	[199].
The back contact Mo and the Cu-In-Cu-In-Al precursor layer depositions					
Argon (Sputtering gas)	-	To form plasma and to sputter material	Not combustible (Inert)	Inhalation causes dizziness, dullness, headache and suffocation	[200].
Mo (Sputtering target)	Magnetron sputtering	Back contact layer	Not Combustible	May be harmful if used in powder form, may be harmful if ingested in quantity, may cause physical damage to eyes.	TLV – 10 mg/m ³ PEL – 5 mg/m ³ [201].
Cu (Sputtering target)	Magnetron sputtering	The precursor layer	Combustible	Harmful by inhalation in powder, fume or dust form and may cause irritation to eyes, Inhalation of fumes may cause metal fume fever, and longer skin exposure may cause skin sensitization.	TLV – 1 mg/m ³ PEL – 1mg/m ³ [202].

Table 6.1 Environmental impact assessment of material used in CIS and CIAS based thin film solar cells (*continued on the next page*).

Material (In the form of)	Deposition process	Role in thin film solar cell development	Hazardous Identifications and related health hazards		Comments [reference]
In (Sputtering targets)	Magnetron Sputtering	The precursor layer	Not Combustible	Dust form inhalation causes cough, shortness of breath, sore throat, exposure to eyes causes redness and pain. Ingestion of indium material causes nausea, vomiting. Precautions need to be taken in case material is released or spilled.	TLV- 0.1 gm/m ³ ; PEL – 0.1 mg/m ³ [203].
Al (Sputtering target)	Magnetron Sputtering	The precursor layer	Flammable, On contact with acid(s), alcohol, oxidants may cause risk of fire and explosion	Fine powder may cause breathing problem, long term or repeated exposure may have effects on the nervous system. Avoid contact with eyes and skin.	TLV / TWA value (Long exposure) 10 mg/m ³ for dust and 5 mg/m ³ [204].
The selenisation process					
Se (Pellets - Elemental form)	Selenisation	CIS and CIAS absorber layer formation by selenisation + annealing	Combustible Creates toxic fumes (or gases) in a fire.	Risk of fire and explosion on contact with oxidants. Inhalation causes irritation of nose, cough, dizziness, headache, breathing problem, nausea, sore throat, vomiting. Skin contact causes redness, skin burns, pain and discolouration. Contact with eyes causes redness, pain and blurred vision	TWA for Se is 0.1 mg/m ³ [205].
Etching process					
KCN (10% KCN concentration in water)	Wet Chemical Etching Process	To remove unwanted Cu ₂ Se surface phases	Very Toxic, Highly Flammable on contact with acid.	Very toxic if in contact with skin, eye and if swallowed. Very hazardous for aquatic environment.	TWA value is 5 mg (CN)/m ³ [206].

Table 6.1 Environmental impact assessment of material used in CIS and CIAS based thin film solar cells (*continued on the next page*).

Material (In the form of)	Deposition Process	Role in thin film solar cell development	Hazardous Identifications and related Health Hazards		Comments [reference]
CdS layer by Chemical Bath Deposition					
Ammonia -NH ₃ (Liquid)	CBD method	major reactant in CdS CBD method	low toxicity Flammable	May be poisonous if ingested and inhaled.	OEL 14 mg/m ³ [207].
Cadmium-Chloride CdCl ₂ (Solid)	CBD method	Source of Cd	eco-toxic	Poisonous and an irritant effect on human being and considered to be. It is also has high bioaccumulation potential. This non-volatile material consider as a suspected carcinogenic to human health.	TWA 0.025 mg (Cd)/m ³ [208].
Thiourea CS(NH ₂) ₂	CBD method	Key reactant and source for supply of S-ion in CBD method	highly toxic	Hazards to human health and poisonous if ingested and harmful by inhalation. It is skin and eyes irritant. Limited evidence of carcinogenic to human health.	OEL value is 0.3 mg/m ³ [209].
Sodium hydroxide - NaOH (Liquid)	CBD method	Strong base act as key reactant in CBD process	-	It is irritant, corrosive to eyes and skin.	OEL value is 14 mg/m ³ [210].
The window layer, transparent conducting oxide (TCO) layer and front contact depositions					
ZnO (Solid Target)	Magnetron Sputtering	Window layer	-	Inhalation of dust from deposited material causes fever, fatigue, cough, shortness of breath and also mild eye irritant.	[211].
ITO (Solid Target)	Magnetron Sputtering	TCO layer	No human toxicity	On overexposure causes mucous membrane and pulmonary irritation and mild eye irritation.	[212].
Ni (Solid Target)	Magnetron Sputtering	In conjunction with Al to deposit Ni-Al front (top) contacts	-	On overexposure causes mucous membrane and possibly irritation of the respiratory tract due to nickel dust or fume. Redness of eyes.	[213].

Table 6.1 Environmental impact assessment of material used in CIS and CIAS based thin film solar cells.

irrelevant), hazardous identification and related health hazards and finally comments with relevant references.

The column entitled “hazardous identification and related health hazards” contains details of toxicity of the materials which are hazardous to human health and their associated environmental and health impacts. The values for maximum exposure limit are represented in the form of time weighted average (TWA) values defined as per Control of Substance Hazardous to Health (COSHH) essentials published by the Health and Safety Executive (HSE) in the UK. Workplace exposure limits including short-term exposure (15 minutes reference TWA period) and long-term exposure (8 hours reference period) for hazardous material are taken from the amended list on October 2007 HSE website [218]. TWA or Threshold Limit Value (TLV) means the allowable average value of exposure concentration calculated by taking account of 8 working hours per day or 40 hours per week. Some information was taken from material safety data sheets (MSDS) which were generally supplied with ordered material or on the suppliers’ website. The values mentioned in the MSDS are according to Occupational Safety and Health Administration (OSHA) in the United States of America [219]. In some cases, especially for volatile liquids and gases the exposure limit is displayed as an occupation exposure limit (OEL), which means a limit on amount or concentration of volatile liquid or gases to which workers may be exposed. The Permissible Exposure Limit (PEL) value is defined by OSHA to protect workers in the manufacturing plant against the hazardous materials. This specifies concentration of substance in the air in the working environment.

The environmental impact assessment may be extended to cover all possible processes and materials which were used in the fabrication of CIS and $\text{CuIn}_{1-x}\text{Al}_x\text{Se}_2$ (CIAS) based thin film solar cells. A literature survey was carried out for relevant

processes and materials that have been reported by the world leaders in PV technology.

6.2 The Soda-Lime Glass Cleaning Process

In this work

Process

The soda-lime glass (SLG) substrate cleaning process involves cleaning of the substrate in several stages with de-ionised (DI) water and cleaning solutions. This process ensures removal of any dust or foreign particles, organic impurities and glass particles from the surface of the glass substrate before depositing any layer on it.

Materials and handling procedures

Two main chemicals – Decon90 detergent and IPA were used to clean and to remove water content from the glass slide surface, respectively. Finally nitrogen gas was used to dry the slides. Plenty of water was allowed to drain in the sink after usage of Decon90 and IPA in order to dilute the liquid waste.

Literature

European Commission (EC) directive 93/67/EEC regarding assessment of the environmental release of chemicals from the soap and liquid cleaning industry [220]. The guidelines reported are used to correlate with the release of chemicals in this process. In case of the manufacturing plant, the waste detergent is released into the river near the sea.

6.3 The Back Contact Molybdenum Deposition on SLG

In this work

Process

The back contact Mo layers were deposited onto the SLG substrates by sputtering from a Mo target. The sputtering process took place inside the main chamber in an Ar atmosphere.

Materials and handling procedures

The toxicity of Mo was considered not to be critical as long as it was not inhaled in the form dust or fumes. During normal operation this material was handled in the form of a solid target and during deposition the Mo disc was fitted inside a closed chamber under vacuum conditions in which the potential for accidental release was very low. As there is insignificant exposure to the atmosphere and the non-powder form of the materials, the risk to human health and its impact on the environment is minimal. There is a possibility for humans to come into contact with Mo dust during periodic cleaning of the deposition chamber. This was avoided by wearing apron, gloves and respirators with proper handling procedures for these materials [221]. Sputter deposited films on the substrate were exposed to air for a minimum time as usually those samples were kept in an air tight slide box and then used for further processing. All samples were handled wearing gloves. So there was no hazardous threat to human beings or the environment (inside the laboratory) as far as storage of the samples is concerned.

Literature

The CIS manufacturers (Fig. 6.1) have reported sputtering as a main technique to deposit Mo onto the glass substrate. As assessed earlier the risk to human health and impact on environment due to Mo is not critical. In table 6.1, the TLV and PEL values are comparatively higher than hazardous materials. There is no detailed discussion in the literature about precautions to be taken relating to Mo material.

6.4 The Cu-In and Cu-In-Al Precursor Layer Depositions and CuInSe₂/Cu(In,Al)Se₂ Absorber Formations on Mo-coated Glass Substrates

In this work

Process

The Cu-In and Cu-In-Al precursor layers were sputter deposited from separate Cu, In and Al targets in an Ar atmosphere. These precursors were selenised in a Se environment in the tube furnace to form CIS and CIAS films, respectively.

Materials and handling procedure

As discussed earlier about Mo material, Cu, In and Al do not cause any potential risk during deposition and handling of targets. Both TLV and PEL values are higher for Cu and Al than those values for In material. The selenisation process was carried out in a sealed tube furnace using elemental Se which was in the form of shot, or using Se capped glass slides, thus it is also environmentally safe. Care was taken during the cleaning of the tube as Se dust may have been present.

Literature

CIS Absorber

The CIS technology from the research laboratory has been transferred to the large scale in the industries around the world. The absorber layer has been produced using two main techniques by various manufactures (Fig. 6.1), co-evaporation of the elements and selenisation of the sputter deposited metallic precursor layers. These absorber films of quaternary CIGS and/or pentenary CIGSS are produced from a commercial point of view. In a production plant, there is a serious issue, however,

related to the higher toxicity of H₂Se. Only 1 ppm of concentration of H₂Se has an Immediately Dangerous to Life and Health (IDLH) rating. Hydrogen selenide has a TLV of 0.05 ppm above which it causes irritation and the onset of chronic disease [222].

A simplified hazardous management approach was reported by Moskowitz *et al.* [223]. They suggested the most efficient way to minimise health risk from hazardous material is to choose alternative technologies which do not use hazardous materials in large quantities. In addition they described a few useful things regarding hazard management strategies and these are summarised as follow:

- It is very important to select an alternative to specific hazardous processes and materials; also the plant safety authority should identify and assess strategies to prevent accidents or risk that may happen in the plant. These strategies include administrative (quality control and company worker training) and engineering (periodic maintenance and safeguard against process fluctuations).
- In case of release of hazardous materials or gases there should be strategies to prevent exposure to the general public. They stated strategies that may include storage of hazardous gas in a remote location, in cooperation with local government arrangement of an exclusion zone adjacent to production plant boundaries.

In conclusion, they stated that the growth of the PV industry will be only possible if both technical and process non-hazardous alternatives are implemented and effectively managed so that the risk to public health and safety will be minimised.

In 1988, Fthenakis *et al.* published a study report on an approach for designing an environmental control system for H₂Se with regard to routine emissions and accidental releases from a hypothetical facility manufacturing PV modules (which can generate 10 MW_p of electric power) [224]. During reactive sputtering, routine emission of H₂Se can be handled by a series of treatment equipment which include a venture scrubber, a packed-bed scrubber and an activated carbon adsorption bed. In case of accidental releases, they have proposed two options - a venture/packed bed scrubber, or containment / scrubbing system. These systems can be operated at reasonable cost and can effectively control the levels of emissions of toxic gas to protect the public health.

The papers have published checklists of safe practices for the storage, distribution, use and disposal of toxic and hazardous gases in PV cell production plant [225, 226]. From these published papers a few relevant guidelines which can be applied to H₂Se or any toxic gas are summarised as follows:

➤ ***Toxic gas cylinder handling and storage***

- Suggested to use specially modified or designed cart with brakes for moving cylinders from delivery van to gas storage room.
- Always store hazardous gas cylinders (H₂Se in this case) outside in an isolated secure area or in a purged gas cabinet.
- Use straps or chains to store gas cylinders firmly and with mechanical security.
- Cylinders which contain highly toxic gas should carry a flow restrictor with the smallest orifice (e.g. 0.006 inch) and this may vary as per process and safety requirements.

- When changing a H₂Se hazardous gas cylinder a cross-flow purge assembly should be attached. This will allow evacuating and flushing the entire lines and regulators with an inert gas several times and will make residual gas highly dilute.
- Gas monitors (which should sample once each half hour) should be installed inside and outside of each gas cabinet where any H₂Se and/or hydrogen mixed gas cylinders are stored.

➤ *Distribution of H₂Se gas*

- A fail-safe system is required to be installed to close gas flow in case of leakage due to rupture in the piping.
- Joints in metallic piping and tubing systems carrying H₂Se gas should be welded properly except for those inside a ventilated enclosure.
- It is suggested that there should be double piping with an outer jacket of inert gas at higher pressure than the pressure inside the tube.
- The distance between toxic gas storage area and process equipment should be short.
- There should be mechanical ventilation throughout the production area; pressure transducers should be fitted and interlocked with the automatic pneumatic valves or gas manifold systems

➤ *Usage of H₂Se gas*

- Respirators of appropriate specifications and approved by the concerned authority should be used during loading and unloading of the samples from the furnace.
- Vacuum loss detection systems should be installed to provide an automatic shutdown in emergency.

➤ **Gas exhaust system**

- The exhaust rate of toxic gas such as H₂Se should be sufficiently high; it is helpful to maintain negative pressure relative to the outside.
- The exhaust system should be fitted with an emergency source of power (backup) so that during a power cut sufficient fan speed (not less than half fan speed during normal operation) of the exhaust system will maintain a safe atmosphere.

Hydrogen selenide causes a potential health hazard not only as a feedstock but also in release of adsorbed gas from the thin films. Concentration of the H₂Se released from exposed absorber thin films may reach to 1 ppm in air in a production plant. The possibility of this type of risk will depend upon storage and handling of absorber films and also volume of air into which the gas is evolved [227].

Avancis GmbH in Germany used evaporation of Se instead of H₂Se in the process called the 'SEL-RTP' technique to fabricate CIGSSE modules [104]. Würth Solar Company has been fabricating CIS-based modules using a co-evaporation technique in which Cu, In, Ga and Se are used in elemental form. In both cases, the potential health hazards to workers arise while doing maintenance or cleaning of deposition equipment.

Hynes *et al.* reported that the development of a CuInS₂ absorber layer could possibly avoid use of Se and Cd (discussed in section 6.4) which are publically unacceptable and hazardous in properties [228].

CIAS Absorber

The advantages of replacing Ga with Al in terms of optical, material and cost-effectiveness factors have been discussed earlier. In addition there is a less impact on the environment with the inclusion of Al in place of Ga. Ga is a toxic material and

toxicity is high via the subcutaneous route. It causes dermatitis and affects bone marrow function [229, 230].

6.5 KCN Etching Process

In this work

Process

The wet etching process was carried out on the absorber film to remove unwanted Cu_xSe and oxide layers present over the surface. The etching process is straightforward and without any special equipment needed. The main concern was safe handling of potassium cyanide (KCN) material and its solution.

Materials and handling procedure

During the etching process, the concentration of KCN in deionised water solvent was generally 5-10 wt%. The etching process took place for between 90-120 s per sample.

The etching process was carried out in a fume cupboard and personnel protected by a face shield, special thicker gloves and an apron to the cover whole body. Maximum precautions were taken while undertaking the KCN etching process such as avoiding any liquid spillage and the process was carried out under supervision of at least one person from a safer distance.

Small quantities of KCN solution were neutralised by mixing in liquid bleach (neutraliser) for few hours. When the cyanide was neutralised, the resultant solution may be drained in the sink with heavy dilution of water [231].

Literature

Unfortunately, there is no literature found related to the KCN etching process in the PV industry. A number of important precautions which need to be taken include avoiding body contact due the very high toxicity of KCN and not to mix KCN solution with any acid as this causes an explosion.

6.6 CdS Deposition by CBD Method

In this work

Process

In this work a CdS layer in the range 70-100 nm was deposited on the absorber layers by chemical bath deposition.

Materials and handling procedure

The materials used to form the CdS bath are listed in table 6.1. The shaded area in the table signifies the hazardous materials which were used to prepare the CdS bath solution. Similar to the KCN etching process, this process was also carried out in an isolated fume cupboard. As explained earlier, skin contact with the CBD solution was avoided by using a full body apron and hand gloves.

After CBD process, the CdS solution which remained in the glass jar was transferred into glass bottles which were sent to the chemistry department for proper disposal by external agency.

Literature

The main concern in CdS deposition process is mainly due to cadmium (Cd) which is a heavy metal, highly toxic and non-degradable in nature. Cadmium is extracted as a by-product from mining, smelting and refining sulphide ores or Zn, and in a lesser quantity from lead and Cu [232]. Use of Cd in CIS based PV modules is mainly in the form CdS and in this case Cd is classified as a non-metallic. Therefore EU's Cd directive 91/338/EEC does allow Cd usage for PV applications. However there are implications of Cd usage in the production plant [233].

During CBD deposition, the vapours from the hot bath may contain airborne carcinogenic aerosols and these includes CdS and thiourea (which is also a suspected carcinogen and toxic to the aquatic world) [234].

Fthenakis published a paper which described environmental and health and safety issues related to PV technologies, and also strategies for reducing risks arising due to hazardous material in a 10 MW_p PV manufacturing plant [235]. According to it, the risk to workers arising from used or released Cd compound will be mainly in CdTe solar cells manufacturing plant. The CdS layer deposited on CIS based absorber is much thinner than that of CdTe and also less material is needed. Therefore the main safety issue in CIS production plant is not related to CdS but to the highly toxic H₂Se gas.

Bohland and Smigielski of First Solar, LLC, reported their company's CdTe module manufacturing (less than 500 KW annually) experience related to environmental, health and safety results [236]. Their main emphasis was to demonstrate that advanced hazardous materials and safety management techniques such as employee medical monitoring and process emission testing can minimise or prevent environmental exposures and human health risks from Cd based on their pilot scale manufacturing plant.

Researchers at Florida Solar Energy Centre suggested recycling of CdS bath to reduce the amount of toxic waste in the CBD method. They demonstrated that morphology of CdS films grown from freshly prepared and recycled CBD solutions were similar [237].

In the last decade, research efforts have been taken to replace toxic CdS buffer layer by other non-toxic or less toxic Cd-free buffer layer without insignificant losses in cell performance. The Cd-free buffer layers are mainly chalcogenides

(oxides, selenides and sulphides) of the two elements Zn and In, e.g. ZnO, ZnMgO, ZnSe, ZnS, In(OH)₃, In₂S₃ and In₂Se₃ [238]. Showa Shell has developed CIGS-based photovoltaic modules with a Cd-free Zn(O,S,OH)_x buffer layer and yielded highest efficiency 13.4% [239].

Nieuwlaar *et al.* reported various issues and approaches regarding the environmental aspects of PV systems discussed in the Utrecht workshop [240]. They stated that the use of Cd material in PV panels gave no signs of immediate risks to human health and environment.

In particular relevance to this work, immediate risks from the production process to the human health or to the environment are considered to be not critical.

6.7 ZnO, TCO and Front Metallic Ni-Al Layers Depositions

In this work

Process

The window layers intrinsic ZnO, ITO as a TCO and front metallic Ni-Al layers were sputter deposited from separate Zn, ITO and Ni, Al targets, respectively. The sputtering process took place in a Kurt J Lesker sputtering system.

Materials and handling procedure

According to table 6.1, materials used for depositions of ZnO, ITO and Ni-Al layers were in the form of solid sputtering targets. The powder form of these materials does not cause any critical problem to human health. In this work, material usage was less in quantity and in frequency compared to that in case of Mo and the precursor layers. Furthermore, the cleaning of the sputtering chamber was carried out much less frequently.

6.8 Discussion

An environmental impact assessment was carried out on the materials and the processes related to the fabrication of CIS and CIAS thin film solar cells.

In the substrate cleaning process, the waste DI water and used IPA were drained safely in a sink by flushing with large amount of tap water. In a production plant the residual water is made non hazardous by passing through multiple filters (to remove solid wastes) and treating in multiple process to neutralise hazardous chemicals. After this only the treated and filtered water is allowed to drain to the local municipal system [241].

The absorber CIS and CIAS layers were produced by a two stage method. In the first stage, materials (Mo, Cu, In and Al) and processes (DC and RF sputtering) were considered an insignificant threat to the human and lab environment. Environmental impact was reduced by the usage of solid metal targets which were fitted inside the close sputtering chamber. In a pilot plant production process the first stage is considered to be safe to workers and the environment; the only risk arises during cleaning or maintaining of the deposition chambers. In this work care was taken to avoid the entry of metal or deposited material dust into the human body by wearing mask, gloves and lab coat. The second stage involved the conversion of precursor into CIS or CIAS thin films in a Se atmosphere. In this case the main concern arises due to the Se material itself, which was minimised by using elemental Se pellets. The selenisation process was carried out in a sealed tube furnace. During the process of loading and unloading of samples, the tube furnace, at room temperature, was flushed with Ar several times to remove unused Se using an air filter. The Se which condensed inside the quartz glass tube was removed and

disposed of carefully. Some commercial companies use elemental Se or H_2Se gas, but there is nothing in the literature reporting procedures for safe handling of Se in a production plant.

The major concern in the production of CIS thin film solar cells has arisen due to the CdS buffer layer. Cd based compounds are used in CBD of CdS buffer layers on CIS thin films. As discussed in section 6.6, maximum care was taken during handling and disposing of Cd compounds in this work. However, the amount of Cd used in CIS based solar cells is less than that used in CdTe thin film solar cells. In a production plant, the environmental impact due to Cd can be decreased by substituting a less hazardous Zn based window layer [234]. The amount of liquid waste from CBD can be reduced by recycling of CdS wastes. In this way there were no serious issues regarding large scale production of CIS modules due to availability of methods to treat liquid waste to environmentally acceptable levels [16].

Depositions of i-ZnO and ITO window layers and Ni-Al front contacts in the development of CIS solar cells does not create a serious impact on workers and the environment. This is because the ZnO, ITO, Ni and Al targets are fitted inside the deposition chamber. As mentioned in table 6.1, these materials causes health problem only when inhaled in dust form. This could only be possible if the deposition chamber was opened during cleaning or maintenance, when care would be taken by wearing face a mask and lab coat to prevent dust ingress into the body.

In summary, the sputtering deposition technique is considered to be adequately safe and causes insignificant impact to human beings and the environment. The selenisation process was carried out using elemental Se which is less hazardous than using H_2Se gas. The environmental impact due to the CdS deposition can be minimised by taking care with liquid waste disposal or recycling

CdS bath or substituting Cd-free buffer layers as described earlier. Depositions of window layers and front contacts created insignificant impact on the environment. In this way, the fabrication of CIS based thin film solar cells can be rendered acceptably safe.

CHAPTER 7

CONCLUSIONS

AND

FUTURE WORK

7.1 Conclusions

In this project, RF sputtered Mo layers to be used as the back contact for the CIS and CIAS thin film solar cells were optimised. The best Mo layers had a resistivities as low as $29 \mu\Omega\cdot\text{cm}$, were conformal to the substrate, had good crystallinity and were deposited under the following sputtering conditions; Mo target power 300 W, deposition time 90 min, Ar flow 30 sccm and sputtering pressure 5.3 mTorr. The optimum conditions were consistent with those reported by leading groups around the World [118, 122, 165, 169]. NREL reported producing an optimised Mo bilayer as a back contact layer for CIGS solar cells. In the case of work described in this thesis the optimised single layer of Mo was found to be better than the Mo bilayer structure in terms of absorber film adhesion. It was therefore decided to use the optimised single Mo layers as the back contact for CIS and CIAS thin film solar cells. These layers were typically 730 nm-thick.

CIS absorber layers were produced by RF magnetron sputter depositions of the Cu-In precursor layers followed by selenisation using elemental Se. The absorber layers were produced using an annealing temperature of 500°C , under pressure of 2 mbar and for a duration 30 min. It was also found that the films selenised using a Se capping method had better structural and optical properties than films selenised using Se vapour alone. These layers also had improved adherence to Mo-coated glass substrates. The investigations of sputtering and selenisation processes also made it possible to set a baseline for production of CIAS thin films.

The influence of altering the Cu-In precursor thicknesses in the range 90-400 nm, on the structural and optical properties of subsequently CIS thin films was also investigated. The synthesised CIS layers were typically 400-1600 nm-thick. The Cu-

In precursor layers used were found to be intermixed, with the Cu and In, uniformly distributed throughout the layers (as confirmed by XRD, SEM, and MiniSIMS). Analysis of the surface morphologies of thinner precursor layers by SEM revealed an increase in In-rich island density with increasing thickness. This was reflected in the roughness values measured using an AFM, from 6.9 nm for a 130 nm-ultra thin precursor layer, to 25.2 nm for a 400 nm-thin precursor layer. XRD characterisation of CIS films of different thicknesses showed a loss in preferred orientation with increasing film thickness. The CIS films had composition ratios of Cu/In within the range 0.85-1.20 and Se/(Cu+In) in between 1.04 and 1.32. According to SEM and AFM images, surface features showed that the absorber surface became rougher due to enlargement in grain size with thickness. MiniSIMS depth profiles of the metallic elements in the CIS thin films formed indicated uniform conversion of the metallic precursor layer. The energy band gaps of the CIS thin films formed were found to be in the range 0.94-0.98 eV. The CIS solar cells made using such layers had conversion efficiencies of 4.3% and 8.2%, for a total cell area 0.229 cm², were fabricated from the CIS absorbers of thicknesses 500 nm and 900 nm, respectively. These efficiencies were promising recorded for an un-optimised cell design as compared with NREL's 15.0% efficient CIS solar cells [81]. The thinner absorber layers used in these cells were without any band gap grading [185] (or back surface field (BSF) [94]). These would enhance current collection by reducing recombination losses near the back contact. By minimising losses due to the measuring probe, grid contact shadowing and adding an anti reflection coating it was determined that the cells conversion efficiencies would be > 11% for an absorber layer thickness of 1600 nm. This work also demonstrated an approach for cost-effective production of thin film solar cells by minimising material used and decreasing the thickness needed to form

a layer. The former point is particularly significant because In is a very expensive metal. Most of the work reported on thinner absorber layers has been concentrated on the CIGS thin films. NREL reported a highest efficiency of 17.1% cell using a 1.0 μm -thick CIGS absorber film [185]. This absorber layer had a graded band gap. A Swedish group at Uppsala University developed a 1.0 μm CIGS absorber film which yielded a cell conversion efficiency of 15.0% [94]. The thinner CIS absorber films developed in this work of lower energy band gap (~ 1.0 eV) would be suitable in fabricating a lower cell and using the CIGS material to make an upper cell in a multijunction device.

The fabrication of CIAS thin films using selenisation of Cu-In-Al precursor layers was also investigated. The characterisation of these layers using EDS, XRD and SEM showed a critical problem of negligible solubility of In in Al; this is also reported in literature [187, 242]. The phases found in the sputter deposited Cu-In-Al precursor layers were $\text{Cu}_{11}\text{In}_9$, CuIn_2 , AlCu_3 , AlCu_4 and CuAlO_2 . The oxidised phase could be formed due to the exposure of the precursor layer to air. The precursor layers adhered well to the SLG substrates due to use of a Cu seed layer (~ 5 nm) at the bottom of the layers. The conversion of Cu-In-Al and Cu-Al precursor layers was carried out in a Se environment (at 550°C , Ar pressure of 5 mbar and duration of 30 min) to form the absorber layers. The layers deposited were investigated using XRD, SEM and MiniSIMS to determine the chemical and physical properties of the selenised films. When using Cu-In-Al precursor layers with $n = 0.17$ to 0.84 XRD analyses showed the formation of phases mainly related to CIAS and Al_2Se_3 in thin films selenised. The CIAS related (112) peak was shifted in position towards higher angles on the 2θ scale with respect to the CIS (112) peak. SEM observations revealed that the surface morphologies of converted films were found to be poorer with

increasing 'n' value. Some of the cross-sectional images of the layers showed a bilayer morphology. Depth profiles indicated a non-uniform distribution of Al, but uniform distribution of the other three elements (Cu, In and Se) indicating accumulation of Al-rich phases near the bottom of the films. This "phase segregation" is attributed to incomplete incorporation of Al throughout the converted film. It was also confirmed from IPCE measurement that the energy band gap of the absorber film was estimated to be near to that for CIS. This work was found to be an important milestone in identifying several problems associated with formation of CIAS thin films. These are related to the incorporation of Al in thin films. From these investigations and reports in the literature it was concluded that this could be improved by reducing the precursor layer thickness and minimising air exposure of the precursor layers [193].

Three batches of the Cu-In-Al precursor layers with thicknesses ≤ 1000 nm and with 'n' in the range 0.28-0.54 were sputter deposited. The last layer deposited was an In cap layer to prevent oxidation of the Al. The precursor layers were then transferred to a separate chamber and a Se cap layer evaporated onto the precursor layers. XRD patterns of the precursor layers confirmed that there was formation of binary phases related to Cu-In and Cu-Al; however there was no phase related to Al-In present in these layers. MiniSIMS showed that the Cu, In and Al had uniform distributions throughout the thickness of the precursor layer. Cu-In-Al precursor layers with thicknesses in the range 1.3-2.0 μm were selenised and the resulting layers formed to have good adhesion to the substrate with good crystallinity and uniform surface morphology. XRD data of these films showed a shift in the prominent CIAS related (112) peak and a corresponding shift in lattice parameter with a change in Al content of the films. The lattice constants a and c values

decreased with increasing 'n' with non-linear behaviour i.e. Vegard's law was not obeyed [191]. The lattice spacing also decreased with Al in the precursor layers. The calculated value of d for the (112) reflection of a film with $n = 0.28$ corresponded to $x \approx 0.20$ [115]. This behaviour confirms that Al was incorporated in the film. However for layers with $n = 0.47$ and 0.54 the x values did not vary systematically. SEM images of these films showed loss in uniform grain morphology with increased Al content and there was found to be present a thin layer of second phase material in between the CIAS thin film and the Mo back contact. MiniSIMS showed that this thin layer was Al-rich which had segregated out during the selenisation process. The absorber film with $n = 0.28$ was found to be photoactive with an energy band gap of 1.10 eV i.e. higher than for CIS. The solar cells made from these CIAS absorber films had efficiencies up to 4.9%, $V_{OC} \sim 364$ mV, $J_{SC} \sim 28.2$ mA/cm² and the FF = 0.47. The reason for such a low FF was a high series resistance (~ 5 Ω .cm²) and low shunt resistance (~ 80 Ω .cm²).

The results obtained from using the CIAS absorber films demonstrated several advantageous factors associated with cost-effective production. In these films Ga was completely eliminated and the amount of In used reduced due to a reduction in absorber layer thickness. The energy band gap was also widened to some extent. These factors could make production of CIAS thin films and therefore solar cells production cost-effective.

The work contributed within Northumbria University research group is one of very few groups working on CIAS and one of two in the World (at present) on the 2-stage CIAS synthesis method described in this thesis. This demonstrated the most comprehensive work on this type of processing route and a major contribution to CIAS knowledge.

The processes and associated materials involved in the fabrication of CIAS thin films and solar cells were assessed for impact on the environment. From the assessment it was found that the main concern was related to use of Cd and Se which are hazardous. However with these materials the risks can be minimised. The use of Cd can be avoided by using a Cd-free buffer layer instead of CdS e.g. In_2S_3 , $\text{Zn}(\text{S},\text{O})$ and ZnO [243-245]. In the selenisation process, the elemental Se has less potential impact on humans and the environment than H_2Se gas. Hence the production of CIAS thin films solar cells can be rendered acceptably safe.

This work has demonstrated that production of thinner CIS and CIAS absorbers are cost-effective and makes them suitable promising components lower and upper cells, respectively, for a multijunction device. This may lead toward the development of a high efficiency CIAS device and manageable environmental impact.

7.2 Future Work

From the research work described in this thesis the following are the future work which needs to be continued:

- Investigations of the influence of the thinner layer of Cu-In precursors on the properties of CIS thin films and solar cells were carried out which demonstrated promising results. The solar cells fabricated from these films yielded a highest efficiency of value 8.2% recorded for a solar cell prepared from 900 nm, and 4.3% recorded for a cell made from 500 nm thick absorber films. Further work needs to be done to produce an absorber layer with band gap grading in order to enhance collection within it. The efficiencies were recorded for solar cells with an unoptimised design. The improvement in cell design including appropriate grid design and AR coating will improve the cell performance.
- The work on the sputter deposition of the Cu-In-Al precursor layers (thicknesses in the range 0.9-2.1 μm) has shown inadequate mixing of Cu, In and Al. This was believed to be associated with the reported low solubility of In in Al. Further investigations will be required to find broad sputtering procedures to deposit high quality, well mixed Cu-In-Al precursor layers. It could be achieved by trying depositions of well mixed Cu-In (Fig. F in Appendix I) and Cu-Al layers in stacked form (Fig. H in Appendix I) [246, 247].
- More effort is needed in future work to optimise the selenisation process for converting thicker (1-2 μm) Cu-In-Al precursor layers into CIAS films. These films should be single phase chalcopyrite structure, photoactive

material, be uniform in surface morphology with good adherence to the Mo-coated glass substrate. This should also ensure that there is no Al segregation or presence of a bilayer in the absorber layer structure. It may be due to problems associated with Se diffusion into the precursor layers. That may be made possible with a selenisation temperature higher than 600°C using high temperature compatible substrates (quartz glass or metallic substrates) and rapid thermal processing. Similarly it can be applicable to formation of CuAlSe₂ (CAS) thin films. The wider band gap of 2.67 eV CAS absorber films on transparent substrate could be incorporated as a window in the heterostructure solar devices.

List of references

1. A. E. Becquerel, *Recherches sur les effets de la radiation chimique de la lumière solaire, au moyen des courants électriques*, Compt. Rend. Acad. Sci. 9 (1839) 145-149, 561-567.
2. W. G. Adams and R. E. Day, *The action of light on selenium*, Proceedings of the Royal Society, London A25 (1877) 113.
3. D. M. Chapin, C. S. Fuller and G. L. Pearson, *A new silicon p-n junction photocell for converting solar radiation into electrical power*, Journal of Applied Physics 25 (1954) 676-677.
4. J. J. Loferski, *The first forty years: A brief history of the modern photovoltaic age*, Progress in Photovoltaics: Research and Applications 1 (1993) 67-78.
5. J. J. Loferski, *Theoretical considerations governing the choice of the optimum semiconductor for photovoltaic solar energy conversion*, Journal of Applied Physics 27 (1956) 777-784.
6. D. C. Reynolds, G. Leies, L. L. Antes and R. E. Marburger, *Photovoltaic effect in cadmium sulfide*, Physical Review 96 (1954) 533 - 534.
7. A. Carlson, *Research on semiconductor films*, WADC-TR-56-52 AD (1956) 97494.
8. R. J. Mytton, *Comparative review of silicon and thin film solar cells for space applications*, Physics in Technology 4 (1973) 92-112.
9. M. Archer and R. Hill, *Clean electricity from photovoltaics* Series on Photoconversion of Solar Energy Vol. 1 Imperial College Press (2001).
10. M. Yamaguchi, *Radiation-resistant solar cells for space use*, Solar Energy Materials and Solar Cells 68 (2001) 31-53.
11. R. W. Miles, *Photovoltaic solar cells: Choice of materials and production methods*, Vacuum, The World Energy Crisis: Some Vacuum-based Solutions 80 (2006) 1090-1097.
12. R. R. King, D. C. Law, K. M. Edmondson, C. M. Fetzer, G. S. Kinsey, H. Yoon, R. A. Sherif and N. H. Karam, *40% efficient metamorphic GaInP/GaInAs/Ge multijunction solar cells*, Applied Physics Letters 90 (2007) 183516.

13. J. Zhao, A. Wang, M. A. Green and F. Ferrazza, *Novel 19.8% efficient "honeycomb" textured multicrystalline and 24.4% monocrystalline silicon solar cells*, Applied Physics Letters 73 (1998) 1991–1993.
14. J. Zhao, A. Wang, F. Yun, G. Zhang, D. M. Roche, S. R. Wenham and M. A. Green, *20,000 PERL silicon cells for the "1996 World Solar Challenge" solar car race*, Progress in Photovoltaics: Research and Applications 5 (1997) 269–276.
15. O. Schultz, S. W. Glunz and G. P. Willeke, *Short Communication: Accelerated Publication: Multicrystalline silicon solar cells exceeding 20% efficiency*, Progress in Photovoltaics: Research and Applications 12 (2004) 553-558.
16. R. W. Miles, K. M. Hynes and I. Forbes, *Photovoltaic solar cells: An overview of state-of-the-art cell development and environmental issues*, Progress in Crystal Growth and Characterization of Materials 51 (2005) 1-42.
17. D. Ginley, M. A. Green and R. Collins, *Solar energy conversion toward 1 Terawatt*, article in the Material Research Society Bulletin "Harnessing materials for energy ", A publication of the Material Research Society 33 (2008)
18. <http://www.photon-magazine.com>.
19. D. L. Staebler and C. R. Wronski, *Optically induced conductivity changes in discharge-produced hydrogenated amorphous silicon*, Journal of Applied Physics 51 (1980) 3262-3268.
20. X. Wu, J. C. Keane, R. G. Dhere, C. DeHart, A. Duda, T. A. Gessert, S. Asher, D. H. Levi and P. Sheldon, *16.5%-efficient CdS/CdTe polycrystalline thin-film solar cell*, Proceeding of the 17th European Photovoltaic Solar Energy Conference, Munich, Germany (2001) 995-1000.
21. D. Cunningham, K. Davies, L. Grammond, E. Mopas, N. O'Connor, M. Rubcich, M. Sadeghi, D. Skinner and T. Trumbly, *Large area ApolloTM module performance and reliability*, Proceeding of the 28th IEEE Photovoltaic Specialists Conference, Alaska, USA (2000) 13-18.
22. H. S. Ullal and B. v. Roedern, *Thin-film CIGS and CdTe photovoltaic technologies: Commercialization, critical issues, and applications*,

- Proceedings of the 22nd European Photovoltaic Solar Energy Conference, Milan, Italy (2007) 1926-1929.
23. R. A. Mickelsen and W. S. Chen, *Polycrystalline thin-film CuInSe₂ solar cells*, Proceedings of the 16th IEEE Photovoltaic Specialists Conference, San Diego, CA, USA (1982) 781-785.
 24. J. AbuShama, S. Johnston, T. Moriarty, G. Teeter, K. Ramanathan and R. Noufi, *Properties of ZnO/CdS/CuInSe₂ solar cells with improved performance*, Progress in Photovoltaics: Research and Applications 12 (2004) 39-45.
 25. J. Schon, V. Alberts and E. Bucher, *Structural and optical characterization of polycrystalline CuInSe₂*, Thin Solid Films 301 (1997) 115-121.
 26. W. N. Shafarman, R. Klenk and B. E. McCandless, *Device and material characterization of Cu(InGa)Se₂ solar cells with increasing band gap*, Journal of Applied Physics 79 (1996) 7324-7328.
 27. I. Repins, M. A. Contreras, B. Egaas, C. DeHart, J. Scharf, C. L. Perkins, B. To and Rommel Noufi, *Short Communication: Accelerated Publication 19.9%-efficient ZnO/CdS/CuInGaSe₂ solar cell with 81.2% fill factor*, Progress in Photovoltaics: Research and Applications 16 (2008) 235-239.
 28. M. Kemell, M. Ritala and M. Leskela, *Thin film deposition methods for CuInSe₂ solar cells*, Critical Reviews in Solid State and Materials Sciences 30 (2005) 1-31.
 29. M. A. Green, *Consolidation of thin-film photovoltaic technology: The coming decade of opportunity*, Progress in Photovoltaics: Research and Applications 14 (2006) 383-392.
 30. P. D. Paulson, M. W. Haimbodi, S. Marsillac, R. W. Birkmire and W. N. Shafarman, *CuIn_{1-x}Al_xSe₂ thin films and solar cells*, Journal of Applied Physics 91 (2002) 10153-10156.
 31. W. N. Shafarman, S. Marsillac, T. Minemoto, P. D. Paulson and R. Birkmire, *Critical issues for Cu(In,Al)Se₂ thin film solar cells*, Proceedings of the IEEE 3rd Conference on Photovoltaic Energy Conversion, Osaka, Japan (2003) 2869-2873.

32. S. Marsillac, P. D. Paulson, M. W. Haimbodi, R. W. Birkmire and W. N. Shafarman, *High-efficiency solar cells based on Cu(InAl)Se₂ thin films*, Applied Physics Letters 81 (2002) 1350-1352.
33. J. Yun, R. Chalapathy, S. Ahn, J. Lee, J. Song and K. Yoon, *Growth of CuIn_{1-x}Al_xSe₂ thin films by selenization of metallic precursors in Se vapor*, Proceedings of the 4th IEEE World Conference on Photovoltaic Energy Conversion, Hawaii, USA (2006) 579-581.
34. K. J. H. Phillips *Guide to the Sun* Cambridge University Press (1992).
35. S. M. Sze, *Semiconductor devices - Physics and Technology* John Willey & Sons (1985).
36. www.nrel.gov.
37. B. G. Streetman and S. Banerjee, *Solid state electronic devices* 5th edition Prentice Hall (2000).
38. R. L. Anderson, *Experiments on Ge-GaAs heterojunctions*, Solid-State Electronics 5 (1962) 341-344.
39. S. S. Perlman and D. L. Feucht, *P-n heterojunctions*, Solid-State Electronics 7 (1964) 911-923.
40. R. H. Rediker, S. Stopek and J. H. R. Ward, *Interface-alloy epitaxial heterojunctions*, Solid-State Electronics 7 (1964) 621-622.
41. A. R. Riben and D. L. Feucht, *nGe---pGaAs Heterojunctions*, Solid-State Electronics 9 (1966) 1055-1065.
42. T. Schulmeyer, R. Kniese, R. Hunger, W. Jaegermann, M. Powalla and A. Klein, *Influence of Cu(In,Ga)Se₂ band gap on the valence band offset with CdS*, Thin Solid Films, Proceedings of Symposium D on Thin Film and Nano-Structured Materials for Photovoltaics, of the E-MRS 2003 Spring Conference 451-452 (2004) 420-423.
43. S.-H. Wei and A. Zunger, *Band offsets at the CdS/CuInSe₂ heterojunction*, Applied Physics Letters 63 (1993) 2549-2551.
44. T. Yamaguchi, J. Matsufusa and A. Yoshida, *Thin films of CuInSe₂ prepared by RF sputtering from various compositional powder targets*, Solar Energy Materials and Solar Cells 27 (1992) 25-35.
45. J. P. Donnelly and A. G. Milnes, *Current/voltage characteristics of p-n Ge-Si and Ge-GaAs heterojunctions (Current characteristics of solution and vapor*

- grown *p-n Ge-Si and Ge-GaAs heterojunctions as function of voltage and temperature*), Proceedings of the IEE, 113, (1966) 1468-1476.
46. J. Nelson, *The physics of solar cells*, Imperial College Press (2003).
 47. R. H. Bube, *Photovoltaic Materials-Series on Properties of Semiconductor Materials* Imperial College Press (1998).
 48. S. Tsurekawa, K. Kido and T. Watanabe, *Interfacial state and potential barrier height associated with grain boundaries in polycrystalline silicon*, Materials Science and Engineering: A, International Symposium on Physics of Materials, 2005 462 (2007) 61-67.
 49. L. D. Partain, *Solar cells and their applications* Wiley series in microwave and optical engineering, John Wiley & Sons, Inc (1995).
 50. J. R. Sites, J. E. Granata and J. F. Hiltner, *Losses due to polycrystallinity in thin-film solar cells*, Solar Energy Materials and Solar Cells 55 (1998) 43-50.
 51. Y. Hamakawa, *Thin-film solar cells-Next generation photovoltaics and its applications* Springer Series in Photonics, Vol. 13, Springer (2004).
 52. C. Guillén, M. Martínez and J. Herrero, *CuInSe₂ thin films obtained by a novel electrodeposition and sputtering combined method*, Vacuum 58 (2000) 594-601.
 53. U. Rau and H. Schock, *Electronic properties of Cu(In,Ga)Se₂ heterojunction solar cells-recent achievements, current understanding, and future challenges*, Applied Physics A: Materials Science & Processing 69 (1999) 131 - 147.
 54. L. L. Kazmerski, M. Hallerdt, P. J. Ireland, R. A. Mickelsen and W. S. Chen, *Optical properties and grain boundary effects in CuInSe₂*, Journal of Vacuum Science & Technology A: Vacuum, Surfaces, and Films 1 (1983) 395-398.
 55. J. R. Tuttle, D. Albin, R. J. Matson and R. Noufi, *A comprehensive study on the optical properties of thin-film CuInSe₂ as a function of composition and substrate temperature*, Journal of Applied Physics 66 (1989) 4408-4417.
 56. R. Caballero and C. Guillén, *CuInSe₂ Formation by selenization of sequentially evaporated metallic layers*, Solar Energy Materials and Solar Cells 86 (2005) 1-10.
 57. H. Hahn, G. Frank, W. Klingler, A.-D. Meyer and G. Störger, *Untersuchungen über ternäre Chalkogenide. V. Über einige ternäre*

- Chalkogenide mit Chalkopyritstruktur*, Zeitschrift für anorganische und allgemeine Chemie 271 (1953) 153-170.
58. I. G. Austin, C. H. L. Goodman and A. E. Pengelly, *New semiconductors with the chalcopyrite structure*, Journal of The Electrochemical Society 103 (1956) 609-610.
 59. S. Wagner, J. L. Shay, P. Migliorato and H. M. Kasper, *CuInSe₂/CdS heterojunction photovoltaic detectors*, Applied Physics Letters 25 (1974) 434-435.
 60. J. L. Shay, S. Wagner and H. M. Kasper, *Efficient CuInSe₂/CdS solar cells*, Applied Physics Letters 27 (1975) 89-90.
 61. L. L. Kazmerski, M. S. Ayyagari and G. A. Sanborn, *CuInS₂ thin films: Preparation and properties*, Journal of Applied Physics 46 (1975) 4865-4869.
 62. L. L. Kazmerski, F. R. White and G. K. Morgan, *Thin-film CuInSe₂/CdS heterojunction solar cells*, Applied Physics Letters 29 (1976) 268-270.
 63. R. A. Mickelsen and W. S. Chen, *Development of a 9.4% Efficient Thin-film CuInSe₂/CdS solar cells*, Proceedings of the 15th IEEE Photovoltaic Specialists Conference, Kissimmee, Florida, USA (1981) 800-803.
 64. J. Palm, S. Visbeck, W. Stetter, T. Niesen, M. Fürfänger, H. Vogt, H. Calwer, J. Baumbach, V. Probst and F. Karg, *CIS Process for commercial power module production*, 21st European Photovoltaic Solar Energy Conference, Dresden, Germany (2006) 1796-1800.
 65. W. E. Devaney, *Recent improvement in CuInSe₂/ZnCdS thin film solar cell efficiency*, Proceedings of the 18th IEEE Photovoltaic Specialist Conference, NY, USA (1985) 1733-1734.
 66. J. A. Thornton, D. G. Cornog, R. B. Hall, S. P. Shea and J. D. Meakin, *An investigation of reactive sputtering for depositing copper indium diselenide films for photovoltaic applications*, Proceedings of the 17th IEEE Photovoltaic Specialist Conference, NY (1984) 781-785.
 67. J. H. Ermer, R. B. Love, A. K. Khanna, S. C. Lewis and F. Cohen, *CdS/CuInSe₂ junctions fabricated by DC magnetron sputtering of Cu₂Se and In₂Se₃*, Proceedings of the 18th IEEE Photovoltaic Specialists Conference, NY, USA (1985) 1655-1658.

68. R. R. Potter, C. Eberspacher and L. E. Fabik, *Device analysis of CuInSe₂/(Cd.Zn)S/ZnO solar cells*, Proceedings of the 15th IEEE Photovoltaic Specialists Conference, Las Vegas, NV, USA (1985) 1659-1664.
69. K. Zweibel, H. S. Ullal and R. L. Mitchell, *Polycrystalline thin film photovoltaics*, Proceedings of the 21st IEEE Photovoltaic Specialists Conference, Kissimmee, FL, USA (1990) 458-466.
70. K. Mitchell, C. Eberspacher, J. Ermer and D. Pier, *Single and tandem junction CuInSe₂ cell and module technology*, Proceedings of the 20th IEEE Photovoltaic Specialists Conference, Las Vegas, USA (1988) 1384-1389.
71. C. Eberspacher, J. H. Ermer and K. W. Mitchell, *Process for making thin film solar cell*, US Patent number 5,045,409 (1991) Atlantic Richfield Company, Los Angeles, CA, USA.
72. A. Knowles, H. Oumous, M. Carter and R. Hill, *Thin films of CuInSe₂ produced by a solid state reaction from stacked elemental layers*, Semiconductor Science and Technology 3 (1988) 1143-1144.
73. A. Knowles, H. Oumous, M. J. Carter and R. Hill, *Properties of copper indium diselenide thin films produced by thermal annealing of elemental sandwich structures*, Proceedings of the 20th IEEE Photovoltaic Specialists Conference, Vol. 2, Las Vegas, USA (1988) 482-486.
74. V. K. Kapur and B. M. Basol, *Key issues and cost estimates for the fabrication of CuInSe₂ (CIS) PV modules by the two-stage process*, Proceedings of the 21st IEEE Photovoltaic Specialists Conference, Kissimmee, FL, USA (1990) 467-470.
75. B. M. Basol, V. K. Kapur and A. Halani, *Advances in high efficiency CuInSe₂ solar cells prepared by the selenization technique*, Proceedings of the 22nd IEEE Photovoltaic Specialists Conference, Vol. 2, Las Vegas, NV, USA (1991) 893-897.
76. R. Gay, J. Ermer, C. Fredric, K. Knapp, D. Pier, C. Jensen and D. Willett, *Progress in large-area CuInSe₂ thin film modules*, Proceedings of the 22nd IEEE Photovoltaic Specialists Conference, Las Vegas, NV, USA (1991) 848-852.
77. F. J. Pern, R. Noufi, A. Mason and A. Swartzlander, *Fabrication of polycrystalline thin film of CuInSe₂ by a one-step electrodeposition process*,

- Proceedings of the 19th IEEE Photovoltaic Specialist Conference, NY (1987) 1295-1298.
78. T. Arita, N.Suyama, Y. Kita, S. Kitamura and T. Hibino, *CuInSe₂ films prepared by screen-printing and sintering method*, Proceedings of the 20th IEEE Photovoltaic Specialists Conference, Las Vegas, NV, USA (1988) 1650-1655.
 79. J. Hedström, H. Ohlsen, M. Bodegard, A. Kylner, L. Stolt, D. Hariskos, M. Ruckh and H.-W. Schock, *ZnO/CdS/Cu(In,Ga)Se₂ thin film solar cells with improved performance*, Proceedings of the 23rd IEEE Photovoltaic Specialists Conference, Louisville, KY, USA (1993) 364-371.
 80. *American National Standards Institute ANSI C78.1431-1997*, First Edition, American National Standards for electric lamps, National Electrical Manufacturers Association (1997).
 81. J. AbuShama, R. Noufi, S. Johnston, S. Ward and X. Wu, *Improved performance in CuInSe₂ and surface-modified CuGaSe₂ solar cells*, Proceedings of the 31st IEEE Photovoltaic Specialists Conference, FL, USA (2005) 299-302.
 82. D. Tarrant and J. Ermer, *I-III-VI₂ multinary solar cells based on CuInSe₂*, Proceedings of the 23rd IEEE Photovoltaic Specialists Conference, Louisville, KY, USA (1993) 372-378.
 83. W. S. Chen, J. M. Stewart, B. J. Stanbery, W. E. Devaney and R. A. Mickelsen, *Development of thin film polycrystalline CuIn_{1-x}Ga_xSe₂ solar cells*, Proceedings of the 19th IEEE Photovoltaic Specialists Conference, NY, USA (1987) 1445-1447.
 84. B. Dimmler, H. Dittrich, R. Menner and H. W. Schock, *Performance and optimization of heterojunctions based on Cu(Ga,In)Se₂*, Proceedings of the 19th IEEE Photovoltaic Specialist Conference, NY, USA (1987) 1455-1459.
 85. R. Klenk, R. Menner, D. Cahen and H. W. Schock, *Improvement of Cu(Ga,In)Se₂ based solar cells by etching the absorber*, Proceedings of the 21st IEEE Photovoltaic Specialists Conference, FL, USA (1990) 481 - 486.
 86. L. Stolt, J. Hedstrom, J. Kessler, M. Ruckh, K.-O. Velthaus and H.-W. Schock, *ZnO/CdS/CuInSe₂ thin-film solar cells with improved performance*, Applied Physics Letters 62 (1993) 597-599.

87. V. Probst, J. Rimmasch, W. Riedl, W. Stetter, J. Holz, H. Harms, F. Karg and H. W. Schock, *The impact of controlled sodium incorporation on rapid thermal processed Cu(InGa)Se₂ thin films and devices*, Proceedings of the 1st IEEE World Conference on Photovoltaic Energy Conversion and the 24th IEEE Photovoltaic Specialists Conference, Waikoloa, HI, USA (1994) 144-147.
88. M. A. Contreras, A. M. Gabor, A. L. Tennant, S. Asher, J. Tuttle and Rommel Noufi, *Short Communication: Accelerated publication: 16.4% total-area conversion efficiency thin-film polycrystalline MgF₂/ZnO/CdS/Cu(In,Ga)Se₂/Mo solar cell*, Progress in Photovoltaics: Research and Applications 2 (1994) 287-292.
89. M. A. Contreras, J. Tuttle, A. Gabor, A. Tennant, K. Ramanathan, S. Asher, A. Franz, J. Keane, L. Wang, J. Scofield and R. Noufi, *High efficiency Cu(In,Ga)Se₂-based solar cells: processing of novel absorber structures*, Proceedings of the 24th IEEE Photovoltaic Specialists Conference and IEEE 1st World Conference on Photovoltaic Energy Conversion, Hawaii, USA (1994) 68-75.
90. K. Ramanathan, M. A. Contreras, C. L. Perkins, S. Asher, F. S. Hasoon, J. Keane, D. Young, M. Romero, W. Metzger, R. Noufi, J. Ward and A. Duda, *Properties of 19.2% efficiency ZnO/CdS/CuInGaSe₂ thin-film solar cells*, Progress in Photovoltaics: Research and Applications 11 (2003) 225-230.
91. K. Ramanathan, J. Keane and R. Noufi, *Properties of high-efficiency CIGS thin-film solar cells*, Proceedings of the 31st IEEE Photovoltaic Specialists Conference, FL, USA (2005) 195 - 198.
92. J. Kessler, M. Bodegård, J. Hedstrom and L. Stolt, *Baseline Cu(In,Ga)Se₂ device production: Control and statistical significance*, Solar Energy Materials and Solar Cells 67 (2001) 67-76.
93. J. Kessler, J. Wennerberg, M. Bodegard and L. Stolt, *Highly efficient Cu(In,Ga)Se₂ mini-modules*, Solar Energy Materials and Solar Cells 75 (2003) 35-46.
94. O. Lundberg, M. Bodegård, J. Malmström and L. Stolt, *Influence of the Cu(In,Ga)Se₂ thickness and Ga grading on solar cell performance*, Progress in Photovoltaics: Research and Applications 11 (2003) 77-88.

95. M. Powalla, *The R&D potential of CIS thin-film solar modules*, Proceedings of the 21st European Photovoltaic Solar Energy Conference, Dresden, Germany (2006) 1789-1795.
96. P. Jackson, R. Würz, U. Rau, J. Mattheis, M. Kurth, T. Schlötzer, G. Bilger and Jürgen H. Werner, *High quality baseline for high efficiency, Cu(In_{1-x}Ga_x)Se₂ solar cells*, Progress in Photovoltaics: Research and Applications 15 (2007) 507-519.
97. W. N. Shafarman and J. Zhu, *Effect of substrate temperature and deposition profile on evaporated Cu(InGa)Se₂ films and devices*, Thin Solid Films 361-362 (2000) 473-477.
98. D. Rudmann, A. F. d. Cunh, M. Kaelin, F.-J. Haug, H. Zogg and A. N. Tiwari, *Effects of Na on the growth of Cu(In,Ga)Se₂ thin films and solar cells*, Proceeding of the Material Research Society Symposium, Spring Meeting, San Francisco, USA (2003) B1.9.1-B1.9.12.
99. D. Rudmann, M. Kaelin, F. Haug, F. Kurdesau, H. Zogg and A. Tiwari, *Impact of Na on structural properties and interdiffusion of CuInSe₂ and CuGaSe₂ thin films*, Proceedings of 3rd World Conference on Photovoltaic Energy Conversion, Osaka, Japan (2003) 376 - 379.
100. T. Negami, Y. Hashimoto and S. Nishiwaki, *Cu(In,Ga)Se₂ thin-film solar cells with an efficiency of 18%*, Solar Energy Materials and Solar Cells 67 (2001) 331-335.
101. T. Negami, T. Satoh, Y. Hashimoto, S. Nishiwaki, S.-i. Shimakawa and S. Hayashi, *Large-area CIGS absorbers prepared by physical vapor deposition*, Solar Energy Materials and Solar Cells 67 (2001) 1-9.
102. J. Muller, J. Nowoczin and H. Schmitt, *Composition, structure and optical properties of sputtered thin films of CuInSe₂*, Thin Solid Films 496 (2006) 364-370.
103. K. Kushiya, *Progress in large-area Cu(In,Ga)Se₂-based thin-film modules with the efficiency of over 13%*, Proceedings of the 3rd World Conference on Photovoltaic Energy Conversion, Osaka, Japan (2003) 319-324.
104. V. Probst, W. Stetter, J. Palm, R. Toelle, S. Visbeck, H. Calwer, T. Niesen, H. Vogt, O. Hernandez, M. Wendl and F. H. Karg, *CIGSSE module pilot processing: from fundamental investigations to advanced performance*,

- Proceedings of 3rd World Conference on Photovoltaic Energy Conversion, Osaka, Japan (2003) 329-334.
105. M. A. Green, K. Emery, D. L. King, S. Igari and W. Warta, *Solar cell efficiency tables (version 24)*, Progress in Photovoltaics: Research and Applications 12 (2004) 365-372.
 106. R. N. Bhattacharya, W. Batchelor, K. Ramanathan, M. A. Contreras and T. Moriarty, *The performance of CuIn_{1-x}Ga_xSe₂-based photovoltaic cells prepared from low-cost precursor films*, Solar Energy Materials and Solar Cells 63 (2000) 367-374.
 107. S. Taunier, J. Six-Kurdi, P. P. Grand, A. Chomont, O. Ramdani, L. Parissi, P. Panheleux, N. Naghavi, C. Hubert, M. Ben-Farah, J. P. Fauvarque, J. Connolly, O. Roussel, P. Mogensen, E. Mahe, J. F. Guillemoles, D. Lincot and O. Kerrec, *Cu(In,Ga)(S,Se)₂ solar cells and modules by electrodeposition*, Thin Solid Films, E-MRS 2004 480-481 (2005) 526-531.
 108. K. T. Ramakrishna Reddy and R. W. Miles, *Surface characterization of sprayed CuGa_xIn_{1-x}Se₂ layers*, Journal of Materials Science: Materials in Electronics 14 (2003) 529-532.
 109. J. Kessler, J. Six-Kurdi, N. Naghavi, J.-F. Guillemoles, D. Lincot, O. Kerrec, M. Lamirand, L. Legras and P. Mogensen, *Progress in low-cost electrodeposition of Cu(In,Ga)(S,Se)₂ : The CISEL project*, Proceedings of the 20th European Photovoltaic Solar Energy Conference, Barcelona, Spain (2005) 1704-1708.
 110. E. Niemi and L. Stolt, *CuAlSe₂ for thin film solar cells*, Proceedings of the 8th International European Photovoltaic Solar Energy Conference, Florence, Italy (1988) 1070-1074.
 111. J. C. Bernède, S. Marsillac, C. E. Moctar and A. Conan, *Optical and electrical properties of CuAlSe₂ thin films obtained by selenization of Cu/Al/Cu . . Al/Cu layers sequentially deposited*, phys. stat. sol. (a) 161 (1997) 185-191.
 112. Y. B. K. Reddy and V. S. Raja, *Effect of Cu/Al ratio on the properties of CuAlSe₂ thin films prepared by co-evaporation*, Materials Chemistry and Physics 100 (2006) 152-157.

113. W. Gebicki, M. Igalson, W. Zajac and R. Trykozko, *Growth and characterisation of $CuAl_xIn_{1-x}Se_2$ mixed crystals*, Journal of Physics D: Applied Physics 23 (1990) 964-965.
114. F. Itoh, O. Saitoh, M. Kita, H. Nagamori and H. Oike, *Growth and characterization of $Cu(In,Al)Se_2$ by vacuum evaporation*, Solar Energy Materials and Solar Cells 50 (1998) 119-125.
115. M. W. Haimbodi, E. Gourmelon, P. D. Paulson, R. W. Birkmire and W. N. Shafarman, *$Cu(InAl)Se_2$ thin films and devices deposited by multisource evaporation*, Proceedings of the 28th IEEE Photovoltaic Specialists Conference, Anchorage, AK, USA (2000) 454-457.
116. W. N. Shafarman, S. Marsillac, P. D. Paulson, M. W. Haimbodi, T. Minemoto and R. W. Birkmire, *Material and device characterization of thin film $Cu(InAl)Se_2$ solar cells*, Proceeding of the 29th IEEE Photovoltaic Specialists Conference, New Orleans, Louisiana, USA (2002) 519-522.
117. Y. B. K. Reddy and V. S. Raja, *Preparation and characterization of $CuIn_{0.3}Al_{0.7}Se_2$ thin films for tandem solar cells*, Solar Energy Materials and Solar Cells 90 (2006) 1656-1665.
118. J. Scofield, A. Duda, D. Albin, B. Ballard and P. Predecki, *Sputtered molybdenum bilayer back contact for copper indium diselenide-based polycrystalline thin-film solar cells*, Thin Solid Films 260 (1995) 26-31.
119. K. Orgassa, H. Schock and J. Werner, *Alternative back contact materials for thin film $Cu(In,Ga)Se_2$ solar cells*, Thin Solid Films 431-432 (2003) 387-391.
120. U. Schmid and H. Seidel, *Effect of substrate properties and thermal annealing on the resistivity of molybdenum thin films*, Thin Solid Films 489 (2005) 310-319.
121. I. V. Malikov and G. M. Mikhailov, *Electrical resistivity of epitaxial molybdenum films grown by laser ablation deposition*, Journal of Applied Physics 82 (1997) 5555-5559.
122. C. Guillén and J. Herrero, *Low-resistivity Mo thin films prepared by evaporation onto 30 cm x 30 cm glass substrates*, Journal of Materials Processing Technology 143-144 (2003) 144-147.
123. D. C. Fisher, I. L. Repins, J. Schaefer, M. E. Beck, W. K. Batchelor, M. Young and S. Asher, *The effect of Mo morphology on the performance of*

- Cu(In,Ga)Se₂ thin films*, Proceedings of the 31st IEEE Photovoltaic Specialists Conference, FL, USA (2005) 371-374.
124. J. L. Alleman, H. Althani, R. Noufi, H. Moutinho, M. M. Al-jassim and F. Hasoon, *Dependence of the characteristics of Mo films on sputter conditions*, NCPV Program Review Meeting Report, NREL (2000) 239-240.
125. H. Al-Thani, F. S. Hasoon, M. Young, S. Asher, J. L. Alleman, M. M. Al-Jassim and D. L. Williamson, *The effect of Mo back contact on Na out-diffusion and device performance of Mo/Cu(In,Ga)Se₂/CdS/ZnO solar cells*, Proceedings of the 29th IEEE Photovoltaic Specialists Conference, New Orleans, Louisiana, USA (2002) 720- 723.
126. K. Granath, A. Rockett, M. Bodegård, C. Nender and L. Stolt, *Mechanical issues of Mo back contacts for Cu(In,Ga)Se₂ devices*, Proceedings of the 13th European Photovoltaic Solar Energy Conference, Nice, France (1995) 1983-1986.
127. K. Yoon, S. K. Kim, R. B. V. Chalapathy, J. H. Yun, J. C. Lee and J. Song, *Characterization of a molybdenum electrode deposited by sputtering and its effect on Cu(In,Ga)Se₂ solar cells*, Journal of the Korean Physical Society 45 (2004) 1114-1118.
128. N. B. Chaure, S. Bordas, A. P. Samantilleke, S. N. Chaure, J. Haigh and I. M. Dharmadasa, *Investigation of electronic quality of chemical bath deposited cadmium sulphide layers used in thin film photovoltaic solar cells*, Thin Solid Films 437 (2003) 10-17.
129. B.-S. Moon, J.-H. Lee and H. Jung, *Comparative studies of the properties of CdS films deposited on different substrates by R.F. sputtering*, Thin Solid Films, EMSR 2005 - Proceedings of Symposium F on Thin Film and Nanostructured Materials for Photovoltaics - EMRS 2005- Symposium F 511-512 (2006) 299-303.
130. V. Singh, B. P. Singh, T. P. Sharma and R. C. Tyagi, *Effect of ambient hydrogen sulphide on the optical properties of evaporated cadmium sulphide films*, Optical Materials 20 (2002) 171-175.
131. A. Romeo, M. Terheggen, D. Abou-Ras, D. L. Bätzner, F.-J. Haug, M. Kälin, D. Rudmann and A. N. Tiwari, *Development of thin-film Cu(In,Ga)Se₂ and*

- CdTe solar cells*, Progress in Photovoltaics: Research and Applications 12 (2004) 93-111.
132. J. Herrero, M. T. Gutierrez, C. Guillen, J. M. Dona, M. A. Martinez, A. M. Chaparro and R. Bayon, *Photovoltaic windows by chemical bath deposition*, Thin Solid Films 361-362 (2000) 28-33.
133. F. Adurodija, *Production of CuInSe₂ photovoltaic devices for commercial application*, PhD Thesis (1994) University of Northumbria, Newcastle upon Tyne, UK.
134. L. C. Olsen, P. Eschbach and S. Kundu, *Role of buffer layers in CIS-based solar cells*, Proceeding of the 29th IEEE Photovoltaic Specialists Conference, New Orleans, Louisiana, USA (2002) 652-655.
135. K. M. Hynes and J. Newham, *An investigation of the environmental implications of the chemical bath deposition of CdS through environmental risk assessment*, Proceedings of the 16th European Photovoltaic Solar Energy Conference, Glasgow, UK (2000) 2297-2300.
136. S. Siebentritt, *Alternative buffers for chalcopyrite solar cells*, Solar Energy, Thin Film PV 77 (2004) 767-775.
137. U. Zimmermann, M. Ruth and M. Edoff, *Cadmium-free CIGS mini-modules with ALD-grown Zn(O, S)-based buffer layers*, Proceedings of the 21st European Photovoltaic Solar Energy Conference, Dresden, Germany (2006) 1831-1834.
138. U. Rau and M. Schmidt, *Electronic properties of ZnO/CdS/Cu(In,Ga)Se₂ solar cells - aspects of heterojunction formation*, Thin Solid Films 387 (2001) 141-146.
139. E. Fortunato, D. Ginley, H. Hosono and D. C. Paine, *Transparent Conducting Oxides for Photovoltaics*, Material Research Society Bulletin 32 (2007) 242-247.
140. I. Konovalov, *Material requirements for CIS solar cells*, Thin Solid Films, Proceedings of Symposium D on Thin Film and Nano-Structured Materials for Photovoltaics and E-MRS 2003 Spring Conference 451-452 (2004) 413-419.
141. *Standard soda-lime glass substrate cleaning procedure established in the NPAC research lab by private communications with researchers.*

142. B. Chapman *Glow Discharge Processes-Sputtering and Plasma Etching* A Wiley-Interscience Publication (1980).
143. J. Vossen and W. Kern, eds. *Thin film processes* Academic Press Inc.(London)Ltd (1978).
144. D. Johnston, *Thin Films of Copper Indium Disulphide and Zinc-based Buffer Layers for Application in Photovoltaic Devices*, PhD Thesis (2005) University of Northumbria at Newcastle.
145. S. Munekawa, *Technical Note "Application of X-ray diffraction techniques to the semiconductor field"*, The Rigaku Journal 5 (1998) 31-34.
146. B. D. Cullity *Elements of X-ray Diffraction* 2nd Edition Addison-Wesley Publishing Company, Inc. (1978).
147. Siemens D5000 Diffractometer Manual Order No. C79000-G3476-C137-07 3-12.
148. H. Khatri and S. Marsillac, *The effect of deposition parameters on radiofrequency sputtered molybdenum thin films*, Journal of Physics: Condensed Matter 20 (2008) 055206-11.
149. M. I. Jones, I. R. McColl and D. M. Grant, *Effect of substrate preparation and deposition conditions on the preferred orientation of TiN coatings deposited by RF reactive sputtering*, Surface and Coatings Technology 132 (2000) 143-151.
150. G. Zoppi, K. Durose, S. J. C. Irvine and V. Barrioz, *Grain and crystal texture properties of absorber layers in MOCVD-grown CdTe/CdS solar cells*, Semicond. Sci. Technol. 21 (2006) 763–770.
151. *Oxford Instrument Information sheet obtained from Robert Best-Research Technician in NPAC (AMRI), Northumbria University, UK.*
152. M. T. Postek, K. S. Howard, A. H. Johnson and K. McMichael *Scanning electron microscopy- A student's handbook* Michael T. Postek, Jr. and Ladd Research Industries Inc. (1980).
153. *Personal Communication with Robert Best-AMRI Technician, AMRI, Northumbria University, UK.*
154. *Shimadzu Solidspec3700 Spectrophotometer- Instruction manual*, Shimadzu.

155. N. R. Aghamalyan, E. A. Kafadaryan, R. K. Hovsepyan and S. I. Petrosyan, *Absorption and reflection analysis of transparent conductive Ga-doped ZnO films*, *Semiconductor Science and Technology* 20 (2005) 80-85.
156. J. Vickerman *Surface Analysis-The Principal techniques* John Wiley & Sons (1997).
157. *The Millbrook MiniSIMS user manual-version 3.03*, Millbrook instruments limited (2004).
158. R. Howland and L. Benatar *A practical guide to scanning probe microscopy* Park Scientific Instruments (1997).
159. R. G. Seippel *Photovoltaics* Reston publishing company (1983).
160. A. L. Fahrenbruch and R. H. Bube *Fundamentals of solar cells: Photovoltaic solar energy conversion* Academic Press Inc. (1983).
161. L. M. Peter and H. Tributsch *Experimental techniques in photoelectrochemistry* Unpublished).
162. D. D. Shivagan, P. J. Dale, A. P. Samantilleke and L. M. Peter, *Electrodeposition of chalcopyrite films from ionic liquid electrolytes*, *Thin Solid Films*, Proceedings of Symposium O on Thin Film Chalcogenide Photovoltaic Materials, EMRS 2006 Conference 515 (2007) 5899-5903.
163. A. Kadam, N. Dhere, P. Holloway and E. Law, *Study of molybdenum back contact layer to achieve adherent and efficient CIGS₂ absorber thin-film solar cells*, *Journal of Vacuum Science & Technology A: Vacuum, Surfaces, and Films* 23 (2005) 1197-1201.
164. (PDF No.-00-042-1120) *Inorganic Crystal Structure Database (ICSD)*, (2006).
165. L. Assmann, J. Bernede, A. Drici, C. Amory, E. Halgand and M. Morsli, *Study of the Mo thin films and Mo/CIGS interface properties*, *Applied Surface Science* 246 (2005) 159-166.
166. T. Vink, M. Somers, J. Daams and A. Dirks, *Stress, strain, and microstructure of sputter-deposited Mo thin films*, *Journal of Applied Physics* 70 (1991) 4301-4308.
167. S. Marsillac and H. Khatri, *Study of CIGS solar cells back contact*, *Thin-Film Compound Semiconductor Photovoltaics*, Proceedings of the Material Research Society Symposium, San Francisco, USA 1012 (2007) 101-106.

168. G. Gordillo, F. Mesa and C. Calderón, *Electrical and morphological properties of low resistivity Mo thin films prepared by magnetron sputtering*, Brazilian Journal of Physics 36 (2006) 982 - 985.
169. A. Kadam, A. Jahagirdar and N. Dhere, *Effect of stresses in molybdenum back contact film on properties of CIGSS absorber layer*, Thin-Film Compound Semiconductor Photovoltaics, Proceedings of the Material Research Society Symposium, San Francisco, USA 865 (2005) 423-429.
170. M. Martínez and C. Guillén, *Effect of r.f.-sputtered Mo substrate on the microstructure of electrodeposited CuInSe₂ thin films*, Surface and Coatings Technology 110 (1998) 62-67.
171. *The standard CuInSe₂-based thin film solar cell processing method developed at NPAC, Northumbria University.*
172. G. Zoppi, K. Durose, S. J. C. Irvine and V. Barrioz, *Grain and crystal texture properties of absorber layers in MOCVD-grown CdTe/CdS solar cells*, Semiconductor Science and Technology 21 (2006) 763-770.
173. M. Gossila, H. Metzner and H.-E. Mahnke, *Coevaporated Cu-In films as precursors for solar cells*, Journal of Applied Physics 86 (1999) 3624-3632.
174. K. T. R. Reddy, I. Forbes, R. W. Miles, M. J. Carter and P. K. Dutta, *Growth of high-quality CuInSe₂ films by selenising sputtered Cu-In bilayers using a closed graphite box*, Materials Letters 37 (1998) 57-62.
175. V. Alberts and R. Swanepoel, *Material properties of CuInSe₂ prepared by H₂Se treatment of CuIn alloys*, Journal of Materials Science 33 (1998) 2919-2925.
176. P. Menna, A. Parretta, M. Pellegrino, L. Quercia and M. L. Addonizio, *Study of the selenium incorporation in sputtered Cu, in alloys*, Solar Energy Materials and Solar Cells 35 (1994) 165-170.
177. K. T. R. Reddy, P. K. Datta and M. J. Carter, *Detection of Crystalline Phases in CuInSe₂ Films Grown by Selenisation Process*, physica status solidi (a) 182 (2000) 679-685.
178. F. Jiang and J. Feng, *Effect of temperature on selenization process of metallic Cu-In alloy precursors*, Thin Solid Films 515 (2006) 1950-1955.

179. R. Caballero and C. Guillén, *CuInSe₂ Formation by selenization of sequentially evaporated metallic layers*, *Solar Energy Materials & Solar Cells* 86 (2005) 1–10.
180. T. Nakano, H. Mizuhashi and S. Baba, *Transition of roughness evolution in Cu-In alloy films by the formation of intermetallic compounds*, *Japanese Journal of Applied Physics* 44 (2005) 1932-1938.
181. R. Mitra, R. A. Hoffman, A. Madan and J. R. Weertman, *Effect of process variables on the structure, residual stress, and hardness of sputtered nanocrystalline nickel films*, *Journal of Materials Research* 16 (2001) 1010-1027.
182. T. Negami, S. Nishiwaki, Y. Hashimoto, N. Kohara and T. Wada, *Effect of absorber thickness on performance of Cu(In,Ga)Se₂ solar cells*, *Proceeding of the 2nd World Conference and Exhibition on Photovoltaic Solar Energy Conversion*, Vienna, Austria (1998) 1181-1184.
183. W. N. Shafarman, R. W. Birkmire, S. Marsillac, M. Marudachalam, N. Orbey and T. W. F. Russel, *Effect of reduced deposition temperature, time and thickness on Cu(In,Ga)Se₂ films and devices*, *Proceedings of the 26th IEEE Photovoltaic Specialist Energy Conference*, Anaheim (1997) 331–334.
184. S. S. Hegedus and W. N. Shafarman, *Thin-film solar cells: device measurements and analysis*, *Progress in Photovoltaics: Research and Applications* 12 (2004) 155-176.
185. K. Ramanathan, R. Noufi, B. To, D. L. Young, R. Bhattacharya, M. A. Contreras, R. G. Dhere and G. Teeter, *Processing and Properties of Sub-micron CIGS Solar Cells*, *Proceeding of the 4th World Conference on Photovoltaic Energy Conversion*, IEEE, Waikoloa, Hawaii (2006) 380-383.
186. G. Zoppi, I. Forbes, P. Nasikkar and R. Miles, *Physical Properties of CuAl_{1-x}In_xSe₂ Produced by Selenisation of Cu/Al/In(Se) Precursor Layers*, *Proceedings of the 21st European Photovoltaic Solar Energy Conference*, Dresden, Germany (2006) 1998-2001.
187. M. Marques, L. K. Teles, L. M. R. Scolfaro, J. R. Leite and L. G. Ferreira, *Ab initio studies of indium separated phases in AlGaInN quaternary alloys*, *physica status solidi (c)* 2 (2005) 2508–2511.

188. S. Jost, F. Hergert, R. Hock, M. Purwins and R. Enderle, *Real-time investigations of selenization reactions in the system Cu-In-Al-Se*, *physica status solidi (a)* 203 (2006) 2581-2587.
189. *Inorganic Crystal Structure Database (ICSD)*, (2006).
190. C. A. D. Rincon, M. T. Mora and M. Leon, *Growth and characterization of $CuIn_xAl_{1-x}Se_2$* , The 11th Conference on Ternary and Multinary Compounds, ICTMC - 11, Institute of Physics Conference, Salford, UK (1997) 123-126.
191. F. Hergert, R. Hock and S. Schorr, *Pentanary chalcopyrite compounds without tetragonal deformation in the heptanary system $Cu(Al,Ga,In)(S,Se,Te)_2$* , *Solar Energy Materials and Solar Cells* 91 (2007) 44-46.
192. Y. B. K. Reddy, V. S. Raja and B. Sreedhar, *Growth and characterization of $CuIn_{1-x}Al_xSe_2$ thin films deposited by co-evaporation*, *Journal of Physics D: Applied Physics* (2006) 5124-5132.
193. M. W. Haimbodi, *Physical vapor deposition and analysis of copper indium aluminum diselenide thin films for high band gap solar cells*, PhD thesis (2003) University of Delaware, USA.
194. E. Halgand, J. C. Bernede, S. Marsillac and J. Kessler, *Physico-chemical characterisation of $Cu(In,Al)Se_2$ thin film for solar cells obtained by a selenisation process*, *Thin Solid Films* 480-481 (2005) 443-446.
195. G. Zoppi, I. Forbes, P. Nasikkar and R. W. Miles, *Characterisation of thin films $CuIn_{1-x}Al_xSe_2$ prepared by selenisation of magnetron sputtered metallic precursors*, *Thin-Film Compound Semiconductor Photovoltaics*, Proceedings of the Material Research Society Symposium, San Francisco, USA 1012 (2007) 349-354.
196. T. Minemoto, T. Hayashi, T. Araki and H. Takakura, *Electronic properties of $Cu(In,Al)Se_2$ solar cells prepared by three-stage evaporation*, ENERGEX, The 12th International Energy Conference & Exhibition, Singapore (2007).
197. J. Springer, D. Hariskos and F. Gudat, *Recovery of Indium and Gallium From CIGS Manufacturing Wastes*, Proceedings of the 21st European Photovoltaic Solar Energy Conference, Dresden, Germany (2006) 1827-1830.
198. V. Probst, J. Palm, S. Visbeck, T. Niesen, R. Tolle, A. Lerchenberger, M. Wendl, H. Vogt, H. Calwer, W. Stetter and F. Karg, *New developments in*

- Cu(In,Ga)(S, Se)₂ thin film modules formed by rapid thermal processing of stacked elemental layers*, Solar Energy Materials and Solar Cells, 14th International Photovoltaic Science and Engineering Conference 90 (2006) 3115-3123.
199. K. Kushiya, M. Ohshita, I. Hara, Y. Tanaka, B. Sang, Y. Nagoya, M. Tachiyuki and O. Yamase, *Yield issues on the fabrication of 30 cmx30 cm-sized Cu(In,Ga)Se₂-based thin-film modules*, Solar Energy Materials and Solar Cells 75 (2003) 171-178.
 200. S. Wiedeman, R. Butcher, J. Fogleboch, J. Muha, R.G. Wendt, M. Beck and J. Britt, *CIGS Processing on flexible polyimide substrates*, National Centre for Photovoltaics Program Review Meeting Proceedings (2001) 49 - 50.
 201. *Decon 90 Material safety data sheet # 89300*, Fisher Scientific UK (2005).
 202. *Isopropanol (IPA) Material safety data sheet # 95533*, Fisher Scientific UK (2006).
 203. *Nitrogen (N₂ - Oxygen free), Material Safety Data Sheet*. (2006), BOC.
 204. *Argon, International Chemical Safety Cards # 0154, National Institute for Occupational Health and Safety*, <http://www.cdc.gov/niosh/ipcsneng/neng0154.html>, (2003).
 205. *Molybdenum (Mo), Material safety data sheet*. Kurt J. Lesker Company (1994).
 206. *Copper (Cu), Material safety data sheet* Kurt J. Lesker Company (2005).
 207. *Indium (In), Material safety data sheet* Kurt J. Lesker Company (1996).
 208. *Aluminum (Al), Material safety data sheet* Kurt J. Lesker Company (1993).
 209. *Selenium (Se) Shot, Material safety data sheet* Alfa Aesar (2007) 1-3.
 210. *Potassium cyanide (KCN) Material safety data sheet*, Sigma-Aldrich (2006) 1-8.
 211. *Ammonia (NH₃) Material safety data sheet*, Sigma-Aldrich (2006) 1-7.
 212. *Cadmium Chloride (CdCl₂) Material safety data sheet*, Sigma-Aldrich (2006) 1-20.
 213. *Thiourea (CS(NH₂)₂) Material safety data sheet*, Sigma-Aldrich (2006) 1-9.
 214. *Sodium hydroxide (NaOH) Material safety data sheet*, Acros Organics (2002).

215. *Zinc Oxide (ZnO), Material safety data sheet.* (1991) Kurt J. Lesker Company.
216. *Indium-Tin Oxide (ITO), Material safety data sheet.* (2006) Kurt J. Lesker Company.
217. *Nickel (Ni), Material safety data sheet.* (2006) Kurt J. Lesker Company.
218. www.hse.gov.uk.
219. www.osha.gov.
220. *Technical guidance document in support of commission directive 93/67/EEC on risk assessment for new notified substances and commission regulation (EC) No 1488/94 risk assessment for existing substances - Part IV,* Luxembourg: Office for official Publications of the European Communities (1996) 629-739.
221. *Copper Indium diselenide Photovoltaic Technology- Photovoltaic Industry Information Service Report T-8,* (1989) 50.
222. V. M. Fthenakis and P. D. Moskowitz, *Photovoltaics: environmental, health and safety issues and perspectives,* Progress in Photovoltaics: Research and Applications 8 (2000) 27-38.
223. P. D. Moskowitz, V. M. Fthenakis, L. D. Hamilton and J. C. Lee, *Public health issues in photovoltaic energy systems: an overview of concerns,* Solar Cells 19 (1987) 287-299.
224. V. M. Fthenakis, P. D. Moskowitz and R. D. Sproull, *Control of accidental releases of hydrogen selenide and hydrogen sulphide in the manufacture of photovoltaic cells: a feasibility study,* Journal of Loss Prevention in the Process Industries 1 (1988) 206-212.
225. P. D. Moskowitz and V. M. Fthenakis, *A checklist of suggested safe practices for the storage, distribution, use and disposal of toxic and hazardous gases in photovoltaic cell production,* Solar Cells 31 (1991) 513 - 525.
226. R. G. Wolfson and S. M. Vernon, *Safety in thin film semiconductor deposition,* Solar Cells 19 (1987) 215-224.
227. J. J. Roy, *Precautions with hydrogen selenide,* Solar Cells 19 (1987) 283-285.
228. K. M. Hynes, I. Forbes, R. W. Miles, P. Nasikkar, D. Lane, K. D. Rogers and J. D. Painter, *The Manufacture of CIGS Based Thin Film PV Cells With Minimal Environmental Impact,* Proceedings of the Photovoltaic Science,

- Applications and Technology (PVSAT-2) Conference, Loughborough, UK (2005) 69-76.
229. *Gallium (Ga)*, *Material safety data sheet* Sigma-Aldrich (2007).
 230. J. M. Stewart, *Some health and safety concerns in the research and production of CuInSe₂/CdZnS solar cells*, *Solar Cells* 19 (1987) 237-243.
 231. Personal Communication with Dr. Phillip Dale at University of Bath, UK (2005).
 232. www.webelements.com.
 233. M. J. d. Wild-Scholten, K. Wambach, E. A. Alsema and A. Jäger-Waldau, *Implications of European environmental legislation for photovoltaic systems*, *Proceedings of the 20th European Photovoltaic Solar Energy Conference*, Barcelona, Spain (2005) 3143-3147.
 234. K. M. Hynes, I. Forbes, R. W. Miles, J. D. Painter, D. W. Lane and K. D. Rogers, *An environmental assessment of the manufacture of CIGS based thin film PV cells*, *Proceedings of the 19th European Photovoltaic Solar Energy Conference*, Paris, France (2004) 2529-2532.
 235. V. M. Fthenakis, *Multilayer Protection Analysis for Photovoltaic Manufacturing Facilities*, *Process Safety Progress* 20 (2001) 87-94.
 236. J. R. Bohland and K. Smigielski, *First Solar's CdTe module manufacturing experience; environmental, health and safety results*, *Proceedings of the 28th IEEE Photovoltaic Specialists Conference*, Anchorage, USA (2000) 575-578.
 237. N. G. Dhere, S. S. Kulkarni and A. A. Kadam, *CdS bath recycling and toxic waste reduction*, *Proceedings of the 19th European Photovoltaic Solar Energy Conference*, Paris, France (2004) 1966-1968.
 238. D. Hariskos, S. Spiering and M. Powalla, *Buffer layers in Cu(In,Ga)Se₂ solar cells and modules*, *Thin Solid Films*, EMRS-2004, 480-481 (2005) 99-109.
 239. Y. Tanaka, N. Akema, T. Morishita, D. Okumura and K. Kushiya, *Improvement of V_{oc} upward of 600 mV/cell with CIGS-based absorber prepared by selenization/sulfurization.*, *Proceedings of the 17th European Photovoltaic Solar Energy Conference*, Munich, Germany (2001) 989-994.
 240. E. A. Evert Nieuwlaar, *PV power systems and the environment: results of an expert workshop*, *Progress in Photovoltaics: Research and Applications* 6 (1998) 87-90.

241. <http://www.firstsolar.com/production.php>.
242. http://www.crct.polymtl.ca/FACT/phase_diagram.php?file=Al-In.jpg&dir=SGTE.
243. R. Sáez-Araoz, A. Ennaoui, T. P. Niesen, A. Neisser and M. C. Lux-Steiner, *Scaling up of efficient Cd-free thin film Cu(In,Ga)(S,Se)₂ and CuInS₂ PV-devices with a Zn(S,O) buffer layer*, Proceeding of the 22nd European Photovoltaic Solar Energy Conference, Milan, Italy (2007) 2360-2363.
244. R. Verma, D. Brémaud, S. Bücheler, S. Seyrling, H. Zogg and A. N. Tiwari, *Physical vapor deposition of In₂S₃ buffer on Cu(In,Ga)Se₂ absorber: optimization of processing steps for improved cell performance*, Proceeding of the 22nd European Photovoltaic Solar Energy Conference, Milan, Italy (2007) 2315-2319.
245. A. Yamada, H. Miyazaki, Y. Chiba and M. Konagai, *High-efficiency Cu(InGa)Se₂ solar cells with a zinc-based buffer layer*, Thin Solid Films, E-MRS 2004 480-481 (2005) 503-508.
246. http://www.crct.polymtl.ca/FACT/phase_diagram.php?file=Cu-In.jpg&dir=FScopp.
247. http://www.crct.polymtl.ca/FACT/phase_diagram.php?file=Cu-Al.jpg&dir=FScopp.

APPENDICES

Appendix I

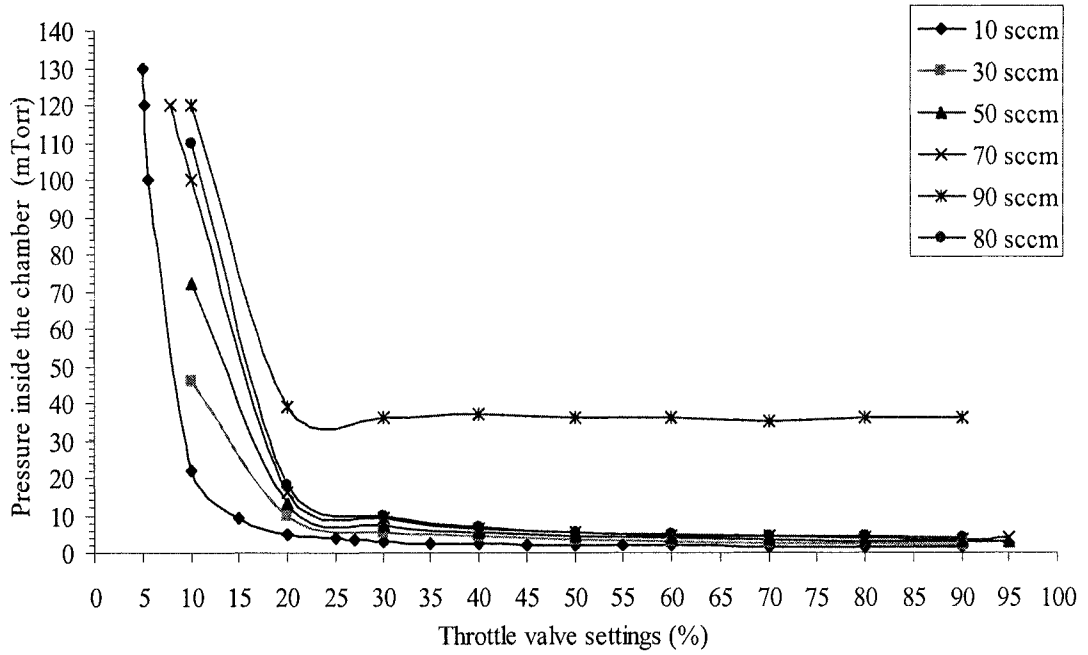


Figure A Pressure inside the Nordiko 2000 RF magnetron sputtering system chamber with different Ar gas flow and throttle valve settings.

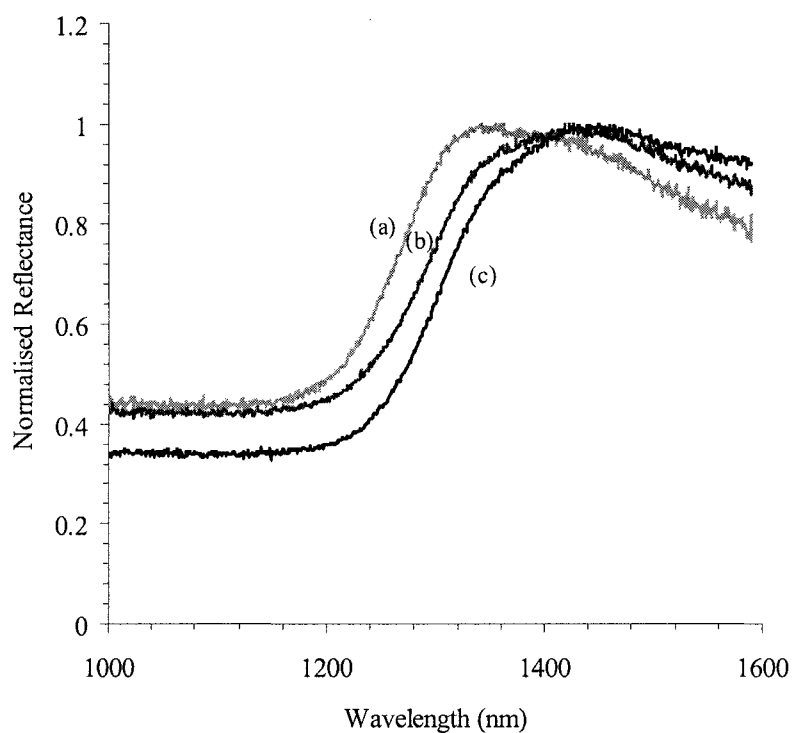
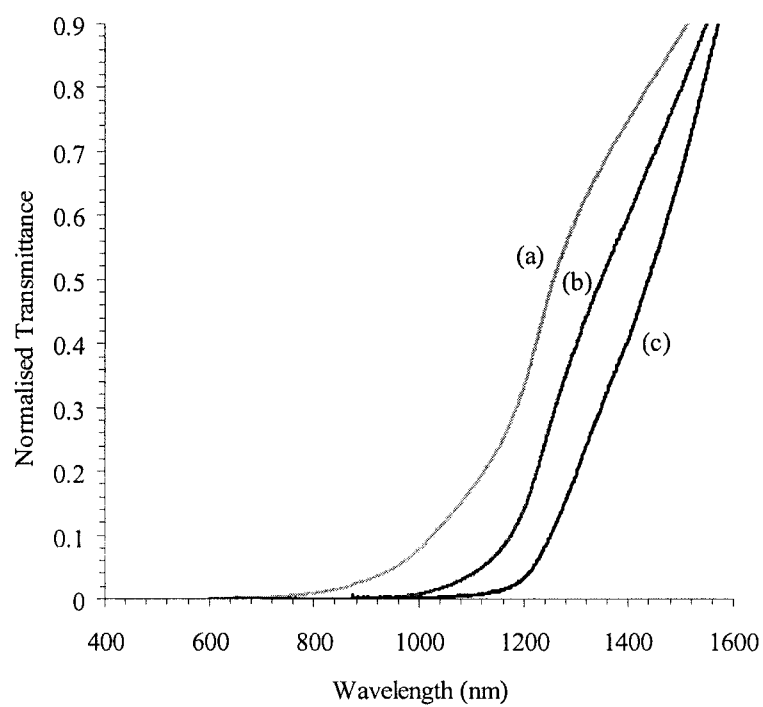


Figure B Normalized transmittance (top) and reflectance (bottom) versus wavelength pattern of CIS thin films of samples (a) B (500 nm); (b) D (900 nm) and (c) F (1600 nm).

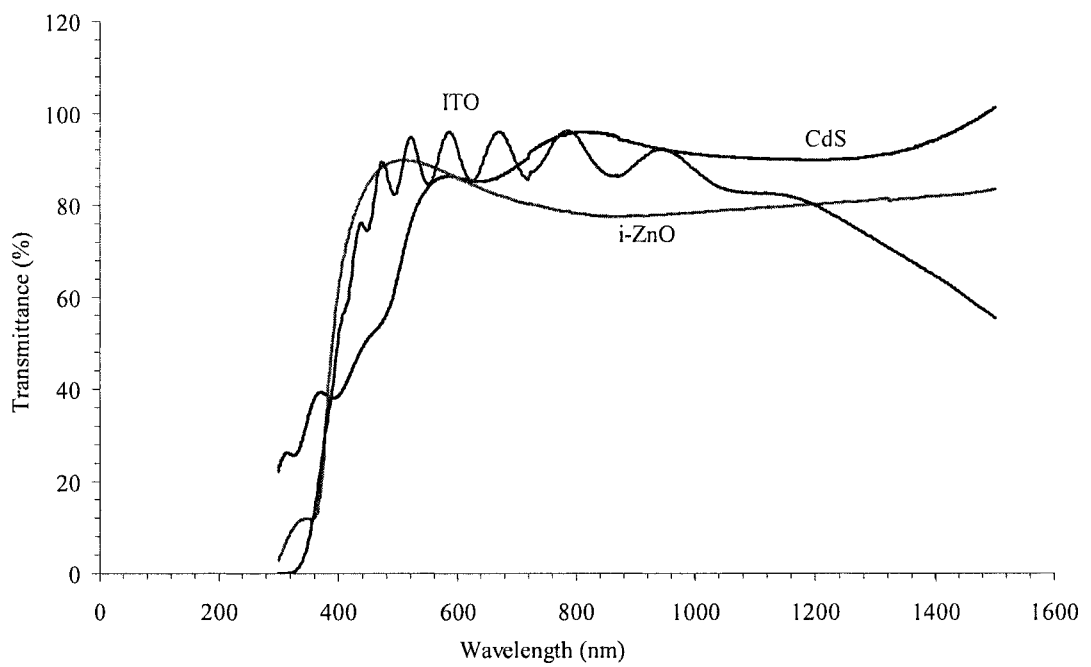


Figure C The graph of transmittance versus wavelength of optimised CdS, i-ZnO and ITO layers.

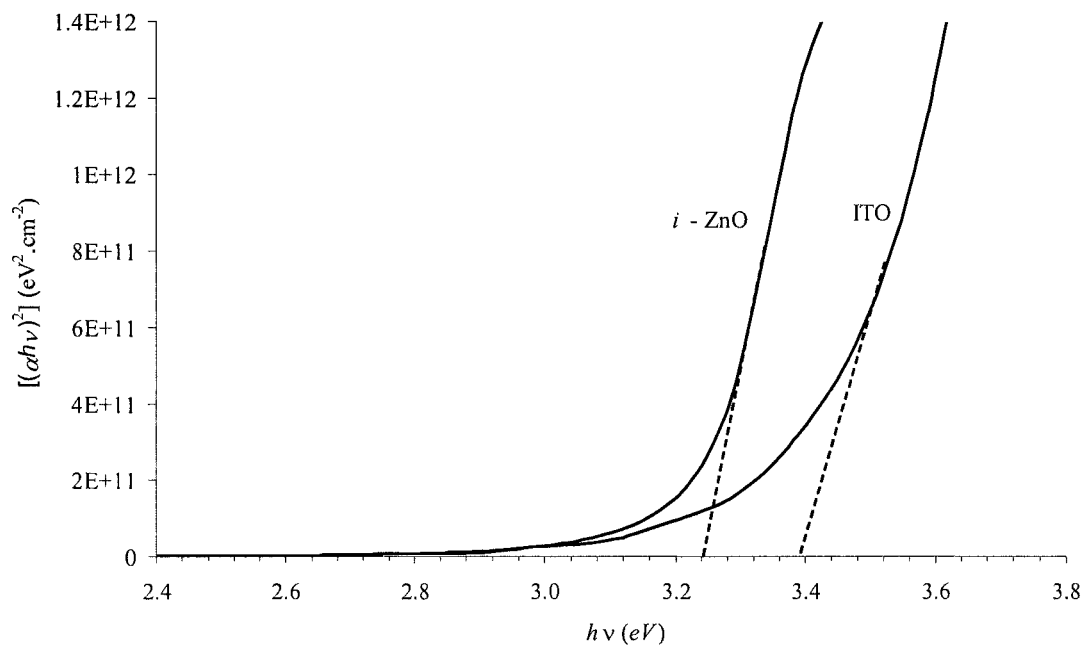


Figure D The graph of $(\alpha h\nu)^2$ versus $h\nu$ of good quality *i*-ZnO and ITO layers.

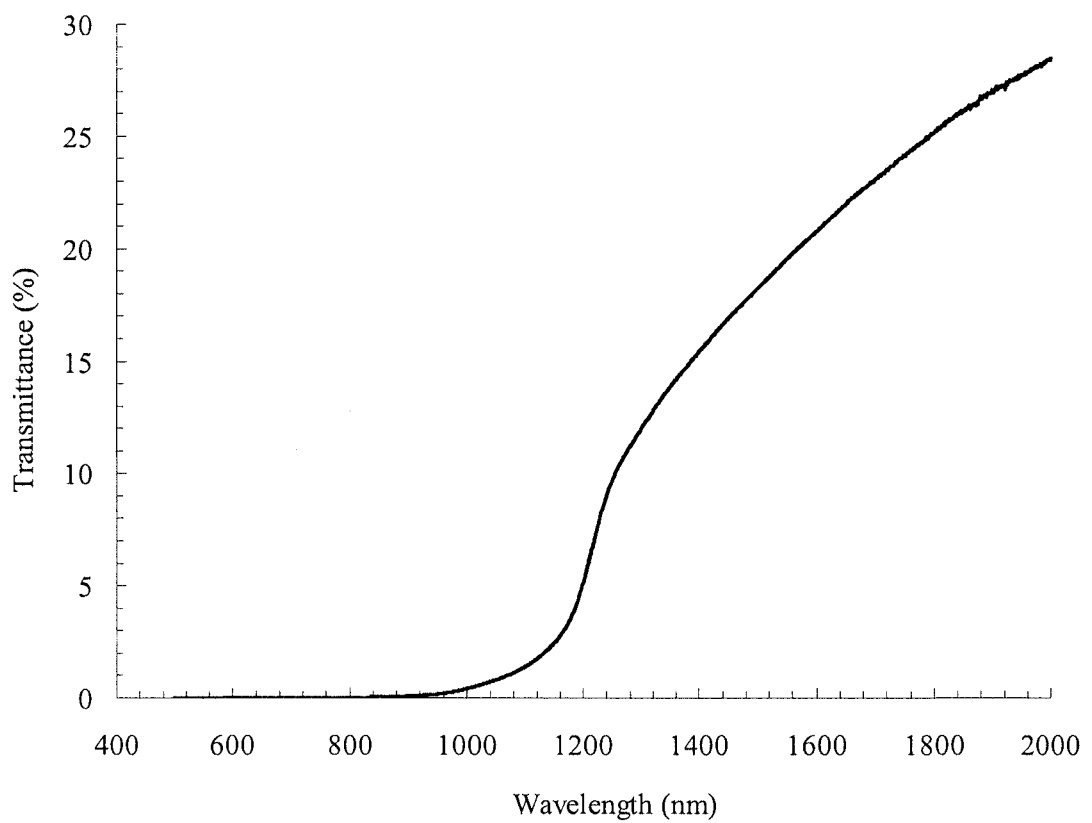


Figure E The graph of transmittance (%) versus wavelength of CIAS thin film on the glass substrate prepared from precursor layer with $n = 0.28$ (Sample KJL-G).

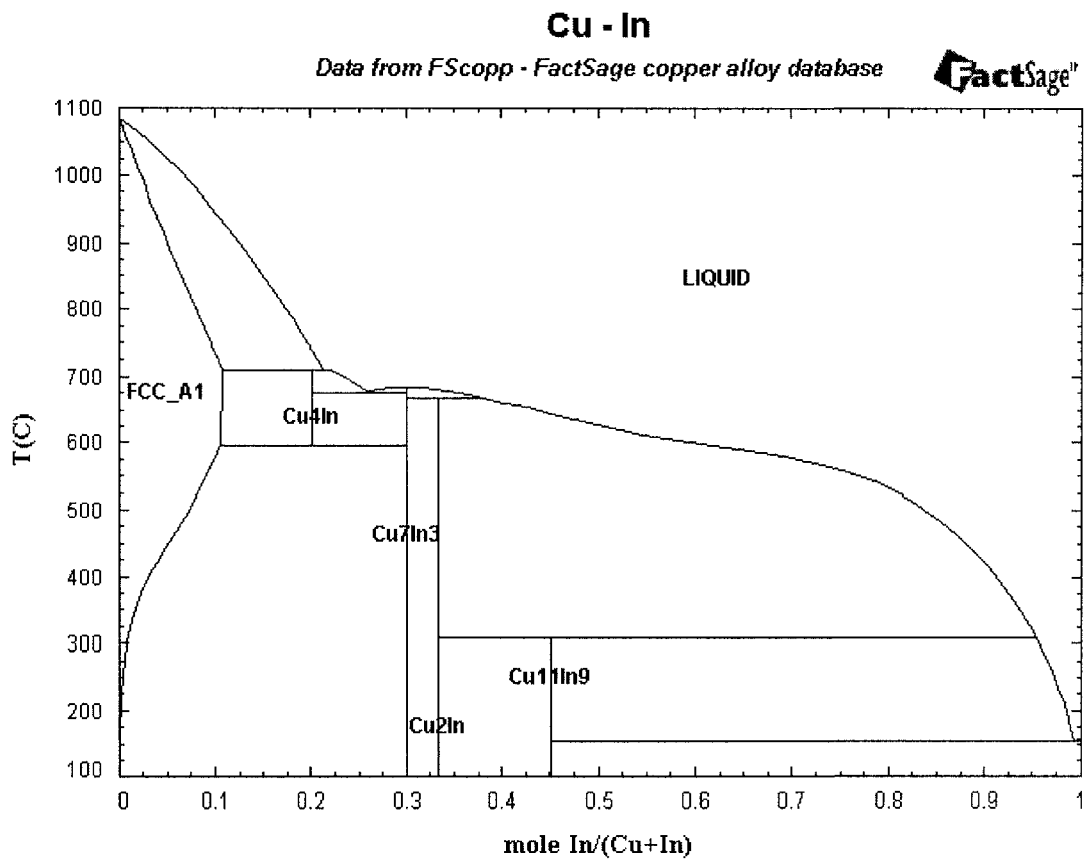


Figure F Phase diagram of Cu-In alloy [246].

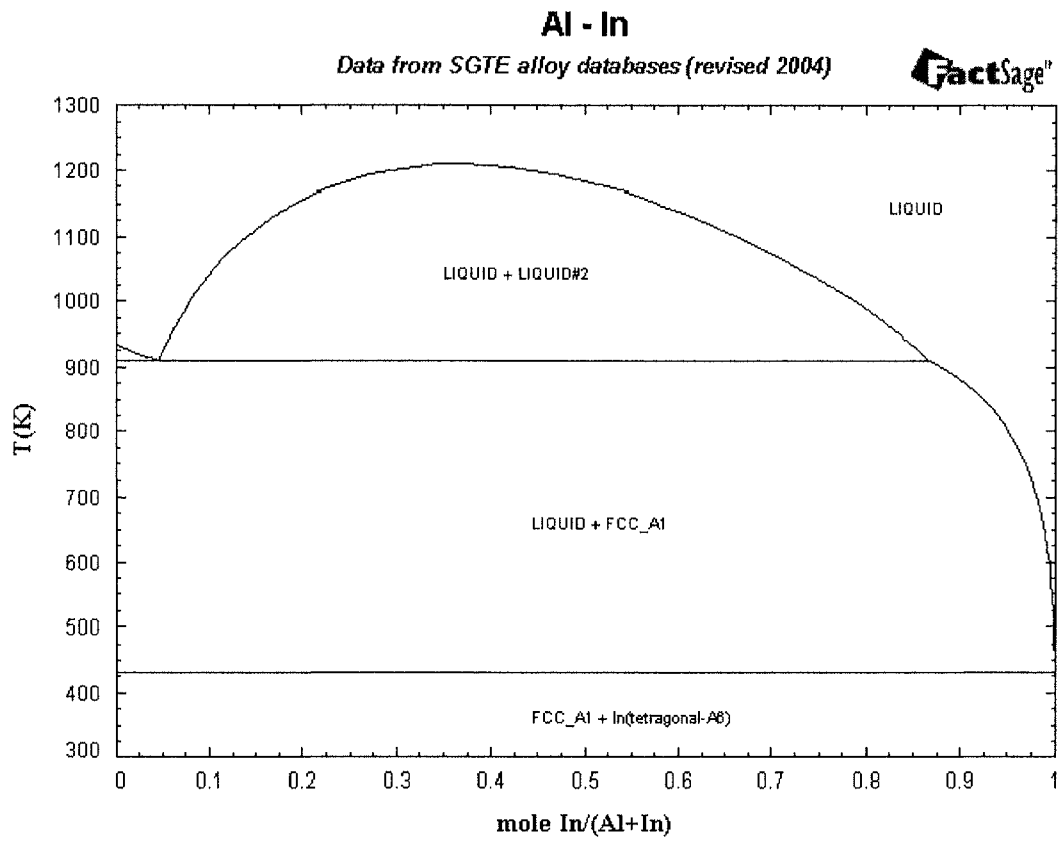


Figure G Phase diagram of Al-In alloy [247].

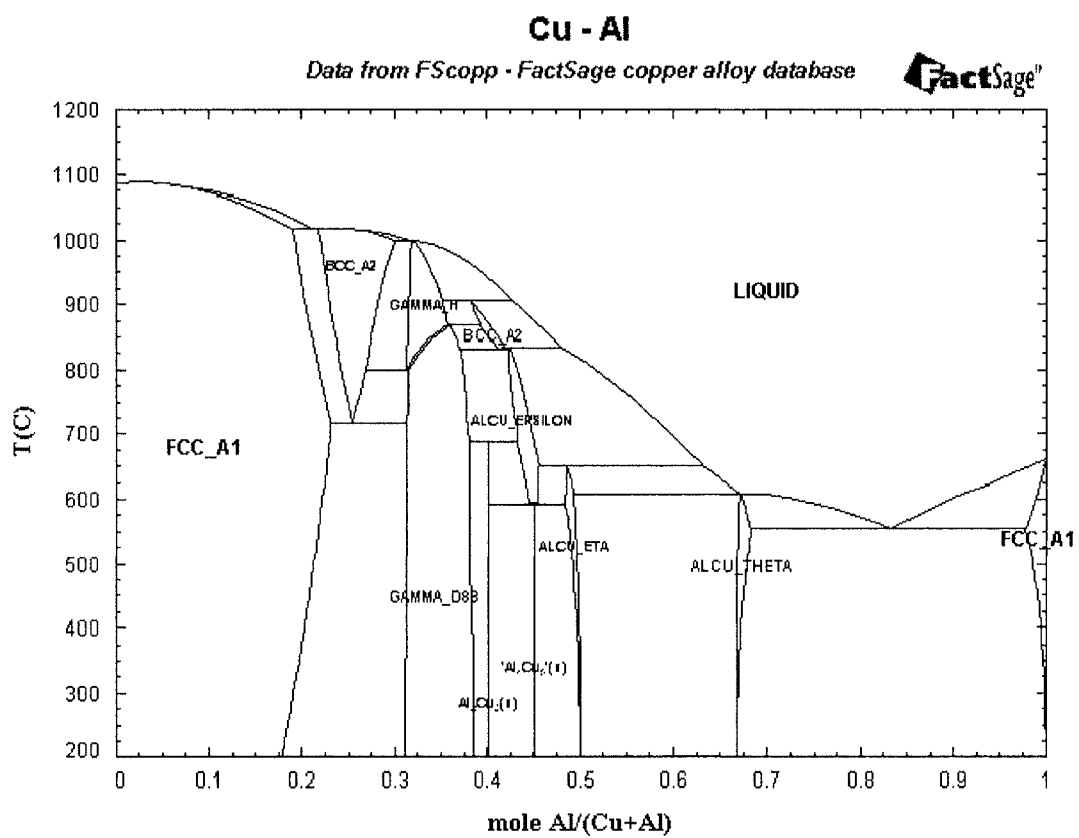


Figure H Phase diagram of Cu-Al alloy [248].

Appendix II

List of Actual Sample Names

Sample IDs in the thesis	Actual batch IDs used in the experiment (samples)
A	N107(A-F)
B	N122(A-G)
C	N111(O-U)
D	N122(H-N)
E	N111(A-N)
F	N122(O-U)
KJL-A	N109R
KJL-B	N64N
KJL-C	N65K2
KJL-D	N109D
KJL-E	N15Z
KJL-F	N115O
KJL-G	N172G
KJL-H	N171L
KJL-I	N170R

Appendix III

List of Publications and Presentations during PhD

- **List of Publications**

- [1] P. Nasikkar, G. Zoppi, I. Forbes, R. W. Miles, P. J. Dale, L. M. Peter, J. D. Major, and K. Durose, *Investigation and characterisation of the Influence of metallic precursor thickness on the properties of CuInSe₂ thin films*, Proceedings of the Photovoltaic Science Applications and Technology (PVSAT)-3 Conference, Durham University, UK (2007) 81-84.
- [2] G. Zoppi, I. Forbes, P. Nasikkar, and R. W. Miles, *Characterisation of thin films CuIn_{1-x}Al_xSe₂ prepared by selenisation of magnetron sputtered metallic precursors*, Thin-Film Compound Semiconductor Photovoltaics, Proceedings of the Material Research Society Symposium, San Francisco, USA 1012 (2007) 349-354.
- [3] G. Zoppi, I. Forbes, P. Nasikkar, and R. W. Miles, *Physical properties of CuAl_{1-x}In_xSe₂ produced by selenisation of Cu/Al/In(Se) precursor layers*, Proceedings of the 21st European Photovoltaic Solar Energy Conference, Dresden, Germany (2006) 1998-2001.
- [4] K. M. Hynes, I. Forbes, R. W. Miles, P. Nasikkar, D. Lane, K. D. Rogers and J. D. Painter, *The manufacture of CIGS based thin film PV cells with minimal environmental impact*, Proceedings of the PVSAT-2 Conference, Loughborough University, UK (2005) 69-76.

- **List of Presentations**

- [1] P. Nasikkar, G. Zoppi, I. Forbes and R. W. Miles, *Influence of metallic precursor thickness on the properties of CuInSe₂ thin films*, Northumbria University Research Forum, UK, January (2008).
- [2] P. Nasikkar, G. Zoppi, I. Forbes, R. W. Miles, P. J. Dale, L. M. Peter, J. D. Major, and K. Durose, *Investigation and characterisation of the Influence of metallic precursor thickness on the properties of CuInSe₂ thin films*, PVSAT-3 Conference, Durham University, UK, March (2007).
- [3] G. Zoppi, I. Forbes, P. Nasikkar, and R. Miles, *Physical properties of CuAl_{1-x}In_xSe₂ produced by selenisation of Cu/Al/In(Se) precursor layers*, 21st European Photovoltaic Solar Energy Conference, Dresden, Germany, September (2006).
- [4] P. Nasikkar, G. Zoppi, I. Forbes and R. W. Miles, *Characterisation of Cu(In,Al)Se₂ produced by 2-stage processing*, Institute of Physics meeting, London, UK, April (2006).
- [5] P. Nasikkar, G. Zoppi, I. Forbes and R. W. Miles, *A Study of molybdenum as a back contact layer for thin film solar cells*, Northumbria University Research Forum, UK, January (2006).
- [6] G. Zoppi, P. Nasikkar, and I. Forbes, *Fabrication and analysis of component layers for thin film CuInSe₂ solar cells*, Northumbria University Research Forum, UK, January (2006).